Photon scattering in 3D radiation-hydrodynamical simulations of late-type stellar atmospheres

Wolfgang Simon Hayek

A thesis submitted for the degree of

Doctor of Philosophy

of The Australian National University

ANU
THE AUSTRALIAN NATIONAL UNIVERSITY

Research School of Astronomy and Astrophysics
The Australian National University
Canberra ACT 0200
Australia

August 2010

Disclaimer

I hereby declare that the work in this thesis is that of the candidate alone, except where indicated below or in the text of the thesis.

- Chapter 3: The `BIFROST` code is developed by the solar physics group at the Institute for Theoretical Astrophysics at the University of Oslo; the radiative transfer module was developed, implemented and tested by the candidate.
- Chapter 4: The text was written by the candidate and co-authored by M. Asplund (Max Planck Institut für Astrophysik), M. Carlsson (University of Oslo), R. Trampedach (University of Boulder), R. Collet (Max Planck Institut für Astrophysik), B. V. Gudiksen (University of Oslo), V. H. Hansteen (University of Oslo) and J. Leenaarts (Utrecht University), based on simulations and analyses conducted by the candidate. It was published in *W. Hayek et al., "Radiative transfer with scattering for domain-decomposed 3D MHD simulations of cool stellar atmospheres", 2010, A&A, 517, 49.*
- Chapter 5: The text was written by the candidate, the simulations and analyses were conducted by the candidate in collaboration with R. Collet and M. Asplund. The results presented in this chapter will be published in a refereed journal.
- Chapter 6: The `SCATE` code is based on a line formation program written by Å. Nordlund, with contributions from M. Asplund, R. Trampedach, R. Collet and T. Pereira. It was partly rewritten and extended by the candidate.
- Chapter 7: The text was written by the candidate and co-authored by M. Asplund, R. Collet, and Å. Nordlund (University of Copenhagen), based on simulations and analyses conducted by the candidate. It will be published in *Hayek et al., "3D LTE spectral line formation with scattering in red giant stars", A&A submitted*

W.

Wolfgang Hayek
20 August, 2010

Abstract

Numerical models of stellar atmospheres fulfill an important role in astrophysical research. They describe the physical environment from which stellar radiation originates, allowing detailed analyses of the temperature and pressure stratification in the atmosphere, of the chemical composition, atmospheric motion, phenomena related to magnetic fields and more. Theoretical studies of stellar atmospheres usually involve two steps: first, the model atmosphere is constructed according to a set of parameters. Based on this model, a theoretical representation of an observable is produced, e.g., spectral lines or the center-to-limb variation of continuum radiation.

3D time-dependent radiation-hydrodynamical simulations of stellar atmospheres have been very successful in reproducing observations and have become a viable tool for solar physics and stellar astrophysics. Coupling detailed radiative transfer with a hydrodynamical description of stellar surface granulation, they allow accurate predictions of the atmospheric stratification, velocity fields, spectral line formation, magnetic phenomena etc.

The complexity and computational effort of 3D radiation-hydrodynamical simulations requires a variety of approximations, such as the assumption of local thermodynamic equilibrium (LTE) in the treatment of radiative transfer. This PhD thesis explores the enhancement of the radiation model with coherent photon scattering, studying its importance for radiative heating in 3D radiation-hydrodynamical simulations. By comparing the atmospheric temperature stratification derived from different treatments of scattering opacity, it is demonstrated that a solar-type photosphere is well-approximated when continuum scattering is treated as absorption, while this approach leads to significantly higher temperatures above the photosphere if applied to line-blanketing. In metal-poor giants, Rayleigh scattering is an important continuous opacity source; treating the opacity as absorption leads to significantly higher temperatures above the surface and a shallower temperature gradient. The temperature structure of the model atmosphere with coherent scattering can be approximated with reasonable accuracy by removing scattering opacity above the stellar surface and using a Planck source function, which largely reduces the computational effort.

3D spectral line formation is an essential diagnostic for simulations of stellar atmospheres, and a widely used tool for analyzing, e.g., the chemical composition of stars. Metal-poor giants are interesting astrophysical laboratories in this context, for studying the chemical evolution of the Galaxy and the origin of the elements. The second part of the thesis investigates LTE spectral line formation with continuum scattering in metal-poor giants. It is shown that an increasing thermalization depth through scattering at short wavelengths affects profile shapes and equivalent widths, with important consequences for measured abundances.

Contents

Disclaimer . . . 2
Abstract . . . 3

1 **Introduction** **11**
- 1.1 Radiation in astronomy and astrophysics . . . 11
- 1.2 Stellar atmospheres . . . 12

2 **The physics of late-type stellar atmospheres** **15**
- 2.1 Definition of a stellar atmosphere . . . 15
- 2.2 The hydrodynamical model . . . 16
  - 2.2.1 The equations of compressible hydrodynamics . . . 17
  - 2.2.2 The equation of state . . . 18
  - 2.2.3 Flow numbers . . . 19
- 2.3 Radiative transfer . . . 20
  - 2.3.1 The radiative transfer equation . . . 21
  - 2.3.2 Opacities . . . 22
  - 2.3.3 The source function . . . 23
- 2.4 The equations of radiation-hydrodynamics . . . 24
- 2.5 Convective and radiative heat transport . . . 25
  - 2.5.1 Convective instability . . . 26
  - 2.5.2 Convective energy fluxes . . . 28

3 **Numerical methods of radiation-hydrodynamics** **31**
- 3.1 The hydrodynamical solver . . . 31
  - 3.1.1 Discretization . . . 31
  - 3.1.2 Artificial viscosity . . . 32
- 3.2 Boundary conditions . . . 34
  - 3.2.1 The top boundary . . . 34
  - 3.2.2 The bottom boundary . . . 35
- 3.3 The radiative transfer solver . . . 36
  - 3.3.1 The method of characteristics . . . 36
  - 3.3.2 Radiative transfer regimes . . . 37
  - 3.3.3 The integral method . . . 38
  - 3.3.4 Approximate lambda iteration . . . 39
- 3.4 Time integration . . . 40
  - 3.4.1 The Hyman method . . . 41
  - 3.4.2 The 3rd order Runge-Kutta method . . . 41
  - 3.4.3 Stability limits . . . 42
- 3.5 Analytical test of the radiative transfer solver . . . 44
  - 3.5.1 Derivation of the analytical solution . . . 44

3.5.2 Comparison with the numerical result 46

4 Radiative transfer with scattering for domain-decomposed 3D MHD simulations of cool stellar atmospheres 51
4.1 Introduction 52
4.2 Radiative transfer with scattering and the radiative flux divergence 53
4.2.1 The radiative transfer equation 53
4.2.2 The radiative flux divergence and the wavelength integral 54
4.3 The numerical implementation 56
4.3.1 Short characteristics 56
4.3.2 The Gauss-Seidel scheme and MPI parallelization 58
4.3.3 Interpolation and grid refinement 63
4.3.4 Numerical flux divergences 64
4.4 Absorption and scattering opacity sources in the Sun 65
4.4.1 Continuum opacity 66
4.4.2 Line opacity 66
4.5 The effects of scattering on the photospheric temperature structure of a solar-type star 67
4.5.1 The 3D hydrodynamical surface convection model 67
4.5.2 Scattering in the 1D mean stratification 69
4.5.3 Scattering in the mean 3D model 70
4.5.4 Comparison of the 1D and 3D calculations and with other model atmospheres 71
4.6 Conclusions 75

5 The effects of scattering on the temperature structure of metal-poor giants 77
5.1 Introduction 78
5.2 3D radiation-hydrodynamical model atmospheres 78
5.3 The effects of scattering on the temperature structure 80
5.4 Summary 82

6 Spectral line formation 87
6.1 Spectral line opacity 88
6.1.1 Spectral line opacity in LTE 88
6.1.2 LTE absorber populations 89
6.1.3 Oscillator strength 90
6.1.4 Line profiles 91
6.2 The line source function with a background continuum 95
6.2.1 The LTE line source function 95
6.2.2 Scattering and redistribution 95
6.2.3 LTE lines with a scattering background continuum 96
6.3 Numerical methods for spectral line formation 97
6.3.1 The Gauss-Seidel method for anisotropic source functions 97
6.3.2 The Feautrier method 98
6.4 Rotational broadening 99

7 3D LTE spectral line formation with scattering in red giant stars 101
7.1 Introduction 102
7.2 Line formation with continuum scattering 103
7.3 3D radiation-hydrodynamical model atmospheres 104

7.4 3D line formation computations 106
7.5 The effects of scattering on the continuum flux 107
7.6 Spectral line formation with a scattering continuum 111
7.6.1 Fe I lines at 3000 Å and metallicity [Fe/H]=-3.0 111
7.6.2 Curves of growth for Fe I and Fe II lines 116
7.6.3 Curves of growth for molecular lines 116
7.7 Conclusions 117

8 Summary and outlook **121**

Bibliography **125**

Acknowledgments **137**

A Plasma physics **139**
A.1 The first law of thermodynamics 139
A.2 Plasma relaxation timescales 140

B Numerical methods **143**
B.1 Bézier interpolation of source functions and opacities 143
B.2 Local cubic monotonic interpolation 144
B.3 Angle quadrature 145

C Opacities **149**
C.1 Line scattering with the van Regemorter formula 149
C.2 Continuum opacity sources 150

D The SCATE code **153**
D.1 Numerical solution of the radiative transfer equation 153
D.2 Line opacities in the LTE approximation 154

Chapter 1

Introduction

1.1 Radiation in astronomy and astrophysics

Radiation has always been an important foundation, if not *the* foundation for astronomical and astrophysical research. Stellar light fascinated ancient astronomers, motivating them to chart the sky and to understand its nature. It inspired important scientific progress to explain the observations, leading to advances in the theory of mechanics and many other disciplines. Astronomy also contributed evidence and motivation for philosophers and theologists to understand our existence. Their ideas still influence society and our political life, through religion, our relationship towards nature and many other aspects. Such direct and indirect cultural importance emerges in the continuous public interest in astronomical research.

Radiation is an essential tool to extend our knowledge of the universe, motivating the construction of ever larger telescopes and theoretical efforts to refine our understanding of its sources using mathematical and physical theories. Radiation allows us to probe places in the Universe that are far beyond reach with current technology, either because of their large distance or because of their extreme physical conditions. Already the Sun and the solar-system planets and moons, our closest astrophysical sources of radiation, provide us with numerous puzzles to solve.

The english chemist William Hyde Wollaston[1] was the first scientist who reported dark lines in the visible solar spectrum in 1802, which had previously appeared continuous. Between 1814 and 1824, Joseph von Fraunhofer published a systematic analysis of the solar spectrum, and labeled the most prominent features with letters from A to G. Their origin remained unknown during Fraunhofer's lifetime. Even though scientists have found millions of spectral lines in solar light later on, Fraunhofer's labels are still commonly used in astrophysical literature.

The importance of Wollaston's and Fraunhofer's discovery was understood when Gustav Robert Kirchhoff and Robert Wilhelm Bunsen started to use spectroscopes as tools for chemical analyses, attributing spectral features to specific elements in the mid-19th century. Transferring their findings to Fraunhofer's solar lines, it was realized that the Sun is composed of elements which are also found on earth, and that the same applies to other celestial bodies as well. It is interesting to note in this context that, in the same century, the French philosopher Auguste Comte believed in the impossibility of understanding the structure behind the astronomical discoveries:

> Of all objects, the planets are those which appear to us under the least varied aspect. We see how we may determine their forms, their distances, their bulk, and

---

[1] The historical references in this section are mostly taken from Isaac Asimov's The History of Physics (Walker Publishing, 1966)

> their motions, but we can never know anything of their chemical or mineralogical structure, and, much less, that of organized beings living on their surface. [...]
> Auguste Comte, "The Positive Philosophy", Book II, Chapter 1 (1842)

The bulk of radiation emitted by most stars closely resembles a black body. Wilhelm Wien and Josef Stefan related black body radiation to gas temperature, enabling an important classification of stellar spectra and paving the way to investigate the evolution of stars. At the beginning of the 20th century, Max Planck's explanation of the black body spectrum through statistical mechanics and the quantum hypothesis started a rapid development in atomic physics and our understanding of the detailed mechanisms behind the interaction between radiation and matter.

The fundamental tools became available to investigate the processes that lead to the emission of the radiation that we observe in telescopes and analyze in spectrographs, turning astronomy into astrophysics.

1.2 Stellar atmospheres

Stars consist mainly of opaque hot plasma that makes their interior invisible to observations of electromagnetic radiation. The gas becomes transparent only at the surface, allowing radiation to escape into space. On its way through the outermost shell of the star, the atmosphere, light is absorbed and emitted by atoms and molecules, giving its spectrum a very distinct "fingerprint". The formation of the radiation field and thus the appearance of spectral features depends on microphysical states of the radiating gas and the thermal structure of the atmosphere, as it was demonstrated by Payne (1925), and the interaction between radiation and matter determines, in reverse, states and structure. Understanding stellar radiation thus requires solving the coupled problem of radiative transfer, the thermodynamics of fluids and atomic physics.

The large amount of observational data available for the Sun allows the construction of semi-empirical models that reproduce certain spectral features (e.g., Holweger, 1967). Early efforts to infer the solar (or stellar) atmospheric structure from theory were based on simple models that, among many other approximations, assume a single frequency-independent (or "gray") opacity (e.g., Milne, 1921). It was quickly realized that a too idealized treatment of the problem does not provide a sufficient degree of realism to reproduce observations and to obtain a detailed understanding of the physics; see, e.g., the discussions of the effects of spectral lines using an analytical model by Chandrasekhar (1935) or numerical calculations by Böhm (1954). The rapid development of computers in the mid-20th century allowed astrophysicists to produce more advanced synthetic atmospheres for a large variety of stellar parameters. Numerical programs such as `MARCS` (Gustafsson et al., 1975) or `ATLAS` (Kurucz, 1979) were created, which are still widely used in astrophysical research. They describe the atmosphere in a one-dimensional plane parallel (or spherically symmetric) approximation, which is nowadays often called a "classical" model. In the following decades, these programs were extended and refined, and applied to a larger range of objects, including brown dwarf stars and exoplanetary atmospheres.

Late-type stars like the Sun required further sophistication of theoretical methods: observations provided evidence for the existence of gas motion in the atmosphere that strongly influences the emitted light; theoretical considerations identified convection as the underlying physical process (Unsöld, 1930). This led to the construction of models in 3D to account for inhomogeneities in the stratification and to include time-dependent hydrodynamics to reproduce motion at the stellar surface (e.g., Nordlund, 1982). The larger complexity of a radiation-hydrodynamical description of late-type stellar atmospheres was rewarded by improved agreement of model predictions with the observations and a deeper understanding of the physics.

Modern 3D radiation-hydrodynamical model atmospheres of late-type stars still use numerous approximations to make the problem tractable for currently available computers. The advent of parallel computing with hundreds or thousands of processing units opened up new possibilites for investigating more complex physical mechanisms and for increasing the realism of synthetic models.

Radiative transfer is an essential ingredient for model atmospheres, as radiation becomes the dominant mode of energy transport at the surface. Its numerical treatment is complex and often dominates computation times. Scattering of radiation has therefore mostly been neglected in 3D simulations: the scattering term in the radiative transfer equation makes solutions self-dependent; they need to be determined using an iterative solver rather than by simple numerical integration. However, scattering can have important effects on the radiation field: photons may escape from deeper, hotter layers in the atmosphere, radiative heating is reduced when photons are scattered rather than absorbed, and spectral lines change their shapes as scattering couples radiation from different angles and with different frequencies.

This PhD thesis explores the importance of photon scattering in stellar atmospheres. The focus lies first on 3D radiation-hydrodynamical simulations of stellar surfaces. Chapter 2 describes selected aspects of the underlying physical model of hydrodynamics and radiative transfer. The numerical implementation in the `BIFROST` code (Gudiksen et al., in prep.) which was used for the simulations is discussed in Chapter 3. Chapter 4 contains a refereed publication that describes the radiative transfer method and discusses the effects of scattering on the atmosphere of a solar-type star; a similar analysis for metal-poor giant stars is presented in Chapter 5.

In Chapter 6, the thesis moves towards spectral line formation, an important diagnostic tool for model atmospheres and for astrophysical measurements, discussing some essential models that treat the atomic physics and numerical methods to solve the line formation problem. The effects of continuum scattering on line formation in red giant stars are analyzed in Chapter 7. Chapter 8 gives a summary of the thesis and highlights possible future developments.

Chapter 2

The physics of late-type stellar atmospheres

2.1 Definition of a stellar atmosphere

Similar to the Earth's atmosphere, the stellar atmosphere encloses the star in a spherical shell. Unlike the Earth, however, stellar envelopes mostly consist of hot plasma with a smooth transition from the interior to space instead of cool gas that is bounded by condensed matter. The thickness of the atmosphere varies strongly with stellar type, from a very thin layer in dwarf stars to a considerable fraction of the stellar radius in the case of giants and supergiants. It is therefore not immediately clear how to strictly define a stellar atmosphere. Gray (2005) describes it in general terms as "a transition region from the stellar interior to the interstellar medium".

A fundamental feature of the atmosphere is an exponential outward decrease of gas opacity, producing an optical surface through which radiation can escape into space. Radiation inside the star is optically thick and photons diffuse outward in a random walk, with mean free paths on a centimeter scale or less. Matter is essentially in local thermodynamic equilibrium; the radiation field is thus almost isotropic and follows a Planck distribution. The optically thin outer layers of the atmosphere are characterised by photon mean free paths that reach beyond the stellar atmosphere and photons are lost into space. The radiation field consequently becomes strongly anisotropic above the boundary layer of the optical surface, and numerous atomic and molecular absorbers in the gas add millions of narrow spectral lines to the previously smooth Planck spectrum. This is the part of the atmosphere that is observed in telescopes.

Gray (2005) divides the solar atmosphere into several regions: coming from the interior, the sub-photosphere (at heights $h < 0$ in Fig. 2.1) is still optically thick at all wavelengths with temperatures around some 10000 K. It is roughly bounded by the continuum optical surface in the visual band ($h = 0$). Visual continuum photons contribute most of the solar luminosity, as the Planck function for $T = 5777\,\mathrm{K}$ peaks in this wavelength band. The photosphere starts around the optical surface and extends up to a temperature minimum of about 4000 K at $h \approx 500\,\mathrm{km}$. Most of the visible solar spectrum is formed in this region, apart from the cores of the strongest lines. Above the photosphere, the temperature increases again to about 7000 K in the chromosphere, which reaches up to $h \approx 2000\,\mathrm{km}$. It is important to note that empirically derived temperatures in the chromosphere depend on the chosen spectral feature: studies of CO lines are inconsistent with an inversion in the temperature structure (e.g., Ayres and Testerman, 1981). 3D simulations of a magnetically quiet solar chromosphere have found a bifurcation in the temperature distribution that could explain the co-existence of a hot and cold component (Wedemeyer et al., 2004). The outermost region of the solar atmosphere is called the corona,

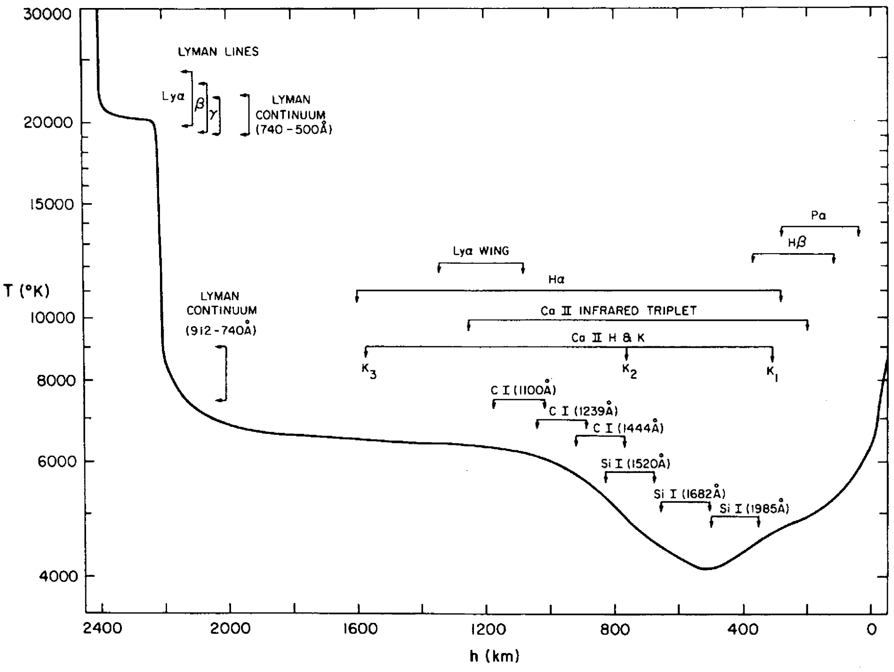

Figure 2.1: Solar temperature structure as a function of atmospheric height derived by Vernazza et al. (1973) using a semi-empirical model atmosphere; the continuum optical surface is at $h = 0$. Arrows indicate the formation height of important spectral features.

which is marked by a sharp increase in temperatures and strong ionization of the coronal gas.

Chromosphere and corona are heavily influenced by magnetic fields: theoretical studies support scenarios in which magnetic heating occurs through twisting of coronal magnetic flux tubes by gas motion beneath the surface, releasing energy by dissipation (e.g., Parker, 1983; Gudiksen and Nordlund, 2005; Nordlund et al., 2009). Such solar (or stellar) magnetic fields are generated in the interior and give rise to a whole variety of different phenomena at the surface, which include spots, faculae, plages, spicules and many more.

2.2 The hydrodynamical model

Stellar surface plasma is a dilute, hot, partly ionized, magnetized gas consisting of molecules, neutral atoms, ions and electrons. Hydrogen and helium dominate the chemical composition, heavier elements ("metals") appear only in traces. A full description of all particles with their individual dynamics and interactions is neither feasible nor necessary. Macroscopic plasma physics may instead be investigated with three complementary approaches (see the discussion in Mihalas and Mihalas, 1984).

The thermodynamic view assumes that the gas is in local thermodynamic equilibrium and governed by macroscopic quantities, such as pressure, temperature, density etc.. The time evolution of the plasma assumes a fluid of one or several components and is described using the hydrodynamic equations, which form the foundation of practically all current 3D simulation codes. The gas density around the surface of late-type stars lets particle motions relax to a statistical equilibrium distribution on very short time scales, making a hydrodynamical description a valid approximation for simulations of stellar surface granulation (see Appendix A.2).

The kinematic view describes individual particles and their interaction with the background medium through equations of motion, which is useful for detailed studies of microscopic mechanisms. A third approach employs statistical mechanics, where detailed phase-space distribution functions of particles are obtained from solving Boltzmann equations.

2.2.1 The equations of compressible hydrodynamics

Stellar atmospheres are strongly stratified by gravity and consist of highly compressible gas. The plasma conducts sound waves and may undergo large-scale pressure oscillations ("p-modes") and gravity oscillations ("g-modes"). Typical microscopic and macroscopic plasma speeds remain far below the relativistic regime; a treatment using Newtonian dynamics is sufficient. The compressible hydrodynamical equations on a stationary grid in the Eulerian picture are an adequate choice for simulating surface convection (see, e.g., Nordlund et al., 2009). They consist of a set of 5 predictive equations for macroscopic states.

The first equation or continuity equation accounts for mass conservation:

$$\frac{\partial \rho}{\partial t} + \nabla \cdot (\rho \mathbf{u}) = 0, \tag{2.1}$$

where ρ is the total gas density and $\mathbf{u}$ is the gas velocity; the gas momentum density $\rho\mathbf{u}$ is equivalent to a local mass flux. The dynamics are governed by the equation of motion for the components of the gas velocity vector or momentum vector, in this representation also called the Navier-Stokes equations:

$$\frac{\partial \rho \mathbf{u}}{\partial t} + \nabla \cdot (\rho \mathbf{u}\mathbf{u}) + \nabla P = -\rho \mathbf{g} + \nabla \cdot \tau_{\text{visc}}, \tag{2.2}$$

where P is the total gas pressure, τ_{visc} is the viscosity tensor and $\mathbf{g}$ is the gravitational acceleration. The tensor term $\rho\mathbf{u}\mathbf{u}$, which is also often called the inertial term, provides kinetic energy flux and is responsible for complex turbulent behavior of gas with a large disparity of inertial and viscous length scales. In stellar atmospheres, plasma viscosity is small and acts on very short length scales (see Sect. 2.2.3), and it would in principle be sufficient to neglect the term $\nabla \cdot \tau_{\text{visc}}$ in the equations. However, numerical stability requires smoothening of the hydrodynamical flow using artificial viscosity (see Sect. 3.1). The simulations assume constant gravity across the entire domain, which is a very good approximation for dwarf stars like the Sun. It breaks down in the case of supergiant stars, where the atmosphere covers a significant fraction of the stellar radius.

The last remaining equation accounts for the conservation of internal energy of the gas. It is also sometimes called the thermodynamic equation due to its equivalence to the first law of thermodynamics (Appendix A.1) in the local co-moving frame of the gas flow:

$$\frac{\partial e}{\partial t} + \nabla \cdot (e\mathbf{u}) + P(\nabla \cdot \mathbf{u}) = Q_{\text{rad}} + Q_{\text{visc}}, \tag{2.3}$$

where e is the internal energy per unit volume. The term $e\mathbf{u}$ represents the internal energy flux, $P(\nabla \cdot \mathbf{u})$ is the rate of change of internal energy through compression and expansion work, and Q_{rad} is a source term that accounts for radiative heating and cooling. The last quantity on the right-hand side corrects the energy budget for viscous dissipation of kinetic energy:

$$Q_{\text{visc}} = \sum_{ij} \tau_{ij} \frac{\partial u_i}{\partial x_j}. \tag{2.4}$$

2.2.2 The equation of state

The hydrodynamic equations (Eq. (2.1), Eq. (2.2), Eq. (2.3)) are not a closed system: in addition to the radiative heating rate Q_{rad}, the gas pressure P must be determined using an equation of state (EOS), which needs to account for all microphysical states that the particles may occupy.

Surface plasma of late-type stars is dilute with small occupation numbers of physical states, so that quantum mechanical degeneracy effects are negligible. However, the gas is at least partly ionized and may form molecules in cooler layers. The electrons of the different atomic and molecular components may populate excited states, and molecules experience vibrational and rotational motion. Including such internal energy states is essential: simulations have shown that most of the energy transported outward by convective flow near the surface is stored in gas ionization rather than thermal motion. The smaller heat capacity of an ideal gas that has no internal degrees of freedom would result in flow speeds that are much larger than observed in the Sun to maintain the solar luminosity (Nordlund et al., 2009).

The fundamental problem of devising a realistic equation of state consists in accounting for all accessible microscopic states of a plasma in atmospheric conditions. Hydrogen and helium are naturally the most important components. Heavier elements, such as carbon, nitrogen and oxygen contribute a significant amount of electrons, affecting the ionization balance of all elements, and may form abundant molecular species. In principle, the microphysical state of the different plasma components changes through electromagnetic interaction with particles and the radiation field, and on varying time scales depending on the physical environment. The complexity of treating all such processes exceeds current computational limits by many orders of magnitude. Non-equilibrium physics can therefore only be approximately included in the EOS for selected mechanisms such as time-dependent hydrogen ionization (Leenaarts and Wedemeyer-Böhm, 2006; Leenaarts et al., 2007). Neglecting the effects of the radiation field and assuming instant equilibration leads to the approximation of local thermodynamic equilibrium (LTE). All microscopic states then only depend on a pair of macroscopic state variables, e.g. internal energy e and density ρ. The EOS can be used in tabulated form, which is a tremendous simplification for simulations of stellar surface granulation.

The Mihalas-Hummer-Däppen equation of state (MHD EOS, Hummer and Mihalas, 1988; Mihalas et al., 1988; Däppen et al., 1988; Mihalas et al., 1990) provides a modern and realistic treatment of stellar plasma in LTE and is well-suited for stellar interiors as well as late-type stellar atmospheres (see, e.g., the discussion in Trampedach et al., 2006). In its current state of development, it only includes the hydrogen molecules H_2 and H_2^+; the MHD EOS would therefore need to be expanded to the describe the complex chemistry of very cool objects such as brown dwarf stars, where heavier elements form dust and large numbers of molecules in the atmosphere.

The MHD EOS is based on the principle of free energy minimisation. The free energy F of a thermodynamic system is defined as

$$F = E - TS, \tag{2.5}$$

where E is the internal energy, T is the temperature and S is the entropy. Inserting the first law of thermodynamics,

$$dE = TdS - PdV + \sum_i \mu_i dN_i \tag{2.6}$$

into the total differential of F leads to the relation

$$dF = -SdT - PdV + \sum_i \mu_i dN_i, \tag{2.7}$$

where V is the gas volume, μ_i is the chemical potential of particle species i, and N_i is the number of particles of this species. F is minimal for a system in equilibrium: $dT = 0$, $dV = 0$ and $\{dN_i\} = 0$ require $dF = 0$ in Eq. (2.7); the entropy S has a maximum in equilibrium and F must consequently be minimal (Eq. (2.5)).

The free energy of stellar plasma is assumed to consist of the following contributions:

$$F_{\mathrm{plasma}} = F_{\mathrm{t}} + F_{\mathrm{i}} + F_{\mathrm{e}} + F_{\mathrm{C}}, \tag{2.8}$$

where F_{t} accounts for translational free energy of all particles, F_{i} is the free energy of internal states, F_{e} is the free energy of electrons (which is treated separately as the electron gas may be partly degenerate deeper in the stellar interior) and F_{C} is the free energy of electrostatic (Coulomb) interactions between charged particles. The different terms are given by analytical expressions which assume an ideal gas for each state component, assisting the minimization process and the derivation of thermodynamic quantities once the EOS is solved.

Transitions between the different particle species follow stoichiometric equations that couple their population numbers $\{N_i\}$. Ionization and recombination processes between the states j and $j+1$ of each atom and molecule are described by expressions of the kind

$$\frac{\partial F}{\partial N_j} - \frac{\partial F}{\partial N_{j+1}} - \frac{\partial F}{\partial N_{\mathrm{e}}} = 0, \tag{2.9}$$

with the chemical potentials $\partial F/\partial N_j \equiv \mu_j$. Formation and dissociation of diatomic molecules with components A and B is included by using a similar set of equations,

$$\frac{\partial F}{\partial N_{\mathrm{AB}}} - \frac{\partial F}{\partial N_{\mathrm{A}}} - \frac{\partial F}{\partial N_{\mathrm{B}}} = 0. \tag{2.10}$$

If the entire system is in equilibrium, the hypothesis of detailed balance requires that each of these equations must vanish individually with $dF = 0$ and $dN_{\mathrm{A}} = dN_{\mathrm{B}} = -dN_{\mathrm{AB}}$ for the various particle reactions. The resulting system of nonlinear equations is solved for population numbers $\{N_i\}$ using a Newton-Raphson scheme. Thermodynamical relations provide, e.g., the gas pressure through the partial derivative

$$P = \left(\frac{\partial F}{\partial V}\right)_{T,\{N_i\}} . \tag{2.11}$$

Similar equations yield temperature, internal energy, and entropy.

A very important problem for the development of an EOS for stellar atmospheres and interiors is the divergence of the partition functions for electron excitation: single atoms and molecules may reach an infinite number of excited states with increasing spatial extent of the corresponding electron wave functions. In stellar plasma, such high-excitation atoms are ionized through Stark interaction with surrounding particles, and the divergence has no practical significance. The MHD EOS includes a detailed treatment of the Stark effect, which defines occupation probabilities for each excitation state that effectively suppress the highest levels.

2.2.3 Flow numbers

Hydrodynamical flow can be characterized by comparing the relative importance of the different terms that appear in the hydrodynamical equations. This leads to the definition of dimensionless flow numbers, which can be used to determine general flow behavior and to compare flows in different physical environments. Depending on the physical model and thus on the appearance of terms in the hydrodynamical equations, there exists a large variety of such numbers. In the context of stellar atmospheres, the Reynolds number, the Prandtl number and the Mach number are of particular interest and shall be discussed in the following.

Dividing the Navier-Stokes equations (Eq. (2.2)) by a characteristic velocity u and a length scale L delivers a flow number that scales the viscous diffusion term, the well-known Reynolds number

$$\mathrm{Re_L} = \frac{uL}{\nu}, \tag{2.12}$$

The length scale L is given by the typical horizontal size of surface flow structures or the local vertical pressure scale height (both are related through mass conservation), and ν is the kinematic viscosity of the plasma. Kippenhahn and Weigert (1990) estimate a plasma viscosity of $\nu = u_{\mathrm{th}} d$, where u_{th} is the thermal velocity and d is the average distance between particles. Since microscopic and macroscopic speeds of the atoms are of similar order, the Reynolds number is dominated by the disparity between microscopic and macroscopic length scales L/d. Solar granules have sizes of $\sim 1000\,\mathrm{km}$, while typical particle distances are small ($d \ll 1\,\mathrm{cm}$). The Reynolds number is very large, and it is clear that stellar surface plasma should have a strong tendency to build up turbulent motion. Numerical simulations of the solar atmosphere have indeed found granulation flow fields that resemble turbulence (Muthsam et al., 2007), but its detailed spatial structures are difficult to observe: photospheric radiation is dominated by the bright granules which exhibit only small intensity variations. Radiation cannot penetrate deep into the convection zone, and very fine structures in the gas flow are not resolved.

The Prandtl number compares the magnitudes of kinematic viscosity ν and thermal conductivity K:

$$Pr = c_{\mathrm{P}} \rho \frac{\nu}{K}, \tag{2.13}$$

with the specific heat c_{P} at constant pressure and the gas density ρ. Thermal conductivity in stellar atmospheres is mostly dominated by radiative transfer; energy transport is so efficient that the Prandtl number is small. Pr can be interpreted as a comparison of inverse time scales of viscous and thermal interaction, or as a comparison of thickness of kinematic and thermal boundary layers: radiative energy transfer in stellar atmospheres happens on very small time scales, producing thermal boundary layers that are larger than kinematic boundary layers.

The Mach number is defined as the ratio of flow speed u and sound speed c_{s},

$$M = \frac{u}{c_{\mathrm{s}}}. \tag{2.14}$$

Flow speeds that exceed the local sound speed ($M > 1$) are called supersonic, $M < 1$ characterizes subsonic flow, which dominates surface granulation. However, acceleration of gas above granules through pressure effects or shock formation forces local supersonic velocities (Stein and Nordlund, 1998).

2.3 Radiative transfer

The propagation of photons and their interaction with matter can be treated in different ways, depending on the physical environment and the quantities of interest. In the high-energy domain of particle physics or when interactions with single photons are investigated, a detailed description in a consistent quantum field theory is required. In typical atomic physics applications, a radiation field of many photons may be approximated using Maxwell's equations, taking time-dependence, phase and polarization into account.

In stellar atmospheres, radiation fields are moderately intense and non-coherent. Radiative energy transfer through bulk absorption and emission of photons in matter is well-approximated in a macroscopic treatment with the radiative transfer equation, assuming linearity in the interaction between the radiation field and the surrounding medium. Gradients in stellar atmospheres are small on the scale of photon wavelengths, allowing a description of radiation in the particle model (see the discussion in Oxenius, 1986).

2.3.1 The radiative transfer equation

There are different ways to establish the radiative transfer equation. Besides postulating the equation with phenomenological arguments, it can be shown that it is equivalent to a Boltzmann equation by assuming that photons behave like a particle gas (Oxenius, 1986). In this particle picture, photons follow a distribution function

$$dN = \phi(\mathbf{x}, \mathbf{p}, t)\mathbf{dxdp}, \tag{2.15}$$

where dN is the number of photons per unit volume in phase space at a given time t. The photon momentum depends on its frequency through $\mathbf{p} = (E/c)\hat{\mathbf{n}} = (h\nu/c)\hat{\mathbf{n}}$, where c is the speed of light, h is the Planck constant and $\hat{\mathbf{n}}$ is the flow direction. The time evolution of the distribution function ϕ is governed by a Boltzmann equation with a source term S^+ and a sink term S^- for the creation and destruction of photons,

$$\frac{\partial\phi}{\partial t} + \frac{h\nu}{c}\hat{\mathbf{n}} \cdot \nabla\phi = S^+ - S^-. \tag{2.16}$$

In astrophysics, the radiation field is traditionally described by the specific intensity I, a distribution function for the energy dE that is radiated through a surface area dA into solid angle $d\Omega$ per time dt and frequency interval $d\nu$; the area dA may be tilted by an angle θ away from the beam direction:

$$dE = I(\mathbf{x}, \hat{\mathbf{n}}, \nu, t)dtd\nu \cos\theta dAd\Omega. \tag{2.17}$$

Specific intensity and the photon distribution function are related through the equality

$$I(\mathbf{x}, \hat{\mathbf{n}}, \nu, t) = \frac{h^4\nu^3}{c^2}\phi(\mathbf{x}, \mathbf{p}, t). \tag{2.18}$$

The Boltzmann equation (Eq. (2.16)) can thus be rewritten as the monochromatic radiative transfer equation for frequency ν,

$$\frac{1}{c}\frac{\partial I_\nu}{\partial t} + \hat{\mathbf{n}} \cdot \nabla I_\nu = -\chi_\nu I_\nu + j_\nu. \tag{2.19}$$

The source and sink terms S^+ and S^- are replaced by the emissivity j_ν and the extinction term $\chi_\nu I_\nu$. The interaction with matter is reduced to these bulk rate coefficients: the radiative transfer equation itself does not include any effects of absorption or emission on the physical state of the material, implicitly assuming a splitting between radiative interaction and material feedback.

In analogy to gas dynamics, one may define moments of the specific intensity I_ν by integration over solid angle. This is particularly useful for solving transport problems if the anisotropy of the radiation field is weak and the series of moments can be truncated at low order; unlike a real particle gas, the photon field does not relax to an isotropic distribution through self-interaction. In stellar atmospheres, I_ν is highly anisotropic due to the dominance of outward energy transport, and it is necessary to solve the radiative transfer equation (Eq. (2.19)) rather than moment equations.

The zeroth moment of the specific intensity I_ν yields the mean intensity

$$J_\nu = \frac{1}{4\pi} \int_{S^2} I_\nu d\Omega, \tag{2.20}$$

where S^2 denotes the unit sphere. J_ν is equivalent to a photon density per unit volume. The first moment yields the components of the radiative flux in direction $\hat{\mathrm{n}}_\mathrm{i}$,

$$F_{\nu,i} = \int_{S^2} I_\nu \left(\hat{\mathrm{n}}_\mathrm{i}, \hat{\mathrm{n}}'\right) d\Omega', \tag{2.21}$$

where $(\hat{\mathrm{n}}_\mathrm{i}, \hat{\mathrm{n}}')$ is the inner product of direction vectors. The second moment defines a radiation pressure tensor.

2.3.2 Opacities

The radiative transfer equation (Eq. (2.19)) for a medium with zero emission ($j_\nu = 0$) predicts that the amount of radiation dI_ν that is removed from the radiation field along the photon path in direction $\hat{\mathrm{n}}$ depends linearly on the incident radiation I_ν and the opacity χ_ν. Opacity is a macroscopic material coefficient that includes both absorption of photons, with subsequent thermalization of its energy, and scattering of photons away from the incident beam:

$$\chi_\nu = \kappa_\nu + \sigma_\nu, \tag{2.22}$$

where κ_ν is the absorption coefficient and σ_ν is the scattering coefficient.

In general, the opacity at a given frequency ν can consist of many processes: bound-bound transitions in atoms or molecules, bound-free transitions that ionize the medium, and free-free transitions where photons interact with charged particles in a three-body process. Opacity is commonly separated into two groups, continuous opacity which is characterized by small wavelength dependence across a given spectral range, and spectral line opacity with much stronger variation.

Opacities appear as a constant in the radiative transfer equation, which does not include material feedback of radiative processes. The treatment of opacities must therefore be supplemented with appropriate atomic models, depending on the application. Radiative processes such as photo-ionization compete with collisional interaction of material components in the gas. If collisional processes dominate, the material is driven towards local thermodynamic equilibrium (LTE) and the opacity of gas with a given chemical composition only depends on the local gas temperature and pressure. It is this parameterization that makes LTE a drastic simplification, since no additional information is needed about the detailed processes (see Chapter 6). LTE is usually a good approximation deeper in the atmosphere.

If LTE does not hold, the atomic model must be coupled with the radiation field to obtain a consistent description of the physical state of matter in the atmosphere. This treatment requires detailed knowledge of reaction rates, such as Einstein coefficients and collisional excitation rates, to obtain population numbers of atomic levels, which is generally called non-LTE (NLTE) radiative transfer. The models usually assume statistical equilibrium: processes that populate and depopulate atomic levels must in total be exactly balanced, leading to time-independent population numbers and a time-independent radiation field. The complexity of NLTE calculations usually limits applications to the important case of accurate spectral line formation (e.g., Carlsson et al., 1994; Mashonkina et al., 2008; Bergemann and Gehren, 2008), although NLTE techniques have been used in the context of 1D hydrostatic stellar atmospheres (Anderson, 1989; Short and Hauschildt, 2005) and 1D radiation-hydrodynamical simulations (Carlsson and Stein, 1997).

2.3.3 The source function

The photon emissivity j_ν has an exponential depth variation in stellar atmospheres, similar to the opacity χ_ν. It is therefore customary to use the source function

$$S_\nu \equiv \frac{j_\nu}{\chi_\nu} \tag{2.23}$$

instead of j_ν. S_ν is the number of photons emitted into the beam per photon removed from a beam with unit intensity. The source function is a material property like the opacity χ_ν, which needs to be derived from an atomic model. If thermodynamic equilibrium holds, matter emits radiation from its thermal pool in equilibrium with absorption according to Kirchhoff's law, and the source function is equal to the Planck function:

$$S_\nu = B_\nu. \tag{2.24}$$

In LTE, this relation is only approximately fulfilled, as the equilibrium may be perturbed by radiation from non-local sources. Thermal emission is generally supplemented with scattering of photons from all directions $\hat{\mathrm{n}}'$ and frequencies ν' into the direction $\hat{\mathrm{n}}$ of the monochromatic specific intensity I_ν. Cold gas with negligible thermal emission scatters photons with a source function

$$S_\nu = \frac{1}{4\pi}\int_0^\infty \int_{S^2} R(\hat{\mathrm{n}}, \hat{\mathrm{n}}', \nu, \nu') I(\hat{\mathrm{n}}', \nu') d\Omega' d\nu', \tag{2.25}$$

where $R(\hat{\mathrm{n}}, \hat{\mathrm{n}}', \nu, \nu')$ is a redistribution function in angle and frequency. In general, R needs to be evaluated for each scattering process separately and leads to a complex coupling between radiation at different angles and frequencies; Mihalas (1978) and Peraiah (2001) discuss several important cases (see also Sect. 6.2.2). Coherent isotropic scattering has $R = \delta(\nu - \nu')$, so that Eq. (2.25) simplifies to

$$S_\nu = J_\nu. \tag{2.26}$$

Radiative and collisional processes couple many excitation levels and ionization stages in real atoms and molecules. In continuum processes and simplified two-level atoms, it is possible to separate thermalization and scattering, weighting their contributions with the probability

$$\epsilon_\nu = \frac{\kappa_\nu}{\kappa_\nu + \sigma_\nu} = \frac{\kappa_\nu}{\chi_\nu} \tag{2.27}$$

that a photon is destroyed by absorption and reemitted from the thermal pool. In the case of two-level atoms, ϵ_ν describes the competition between scattering and absorption/thermal emission for the same transition. In the continuum case, different physical transitions may contribute, such as Rayleigh scattering and radiative ionization/recombination of the H^- ion.

The probability that a photon is scattered is $(1 - \epsilon_\nu)$, and the combined source function for coherent isotropic scattering and thermal emission is given by

$$S_\nu = (1 - \epsilon_\nu) J_\nu + \epsilon_\nu B. \tag{2.28}$$

It is important to note that the coherent scattering source function does not automatically account for departures from LTE populations of emitting particles, except for the idealized case of two-level atoms. Despite its approximate nature, it nevertheless plays an important role for understanding the effects of photon scattering. The general non-LTE case requires a source function that handles the detailed level coupling in the radiating matter, an important ingredient for accurate spectral line formation calculations.

2.4 The equations of radiation-hydrodynamics

The physical model of surface convection in late-type stars describes the time evolution of the plasma by coupling the equations of compressible hydrodynamics with the radiative transfer equation and the equation of state. The general treatment accounts for radiative heating and cooling through photon absorption and emission, and includes the contribution of radiation pressure to the force equation. In late-type stars, radiation pressure is negligible in the force balance: assuming an isotropic LTE radiation field at every atmospheric depth point, the Stefan-Boltzmann law and the Eddington approximation yield a local frequency-integrated radiation pressure

$$P_{\mathrm{rad}} = \frac{4\sigma}{3c} T^4, \tag{2.29}$$

where σ is the Stefan-Boltzmann constant, c is the speed of light and T is the gas temperature. Figure 2.2 compares P_{rad} (dashed line) with the average gas pressure P_{gas} of a solar-type star (solid line). Although Eq. (2.29) yields only a poor estimate for P_{rad} above the surface (at $T \lesssim 5800\,\mathrm{K}$), where the radiation field and radiation pressure are non-local and highly anisotropic, decoupling from the local gas temperature, gas pressure dominates by orders of magnitude.

In stellar atmospheres, the photon propagation time along a mean free path with opacity χ, $\tau_{\mathrm{rad}} = (c\chi)^{-1}$, is orders of magnitude smaller than any hydrodynamic time scale. It is therefore sufficient to solve a time-independent radiative transfer problem at each given point of time in a simulation, assuming instant decay of modes that are related to time-dependent radiative transfer (see Mihalas and Mihalas, 1984). Stellar surface convection can thus be described using a simplified set of 3D radiation-hydrodynamical equations for the gas density ρ, the velocity $\mathbf{u}$, the internal energy e and the monochromatic specific intensity I_ν in direction $\hat{\mathbf{n}}$:

$$\frac{\partial \rho}{\partial t} + \nabla \cdot \rho \mathbf{u} = 0 \tag{2.30}$$

$$\frac{\partial \rho \mathbf{u}}{\partial t} + \nabla \cdot (\rho \mathbf{u}\mathbf{u}) + \nabla P = -\rho \mathbf{g} + \nabla \cdot \tau_{\mathrm{visc}} \tag{2.31}$$

$$\frac{\partial e}{\partial t} + \nabla \cdot (e\mathbf{u}) + P(\nabla \cdot \mathbf{u}) = Q_{\mathrm{rad}} + Q_{\mathrm{visc}} \tag{2.32}$$

$$\hat{\mathbf{n}} \cdot \nabla I_\nu = -\chi_\nu I_\nu + \chi_\nu S_\nu. \tag{2.33}$$

The stellar surface gravity $\mathbf{g}$ is assumed constant. The radiation-hydrodynamical equations are closed through the equation of state to obtain the gas pressure P, as well as through the gas opacity χ_ν, the photon destruction probability ϵ_ν and the LTE source function S_ν with coherent isotropic scattering:

$$P = P(\rho, e) \tag{2.34}$$

$$\chi_\nu = \chi_\nu(\rho, e) \tag{2.35}$$

$$\epsilon_\nu = \epsilon_\nu(\rho, e) \tag{2.36}$$

$$S_\nu = (1 - \epsilon_\nu) J_\nu + \epsilon_\nu B_\nu. \tag{2.37}$$

The viscosity tensor τ_{visc} in Eq. (2.31) is only needed to ensure numerical stability of the discretized equations (see Sect. 3.1.2); viscous heat dissipation contributes to the internal energy through

$$Q_{\mathrm{visc}} = \sum_{ij} \tau_{ij} \frac{\partial u_i}{\partial x_j}. \tag{2.38}$$

The radiative heating rate Q_{rad} is defined as

$$Q_{\mathrm{rad}} = -\int_0^\infty \nabla \cdot \mathbf{F}_\nu d\nu = 4\pi \int_0^\infty \chi_\nu (J_\nu - S_\nu) d\nu, \tag{2.39}$$

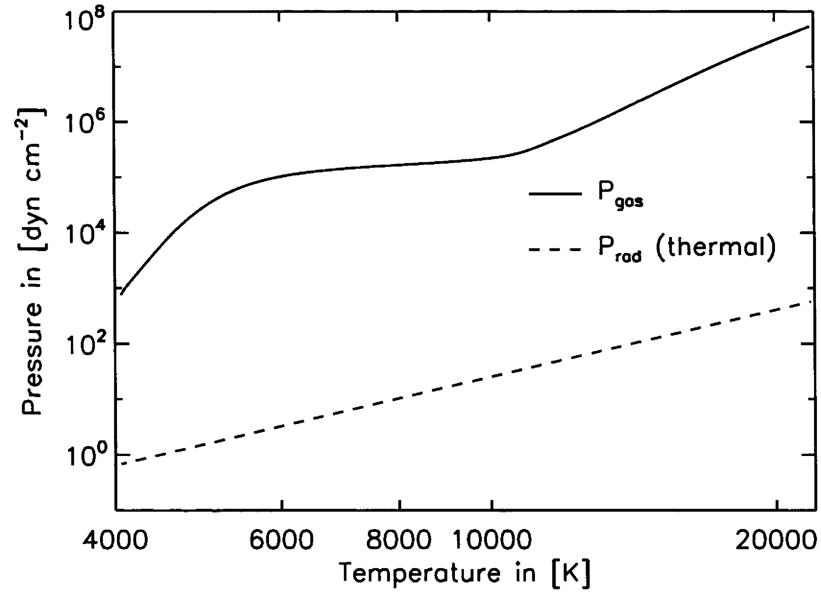

Figure 2.2: Average $\log T$-$\log P_{\mathrm{gas}}$ stratification taken from a snapshot of a radiation-hydrodynamical simulation of a solar-type star (solid line, $T_{\mathrm{eff}} \approx 5800\,\mathrm{K}$, $\log g = 4.44$ (cgs), chemical composition of Asplund et al., 2005) compared to the frequency-integrated local thermal radiation pressure P_{rad} (dashed line).

where $\mathbf{F}_\nu$ is the radiative flux (Eq. (2.21)). The radiative transfer equation (Eq. (2.33)) was used to obtain the second equality, which illustrates the competition between the absorption of radiation $\chi_\nu J_\nu$ and the emission of radiation $\chi_\nu S_\nu$ at each frequency ν. Radiative heating vanishes if an equal amount of photons is absorbed and emitted, which yields radiative equilibrium:

$$\int_0^\infty \nabla \cdot \mathbf{F}_\nu d\nu = 0. \tag{2.40}$$

The radiative equilibrium condition replaces the energy equation in 1D hydrostatic model atmospheres.

The wavelength integral in Eq. (2.39) is a major complication in the physical model: atomic and molecular absorption in stellar atmospheres produces millions of spectral lines, making radiative heating highly wavelength dependent. Solving radiative transfer equations for millions of frequencies is computationally prohibitive; an approximate treatment of the wavelength-dependence of opacities is required (see Chapter 4.2.2).

2.5 Convective and radiative heat transport

An important goal for simulations of stellar atmospheres is a realistic description of heat transport to determine the temperature stratification. Around the surface of late-type stars, convection and radiative transfer are equally important modes of energy transfer, while heat conduction is negligible. The atmosphere exhibits strong stratification due to the dominant role gravity in the force balance. It is therefore close to hydrostatic equilibrium, which is perturbed by convective motion.

The temperature-pressure gradient and the gas opacities determine whether convective or radiative energy transport dominates beneath the stellar surface in general. The vertical radiative flux in an optically thick diffusion region at height z is given by

$$F_{z,\nu}(z) \approx -\frac{4}{3}\pi\frac{1}{\chi_\nu}\frac{dB_\nu(z)}{dz} \quad \rightarrow \quad F_z(z) = \int_0^\infty F_{z,\nu}(z)d\nu \approx -\frac{16}{3}\frac{\sigma T^3}{\chi^{\mathrm{Ross}}}\frac{dT}{dz}, \tag{2.41}$$

where the diffusion approximation and the Stefan-Boltzmann law have been used (e.g., Rutten, 2003); σ is the Stefan-Boltzmann constant and χ^{Ross} is the Rosseland mean opacity, which depends on the chemical composition of the gas and the local temperature and pressure. For the temperature gradients and opacities encountered in the outer envelope beneath the photosphere of late-type stars, radiative energy transfer is not important. Above the surface, the gas becomes optically thin in large wavelength ranges, and radiative energy transfer dominates.

2.5.1 Convective instability

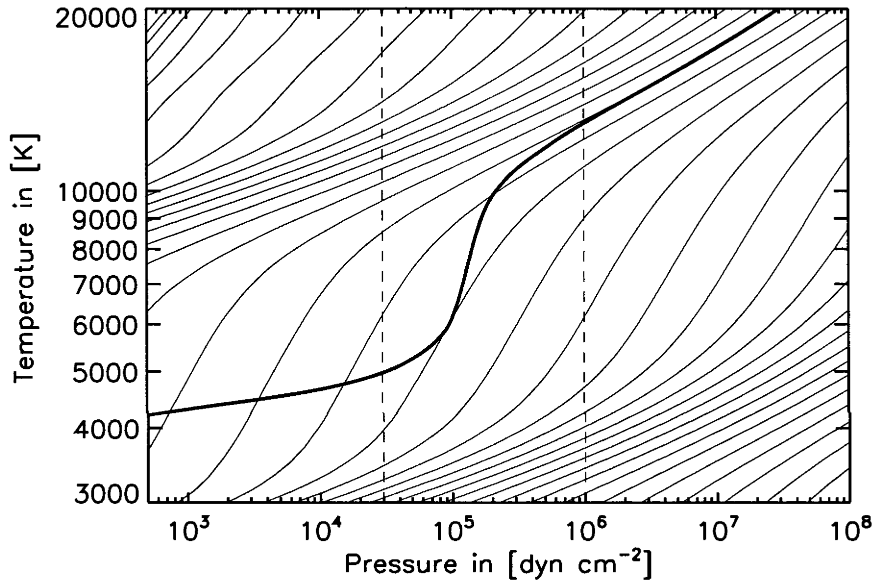

Figure 2.3: Adiabatic curves $ds(P,T) = 0$ derived from the MHD EOS for a solar-type star (thin lines). The thick line shows the horizontal average pressure-temperature stratification of a single snapshot taken from a time-series of a 3D simulation. Dashed lines approximately separate the radiative region above the surface (left), the convective region beneath the surface (right), and the transition between the two around the optical surface (center).

A stratification is convectively unstable if a rising gas parcel experiences continuous buoyancy: assuming optically thick gas with negligible radiative cooling, a parcel that starts with the density of the surrounding medium ($\rho = \rho_{\mathrm{med}}$) thus needs to experience larger adiabatic expansion $-d\rho_s$ than the density change in the medium at depth z, $-d\rho_{\mathrm{med}} = -(\partial\rho_{\mathrm{med}}/\partial z)dz$:

$$\rho_{\mathrm{med}} - d\rho_s < \rho_{\mathrm{med}} - d\rho_{\mathrm{med}} \quad \leftrightarrow \quad d\rho_s > d\rho_{\mathrm{med}}. \tag{2.42}$$

This basic requirement for convective instability can be translated into a critical temperature-pressure gradient: the density variation of a gas parcel in the T-P plane is given by

$$d\rho = \left(\frac{\partial\rho}{\partial T}\right)_P dT + \left(\frac{\partial\rho}{\partial P}\right)_T dP, \tag{2.43}$$

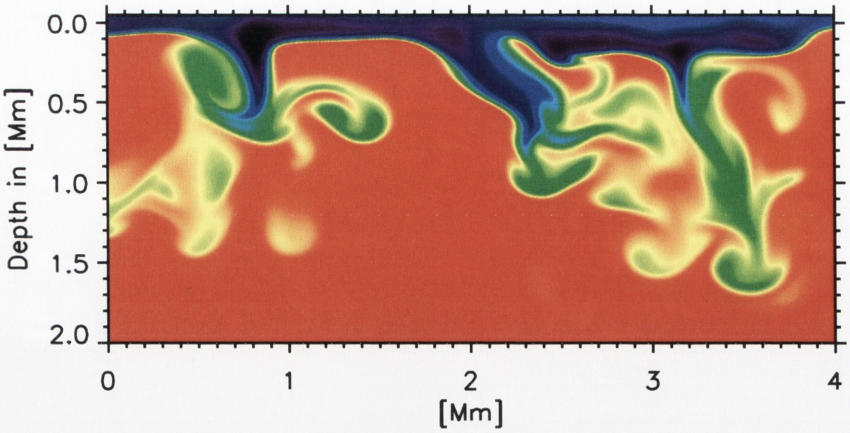

Figure 2.4: Vertical entropy slice taken from a 3D radiation-hydrodynamical model atmospere of a solar-type star. Blue areas represent cool low entropy gas, red areas represent high entropies, the zero point on the vertical axis marks the stellar surface. Radiatively cooled downdrafts mix with the upflowing gas, forming complex structures.

and an adiabatic density change has

$$d\rho_s = \left(\frac{\partial \rho}{\partial P}\right)_s dP, \tag{2.44}$$

if pressure is chosen as the independent variable. The density criterion for convective instability (Eq. (2.42)) is thus equivalent to requiring that

$$\left(\frac{\partial \rho}{\partial P}\right)_s dP > \left(\frac{\partial \rho}{\partial T}\right)_P dT + \left(\frac{\partial \rho}{\partial P}\right)_T dP. \tag{2.45}$$

Reordering terms and solving for the temperature-pressure gradient yields

$$\left(\frac{\partial T}{\partial P}\right) > \frac{(\partial\rho/\partial P)_s - (\partial\rho/\partial P)_T}{(\partial\rho/\partial T)_P} \equiv \left(\frac{\partial T}{\partial P}\right)_s, \tag{2.46}$$

where $(\partial\rho/\partial T)_P < 0$ was used since gas expands when heated. The right-hand side of Eq. (2.46) is equivalent to the adiabatic temperature-pressure gradient $(\partial T/\partial P)_s$ due to Eq. (2.45). It is customary to write the temperature-pressure stratification as a log-log-gradient, which results in the well-known Schwarzschild criterion for convective instability:

$$\left(\frac{\partial \log T}{\partial \log P}\right) > \left(\frac{\partial \log T}{\partial \log P}\right)_s. \tag{2.47}$$

The Schwarzschild criterion can also be derived from an entropy argument: suppose that density is given as a function of pressure and entropy, $\rho = \rho(P, s)$. Rewriting Eq. (2.42), one obtains the condition

$$\left(\frac{\partial \rho}{\partial P}\right)_s dP > \left(\frac{\partial \rho}{\partial P}\right)_s dP + \left(\frac{\partial \rho}{\partial s}\right)_P ds, \tag{2.48}$$

The relation $(\partial\rho/\partial s)_P < 0$ holds again, since gas expands when heated, and Eq. (2.48) yields that the atmospheric stratification is convectively unstable if gas entropy increases inward:

$$ds > 0. \tag{2.49}$$

The Scharzschild criterion will now be used to understand the occurrence of surface convection in late-type stars: if the T-P-stratification in the stellar envelope is steeper than adiabatic ("superadiabatic"), an upflowing gas parcel experiences continuous buoyancy and rises until it penetrates into a "subadiabatic" region, where the stratification is shallow. Buoyancy then reverses sign, since the parcel is pulled back by gravity. In the solar atmosphere, the stratification is convectively unstable beneath the surface (right part of Fig. 2.3). The horizontal average gradient is very close to adiabatic, since adiabatically expanding upflows dominate on average. The stratification is nevertheless slightly superadiabatic, since cool, dense, downflowing plumes of gas create an ambient medium with a steeper gradient (Stein and Nordlund, 1998).

Radiative cooling thus acts as a driver for convection: as soon as the upwelling plasma becomes optically thin, photons escape into space and carry away entropy. The cooled gas gathers in plumes with higher density that sink into the star and provide the kinetic energy to supply the upflows (Stein and Nordlund, 1998). Figure 2.4 shows a vertical entropy slice of a solar simulation; cool low-entropy downdrafts (blue and green) contrast with hot isentropic upflows (red).

Above the surface (left part of Fig. 2.3), the stratification is subadiabatic: gas parcels that were thrown up from the convection zone experience negative buoyancy; gravity pulls them back into the star and the stratification is convectively stable. The T-P gradient is set by radiative heating and it is much shallower than the adiabatic gradient (thin lines).

The shallow regions of the adiabatic curves in Fig. 2.3 are due to latent heat storage through hydrogen ionization (at low pressure and high temperature) and dissociation of hydrogen molecules (at high pressure and low temperature). At medium temperatures and pressures, hydrogen is dominantly atomic and neutral.

2.5.2 Convective energy fluxes

Convective motion propagates energy with the help of several transport agents. Nordlund et al. (2009) derive a conservation equation with the individual energy fluxes by adding the internal energy equation (Eq. (2.32)) and the inner product of the Navier-Stokes equations (Eq. (2.31)) with the gas velocity $\mathbf{u}$. This yields the expression

$$\frac{\partial}{\partial t}\left(e+\frac{1}{2}\rho u^2\right)+\nabla\cdot\left(e\mathbf{u}+P\mathbf{u}+\frac{1}{2}\rho u^2\mathbf{u}+\tau_{\mathrm{visc}}\cdot\mathbf{u}+\mathbf{F}_{\mathrm{rad}}\right)=-\rho\mathbf{g}\cdot\mathbf{u}. \tag{2.50}$$

for the conservation of total energy as the sum of internal energy e and kinetic energy $\rho u^2/2$, where $u^2=\mathbf{u}\cdot\mathbf{u}$.

The first energy flux in the divergence term of Eq. (2.50) is the internal energy flux,

$$\mathbf{F}_{\mathrm{internal}}=e\mathbf{u}=(e_{\mathrm{ion}}+e_{\mathrm{diss}}+e_{\mathrm{therm}})\mathbf{u}, \tag{2.51}$$

which combines the ionization energy e_{ion}, the molecule dissociation energy e_{diss} and the thermal energy e_{therm}. The thermal energy represents translational degrees of freedom through the caloric equation of state,

$$e_{\mathrm{therm}}=\frac{3}{2}nkT=\frac{3}{2}P, \tag{2.52}$$

where n is the total particle density, which depends on T and P through ionization and molecule formation; the second equivalence in Eq. (2.52) holds since the plasma approximately behaves like an ideal gas for fixed temperature and pressure. The internal energy flux and the thermal energy flux are shown in Fig. 2.5 (long dashed line and triple dot-dashed line), computed using a time series of a solar-type simulation. It is clear that ionization is the main heat

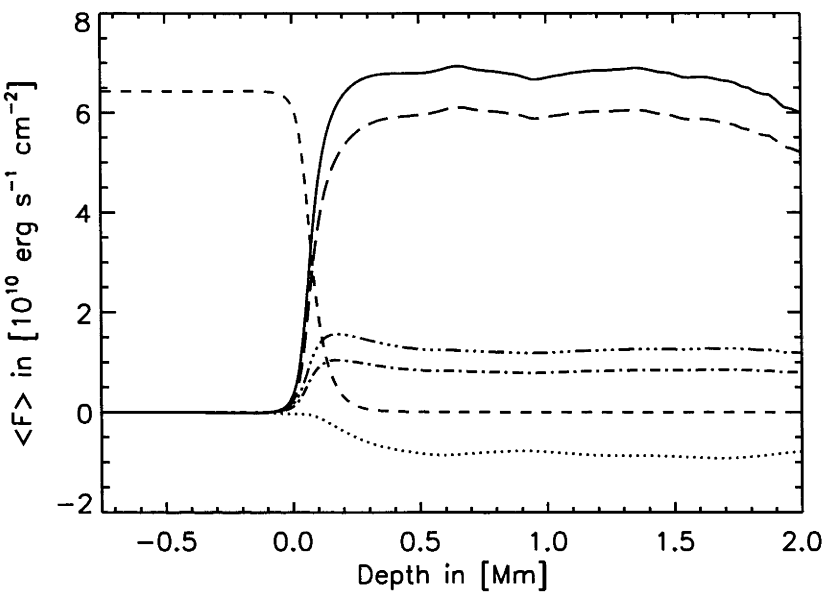

Figure 2.5: Horizontal and temporal averages of vertical energy fluxes as a function of depth, computed using a time series of a solar-type simulation and corrected for vertical bulk mass motion. *Solid line:* convective flux, *short dashed line:* radiative flux, *long dashed line:* internal energy flux, *dotted line:* kinetic energy flux, *dot-dashed line:* acoustic flux, *triple dot-dashed line:* thermal energy flux.

transport agent in this uppermost region of the convection zone, it contributes the largest fraction of energy that is carried upward (compare internal and thermal energy flux in Fig. 2.5; molecules are dissociated beneath the surface). A realistic equation of state for surface convection simulations must therefore include latent heat storage through ionization: an ideal gas can only store thermal energy and would require upflows to reach very high velocities in order to maintain the total energy flux (Stein and Nordlund, 1998; Nordlund et al., 2009)

The second flux term in Eq. (2.50) is the acoustic energy flux

$$\mathbf{F}_{\text{acoustic}} = P\mathbf{u}, \tag{2.53}$$

which accounts for energy transported through gas compression and expansion (dot-dashed line in Fig. 2.5). The internal energy flux and acoustic energy flux constitute the convective flux

$$\mathbf{F}_{\text{conv}} = (e + P)\mathbf{u}, \tag{2.54}$$

which combines all important agents for outward energy transfer beneath the surface (solid line in Fig. 2.5). The convective flux is also called enthalpy flux, since enthalpy density is defined through $h = e + P$.

The kinetic energy flux

$$\mathbf{F}_{\text{kin}} = \frac{1}{2}\rho u^2 \mathbf{u}. \tag{2.55}$$

is the third term in Eq. (2.50), represented by the dotted line in Fig. 2.5. Kinetic energy is dominantly transported into the star, since gas velocities $\mathbf{u}$ and densities ρ are higher in downdrafts (Stein and Nordlund, 1998). The viscous energy flux

$$\mathbf{F}_{\text{visc}} = \tau_{\text{visc}} \cdot \mathbf{u} \tag{2.56}$$

does not contribute significantly to energy transport (not shown in Fig. 2.5). Radiative transfer contributes the radiative energy flux through the first moment of the specific intensities I_ν integrated over the frequency spectrum,

$$F_{\mathrm{rad},i} = \int_0^\infty \int_{S^2} I_\nu(\hat{\mathbf{n}}_\mathrm{i}, \hat{\mathbf{n}}')d\Omega d\nu, \tag{2.57}$$

and becomes the dominant mode of energy transport above the stellar surface (short dashed line in Fig. 2.5).

Chapter 3

Numerical methods of radiation-hydrodynamics

The equations of radiation-hydrodynamics allow analytical solutions only in a few simplified cases (see Mihalas and Mihalas, 1984). Realistic physical models require a numerical solution of the full 3D time-dependent problem. Different codes have been presented in the field of stellar atmospheres, e.g., the code by Stein and Nordlund (1998), the `Stagger` code (Nordlund and Galsgaard, 1995), the `CO`^{5}`BOLD` code (Freytag et al., 2002), the `MURaM` code (Vögler et al., 2005), a code that was described in Jacoutot et al. (2008), the `ANTARES` code (Muthsam et al., 2010) and the `BIFROST` code (Gudiksen et al., in prep.). `BIFROST` was used for the radiation-hydrodynamical calculations presented in this PhD thesis; see Fig. 3.1 for an example.

3.1 The hydrodynamical solver

A numerical solution of the fully compressible hydrodynamical equations needs to handle a variety of difficulties, depending on the physical application. The non-linear and hyperbolic nature of the system of partial differential equations allows discontinuous solutions through the formation of shock waves, even when initial conditions are smooth. Fluids with low viscosity can exhibit complex turbulent behavior; low sound speeds in dilute media support the appearance of transsonic flow. Such conditions are encountered in simulations of stellar surface granulation (Stein and Nordlund, 1998) and constrain the choice of numerical methods.

Current simulation codes follow a "large-eddy" approach, where only the largest flow structures are resolved, and small-scale structures are either suppressed or approximated using a subgrid-scale model. Typical grid lengths reach the order of kilometres in the solar case, which is many orders of magnitude larger than viscous length scales. However, current facilities, such as the HINODE satellite or the Swedish Solar Telescope, achieve a much coarser resolution of $\sim$ 150 km at the surface. Smaller structures that are predicted by the simulations are therefore not yet observable. Simulations of solar surface granulation nevertheless agree well with the observations (e.g. Nordlund et al., 2009).

3.1.1 Discretization

The `BIFROST` code uses a conservative high-order finite difference solver on a staggered mesh, which offers flexibility for including additional physics in the hydrodynamical model and reaches high accuracy in the numerical solution; the method is well-suited for vector processors and MPI parallelization (Nordlund and Galsgaard, 1995; Brandenburg, 2003). The disadvantage of high-order finite difference solvers lies in their treatment of shocks, since the solution of the

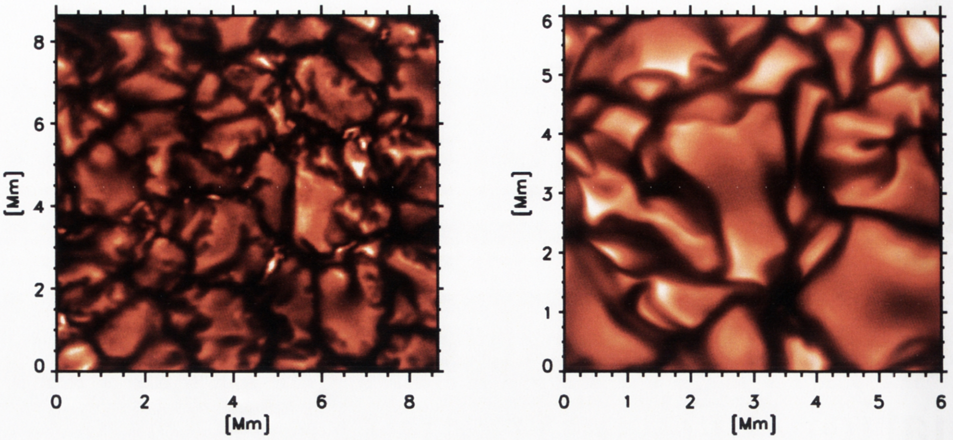

Figure 3.1: *Left:* Solar granulation at 4364 Å near the center of the solar disk ($\theta = 20°$, $\mu = 0.94$), observed with the Swedish Solar Telescope by Göran Scharmer and Kai Langhans (Institute for Solar Physics of the Royal Swedish Academy of Sciences, Sweden). *Right:* Disk-center intensities at 4364 Å for a solar model atmosphere computed with the `BIFROST` radiation-hydrodynamical code and the `SCATE` spectrum formation code.

hydrodynamical equations must remain sufficiently smooth at all times to ensure numerical stability. Strong discontinuities need to be avoided by adding artificial viscosity, which is orders of magnitude larger than plasma viscosity in real stars. Artificial viscosity also suppresses small-scale structures, reducing the effective resolution of the simulation.

Staggered grids improve the accuracy of a discretization: scalar quantities, such as the density ρ or the internal energy e are defined on grid cell centers, while vector quantities, such as the momenta $\mathbf{p}$ or the magnetic field $\mathbf{B}$, are defined on grid cell faces or corners (see Fig. 3.2). The derivative operators gain accuracy by delivering results on the respective staggered mesh, halving the step length Δx of the finite difference quotients compared to a non-staggered grid.

The hydrodynamical solver uses 6th order derivative operators and 5th order interpolation operators along the three spatial dimensions, each of them with a stencil of 6 grid points. The result is defined on the staggered grid, 1/2 step between the two center points of the stencil. The interpolation operators assume the explicit form

$$f_{i+\frac{1}{2},j,k} = a(f_{i,j,k} + f_{i+1,j,k}) + b(f_{i-1,j,k} + f_{i+2,j,k}) + c(f_{i-2,j,k} + f_{i+3,j,k}); \tag{3.1}$$

derivative operators are given by expressions of the kind

$$f'_{i+\frac{1}{2},j,k} = \frac{a}{\Delta x}(f_{i,j,k} + f_{i+1,j,k}) + \frac{b}{\Delta x}(f_{i-1,j,k} + f_{i+2,j,k}) + \frac{c}{\Delta x}(f_{i-2,j,k} + f_{i+3,j,k}), \tag{3.2}$$

with preset constants a, b and c for either case (Nordlund and Galsgaard, 1995).

3.1.2 Artificial viscosity

Although viscous length scales are not resolved in large-eddy simulations, numerical stability requires artificial smoothening of the solution. A viscosity tensor

$$\tau_{ij} = \frac{1}{2}\rho\left(\nu_j\frac{\partial u_i}{\partial x_j} + \nu_i\frac{\partial u_j}{\partial x_i}\right) \tag{3.3}$$

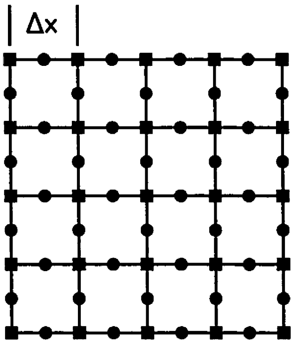

Figure 3.2: Example of a two-dimensional staggered mesh, where scalar quantities are defined on cell centers (squares), and the components of vector quantities (e.g., velocities or momenta) are defined on cell faces (circles). Δx denotes the spatial grid length.

is therefore added to the equation of motion. The kinematic viscosities ν consist of three parts (cf. the discussion in Nordlund and Galsgaard, 1995): the first component damps short-wavelength oscillations, which are not resolved on the numerical grid and which are therefore propagated with erroneous speeds, resulting in phase errors in traveling wave groups. This component is represented by a term

$$\nu_{\mathrm{wave}} = a_1 \Delta x c_{\mathrm{s}}, \tag{3.4}$$

with a scaling constant a_1, the grid length Δx, and the local sound speed c_{s}, which is the fastest wave speed encountered in hydrodynamical simulations. Advective transport of small-scale fluctuations causes amplitude errors that grow over time; they are damped through the term

$$\nu_{\mathrm{advection}} = a_2 \Delta x |\mathbf{u}|, \tag{3.5}$$

which scales with the grid length and the total gas velocity $|\mathbf{u}|$. The third source of instability is the formation of shocks in the compressible gas. They lead to strong discontinuities in the solution which cause ringing and may even destabilize the solver. Shocks are therefore resolved by a diffusion term

$$\nu_{\mathrm{shock}} = a_3 \Delta x^2 |\nabla \cdot \mathbf{u}|^-; \tag{3.6}$$

the minus sign indicates that only gas compression ($\nabla \cdot \mathbf{u} < 0$) is considered.

Artificial diffusion leads to unrealistically large plasma viscosities. It is therefore important to apply the smoothening only where it is necessary. Quenched diffusion, sometimes also called "hyperdiffusion", is a method to keep artificial viscosity local. This is accomplished by scaling the viscosity tensor with quenching factors

$$q(\partial U/\partial x) = \frac{|\Delta^2(\partial U/\partial x)|}{|\partial U/\partial x| + |\Delta^2(\partial U/\partial x)|/q_{\mathrm{max}}}, \tag{3.7}$$

which depend on the spatial derivatives of a hydrodynamical variable U and their second numerical derivative Δ^2. q vanishes if $\partial U/\partial x$ is smooth and removes viscosity from this point, but amplifies diffusion where strong discontinuities appear. Quenching factors are bounded by the parameter q_{max}.

3.2 Boundary conditions

Solving the radiative-hydrodynamical equations requires appropriate start values and boundary values. The simulations should cover a small representative fraction of the stellar surface to reproduce granulation flow in the atmosphere in a statistical sense. The horizontal boundaries are therefore periodic, and the simulation behaves like an infinitely expanded atmosphere. In order to avoid self-interaction of granules, the 3D box has to be larger than the distance that a sound wave travels during a typical granule life time. In solar simulations, sound speeds reach $\sim 10\,\mathrm{km\,s^{-1}}$ at the surface; a width of 6 Mm is thus sufficient for granules that typically live about 10 min.

The vertical boundary conditions are implemented by adding extra layers ("ghost zones") to the simulation box. These ghost zones are filled by extrapolation to either force boundary values $\mathrm{U}_{\mathrm{bound}}$ (Diriclet boundary conditions) or to set their spatial derivatives $\partial \mathrm{U}_{\mathrm{bound}}/\partial z$ (Neumann boundary conditions) at a given time step. The temporal behavior of the boundaries is controlled by adding terms to the hydrodynamic equations that affect the time derivatives $\partial \mathrm{U}_{\mathrm{bound}}/\partial t$.

3.2.1 The top boundary

For simulations of magnetically quiet stellar photospheres, the top boundary is usually placed at a continuum optical depth of $\tau_{5000} \approx 10^{-6}$. Gas densities are very low at this optical depth, mass flux and internal energy flux across the top boundary are therefore negligible.

Instantaneous boundary values for the gas density in each time step are set by antisymmetric logarithmic extrapolation,

$$\log \rho(z_{\mathrm{top}} - h) = 2 \log \rho(z_{\mathrm{top}}) - \log \rho(z_{\mathrm{top}} + h), \tag{3.8}$$

accounting for the exponential density stratification; h is the distance from the boundary at the atmospheric height z_{top}.

Atmospheric gas must be free to leave the simulation box to avoid reflection. Such "open" boundaries are approximately implemented by keeping velocities constant across the boundary:

$$u_x(z_{\mathrm{top}} - h) = u_x(z_{\mathrm{top}}) \tag{3.9}$$

$$u_y(z_{\mathrm{top}} - h) = u_y(z_{\mathrm{top}}) \tag{3.10}$$

$$u_z(z_{\mathrm{top}} - h) = u_z(z_{\mathrm{top}}). \tag{3.11}$$

Internal energies e are set as internal energies per unit mass $\epsilon = e/\rho$ using antisymmetric linear extrapolation:

$$\epsilon(z_{\mathrm{top}} - h) = 2\epsilon(z_{\mathrm{top}}) - \epsilon(z_{\mathrm{top}} + h). \tag{3.12}$$

Drifts at the boundary can be prevented by adding a sink term for internal energies in the top layer to relax towards a slowly evolving horizontal average $\langle \epsilon_{\mathrm{top}} \rangle$:

$$Q_\epsilon(z_{\mathrm{top}}) = -\frac{\epsilon(z_{\mathrm{top}}) - \langle \epsilon_{\mathrm{top}} \rangle}{\tau_{\mathrm{top}}}, \tag{3.13}$$

where τ_{top} is a preset relaxation time constant; this boundary condition is modified in some cases (see Sect. 5.2).

Additional restrictions for the hydrodynamical variables are applied to handle extreme conditions, ensuring numerical stability.

3.2.2 The bottom boundary

The bottom of the simulation box lies in the convection zone, where hot gas rises in adiabatic expansion, transporting heat from the interior. Plumes of dense, cool gas sink back down into the star and leave the simulation. The bottom boundary thus needs to regulate heat influx into the 3D box, and it needs to ensure mass conservation to achieve a quasi-stationary state of the atmosphere.

Logarithmic densities $\log \rho$ and internal energies ϵ are set by antisymmetric linear extrapolation, similar to the top boundary:

$$\log \rho(z_{\mathrm{bot}} + h) = 2 \log \rho(z_{\mathrm{bot}}) - \log \rho(z_{\mathrm{bot}} - h) \tag{3.14}$$

$$\epsilon(z_{\mathrm{bot}} + h) = 2\epsilon(z_{\mathrm{bot}}) - \epsilon(z_{\mathrm{bot}} - h). \tag{3.15}$$

The entropy $s(\rho, \epsilon)$ of inflowing gas is regulated by a relaxation term with preset constants ρ_{bot} and ϵ_{bot}:

$$Q_{\rho,\mathrm{ingoing}}(z_{\mathrm{bot}}) = -\frac{\rho(z_{\mathrm{bot}}) - \rho_{\mathrm{bot}}}{\tau_{\mathrm{bot}}} \tag{3.16}$$

$$Q_{\epsilon,\mathrm{ingoing}}(z_{\mathrm{bot}}) = -\frac{\epsilon(z_{\mathrm{bot}}) - \epsilon_{\mathrm{bot}}}{\tau_{\mathrm{bot}}}, \tag{3.17}$$

where τ_{bot} is a relaxation time constant.

Stellar envelopes exhibit pressure oscillations ("p-modes"); the waves are created by stochastic excitation in the convection zone and reflected in the stellar interior. Dynamic forcing of a pressure node at the bottom boundary simulates this behavior approximately. The pressure $P(\rho, \epsilon)$ of inflowing gas is already kept constant through relaxation of ρ and ϵ to preset boundary values. Pressure fluctuations dP of outgoing flow are dynamically damped through an inverse adiabatic response, which will be discussed in the following.

A pressure fluctuation dP is generated by density and energy fluctuations $d\rho$ and de,

$$dP = \left(\frac{\partial P}{\partial \rho}\right)_e d\rho + \left(\frac{\partial P}{\partial e}\right)_\rho de. \tag{3.18}$$

An adiabatic pressure fluctuation dP_s couples $d\rho$ and de through the first law of thermodynamics (see Appendix A.1), since the specific entropy is constant ($ds = 0$). This leads to the relations

$$dP_s = \left(\frac{\partial P}{\partial \rho}\right)_s d\rho_s \tag{3.19}$$

$$dP_s = \left(\frac{\partial P}{\partial e}\right)_s de_s. \tag{3.20}$$

The bottom boundary is set to answer pressure fluctuations dP in outflowing gas with an inverse adiabatic pressure fluctuation: $dP_s = -dP$. Combining Eq. (3.18) with Eq. (3.19) or Eq. (3.20) and using the first law of thermodynamics leads to the damping terms

$$Q_{\rho,\mathrm{outgoing}}(z_{\mathrm{bot}}) = -\frac{(\partial P/\partial \rho)_e \, d\rho + (\partial P/\partial e)_\rho \, de}{(\partial P/\partial \rho)_s} \tag{3.21}$$

$$Q_{e,\mathrm{ingoing}}(z_{\mathrm{bot}}) = -\frac{P + e}{\rho} Q_{\rho,\mathrm{outgoing}}(z_{\mathrm{bot}}). \tag{3.22}$$

The fluctuations $d\rho$ and de in outflows include temporal variations $\partial\rho/\partial t$ and $\partial e/\partial t$ that are predicted by the hydrodynamical solver, as well as general deviations from the boundary conditions through $(\rho - \rho_{\text{bot}})/\tau_{\text{bot}}$ and $(e - e_{\text{bot}})/\tau_{\text{bot}}$. The EOS provides the thermodynamic derivatives in Eq. (3.21) and Eq. (3.22).

The pressure node at the bottom boundary keeps the total mass in the simulation box constant: a plume of gas that leaves through the bottom boundary generates a zone of low gas pressure in the layers above. This low-pressure zone is extrapolated outward into the ghost zone (Eq. (3.14) and Eq. (3.15)); the gradient ∇P steepens and forces material influx through the boundary. Conversely, strong material influx causes a shallower pressure gradient. Vertical mass flux therefore oscillates, the period is set through the time constant τ_{bot}.

An open bottom boundary is achieved by symmetric extrapolation of velocities to set a vanishing vertical derivative:

$$u_x(z_{\text{bot}} + h) = u_x(z_{\text{bot}} - h) \quad \leftrightarrow \quad \left.\frac{\partial u_x}{\partial z}\right|_{\text{bot}} = 0 \tag{3.23}$$

$$u_y(z_{\text{bot}} + h) = u_y(z_{\text{bot}} - h) \quad \leftrightarrow \quad \left.\frac{\partial u_y}{\partial z}\right|_{\text{bot}} = 0 \tag{3.24}$$

$$u_z(z_{\text{bot}} + h) = u_z(z_{\text{bot}} - h) \quad \leftrightarrow \quad \left.\frac{\partial u_z}{\partial z}\right|_{\text{bot}} = 0. \tag{3.25}$$

Horizontal motion of inflows is damped, reducing drifts in the x and y directions:

$$Q_{u_x,\text{ingoing}}(z_{\text{bot}}) = -\frac{u_x}{\tau_{\text{bot}}} \tag{3.26}$$

$$Q_{u_y,\text{ingoing}}(z_{\text{bot}}) = -\frac{u_y}{\tau_{\text{bot}}}. \tag{3.27}$$

3.3 The radiative transfer solver

The time-independent radiative transfer equation with scattering is an integro-differential equation with solutions that are defined in six-dimensional space $(\mathbf{x}, \hat{\mathbf{n}}, \nu)$. Absorption, emission and scattering of photons, as well as Doppler shifts caused by material motion, lead to a complex coupling of the radiation field in space, direction and frequency. Solving the radiative transfer problem thus requires further simplifications. The strategy depends on the specific application, and there exist a variety of methods (see Wehrse and Kalkofen, 2006, for an overview).

3.3.1 The method of characteristics

The time-dependent radiative transfer equation is given by

$$\frac{1}{c}\frac{\partial I_\nu}{\partial t} + \hat{\mathbf{n}} \cdot \nabla I_\nu = -\chi_\nu I_\nu + j_\nu. \tag{3.28}$$

The left-hand side is a simple hyperbolic advection equation for photon motion along straight lines in space-time (light rays) with self-similar solutions in the absence of sources and sinks. Light rays in direction $\hat{\mathbf{n}}$ are characteristics $\mathbf{x}(t)$ of Eq. (3.28) and solutions of the differential equation

$$\hat{\mathbf{n}} \cdot \mathbf{dx} = cdt \equiv ds. \tag{3.29}$$

The last equivalence defines a useful parameterization, the photon path length ds. The total differential of the specific intensity $I_\nu(t(s), \mathbf{x}(s))$ along a characteristic is

$$dI_\nu = \frac{\partial I_\nu}{\partial s} ds = \left(\frac{\partial I_\nu}{\partial t}\frac{\partial t}{\partial s} + \frac{\partial I_\nu}{\partial x}\frac{\partial x}{\partial s} + \frac{\partial I_\nu}{\partial y}\frac{\partial y}{\partial s} + \frac{\partial I_\nu}{\partial z}\frac{\partial z}{\partial s} \right) ds. \tag{3.30}$$

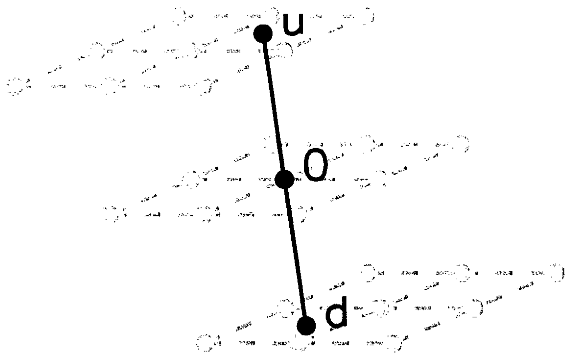

Figure 3.3: Illustration of a short characteristic (black line) in a 3D grid (grey dots and dashed lines) along which radiation is transported from the upwind point "u" to the center point "0". The downwind point "d" is needed for second-order accuracy of the source function integral.

Inserting the differential relations of Eq. (3.29), one obtains

$$dI_\nu = \left(\frac{1}{c}\frac{\partial I_\nu}{\partial t} + n_x \frac{\partial I_\nu}{\partial x} + n_y \frac{\partial I_\nu}{\partial y} + n_z \frac{\partial I_\nu}{\partial z} \right) ds. \tag{3.31}$$

Inserting the radiative transfer equation (Eq. (3.28)) leads to the expression

$$dI_\nu = \left(\frac{1}{c}\frac{\partial I_\nu}{\partial t} + \hat{\mathbf{n}} \cdot \nabla I_\nu \right) ds = (-\chi_\nu I_\nu + j_\nu)\, ds. \tag{3.32}$$

The radiative transfer equation along a characteristic is thus equivalent to the ordinary differential equation

$$\frac{dI_\nu}{ds} = -\chi_\nu I_\nu + j_\nu, \tag{3.33}$$

which describes the propagation of photons along light rays in direction $\hat{\mathbf{n}}$. As it was mentioned before, it is sufficient to solve a time-independent radiative transfer problem at each time step of a hydrodynamical simulation. In the limit of infinite light speed ($c \longrightarrow \infty$), Eq. (3.33) retains its form, and all quantities are time-independent.

3.3.2 Radiative transfer regimes

For the simple case of zero emission ($j_\nu = 0$), Eq. (3.33) has solutions of the form

$$I_\nu(s) = I_\nu(0) e^{-\chi_\nu s}, \tag{3.34}$$

where $I_\nu(0)$ is the incident intensity. The opacity χ_ν acts as an inverse photon mean free path. The magnitude of χ_ν determines the physical as well as the mathematical nature of radiative transfer. In transparent media with small opacity and large photon mean free paths, radiative transfer is a hyperbolic problem for the advection of virtually free photons, with local emission from the source term j_ν and a highly non-local, possibly anisotropic radiation field. This situation is realized in stellar atmospheres for continuum radiation above the stellar surface. In opaque media, χ_ν is large and mean free paths are small; radiative transfer is diffusive and the radiation field is isotropic, dominated by local emission j_ν/χ_ν. If scattering contributes most of the opacity χ_ν, the medium is translucent and radiative transfer turns into an elliptic problem of photon diffusion. The cores of strongly scattering spectral lines represent this case in stellar atmospheres. If absorption dominates χ_ν, the source term is equal to the Planck function and radiative transfer can be treated in a simple diffusion approximation, which is adequate in stellar interiors.

The physical behavior of radiative transfer is determined by the optical depth

$$d\tau_\nu = \chi_\nu ds, \tag{3.35}$$

where $\tau_\nu \ll 1$ marks the optically thin streaming regime, and $\tau_\nu \gg 1$ marks the optically thick diffusion regime. The optical depth τ_ν can be interpreted as the average number of interactions between radiation and matter on a given path s along a light ray. In stellar atmospheres, the zero point of the optical depth scale is commonly set outside the star. The optical surface is reached at $\tau_\nu = 1$, the depth of last interaction before outgoing photons escape into space. The presence of spectral lines leads to strong fluctuations of the opacity with frequency ν, which translates into a depth variation of monochromatic optical surfaces.

3.3.3 The integral method

Dividing Eq. (3.33) by the opacity χ_ν and using Eq. (3.35) leads to the expression

$$\frac{dI_\nu}{d\tau_\nu} = -I_\nu + S_\nu, \tag{3.36}$$

introducing the source function $S_\nu = j_\nu / \chi_\nu$. For known S_ν, Eq. (3.36) has the formal solution

$$I_\nu(\tau_\nu) = I_\nu(\tau_{\mathrm{u},\nu}) e^{-(\tau_\nu - \tau_{\mathrm{u},\nu})} + \int_{\tau_{\mathrm{u},\nu}}^{\tau_\nu} S_\nu(t) e^{t-\tau_\nu} dt \tag{3.37}$$

for $\tau_\nu > \tau_{\mathrm{u},\nu}$. The first term on the right-hand side describes the attenuation of an incident specific intensity I_ν at $\tau_{\mathrm{u},\nu}$ along the ray. The second term accumulates the local contributions from the source function S_ν.

A simple discretization of Eq. (3.37) uses a first-order or second-order polynomial to interpolate the source function S_ν, called the integral method. Inserting such a polynomial approximation of S_ν in Eq. (3.37) and evaluating the integral over optical depth leads to the discrete expression

$$I_{0,\nu} = I_{\mathrm{u},\nu} e^{-\Delta\tau_{\mathrm{u},\nu}} + \Psi_{\mathrm{u},\nu} S_{\mathrm{u},\nu} + \Psi_{0,\nu} S_{0,\nu} + \Psi_{\mathrm{d},\nu} S_{\mathrm{d},\nu}, \tag{3.38}$$

where the subscripts "u" "0" and "d" denote the upwind, center and downwind points along the characteristic, at which discrete values are needed to compute the specific intensity $I_{0,\nu}$ with second-order accuracy. Ψ_u, Ψ_0 and Ψ_d are integration constants that depend on the upwind and downwind optical depth steps $\Delta\tau_{\mathrm{u},\nu}$ and $\Delta\tau_{\mathrm{d},\nu}$, and the type of interpolation (see Appendix B.1).

The characteristics are either extended across the entire simulation domain (sometimes called the "long characteristics" method), or they are cut off at the intersection points with neighbor grid cells (the "short characteristics" method, see Fig. 3.3 for an illustration). The best choice of method depends on the nature of the problem; both approaches are found in 3D radiation-hydrodynamical simulations of stellar atmospheres (see Sect. 4.3.1 and, e.g., Vögler et al., 2005; Heinemann et al., 2006).

3.3.4 Approximate lambda iteration

Solving the radiative transfer equation with a scattering term leads to an integro-differential problem with a self-dependent solution. The coherent scattering source function is given by

$$S_\nu = (1-\epsilon_\nu)J_\nu + \epsilon_\nu B_\nu. \tag{3.39}$$

The formal solution of the radiative transfer equation is commonly abbreviated by introducing the operator equation

$$J_\nu = \Lambda_\nu S_\nu, \tag{3.40}$$

where Λ_ν is a linear operator if the opacities are constant. Inserting Eq. (3.40) into Eq. (3.39) yields

$$S_\nu = (1-\epsilon_\nu)\Lambda_\nu S_\nu + \epsilon_\nu B_\nu \quad \leftrightarrow \quad [\mathbb{1} - (1-\epsilon_\nu)\Lambda_\nu]\, S_\nu = \epsilon_\nu B_\nu. \tag{3.41}$$

The operator Λ_ν reduces to a matrix in the discretize case. The numerical solution of the radiative transfer equation with coherent scattering and given opacities is equivalent to solving a system of linear equations

$$Au = b. \tag{3.42}$$

The amount of equations to solve may be moderate ($\sim$ 100) in the 1D case, but it becomes huge ($\gtrsim 10^6$) in 3D. A direct inversion of the matrix operator A is computationally expensive: A needs to be constructed, stored and inverted, and the procedure is not always numerically stable. It is therefore advantageous to use iterative methods for the solution of the problem. Approximate Lambda Iteration (ALI, also sometimes called Accelerated Lambda Iteration, Cannon, 1973) has become very popular in the field of stellar atmospheres. It belongs to a class of stationary iteration methods for solving systems of linear equations.

The solver starts with an approximate solution u^n with the residual

$$r = b - Au^n = Au - Au^n = A(u - u^n) \equiv Ae, \tag{3.43}$$

where $e = u - u^n$ is the error of the approximate solution u^n with respect to the true solution u. A direct solution of this error equation is equivalent to the original problem. ALI solvers therefore compute approximate corrections Δu for a given residual r of the approximate solution u^n using a matrix A^*, which represents a simplified version of the original matrix A:

$$A^*\Delta u \equiv A^*(u^{n+1} - u^n) = r \tag{3.44}$$

The matrix A^* should be chosen in a way that the resulting system of linear equations,

$$A^*\Delta u = b - Au^n, \tag{3.45}$$

is computationally easier to solve. A new approximation to the solution is then obtained through

$$u^{n+1} = u^n + (A^*)^{-1}(b - Au^n), \tag{3.46}$$

which emphasizes the role of A^* as a convergence accelerator, since it amplifies the residuals $r = b - Au^n$. Translated back into the original problem of computing a source function with scattering term (or the mean radiation field), one obtains approximate solutions through

$$\begin{aligned}
[\mathbb{1} - (1-\epsilon_\nu)\Lambda^*_\nu]\,\Delta S_\nu &= \epsilon_\nu B_\nu - [\mathbb{1} - (1-\epsilon_\nu)\Lambda_\nu]\, S^n_\nu && (3.47)\\
&= (1-\epsilon_\nu)\Lambda_\nu S^n_\nu + \epsilon_\nu B_\nu - S^n_\nu && (3.48)\\
&= S^{\mathrm{FS}}_\nu - S^n_\nu. && (3.49)
\end{aligned}$$

The source function S_ν^{FS} is based on the radiation field that was obtained from the last formal solution, $J_\nu^{\mathrm{FS}} = \Lambda_\nu S_\nu^n$. The approximate matrix $[\mathbb{1} - (1 - \epsilon_\nu)\Lambda_\nu^*]$ on the left-hand side of Eq. (3.47) is the convergence accelerator.

The best choice for A^* is found through a compromise between convergence speed and computational expense: choosing a simpler operator matrix requires less computation but slows down convergence. The simplest choice, $\Lambda^* = 0$, is the Lambda-iteration method without acceleration ($A^* = \mathbb{1}$). Lambda-iteration is known to suffer from very slow convergence or even no convergence in some situations. Choosing a more complex A^* that includes off-diagonal elements may increase convergence dramatically, but requires larger computational effort (see the discussion in Hauschildt and Baron, 2006).

The local operator method uses the exact diagonal of the Λ matrix (Olson et al., 1986), making A^* easy to invert and well-suited for 3D applications. However, Hauschildt and Baron (2006) warn that such local operators do not necessarily lead to convergence. Scharmer (1981) presented a sparse non-local Λ^* operator, which has been used for various 1D radiative transfer problems; Kiselman and Nordlund (1995) applied the operator to a 3D case.

The radiative transfer computations presented in this thesis are based on the ALI method of Trujillo Bueno and Fabiani Bendicho (1995), which emulates an upper/lower triangular operator matrix with non-local coupling between grid points in the atmosphere. Only the diagonal elements of the Λ operator need to be computed explicitly, the triangular behavior is achieved by applying source function corrections already during the formal solution, in analogy to Gauss-Seidel iteration.

While the Gauss-Seidel method of Trujillo Bueno and Fabiani Bendicho (1995) produced good results, it is generally difficult for iterative solvers to handle scattering-dominated ($\epsilon \longrightarrow 0$) radiative transfer problems in the diffusion regime: convergence of the solution is very slow as the spectral radius of the iteration operator increases (see the discussion in Trujillo Bueno and Fabiani Bendicho, 1995), and the large condition number of the approximate matrix A^* can amplify numerical errors. An efficient and accurate treatment of such cases remains an unsolved problem (Wehrse and Kalkofen, 2006).

3.4 Time integration

The hydrodynamical solver (together with the radiative transfer solver and the EOS) delivers numerical approximations for the right-hand side $f(\mathbf{U})$ of the system of partial differential equations (PDEs) at simulation time t and grid point $\mathbf{x}$,

$$\frac{\partial}{\partial t}\mathbf{U}(\mathbf{x}, t) = f(\mathbf{U}); \tag{3.50}$$

the vector $\mathbf{U}$ consists of the hydrodynamical variables that are propagated in time. The time evolution in the system of PDEs is thereby reduced to solving an initial value problem. There is a large variety of numerical integration methods, which differ in their approximation order and computational expense. High-order methods produce lower amplitude errors in the numerical solution (see, e.g., the advection tests discussed in Brandenburg, 2003), but they need to evaluate several substeps between the main time steps t_0 and $t_0 + \Delta t$, or include several previous steps at $t < t_0$ in the integration. However, computational work is effectively reduced as high-order methods enable larger step sizes Δt.

Explicit time stepping methods extrapolate the solution from one or several previous time steps, while implicit methods include the new solution in the time integration itself. Implicit methods usually offer better numerical stability and larger time stepping, but it is difficult to study detailed wave motion, since time steps in implicit integration are not bounded by wave speed. The `BIFROST` code therefore uses explicit time stepping methods, which will be discussed in the following.

3.4.1 The Hyman method

The predictor-corrector method of Hyman (1979) combines explicit prediction of the solution with a quasi-implicit correction step. The predictor step extrapolates a weighted sum of the previous solution $\mathbf{U}_{i-1}$ and the current solution $\mathbf{U}_i$ forward in time,

$$\mathbf{U}_{i+1}^{\mathrm{pred}} = a_1 \mathbf{U}_{i-1} + b_1 \mathbf{U}_i + \Delta t c_1 \frac{\partial}{\partial t} \mathbf{U}_i, \tag{3.51}$$

which yields an explicit prediction of the solution at $t + \Delta t$. The hydrodynamical solver is called to obtain the derivative $\partial \mathbf{U}_i / \partial t$ through Eq. (3.50). In the corrector step, the prediction $\mathbf{U}_{i+1}^{\mathrm{pred}}$ is refined by obtaining the final solution from the weighted sum

$$\mathbf{U}_{i+1} = a_2 \mathbf{U}_{i-1} + b_2 \mathbf{U}_i + \Delta t c_2 \frac{\partial}{\partial t} \mathbf{U}_i + \Delta t d_2 \frac{\partial}{\partial t} \mathbf{U}_{i+1}^{\mathrm{pred}}, \tag{3.52}$$

where the hydrodynamical solver is called again to compute $\partial \mathbf{U}_{i+1}^{\mathrm{pred}} / \partial t$. The method is semi-implicit, as it employs the approximate solution $\mathbf{U}_{i+1}^{\mathrm{pred}}$ at $t = t_0 + \Delta t$ to obtain $\mathbf{U}_{i+1}$.

3.4.2 The 3rd order Runge-Kutta method

The 3rd order Runge-Kutta method splits the integration into three substeps:

$$\mathbf{k}_1 = \mathbf{U}_i \tag{3.53}$$

$$\mathbf{k}_2 = \mathbf{U}_i + \Delta t \left(a_{11} \frac{\partial}{\partial t} \mathbf{k}_1 \right) \tag{3.54}$$

$$\mathbf{k}_3 = \mathbf{U}_i + \Delta t \left(a_{12} \frac{\partial}{\partial t} \mathbf{k}_1 + a_{22} \frac{\partial}{\partial t} \mathbf{k}_2 \right) \tag{3.55}$$

$$\mathbf{U}_{i+1} = \mathbf{U}_i + \Delta t \left(a_{13} \frac{\partial}{\partial t} \mathbf{k}_1 + a_{23} \frac{\partial}{\partial t} \mathbf{k}_2 + a_{33} \frac{\partial}{\partial t} \mathbf{k}_3 \right). \tag{3.56}$$

The hydrodynamical equations need to be evaluated three times during the integration to obtain $\partial \mathbf{k}_i / \partial t$; the final solution $\mathbf{U}_{i+1}$ is found by adding a weighted sum of all time derivatives to the previous solution $\mathbf{U}_i$ (Eq. (3.56)). The memory requirements of the original Runge-Kutta method are large, since four sets of variables need to be stored ("4N-storage"). Williamson (1980) described a reordering of the scheme into a recurrent 2N-storage algorithm:

1. $\mathbf{k} = \mathbf{U}_i \qquad \frac{\partial}{\partial t}\mathbf{k} \rightarrow f(\mathbf{k})$ (3.57)
2. $\mathbf{k} \rightarrow \mathbf{k} + \Delta t \beta_1 \frac{\partial}{\partial t}\mathbf{k} \qquad \frac{\partial}{\partial t}\mathbf{k} \rightarrow \alpha_2 \frac{\partial}{\partial t}\mathbf{k} + f(\mathbf{k})$ (3.58)
3. $\mathbf{k} \rightarrow \mathbf{k} + \Delta t \beta_2 \frac{\partial}{\partial t}\mathbf{k} \qquad \frac{\partial}{\partial t}\mathbf{k} \rightarrow \alpha_3 \frac{\partial}{\partial t}\mathbf{k} + f(\mathbf{k})$ (3.59)
4. $\mathbf{k} \rightarrow \mathbf{k} + \Delta t \beta_3 \frac{\partial}{\partial t}\mathbf{k}$ (3.60)
5. $\mathbf{U}_{i+1} = \mathbf{k}.$ (3.61)

The arrows symbolize storage associations in the program; $f(\mathbf{k})$ represents the hydrodynamical solver. The constants α and β are combinations of constants a_{ij} of the original method. Only two variable sets $\mathbf{k}$ and $\partial \mathbf{k} / \partial t$ are needed, the memory requirements are the same as for first-order Euler time integration.

3.4.3 Stability limits

The step intervals Δt of explicit numerical integration are subject to restrictions: if Δt is larger than a certain threshold, the method fails to converge and delivers unphysical results. The stability limit depends on the type of equation and the discretization. A strict analysis of finite difference methods is difficult, a general theory does not exist. Some necessary conditions for numerical stability will be illustrated in the following using simplified test equations.

Numerical stability of finite difference schemes is studied using von Neumann stability analysis with a test function

$$\psi(x_i, t_n) = \psi_0 G^n e^{kx_i} \tag{3.62}$$

that produces perturbations with amplitude G^n and wave number k at time step t_n. If a PDE has a bounded solution at all times, a finite difference representation is considered stable if it produces a bounded numerical solution at all times as well. The amplitude G^n of the test function must therefore decay with time for all wave numbers k:

$$\left|\frac{\psi_i^{n+1}}{\psi_i^n}\right| = \left|\frac{G^{n+1}}{G^n}\right| \equiv |G| < 1. \tag{3.63}$$

Reaction terms

A prototypical equation for reaction terms is

$$\frac{\partial}{\partial t}\psi + \kappa\psi = 0 \qquad \kappa > 0; \tag{3.64}$$

κ is a reaction rate that needs to be positive to produce bounded solutions ψ. Spatial discretization and explicit Euler time integration leads to the expression

$$\frac{\psi_i^{n+1} - \psi_i^n}{\Delta t} + \kappa\psi_i^n = 0 \tag{3.65}$$

Inserting the von Neumann test function (Eq. (3.62)) then yields the stability condition

$$|G| = |1 - \kappa\Delta t| < 1 \quad \leftrightarrow \quad \Delta t < \frac{2}{\kappa}. \tag{3.66}$$

Time integration for the chosen discretization is stable as long as Δt is smaller than the given limit, which decreases with increasing rate coefficient κ.

Although reaction terms do not appear explicitly in the hydrodynamical equations, the stability limit (Eq. (3.66)) may be used as a general stability test for the PDEs, to monitor the sum of all terms in the equations:

$$U_i^{n+1} = U_i^n + \Delta t f(U, x) = U_i^n + \Delta t \kappa_i^n U_i^n, \tag{3.67}$$

where $\Delta t \kappa_i^n = (U_i^{n+1} - U_i^n)/U_i^n$ represents the relative change of the hydrodynamical variable U during a time step $t = t_0 + \Delta t$. Note that κ may also be negative, allowing the discrete variables U_i^n to grow if U grows. `BIFROST` performs this stability test for the density equation and for the internal energy equation.

Transport terms

The test equation for transport terms is

$$\frac{\partial}{\partial t}\psi + u\frac{\partial}{\partial x}\psi = 0 \qquad u > 0, \tag{3.68}$$

where u is the local transport speed, which is assumed positive for simplicity of the discussion. Using Euler time integration and upwind spatial discretization, one obtains

$$\frac{\psi_i^{n+1} - \psi_i^n}{\Delta t} + u\frac{\psi_i^n - \psi_{i-1}^n}{\Delta x} = 0, \tag{3.69}$$

with the grid length $\Delta x = x_i - x_{i-1}$. The stability condition for a bounded numerical solution is the limit

$$|G| = \sqrt{1 + 2u\frac{\Delta t}{\Delta x}\left(u\frac{\Delta t}{\Delta x} - 1\right)(1 - \cos[k\Delta x])} < 1 \quad \leftrightarrow \quad \Delta t < \frac{\Delta x}{u}. \tag{3.70}$$

This is the well-known Courant criterion, which requires that the local speed of numerical propagation of information $\Delta x/\Delta t$ must always be faster than the fastest local physical propagation speed u to ensure causal order in the time evolution of the PDE. In hydrodynamical simulations, u is set by the sum of local sound speed and advection speed.

Diffusion terms

A prototypical equation for diffusion terms is given by

$$\frac{\partial}{\partial t}\psi - \nu\frac{\partial^2}{\partial x^2}\psi = 0 \qquad \nu > 0, \tag{3.71}$$

with a diffusion coefficient ν that needs to be positive to produce bounded solutions ψ. Using Euler time integration and centered finite difference spatial discretization, one obtains

$$\frac{\psi_i^{n+1} - \psi_i^n}{\Delta t} - \nu\frac{\psi_{i+1}^n - 2\psi_i^n + \psi_{i-1}^n}{(\Delta x)^2} = 0, \tag{3.72}$$

Time integration for this type of equation is limited by

$$|G| = \left|1 + 2\nu\frac{\Delta t}{(\Delta x)^2}(\cos[k\Delta x] - 1)\right| < 1 \quad \leftrightarrow \quad \Delta t < \frac{(\Delta x)^2}{2\nu}. \tag{3.73}$$

The diffusion time step (Eq. (3.73)) is often the most restrictive limit in simulations due to its $(\Delta x)^2$ dependence. Diffusion terms appear in the artificial viscosity tensor of the hydrodynamical solver. If hyperdiffusion is used, the time step is reduced by the maximum quenching factor $q_{\max}$ to ensure numerical stability.

General stability limits

In the radiation-hydrodynamical equations, combinations of transport terms, diffusion terms and source and sink terms appear. A strict and consistent stability analysis is very difficult. The time integration algorithm therefore applies necessary conditions as illustrated above to produce bounded numerical solutions assuming that the solutions of the PDEs are bounded.

Time integration is considered stable in this context if the most restrictive of all conditions is satisfied at all grid points x_i:

$$\Delta t < C \cdot \min\left(\left\{ \frac{1}{|\Delta U|} \right\}_i, \left\{ \frac{\Delta x}{c_\mathrm{s} + |\mathbf{u}|} \right\}_i, \left\{ \frac{(\Delta x)^2}{\nu} \right\}_i \right), \tag{3.74}$$

where ΔU denotes the local relative change of variable U, c_s is the local sound speed, $\mathbf{u}$ is the local advection velocity and ν is the artificial diffusion coefficient. The constant C is typically set to ~ 0.3, depending on the time integration method. `BIFROST` dynamically adapts the time step Δt to the maximum possible size during the simulation.

3.5 Analytical test of the radiative transfer solver

The complexity of radiative transfer problems only allows a numerical solution of the equations in general. However, there exist simplified situations where an analytical solution is possible, providing useful functionality and accuracy tests for a numerical solver.

Radiative transfer with coherent scattering has an analytical solution in the case of a 1D plane-parallel isothermal atmosphere ("Lambert radiator") in the Eddington approximation. The photon destruction probability ϵ must be assumed constant with depth, and the Eddington approximation constrains the anisotropy of the radiation field, which is assumed to have a linear dependence on the projection factor $\mu = \cos\theta$, where θ is the polar angle. This setup is also known as the "two-stream" approximation that was already employed by Schuster (1905) to discuss effects of scattering in a foggy atmosphere.

Second-order Gauss-Legendre quadrature (see Appendix B.3) yields an exact representation of integrals over a linear polynomial. A numerical computation of the mean radiation field becomes directly comparable to the analytical solution in the two-stream approximation (e.g., Trujillo Bueno and Fabiani Bendicho, 1995).

3.5.1 Derivation of the analytical solution

The time-independent radiative transfer equation[1] for a horizontally homogeneous plane-parallel atmosphere is given by

$$\mu \frac{dI_\nu}{d\tau_\nu} = I_\nu - S_\nu, \tag{3.75}$$

where $\mu = \cos\theta$ is the projection factor for the polar angle θ. The optical depth scale for an outward increasing atmospheric height coordinate z is defined as $d\tau_\nu = -\chi_\nu dz$ with $\tau_\nu = 0$ outside the star. The zeroth, first and second moment of the specific intensity I_ν define the mean intensity J_ν, the radiative flux-like H_ν and the radiation pressure-like K_ν,

$$J_\nu = \frac{1}{2} \int_{-1}^{1} I_\nu d\mu \tag{3.76}$$

$$H_\nu = \frac{1}{2} \int_{-1}^{1} I_\nu \mu d\mu \tag{3.77}$$

$$K_\nu = \frac{1}{2} \int_{-1}^{1} I_\nu \mu^2 d\mu. \tag{3.78}$$

---

[1] The following discussion follows Rutten (2003)

Using these definitions and evaluating the same moments for Eq. (3.75) with an isotropic source function S_ν leads to the differential equations

$$\frac{dH_\nu}{d\tau_\nu} = J_\nu - S_\nu \tag{3.79}$$

$$\frac{dK_\nu}{d\tau_\nu} = H_\nu. \tag{3.80}$$

Inserting Eq. (3.79) into the derivative of Eq. (3.80) with respect to τ_ν yields a second-order equation for K_ν,

$$\frac{d^2K_\nu}{d\tau_\nu^2} = J_\nu - S_\nu. \tag{3.81}$$

The source function S_ν contains a coherent and isotropic scattering term,

$$S_\nu = (1 - \epsilon_\nu)J_\nu + \epsilon_\nu B_\nu, \tag{3.82}$$

where B_ν is the Planck function and ϵ_ν is the photon destruction probability. To proceed with the analytical solution of Eq. (3.81), it is necessary to approximate the anisotropy of the specific intensities I_ν by assuming a linear dependence on μ:

$$I_\nu(\tau_\nu, \mu) = a_{\nu,0}(\tau_\nu) + a_{\nu,1}(\tau_\nu)\mu. \tag{3.83}$$

Second-order Gauss-Legendre quadrature (Appendix B.3) yields an exact integral of Eq. (3.83) over angle by choosing the quadrature nodes $\mu = \pm 1/\sqrt{3}$,

$$\int_{-1}^{1} I_\nu(\tau_\nu, \mu)d\mu = I_\nu(\tau_\nu, -1/\sqrt{3}) + I_\nu(\tau_\nu, +1/\sqrt{3}), \tag{3.84}$$

enabling a direct comparison between the numerical solution and the analytical solution of the radiative transfer equation. Using the abbreviations $I_\nu^\pm = I_\nu(\mu = \pm 1/\sqrt{3})$ for outward and inward traveling photons, the first three moments of the specific intensity are

$$J_\nu = \frac{1}{2}(I_\nu^+ + I_\nu^-) = a_{\nu,0} \tag{3.85}$$

$$H_\nu = \frac{1}{2\sqrt{3}}(I_\nu^+ - I_\nu^-) = \frac{a_{\nu,1}}{3} \tag{3.86}$$

$$K_\nu = \frac{a_{\nu,0}}{3} = \frac{1}{3}J_\nu. \tag{3.87}$$

The last equivalence in Eq. (3.87) is known as the Eddington approximation, which is frequently used to formulate closure relations for computing radiative transfer through moment equations (e.g., Mihalas and Mihalas, 1984); the Eddington approximation is exact for linear anisotropy of I_ν. At the top of the atmosphere ($\tau_\nu = 0$), the assumption of zero irradiation from outside ($I_\nu^- = 0$) and using Eq. (3.85), Eq. (3.86), Eq. (3.80), and Eq. (3.87) lead to the useful relation

$$J_\nu(0) = \frac{1}{2}I_\nu^+(0) = \sqrt{3}H_\nu = \sqrt{3}\frac{dK_\nu}{d\tau_\nu} = \frac{\sqrt{3}}{3}\frac{dJ_\nu}{d\tau_\nu}. \tag{3.88}$$

The Eddington approximation allows a transformation of the second-order equation (Eq. (3.81)) into an equation for the mean intensity J_ν: inserting Eq. (3.87) and Eq. (3.82) yields

$$\frac{1}{3}\frac{d^2J_\nu}{d\tau_\nu^2} = J_\nu - S_\nu = \epsilon_\nu(J_\nu - B_\nu). \tag{3.89}$$

The second derivative of the Planck function B_ν in an isothermal atmosphere vanishes, enabling another transformation

$$\frac{1}{3}\frac{d^2(J_\nu - B_\nu)}{d\tau_\nu^2} = \epsilon_\nu(J_\nu - B_\nu). \tag{3.90}$$

This linear second-order differential equation has solutions of the form

$$J_\nu - B_\nu = C_1 e^{-\sqrt{3\epsilon_\nu}\tau_\nu} + C_2 e^{\sqrt{3\epsilon_\nu}\tau_\nu}. \tag{3.91}$$

At the bottom boundary deep inside the atmosphere ($\tau_\nu \to \infty$), the diffusion approximation $J_\nu = B_\nu$ requires $C_2 = 0$. At the top boundary, the derivative of Eq. (3.91) and relation Eq. (3.88) deliver:

$$\frac{dJ_\nu}{d\tau_\nu} = -\sqrt{3\epsilon_\nu}C_1 \qquad \rightarrow \qquad J_\nu(0) = -\sqrt{\epsilon_\nu}C_1 \equiv C_1 + B_\nu. \tag{3.92}$$

Both constants are now determined:

$$C_1 = -\frac{B_\nu}{1+\sqrt{\epsilon_\nu}} \qquad C_2 = 0. \tag{3.93}$$

Substitution in Eq. (3.91) yields analytical expressions for the mean radiation field, the source function and the outgoing intensity at the top:

$$J_\nu(\tau_\nu) = \left[1 - \frac{e^{-\sqrt{3\epsilon_\nu}\tau_\nu}}{1+\sqrt{\epsilon_\nu}}\right] B_\nu \tag{3.94}$$

$$S_\nu(\tau_\nu) = \left[1 - (1-\sqrt{\epsilon_\nu})\, e^{-\sqrt{3\epsilon_\nu}\tau_\nu}\right] B_\nu \tag{3.95}$$

$$I_\nu^+(0) = 2\frac{\sqrt{\epsilon_\nu}}{1+\sqrt{\epsilon_\nu}}B_\nu. \tag{3.96}$$

The exponential terms in Eq. (3.94) and Eq. (3.95) contain a factor $\sqrt{\epsilon_\nu}$ that defines a thermalization depth $\tau_{\mathrm{therm},\nu} = \tau_\nu/\sqrt{\epsilon_\nu}$ at which photons are destroyed on average and enter the thermal pool. Rutten (2003) separates a scattering atmosphere into a transparent region beneath $\tau_\nu < 1$, a translucent region between $1 < \tau_\nu < \tau_{\mathrm{therm},\nu}$, and a region above $\tau_\nu > \tau_{\mathrm{therm},\nu}$ where the radiation field is entirely thermalized.

At the surface ($\tau_\nu = 0$), the well-known relation

$$S_\nu(0) = \sqrt{\epsilon_\nu}B_\nu \tag{3.97}$$

holds: in the LTE case ($\epsilon_\nu = 1$), the level occupation numbers of two level atoms are dominated by collisions, and gas emission does not depend on the presence of an outward boundary through which radiation is lost. In the scattering case ($\epsilon_\nu < 1$), gas emission decreases, since photons are lost through the boundary and the radiative excitation rates decline. As a consequence, less photons are emitted through radiative de-excitation, and mean intensities decrease (see the discussion in, e.g., Rutten, 2003).

3.5.2 Comparison with the numerical result

The numerical radiative transfer solver is set to reproduce the mean radiation field J_{an} of the analytical solution (Eq. (3.94)), operating on a 3D cube with a resolution of 50 × 50 × 120 grid points and with a horizontally homogeneous stratification. The test does not verify the algorithms for interpolation onto the characteristics grid. The hydrodynamical mesh does not enter

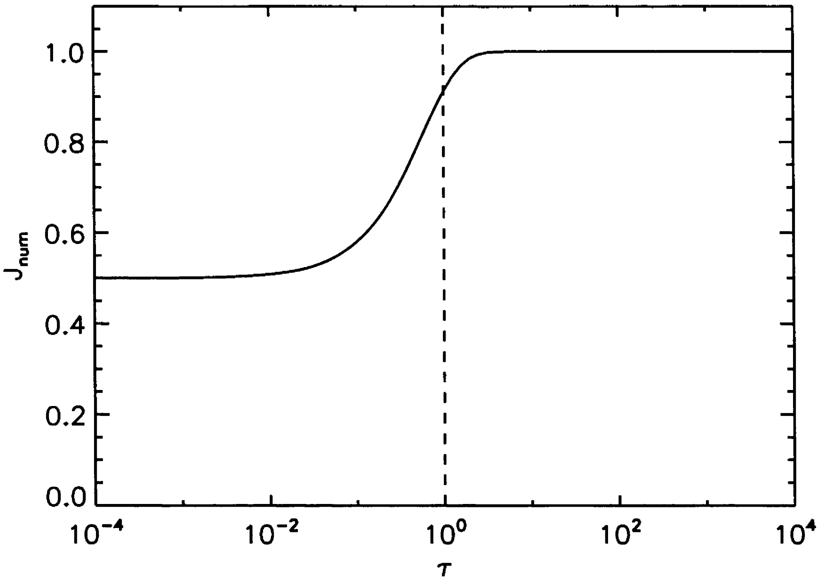

Figure 3.4: Numerical solution for the mean intensity J_{num} in LTE ($\epsilon = 1.0$) as a function of optical depth τ. The dashed line at $\tau = 1$ marks the optical surface.

the computations either, since optical depths are preset on a grid that is equidistant in $\log_{10} \tau$ with 10 grid points per decade. The solver uses second-order Gauss-Legendre quadrature with $\mu = 1/\sqrt{3}$ and arbitrary azimuth angles ϕ to produce mean intensities that are comparable to the analytical solution. Contrary to normal operation in radiation-hydrodynamical simulations, the radiative transfer code is set to double precision arithmetic to handle strong scattering at very large optical depths, which appears due to the (unrealistic) constancy of the photon destruction probability ϵ in the atmosphere. High condition numbers of the accelerator matrix (see Sect. 3.3.4) for very small ϵ in the diffusion region lead to stronger numerical noise and convergence problems in single precision arithmetic. The Planck function is set to $B(\tau) = 1.0$ in arbitrary units for all cases; it is also used as a first-guess source function for the solver.

In the LTE case ($\epsilon = 1$), the solver delivers $I^{+}(\tau) = 1.0$ for outgoing intensities and $I^{-}(\tau) = 1.0 - e^{-\sqrt{3.0}\tau}$ for ingoing intensities (see Fig. 3.4). The deviation from the numerical evaluation of Eq. (3.94) practically vanishes for any grid resolution, as the Gauss-Seidel solver uses the formal solution of the radiative transfer equation, which leads to equivalent expressions. In the scattering case, photon destruction probabilities assume values between $\epsilon = 10^{-1}$ (moderate scattering) and $\epsilon = 10^{-6}$ (strong scattering), decreasing by factors of 10. The left column of Fig. 3.5 shows the numerical results for the radiation field J_{num}. The mean intensity at the surface decreases for smaller ϵ due to outward photon losses and the thermalization depth moves deeper into the atmosphere (dot-dashed line), in agreement with the discussion in Sect. 3.5.1. At the smallest optical depths, the numerical solution delivers $J_{\mathrm{num}}(\tau = 10^{-4}) \approx \sqrt{\epsilon}$ for small ϵ. The radiation field is completely thermal ($J_{\mathrm{num}} = B = 1.0$) above $\tau \gtrsim \tau_{\mathrm{therm}}$.

The center column of Fig. 3.5 shows the optical depth-dependence of the total error of the numerical solution as the relative deviation between J_{num} and J_{an},

$$\Delta J_{\mathrm{rel}}(\tau) = \frac{J_{\mathrm{num}}(\tau) - J_{\mathrm{an}}(\tau)}{J_{\mathrm{an}}(\tau)}. \tag{3.98}$$

At large optical depths, radiative transfer is local and the total error depends on the source

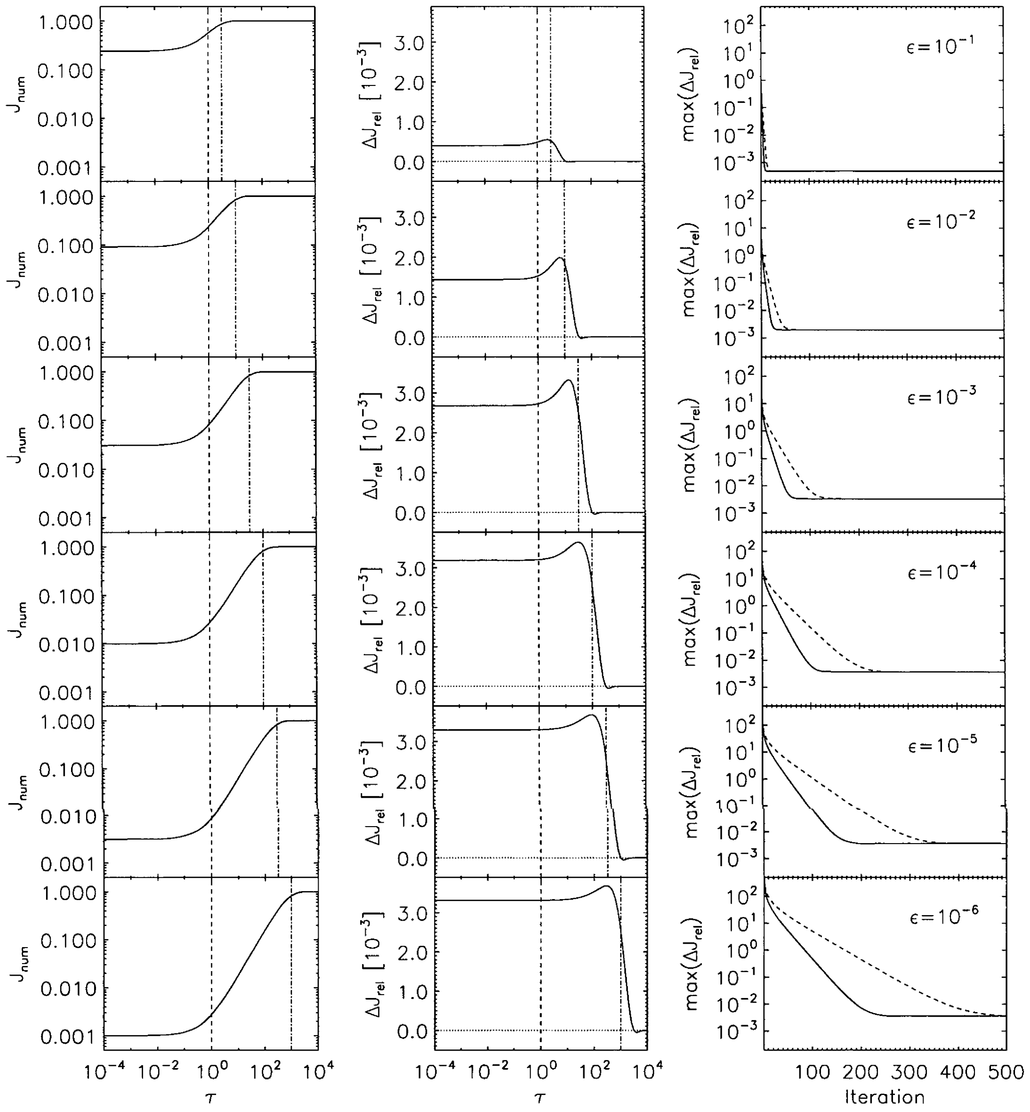

Figure 3.5: Numerical solution for the mean intensity J_{num} as a function of optical depth τ (left column), relative deviation ΔJ_{rel} from the analytical solution as a function of optical depth τ (center column), and maximum relative deviation $\max(\Delta J_{\text{rel}})$ as a function of iteration count (right column). The photon destruction probability ϵ ranges from 10^{-1} (top row) to 10^{-6} (bottom row). The dashed and dot-dashed lines in the left column and center column mark the optical surface at $\tau = 1$ and the thermalization depth at $\tau_{\text{therm}} = 1/\sqrt{\epsilon}$. The dotted line in the center column indicates zero deviation. Dashed lines in the right column show the convergence speed for Gauss-Seidel corrections applied only during upsweeps, solid lines show the convergence speed for corrections applied during both upsweeps and downsweeps.

function gradient through the discretization error of the logarithmic optical depth grid. Using Eq. (3.95), one obtains

$$\Delta S \approx \frac{dS}{d\log\tau}\Delta\log\tau = \tau\frac{dS}{d\tau}\Delta\log\tau = (1-\sqrt{\epsilon})B\left(\sqrt{3\epsilon}\tau e^{-\sqrt{3\epsilon}\tau}\right)\Delta\log\tau \tag{3.99}$$

$$= (1-\sqrt{\epsilon})B\left(\sqrt{3}\frac{\tau}{\tau_{\mathrm{therm}}}e^{-\sqrt{3}\frac{\tau}{\tau_{\mathrm{therm}}}}\right)\Delta\log\tau \tag{3.100}$$

for the variation ΔS of the source function between adjacent grid points with constant spacing $\Delta\log\tau$. In the LTE case, $\Delta S = 0$ everywhere in the atmosphere since $\epsilon = 1.0$ and $S = B = 1.0$, independent of $\Delta\log\tau$. For $\epsilon < 1.0$ and at optical depths $\tau \gtrsim \tau_{\mathrm{therm}}$, the radiation field is entirely thermalized ($J_{\mathrm{num}} \approx B = 1.0$), and ΔJ_{rel} vanishes since $\Delta S \to 0.0$. The source function starts to decrease quickly through the decreasing mean intensity near τ_{therm} due to outward photon losses, causing a sharp increase in the error of the numerical solution. ΔJ_{rel} peaks in the translucent zone as ΔS is largest between $1.0 < \tau < \tau_{\mathrm{therm}}$. The magnitude of the peak grows with decreasing ϵ through the $(1-\sqrt{\epsilon})$ factor in Eq. (3.100); an upper limit is reached with $\epsilon \to 0.0$. It also follows from Eq. (3.100) that $\max(\Delta J_{\mathrm{rel}})$ scales with the grid resolution. Further up in the atmosphere, the error decreases again through the finer grid spacing. At optical depths $\tau \ll \tau_{\mathrm{therm}}$, the local discretization error becomes negligible due to the vanishing $\Delta S \to 0.0$. However, as I^+ and I^- decouple from the local source function and the radiation field becomes anisotropic, the error becomes independent from the source function gradient. ΔJ_{rel} is dominated by the propagated error of outgoing radiation I^+ from deeper layers and is therefore constant.

The right column of Fig. 3.5 shows the convergence speed of the numerical result to the analytical solution, measured through the maximum relative deviation $\max(\Delta J_{\mathrm{rel}})$ in the atmosphere (see Eq. (3.98)). Dashed lines represent computations where Gauss-Seidel corrections for the source function were applied only during upsweeps, while solid lines show the results when both upsweeps and downsweeps were corrected, which increases convergence speeds by about a factor of two, as predicted by Trujillo Bueno and Fabiani Bendicho (1995). Convergence is significantly slower when the thermalization depth moves to deep, very optically thick layers as photon destruction probabilities decrease. The implementation of the Gauss-Seidel solver in upsweep correction mode delivers similar performance to the version of Trujillo Bueno and Fabiani Bendicho (1995) for $\epsilon = 10^{-6}$. Convergence is reached after $\approx$ 450 iterations (dashed line in the lower right panel of Fig. 3.5). $\max(\Delta J_{\mathrm{rel}}) \approx 3.7 \cdot 10^{-3}$ at $\epsilon = 10^{-6}$ is similar to the error quoted by Trujillo Bueno and Fabiani Bendicho (1995), who used a slightly lower grid resolution which reduces the amount of iterations needed to reach the discretization error.

In summary, the results of the test with an isothermal atmosphere in the Eddington approximation and with coherent scattering show that the radiative transfer solver performs as expected: numerical errors remain below the 1% level for all test cases, and the convergence speed is similar to the implementation of Trujillo Bueno and Fabiani Bendicho (1995).

Chapter 4

Radiative transfer with scattering for domain-decomposed 3D MHD simulations of cool stellar atmospheres

W. Hayek, M. Asplund, M. Carlsson, R. Trampedach, R. Collet, B. V. Gudiksen, V. H. Hansteen, and J. Leenarts, *A&A, 517:49, July 2010*

Abstract

Aims. We present the implementation of a radiative transfer solver with coherent scattering in the new `BIFROST` code for radiative magneto-hydrodynamical (MHD) simulations of stellar surface convection. The code is fully parallelized using MPI domain decomposition, which allows for large grid sizes and improved resolution of hydrodynamical structures. We apply the code to simulate the surface granulation in a solar-type star, ignoring magnetic fields, and investigate the importance of coherent scattering for the atmospheric structure.
Methods. A scattering term is added to the radiative transfer equation, requiring an iterative computation of the radiation field. We use a short-characteristics-based Gauss-Seidel acceleration scheme to compute radiative flux divergences for the energy equation. The effects of coherent scattering are tested by comparing the temperature stratification of three 3D time-dependent hydrodynamical atmosphere models of a solar-type star: without scattering, with continuum scattering only, and with both continuum and line scattering.
Results. We show that continuum scattering does not have a significant impact on the photospheric temperature structure for a star like the Sun. Including scattering in line-blanketing, however, leads to a decrease of temperatures by about 350 K below $\log_{10}\tau_{5000} \lesssim -4$. The effect is opposite to that of 1D hydrostatic models in radiative equilibrium, where scattering reduces the cooling effect of strong LTE lines in the higher layers of the photosphere. Coherent line scattering also changes the temperature distribution in the high atmosphere, where we observe stronger fluctuations compared to a treatment of lines as true absorbers.

4.1 Introduction

The atmospheres of late-type stars form the transition from the opaque convective envelope to the interstellar medium. Hot rising plasma transports heat to the surface, becomes transparent and looses its entropy through radiative cooling. Gravity accelerates the cooled gas back into the star, carrying kinetic energy inward and forcing the convective flow. By taking over heat transport and removing entropy, the radiation field therefore indirectly drives convection (Stein and Nordlund, 1998), making radiative and hydrodynamical processes equally important at the surface. Magnetic fields have strong impact on the higher atmosphere and cause local phenomena in the surface granulation, such as spots and pores.

The classical numerical models of cool stellar atmospheres in 1D focused on a detailed description of radiative transfer, with two prominent examples being the `MARCS` code (Gustafsson et al., 1975) and the `ATLAS` code (Kurucz, 1979). Assuming a plane-parallel or spherical-symmetric stratification, they include only a rudimentary treatment of convective energy transport in cool stellar atmospheres. Subsequent updates of these models (e.g., Kurucz, 1996; Gustafsson et al., 2008) benefit from the largely increased computational power, refining the treatment of the strongly wavelength-dependent line opacities. Newer codes, such as `PHOENIX` (Hauschildt et al., 1999) can also include departures from local thermodynamic equilibrium (LTE) in the radiative transfer computation and the absorber populations. The 1D models have not only provided growing insight into the physical environment at the surface of cool stars, but have also become a standard tool for chemical abundance analyses. The wide variety of applications includes studies of galactic chemical evolution and of the origin of the elements.

The advent of fully dynamic 3D surface convection simulations has enabled a much more realistic treatment of the hydrodynamical plasma flow, deepening our understanding of convection and eliminating the need for microturbulent and macroturbulent broadening in line formation computations (see, e.g., Nordlund et al., 2009). The 3D models are capable of accurately reproducing the surface structure of the observed solar granulation with their strongly inhomogeneous surface intensities (Stein and Nordlund, 1998). The velocity fields predicted by the 3D simulations lead to a close match with both the observed spectral line bisectors and the broadening of their profiles in the atmospheres of different stars (e.g., Dravins and Nordlund, 1990; Asplund et al., 2000b; Allende Prieto et al., 2002; Ramírez et al., 2009). Recently, impressive agreement between a new synthetic 3D model and solar observations has been found in a detailed comparison of spectral line shifts, equivalent widths and center-to-limb variations for normalized line profiles (Pereira et al., 2009a,b). In essentially all cases, this 3D model reproduced the observations with an accuracy that is comparable to the semi-empirical model of Holweger and Müller (1974), which is traditionally used in spectroscopy of the solar photosphere.

The accuracy of the treatment of radiation in 3D, however, is still strongly limited by the available computational power. Radiative transfer easily becomes the most computationally expensive part of a simulation, since the equations must be solved for a considerably larger set of transport directions compared to hydrodynamics, and non-grey opacities must be accounted for in realistic simulations. Most of the currently existing 3D radiative (M)HD codes therefore assume LTE and capture the atmospheric height dependence of continuum and line opacities using the opacity binning method (e.g., Nordlund, 1982; Ludwig, 1992): the problem of computing the monochromatic radiation field for a larger number of wavelengths is reduced to the numerical solution of the radiative transfer equation for typically 5 opacity bins. Skartlien (2000) extended the opacity binning method to include coherent scattering, and showed its importance in the solar chromosphere using a 3D radiative transfer solver for parallel shared-memory architectures.

Modern large-scale computer clusters use distributed memory architectures to handle the growing complexity of scientific simulations, allowing, e.g., self-consistent MHD models of the solar chromosphere, transition region and corona (Hansteen, 2004; Hansteen et al., 2007) or detailed hydrodynamical models of giant stars (Collet et al., 2007). We present a new fully MPI-parallelized radiative transfer solver with coherent scattering for the new `BIFROST` code for time-dependent 3D MHD simulations of cool stellar atmospheres (Gudiksen et al., in preparation).

In Sect. 4.2 and 4.3, we discuss the physics of the radiative transfer model and its implementation in the MHD code. Section 4.4 describes the most important continuous and line opacity sources that we include in our simulations. Section 4.5 describes the application of the `BIFROST` code to model the atmosphere of a solar-type star using radiative transfer calculations with scattering, and discusses the effects on the temperature structure.

4.2 Radiative transfer with scattering and the radiative flux divergence

4.2.1 The radiative transfer equation

Hydrodynamical simulations of cool stellar atmospheres need to cover several pressure scale heights above and below the optical surface to minimize the effect of the boundaries on the granulation flow. The exponential density stratification causes the optical depth of the plasma to span about 15 orders of magnitude from the highest to the lowest layers of the simulation. The radiative transfer problem must therefore be solved in very different physical environments: in the extremely optically thick diffusion region at the bottom of the simulation box, all photons are thermalized. At the top, the atmosphere is mostly optically thin and mainly photons in the strongest lines interact with the gas. For the bulk of the photons, the transition between these two domains is rapid; it is confined to a thin layer which appears corrugated due to the different geometrical depth variation of opacities in upflows and downflows (Stein and Nordlund, 1998).

Radiative transfer is, in general, a time-dependent process, which needs to be treated simultaneously with the hydrodynamics. However, the timescale of photon propagation over a mean free path length, $t_\lambda = (c\chi_\lambda)^{-1}$, where χ_λ is the monochromatic opacity and c is the speed of light, is orders of magnitude shorter than any hydrodynamical timescale. Radiative transfer therefore decouples from the hydrodynamics and is well approximated by a time-independent problem, described by a radiative transfer equation for the monochromatic specific intensity $I_\lambda(\mathbf{x}, \hat{\mathbf{n}})$ in direction $\hat{\mathbf{n}}$:

$$\hat{\mathbf{n}} \cdot \nabla I_\lambda(\mathbf{x}, \hat{\mathbf{n}}) = -\chi_\lambda(\mathbf{x}) I_\lambda(\mathbf{x}, \hat{\mathbf{n}}) + j_\lambda(\mathbf{x}, \hat{\mathbf{n}}), \tag{4.1}$$

where j_λ denotes the local emission at wavelength λ (see, e.g., Mihalas, 1978; Rutten, 2003). The left-hand side of Eq. (4.1) is defined in the rest frame of the model atmosphere. The source and sink terms of the right-hand side are naturally described in the co-moving frame of the flowing gas. The consequent Doppler shifts are difficult to treat in 3D time-dependent simulations due to restrictions in computational power, requiring us to compute wavelength-integrated quantities in the opacity binning approximation (see below). We therefore assume a static medium, neglecting possible influences of the velocity field.

The extinction of photons is described, as customary, through the absorption coefficient κ_λ and the scattering coefficient σ_λ, which combine to the gas opacity,

$$\chi_\lambda(\mathbf{x}) = \kappa_\lambda(\mathbf{x}) + \sigma_\lambda(\mathbf{x}), \tag{4.2}$$

and give rise to the definition of the photon destruction probability

$$\epsilon_\lambda(\mathbf{x}) = \frac{\kappa_\lambda(\mathbf{x})}{\kappa_\lambda(\mathbf{x}) + \sigma_\lambda(\mathbf{x})}. \tag{4.3}$$

Recasting the optical path $ds = \hat{\mathbf{n}} \cdot d\mathbf{x}$ along a ray in direction $\hat{\mathbf{n}}$ into the optical depth $d\tau_\lambda = \chi_\lambda ds$ along that direction, gives Eq. (4.1) the form

$$\frac{dI_\lambda}{d\tau_\lambda}(\tau_\lambda) = -I_\lambda(\tau_\lambda) + S_\lambda(\tau_\lambda), \tag{4.4}$$

with the source function $S_\lambda \equiv j_\lambda / \chi_\lambda$. For the numerical computation, we employ the formal solution

$$I_\lambda(\tau_\lambda) = I_\lambda(\tau_{\mathrm{u},\lambda}) e^{-(\tau_\lambda - \tau_{\mathrm{u},\lambda})} + \int_{\tau_{\mathrm{u},\lambda}}^{\tau_\lambda} S_\lambda(t) e^{t-\tau_\lambda} dt, \tag{4.5}$$

where $I_\lambda(\tau_{\mathrm{u},\lambda})$ is the incident intensity at the upwind end of the ray at optical depth $\tau_{\mathrm{u},\lambda} < \tau_\lambda$.

The source function S_λ at optical depth τ_λ in direction $\hat{\mathbf{n}}$ includes local thermal radiation from the gas and coherent scattering of photons:

$$S_\lambda = \frac{\sigma_\lambda}{4\pi\chi_\lambda} \int_{S^2} \phi(\hat{\mathbf{n}}, \hat{\mathbf{n}}') I_{\lambda,\hat{\mathbf{n}}'} d\Omega' + \frac{\kappa_\lambda}{\chi_\lambda} B_\lambda = (1 - \epsilon_\lambda) J_\lambda + \epsilon_\lambda B_\lambda, \tag{4.6}$$

where scattered radiation from direction $\hat{\mathbf{n}}'$ contributes with weight ϕ in the integral over the unit sphere S^2, B_λ denotes the Planck function, and J_λ is the mean intensity. The second equality holds for isotropic angular redistribution of radiation ($\phi = 1$). For $\epsilon_\lambda < 1$, the source function depends on J_λ and thus, through the non-locality of radiative transfer, on radiation processes in the entire simulation domain. This turns Eq. (4.4) from an ordinary differential equation into an integro-differential equation.

Current limitations of available computing resources require the assumption of isotropic coherent scattering. Continuum processes in cool stellar atmospheres and very strong lines fulfill this restriction in very good or reasonable approximation, respectively, due to their weak wavelength dependence. Intermediate and weak lines are more accurately treated in complete spectral redistribution.

4.2.2 The radiative flux divergence and the wavelength integral

Absorption and thermal emission of radiation couples the stellar plasma with the radiation field through the transfer of heat. Photon energies in cool stars are too small to exert a significant force on the fluid compared to the gas pressure and gravity; the coupling is therefore sufficiently described by adding a radiative heating term Q_{rad} to the energy equation.

Evaluating the first moment of Eq. (4.1) and using the above definitions yields

$$-\nabla \cdot \mathbf{F}_\lambda = 4\pi\chi_\lambda (J_\lambda - S_\lambda) = 4\pi\epsilon_\lambda\chi_\lambda (J_\lambda - B_\lambda), \tag{4.7}$$

where $\nabla \cdot \mathbf{F}_\lambda$ is the local monochromatic radiative flux divergence. The second equality holds in the case of the coherent scattering source function (Eq. (4.6)). The scattering term does not contribute to heat exchange by definition, reducing radiative heating and cooling by a factor of ϵ_λ compared to the case where $S_\lambda = B_\lambda$.

Integrating the monochromatic flux divergence in Eq. (4.7) over the whole wavelength spectrum of the star yields the local heating rate Q_{rad}:

$$Q_{\mathrm{rad}} = -\int_0^\infty \nabla \cdot \mathbf{F}_\lambda d\lambda. \tag{4.8}$$

In the optically thick regime, where radiative transfer is diffusive, this integral may be simplified with good accuracy by assuming the Rosseland mean opacity in the so-called gray approximation. However, gray opacities are not sufficient for a realistic treatment of the height-dependent line-blanketing above the surface, where the atmospheric structure is very sensitive to the radiation field. Atomic and molecular lines are important opacity sources in this region, changing the radiative heating and cooling compared to the simplified case of a gray atmosphere (see, e.g., Vögler et al., 2004, for a detailed discussion). The current version of the `MARCS` 1D atmosphere code uses the opacity sampling technique (Peytremann, 1974), which approximates the spectrum through statistical sampling at $\sim$ 100 000 wavelength points. This resolution is sufficient to capture continuum absorption and line-blanketing without bias, at least in the lower parts of the atmosphere where the spectral distribution of absorbers is sufficiently widespread. Stellar atmosphere models in 3D do not allow for such a detailed treatment yet, since a single formal solution is many orders of magnitude more expensive to compute: the radiative transfer equation in our radiation-hydrodynamical model (Sect. 4.5.1) is solved for 240×240 columns and 24 transport directions, which is equivalent to $\sim 10^5$ 1D calculations for each time step.

Nordlund (1982), Ludwig (1992) and Skartlien (2000) have described opacity binning techniques, where wavelength integration is performed over subsets of the spectral range before the solution of the radiative transfer equation, and the radiation field is computed for only a few mean opacities instead of the full spectrum. We will give a brief description of the technique in the following; see Skartlien (2000) for a more detailed discussion.

Integrating the radiative transfer equation (Eq. (4.1)) over wavelength leads to the definition of a mean opacity, mean scattering coefficient and mean absorption coefficient:

$$\chi^{\mathrm{I}} = \frac{\int \chi_\lambda I_\lambda d\lambda}{\int I_\lambda d\lambda} \tag{4.9}$$

$$\sigma^{\mathrm{J}} = \frac{\int \sigma_\lambda J_\lambda d\lambda}{\int J_\lambda d\lambda} \tag{4.10}$$

$$\kappa^{\mathrm{B}} = \frac{\int \kappa_\lambda B_\lambda d\lambda}{\int B_\lambda d\lambda}. \tag{4.11}$$

The intensity-weighted mean opacity χ^{I} and the mean-intensity-weighted mean scattering coefficient σ^{J} depend on the unknown radiation field I_λ and its angular average J_λ, which must be estimated: we use 1D radiative transfer calculations on the mean stratification of the atmosphere (see Sect. 4.5.2), which yield approximations for $\chi^{\mathrm{I}} \approx \chi^{\mathrm{J,1D}}$ and $\sigma^{\mathrm{J}} \approx \sigma^{\mathrm{J,1D}}$.

These three mean coefficients represent absorption, scattering and thermal emission of photons with good accuracy where the stellar atmosphere is optically thin across the spectrum. However, $\chi^{\mathrm{J,1D}}$ does not ensure a correct total radiative energy flux at optical depths $\tau \gg 1$ where radiative transfer is diffusive. It needs to be replaced by the Rosseland mean opacity, defined as the weighted harmonic mean

$$\chi^{\mathrm{R}} = \frac{\int (dB_\lambda/ds)\, d\lambda}{\int (1/\chi_\lambda)\, (dB_\lambda/ds)\, d\lambda}. \tag{4.12}$$

We consequently use a τ-weighted sum of the two quantities $\chi^{\mathrm{J,1D}}$ and χ^{R}. The geometrical depth of the transition between the two regimes near $\tau \approx 1$ varies quickly with wavelength where spectral lines are present, and it is not sufficient to consider only a single pair of mean opacities $\chi^{\mathrm{J,1D}}$ and χ^{R}. The opacity binning method therefore defines several opacity groups, where each member reaches unit optical depth ($\tau_\lambda = 1$) at a similar geometrical depth. The integrals in Eq. (4.9) - Eq. (4.12) are then evaluated only for a set of member wavelengths $\{\lambda_i\}$ in each bin i, which does not have to be continuous.

Depending on the height range of the stellar atmosphere model and the wavelength selection method, it turns out that about 5 such opacity bins are enough to capture the essence of the line-blanketing and continuum opacity and to obtain a realistic temperature structure (Vögler et al., 2004). More recent atmosphere models have been extended to 12 bins (Caffau et al., 2008). For the simulations presented in this work, we compute radiative transfer with 12 bins, where wavelengths are sorted not only by the geometrical height of the monochromatic optical surface, but also by wavelength, separating opacities in the UV, visual and infrared bands (Trampedach et al., in preparation).

It is difficult to assess the quality of the opacity binning method in realistic 3D simulations: deviations of the resulting radiative heating rates Q_{rad} from an accurate monochromatic solution have a height-dependent impact on the temperature structure (see Sect. (4.5)), making the long-term behavior of the simulation hard to predict. The agreement of 3D model atmospheres with various observational tests indicates that opacity binning still yields a reasonable estimate for the line-blanketing.

4.3 The numerical implementation

The large variety of radiative transfer models for astrophysical problems inspired the development of very different analytical and numerical methods to obtain the radiation field (see, e.g., Wehrse and Kalkofen (2006) for an overview). For our given problem of computing radiative heating rates as the flux divergence $-\nabla \cdot \mathbf{F}$ of a time-independent radiation field in 3D, the direct solution of Eq. (4.4) yields accurate results with efficient numerical schemes.

Characteristics methods, which solve the transfer problem along a discrete set of light rays to capture the anisotropy of the radiation field in the optically thin atmosphere, are a popular choice in stellar atmosphere models. Nordlund (1982) and Skartlien (2000) use Feautrier-type differential radiative transfer solvers (Feautrier, 1964) for solving Eq. (4.4) on long characteristics. They span across the entire simulation domain, which is an obstacle for a domain-decomposed parallelization of the MHD code (see Sect. 4.3.2 below). Bruls et al. (1999), Vögler et al. (2005) and Muthsam et al. (2010) employ the short characteristics method (Mihalas et al., 1978; Olson and Kunasz, 1987; Kunasz and Auer, 1988), where the radiative transfer equation is solved on characteristics which only extend to the adjacent upwind and downwind grid layers. This method is required by our choice of iteration technique for an efficient solution of the scattering problem.

4.3.1 Short characteristics

The short characteristics method employs the formal solution (Eq. (4.5)) of the monochromatic radiative transfer equation (Eq. (4.4)) to compute the radiation field at the center of a three-point ray for a known source function S_λ. The discretization is performed by interpolating the source function for a given wavelength λ (or bin number) along the ray using a second-order Bézier curve (see, e.g., the discussion in Auer, 2003)

$$S(t) = (1-t)^2 S_{\mathrm{u}} + t^2 S_0 + 2t(1-t) S_{\mathrm{c}}, \tag{4.13}$$

where S_{u} and S_0 are the upwind and local source functions and $t = (\tau - \tau_{\mathrm{u}})/(\tau_0 - \tau_{\mathrm{u}})$ is the curve parameter. S_{c} is a control point, which shapes the interpolating curve by restricting it to the convex hull laid out by S_{u}, S_{c} and S_0. This characteristic of Bézier curves may be exploited to detect and suppress overshoots, which destabilize the numerical solution at places in the atmosphere where strong opacity and temperature gradients occur. Inserting Eq. (4.13) into the formal solution (Eq. (4.5)), evaluating the integral and reordering the terms yields the discretized expression

$$I(\tau) = I(\tau_\mathrm{u})e^{-(\tau-\tau_\mathrm{u})} + \Psi_\mathrm{u} S_\mathrm{u} + \Psi_0 S_0 + \Psi_\mathrm{d} S_\mathrm{d}. \tag{4.14}$$

The shape of the three interpolation coefficients Ψ_u, Ψ_0 and Ψ_d for the upwind, center and downwind source functions depends on the control point S_c. Choosing

$$S_\mathrm{c} = S_0 - \frac{\tau_0 - \tau_\mathrm{u}}{2} S'_0, \tag{4.15}$$

where S'_0 is the centered derivative on the three-point stencil $(S_\mathrm{u}, S_0, S_\mathrm{d})$, yields second-order interpolation. It is used where no overshoots happen and correctly reproduces the diffusion approximation at optical depths $\tau \gtrsim 30$ (see Appendix B.1 for the detailed shape of the Ψ coefficients). In the optically thin atmosphere where $\tau \lesssim 10^{-3}$, a second-order expansion of the $(1 - e^{-\tau})$ terms in the Ψ constants stabilizes the solver, which may therefore be implemented with single precision floating point numerics throughout the simulation domain. Optical depths $\Delta\tau$ along the characteristics are similarly computed using the Bézier interpolation technique.

The mean intensities J and the components of the flux vector $\mathbf{F}$ are computed by approximating the zeroth and first moment integrals by a quadrature sum over selected ray angles ("method of discrete ordinates"),

$$J \approx \frac{1}{4\pi} \sum_i w_i I(\hat{\mathrm{n}}_\mathrm{i}); \qquad F_j \approx \sum_i w_i I(\hat{\mathrm{n}}_\mathrm{i})(\hat{\mathrm{n}}_\mathrm{i} \cdot \hat{\mathrm{n}}_\mathrm{j}), \tag{4.16}$$

where w_i is the weight of direction $\hat{\mathrm{n}}_\mathrm{i}$. The best choice of quadrature depends on the expected anisotropy of the radiation field and on the quantity that needs to be computed. In our case, the components of the flux vector $\mathbf{F}$ need to be calculated explicitly, requiring the quadrature be invariant to rotation by $\pi/2$ to avoid directional bias. Carlson's A4 quadrature (Carlson, 1963) with 3 rays per octant is an appropriate choice and represents the anisotropy with good accuracy.

Short characteristics require knowledge of the upwind intensities $I(\tau_\mathrm{u})$ for each ray direction $\hat{\mathrm{n}}$, on which the sweep direction for a formal solution therefore depends. Interpolation yields all such quantities (Sect. 4.3.3). Shallow rays, that fail to hit the upwind layer within the grid cells, need to be extended and may cross several cells, possibly across subdomain boundaries. For the first formal solution of a simulation run, a Feautrier-type long characteristics solver delivers boundary intensity estimates; intensities from the previous iteration in the neighbor subdomains are used for all subsequent computations. Once $I(\tau)$ is known along two edges of the current layer, the remaining unknown intensities may be computed away from the boundary through vertical interpolation between the upwind layer and the current layer. It is worth noting that some long characteristics codes turn transport directions around the vertical axis with every time step to avoid numerical artefacts stemming from a fixed set of discrete ordinates. Such an effect is not observed in our short characteristics implementation. Moreover, the anisotropy of the radiation field slows down convergence of an iterative solution in optically thin parts when transport directions are turned between time steps, since the stored boundary intensities come from the previous solution (see Sect. 4.3.2 for further details). All ray directions are therefore kept fixed.

The discretized formal solution (Eq. 4.14) in the simulation domain and averaging of the radiation field over solid angle will be abbreviated in the following using the Λ operator, which is commonly defined through

$$J = \Lambda S. \tag{4.17}$$

Λ is a linear matrix operator on the source functions S which represents the numerical algorithm used to compute the radiation field in the code.

4.3.2 The Gauss-Seidel scheme and MPI parallelization

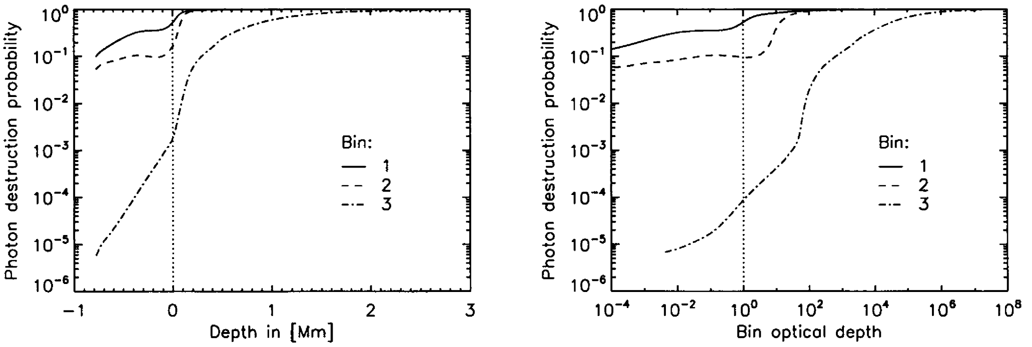

Figure 4.1: Horizontal mean photon destruction probability ϵ for three bins representing continuum and weak lines (1), intermediate lines (2) and strong lines (3) in the UV, plotted as a function of geometrical depth (left) and optical depth in the respective bin (right, the average is taken over surfaces with the same vertical optical depth). The dotted line marks the stellar surface (left) and unit optical depth in each bin (right).

As noted in Sect. 4.2.1, the coherent scattering term turns the transfer equation into an integro-differential equation for the specific intensity I. Using the Λ operator defined in Eq. (4.17), the problem may be rewritten into the matrix equation

$$[\mathbb{1} - (1-\epsilon)\Lambda]\, S = \epsilon B, \tag{4.18}$$

with the identity matrix $\mathbb{1}$. The expression represents a very large system of linear equations. Its direct solution in 3D through inversion of the operator on the left-hand side is far too complex and numerically unstable in some cases, to be of practical use. Most solvers therefore apply an iteration scheme, the choice of which depends on the structure of the Λ operator matrix. Approximate Lambda Iteration (ALI, sometimes also called Accelerated Lambda Iteration, Cannon, 1973) is a popular method to obtain a good approximation of the radiation field with fast convergence. J is computed through a formal solution and used to correct the source function. Rather than just inserting J in S, which leads to very slow convergence (or no convergence at all), a largely simplified approximate operator Λ^* is used to compute correction values ΔS at low cost, speeding up convergence tremendously.

We employ the Gauss-Seidel scheme (Trujillo Bueno and Fabiani Bendicho, 1995), an ALI method that combines the formal solution and correction steps. It mimics an upper/lower triangular Λ^* operator, but the scheme does not require the expensive construction of the matrix. Source function corrections at the grid point i are obtained during a solver sweep from the expression

$$\Delta S_i = \frac{(1-\epsilon_i) J_i^{\mathrm{old/new}} + \epsilon_i B_i - S_i^{\mathrm{old}}}{1 - (1-\epsilon_i)\Lambda_{ii}}. \tag{4.19}$$

$J_i^{\mathrm{old/new}}$ is the radiation field that includes the corrections in the upwind part of the simulation domain, which have already been computed during the current sweep. The dependence of ΔS_i on J_i in each layer for immediate correction of S_i during the sweep requires employing the short characteristics method. The denominator contains the diagonal element Λ_{ii} of the

Λ operator, which may be computed using Eq. (4.14) and therefore reduces to a sum of Ψ constants. Source function corrections may be applied during both upsweeps and downsweeps for faster convergence.

We tested our radiative transfer code by comparing the numerical results with an analytical solution for the case of an isothermal 1D atmosphere with constant photon destruction probability ϵ (see the discussion in Trujillo Bueno and Fabiani Bendicho, 1995) and found very good agreement.

The radiation solver is parallelized using spatial domain decomposition and communication with the MPI library, adopting the virtual topology given by the MHD solver of the `BIFROST` code. The grid is decomposed into cuboid subdomains, allowing an arbitrary number of divisions on all three spatial axes. While this parallelization lends itself to a mixed initial and boundary value problem found in computational hydrodynamics, it is harder to apply in an efficient way to the pure boundary value problem of time-independent radiative transfer. Concurrent computation of spectral subdomains (or opacity bins) would provide a higher degree of parallelism considering the non-local dependencies in a monochromatic formal solution of our given coherent scattering problem, but such an approach would cause severe load balancing issues and suffer from node memory limitations when applying the code to very large simulations. Spatial domain decomposition may still be combined with spectral domain decomposition if radiative transfer needs to be solved for a large number of wavelengths.

Heinemann et al. (2006) have presented a domain-decomposed method based on a variant of the formal solution (Eq. (4.5)) on long characteristics. The solver bypasses the problem of missing incident intensities at subdomain boundaries by splitting the local and boundary contributions. While their approach efficiently solves the radiative transfer equation without scattering, the long characteristics solver would have to be combined with a different ALI scheme than Gauss-Seidel. An approximate Λ^* operator needs a certain bandwidth around its matrix diagonal to achieve good convergence (see, e.g., the discussion in Hauschildt and Baron, 2006). It is therefore more expensive to construct and invert than the diagonal operator used for the Gauss-Seidel scheme.

Our code iterates the solution, starting with the source function and subdomain boundary intensities from the previous hydrodynamical time step, until the maximum relative source function correction in the domain after the nth iteration is smaller than a preset threshold C:

$$\max\left(\frac{\left|S_i^n - S_i^{n-1}\right|}{S_i^{n-1}}\right) \leqslant C. \tag{4.20}$$

When scattering is not included, the maximum relative change of mean intensities at the boundary is used instead to test the convergence of the radiation field:

$$\max\left(\frac{\left|J_i^n - J_i^{n-1}\right|}{J_i^{n-1}}\right) \leqslant C. \tag{4.21}$$

If too few iterations are performed, the subdomain boundaries produce artifacts in the upper parts of the atmosphere, where photon mean free paths are comparable to or larger than the subdomain size. In practice, it turns out that a threshold of $C \sim 10^{-3}$ yields good results in either case.

The convergence speed of an iterative method depends on the spectral radius ρ of the operator with which corrections are computed, as the error of the solution after n iterations decreases with ρ^n. The spectral radius approaches $\rho \approx 1 - \epsilon$ for optically thick scattering media (see, e.g., the discussion in Trujillo Bueno and Fabiani Bendicho, 1995). Strong scattering at high optical

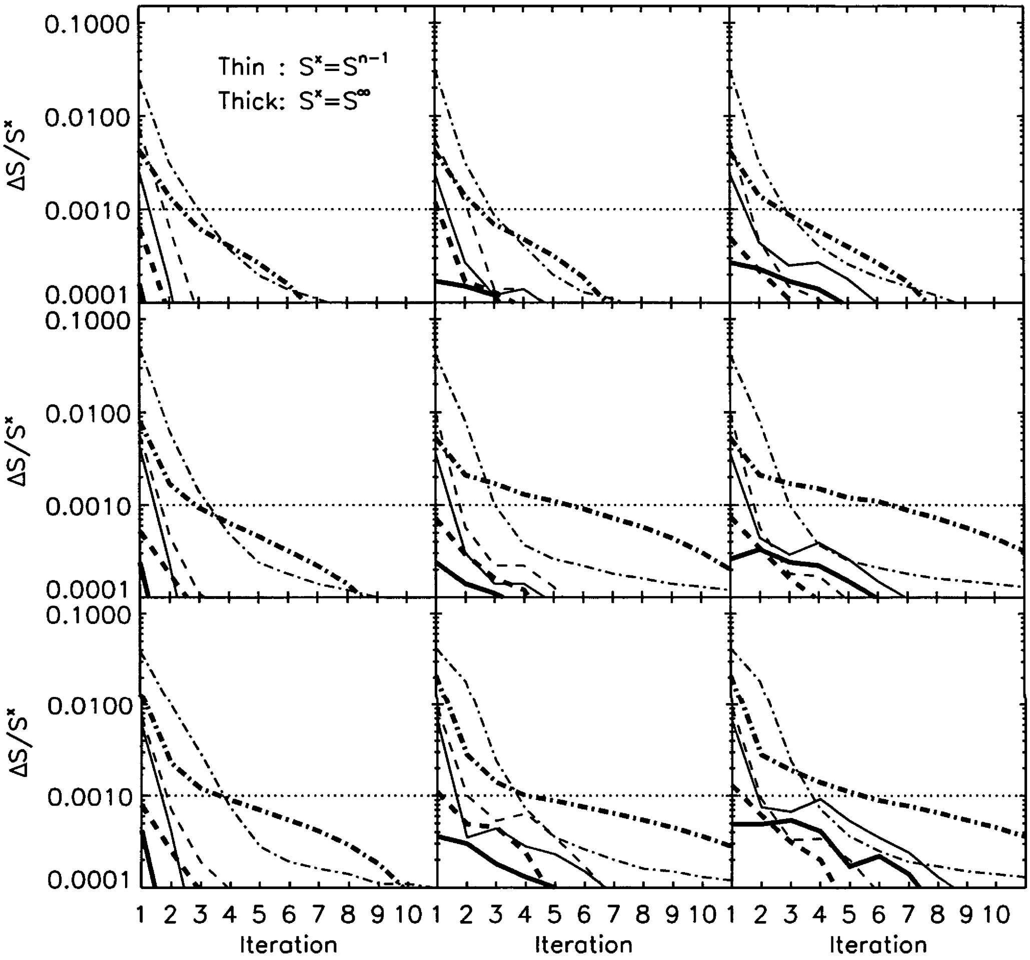

Figure 4.2: Convergence of the source function for bins 1-3 (see Fig. 4.1) during a simulation run without domain decomposition (left column), with $2 \times 2 \times 2$ decomposition (center column) and $3 \times 3 \times 3$ decomposition (right column), and with a time step of $\Delta t = 0.03\,\mathrm{s}$ (upper row), $\Delta t = 0.04\,\mathrm{s}$ (center row) and $\Delta t = 0.08\,\mathrm{s}$ (lower row). Line styles represent the same bins as in Fig. 4.1. Thin lines: relative source function correction ΔS after n iterations with respect to S^{n-1} from the previous iteration $n-1$. Thick lines: relative source function correction ΔS with respect to the "true" solution S^{∞}. Dotted lines mark the threshold C beneath which convergence is assumed (see text).

depths therefore leads to very poor convergence rates of the Gauss-Seidel solver, requiring hundreds of iterations in extreme situations. However, this difficulty is mostly alleviated by using the source function solution from the previous time step and the slow evolution of the plasma flow between consecutive time steps, so that the code ideally needs to fully converge the solution only once at the beginning. Domain decomposition additionally slows down convergence if the photon mean free paths cross subdomain boundaries, which is the case at continuum wavelengths in the thin atmosphere, since the subdomain boundary intensities are not initially known. Storing intensities from the previous time step again largely circumvents this problem, and the actual number of iterations per time step that is required during a simulation run depends on how fast the atmosphere evolves.

We therefore test the convergence of the solution for arbitrary time steps of our solar-type simulation using 12 opacity bins with continuum and line scattering (see Sect. 4.5), following a similar discussion in Skartlien (2000). The tests were run at half resolution on all axes to facilitate computation on a single core, which yields slightly faster convergence. Since the true solution S of our radiative transfer problem is unknown, we compare the approximate solution after n iterations, S^n, with an approximate solution S^∞ which we obtained after additional iterations with a lower convergence threshold of $C \sim 10^{-4}$, assuming $S^\infty \approx S$ with good accuracy.

We use three representative opacity bins, which cover weak, intermediate and strong opacities in the UV, with different depth-dependence of the scattering strengths. The remaining nine bins at longer wavelengths behave in a similar way. Figure 4.1 shows horizontal averages of the photon destruction probabilities ϵ for each bin in an arbitrary snapshot of our photospheric simulation: averages over layers with the same geometrical depth are plotted in the left panel, averages over surfaces with the same vertical optical depth are plotted in the right panel.

Figure 4.2 compares the convergence speed for the radiative transfer solution of the sample bins with and without domain decomposition, and with different time step lengths. Thick lines represent convergence relative to the true solution S^∞ for each bin, thin lines show the convergence relative to the solution obtained in the previous iteration, which we use as the convergence criterion. In normal operation, the solver would stop as soon as the thin line of the currently computed opacity bin has crossed the dotted horizontal line. We caution that the number of iterations needed for a solution also depends mildly on the time stepping algorithm, since the choice of method affects the deviation of stored boundary intensities and source functions between substeps of the time integration. We therefore only analyze the behavior for the first extrapolation step of a 3rd order Runge-Kutta time stepper.

The poorer convergence speed caused by scattering at high optical depths in bin 3 is evident in all plots (thick dot-dashed line), compared to the situation in bin 1, where the photon destruction probability is larger. The small optical path lengths of bin 3 reduce the impact of domain decomposition, since the radiation field is essentially local in most parts of the simulation box. Contrary to that, bin 1 suffers most strongly from slower convergence with increasing number of subdomain divisions, as well as from some flip-flopping of ΔS. The latter is caused by high-order interpolation (see Sect. 4.3.3) and disappears when the solver is set to linear interpolation. High order interpolation of upwind intensities widens the domain of dependence of the short characteristics, and the effect is amplified where large path lengths in the optically thin regime cross subdomain boundaries.

Domain decomposition mildly slows down convergence, and the accuracy of the solution in bin 3 slightly deteriorates for a larger number of subdomains. Longer time steps have the same effect on that bin, causing slower convergence towards S^∞ than indicated by the relative corrections with respect to S^{n-1} (thick and thin dot-dashed lines in Fig. 4.2). The method devised by Skartlien (2000) exhibits similar behavior for bins with strong scattering lines.

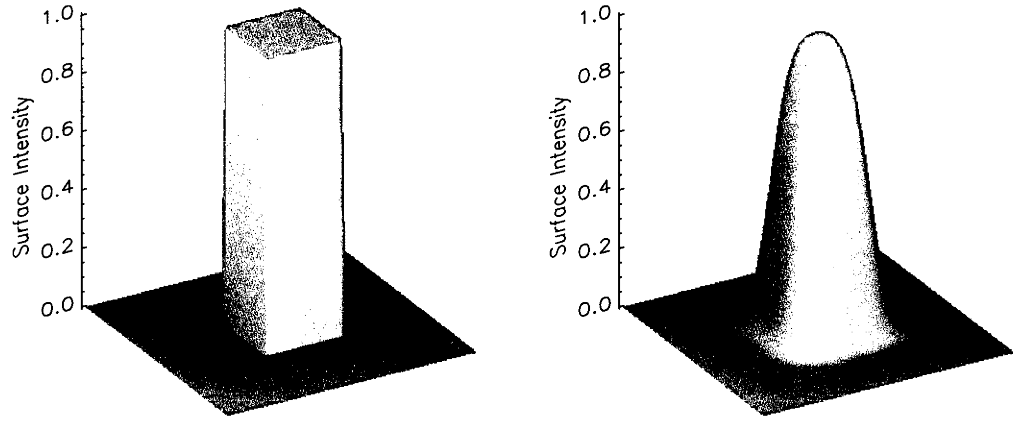

Exact solution

Linear interpolation

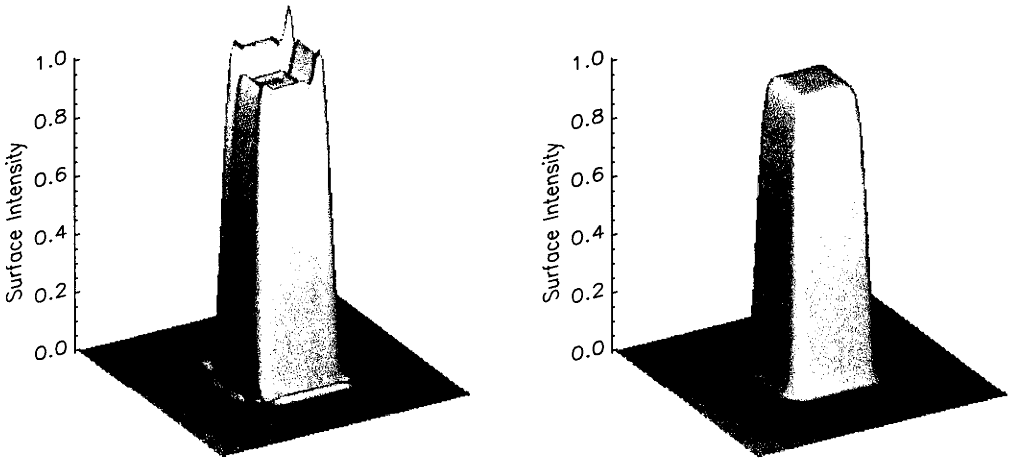

Local cubic interpolation

Local cubic monotonic interpolation

Figure 4.3: Numerical diffusion of a searchlight beam with rectangular cross-section using linear (upper right), local cubic (lower left) and local cubic monotonic (lower right) interpolation, compared to the exact solution (upper left).

The effect of such inaccuracies in the numerical solution of S and J on the energy transfer between the radiation field and the gas are nevertheless small or even vanish in some regions: radiative heating is reduced in the atmosphere where coherent scattering is important (see Eq. (4.7) and Fig. 4.1). Coherent scattering also effectively damps the impact of any remaining discontinuities in the radiation field across subdomain boundaries on the flux divergence in the optically thin atmosphere, so that no visible artifacts from the domain decomposition remain in the gas temperatures.

Compared to the solver proposed by Heinemann et al. (2006), it is clear that our method is not optimal for the case without scattering, since several computationally expensive formal solution and communication steps are required to obtain a radiation field that is consistent in the whole domain. It offers good performance when scattering is included, which is not considered in their method.

4.3.3 Interpolation and grid refinement

At every time step, the hydrodynamical solver updates mass densities and internal energy densities. These quantities are used to look up tabulated opacities, bin-integrated Planck functions and photon destruction probabilities at every grid point. In general, the characteristics grid needed to represent the anisotropy of the radiation field does not coincide with the hydrodynamical mesh, requiring the interpolation of χ, S and the upwind intensities I_{u} during the formal solution.

The accuracy of this interpolation strongly influences the overall accuracy of the solver, and there is a large choice of possible methods (see, e.g., the discussion in Auer, 2003). Linear interpolation is fast and avoids instabilities produced by interpolation overshoots, but yields poor estimates where the radiation field is not well-resolved, e.g. between granules and intergranular lanes at the optical surface. It also amplifies the numerical diffusion effect of short characteristics, where lateral diffusion artificially transports radiation away from the beam.

To illustrate this behavior, we repeat the searchlight test of Kunasz and Auer (1988), where a rectangular light beam is cast through an empty 3D box with a 100^3 mesh and zero opacity. Any diffusion of radiation away from the beam results in a broadening of the beam profile at the surface and can only stem from the interpolation of unattenuated upwind intensities. The light source illuminates the bottom of the 3D box, where it initially covers an area of 30^2 mesh points; it is slanted with an angle of $\theta = 28.1°$ off the vertical and an azimuth of $\phi = 45.0°$. The upper left panel in Fig. 4.3 shows the beam profile at the top of the 3D box expected from an exact solution of the unattenuated transfer problem through vacuum; note that the finite resolution of the surface in the plot leads to a slightly widened profile. The upper right panel shows the broadening of the beam profile caused by 100 consecutive linear interpolations applied for the numerical transfer through the box. Although the area-integrated intensity is conserved with good accuracy, limited by the machine precision, the beam is visibly widened through numerical diffusion. The lower left panel in Fig. 4.3 shows the result when using local cubic interpolation for the transport problem. The broadening is reduced, but the overshooting cubic polynomials produce ringing and negative intensities. We therefore use the local cubic monotonic interpolation scheme of Fritsch and Butland (1984), which effectively suppresses overshoots by using weighted harmonic mean derivatives, in consecutive 1D-1D interpolation on horizontal planes, and local quadratic interpolation on vertical cell walls (see Appendix B.2 for further details). The lower right panel in Fig. 4.3 shows the result from the searchlight test, where the beam profile is conserved to a satisfactory degree. Numerical diffusion is reduced and reaches a level which renders the computed flux divergences comparable to those obtained with long characteristics codes: although upwind intensities do not need interpolation along the beam, diffusion affects the local flux divergences when transfered from the slanted long characteristics grid back to the hydrodynamical grid.

The basic mesh on which radiative transfer is computed is imposed by the MHD solver. This is usually not critical in the optically thin upper atmosphere and the optically thick interior, where radiative transfer is simple and may even be over-resolved. The opposite is the case in the transition region around the optical surface, where opacities drop rapidly due to their strong temperature dependence and cause a runaway cooling effect (Stein and Nordlund, 1998). For a solar simulation, 1D tests performed by Nordlund and Stein (1991) indicate that a vertical spacing of $\lesssim 10\,\mathrm{km}$ is desirable at this atmospheric height. Using a non-linear vertical grid with the finest resolution around the surface, this is easily achievable in 3D for modern MPI-based domain decomposed radiative hydrodynamics codes. However, for large coronal simulations or in the case of giant stars, where the spatial scales needed to resolve hydrodynamics and radiation transport exhibit much larger disparity than in the Sun, finding the optimal grid leads to a conflict. Besides the larger simulation size, too small length intervals Δx drastically increase the stiffness of the hydrodynamical equations, where the stability-limited time steps of the transport and diffusion terms scale with Δx and Δx^2, respectively, and quickly become exceedingly small. In extreme cases, both effects may increase computation times of a model beyond tractability.

A fully adaptive mesh for computing radiative transfer would yield optimal results without affecting the stiffness of the equations, but is difficult to realize in a characteristics method. We achieve partial adaptivity by inserting horizontal layers in the hydrodynamical mesh for the radiative transfer computation, reducing optical path lengths without reducing the time steps. The refinement is based on the maximum vertical gradient of the Rosseland mean opacity in each layer and reassessed in regular intervals. While inserting additional layers slows down convergence of the Gauss-Seidel method (see Sect. 4.3.2), this is again overcome by storing the source function from the previous time step.

4.3.4 Numerical flux divergences

Having established a method for numerically computing radiative transfer with coherent scattering in a decomposed simulation domain, we now need to obtain flux divergences $\nabla \cdot \mathbf{F}$, a derivative of the radiation field.

The right-hand side of Eq. (4.7) involves only local quantities that are defined on the cell centers of the hydrodynamical mesh, where Q_{rad} is eventually needed, and therefore seems a natural choice. The expression $\chi(J - S)$ is numerically stable in the optically thin regime, where round-off errors of a possibly vanishing difference between J and S are attenuated by the exponential outward decrease of the opacity χ. At the same time, χ amplifies round-off errors of $(J - S)$ beneath the optical surface, where the radiation field thermalizes ($J \approx B$, also in the scattering case since $\epsilon > 0$): the flux divergence again vanishes, but the finite machine precision prevents complete cancellation of the terms.

It is possible to stabilize a short characteristics solver in the whole simulation domain by subtracting S_0 from the discretized formal solution (Eq. (4.14)), which yields the modified integration constant $\tilde{\Psi}_0 = \Psi_0 - 1$. Using this equation, one obtains a monochromatic $Q_{\mathrm{rad},\lambda}(\mathbf{x}, \hat{\mathbf{n}})$ along each ray. We note, however, that this leads to a deviation between the radiative energy $\iint Q_{\mathrm{rad},\lambda}(\mathbf{x}, \hat{\mathbf{n}}) d\Omega dV$ that is emitted by the gas in the simulation volume V per time unit, and the outgoing radiative flux computed from the specific intensities at the surface: the expressions are not equivalent anymore in their discretized form, and numerical errors affect the two values in a different way.

The discretized flux divergence $\nabla \cdot \mathbf{F}$ on the left-hand side of Eq. (4.7) using finite difference quotients is stable in the optically thick regime, but its accuracy deteriorates outward: round-off errors quickly become significant, as the internal energy per gas volume decreases exponentially (see also the discussion in Bruls et al., 1999).

Adopting the approach presented in Bruls et al. (1999) and Vögler et al. (2005), we combine both expressions through exponential bridging in each vertical column of the simulation domain as a function of bin optical depth to benefit from their respective advantages. We slightly reduce the transition range between the regimes by a squared exponent, resulting in the expression:

$$Q_{\mathrm{rad}} = e^{-(\tau/\tau_0)^2} Q^{J}_{\mathrm{rad}} + \left(1 - e^{-(\tau/\tau_0)^2}\right) Q^{\mathrm{F}}_{\mathrm{rad}}, \tag{4.22}$$

where $\tau_0 = 0.1$, $Q^{J}_{\mathrm{rad}} = 4\pi\chi(J - S)$ and $Q^{F}_{\mathrm{rad}} = -\nabla \cdot \mathbf{F}$, representing the two sides of Eq. (4.7). The total radiative energy computed with this expression delivers a consistent surface flux, since Q^{F}_{rad} contributes most of the radiative heating.

Following Vögler et al. (2005), we compute radiative transfer on cell corners to improve the accuracy of $Q^{\mathrm{F}}_{\mathrm{rad}}$. Radiative fluxes $\mathbf{F}$ are averaged over cell corners surrounding each face before computing difference quotients, while Q^J_{rad} is averaged over all eight cell corners surrounding each grid point. Both expressions use exactly the same stencil and exhibit very good agreement around the threshold optical depth τ_0 in our solar-type simulation.

Flux divergences are computed only on the hydrodynamical grid. Additional layers that are possibly inserted by the radiative transfer solver just serve to stabilize the computation and may simply be omitted when computing Q_{rad}, since conservation of the radiative energy flux through the hydrodynamical cell surfaces must hold.

4.4 Absorption and scattering opacity sources in the Sun

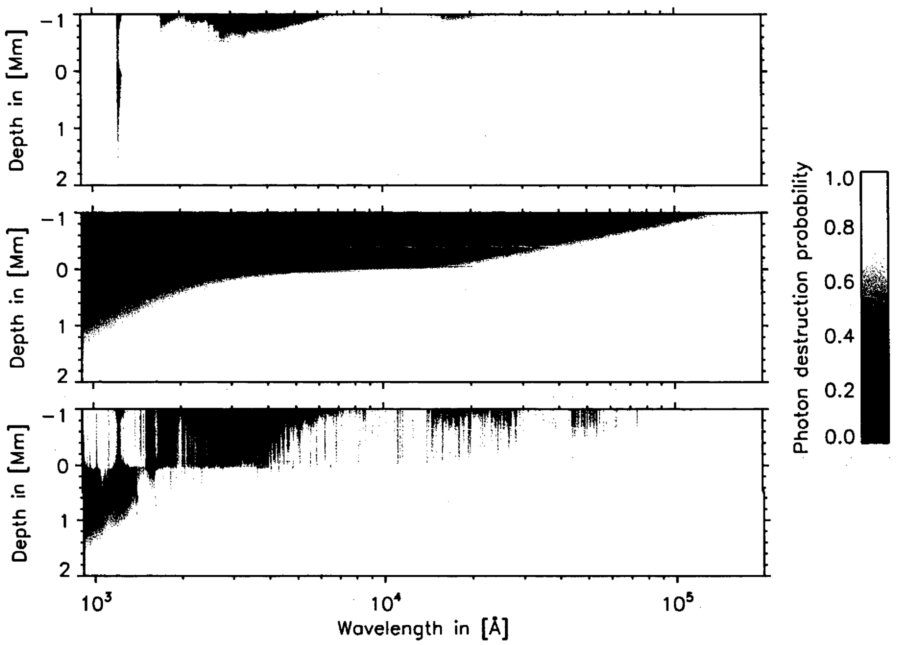

Figure 4.4: Wavelength and depth dependence of the continuum photon destruction probabilities ϵ^c_λ (upper panel), the van Regemorter (1962) line photon destruction probabilities ϵ^l_λ (center panel) and the total photon destruction probabilities ϵ_λ (lower panel) for the mean solar-type stratification. The zero point on the depth axis marks the stellar surface.

A complete description of radiative transfer in stellar atmospheres requires a detailed wavelength-resolved treatment of numerous radiative absorption and emission processes, collisions with neutral atoms, electrons and ions in the plasma, as well as an evaluation of the feedback of the radiation field on the level populations of the interacting particles. The complexity of the resulting problem vastly exceeds current computational resources. We therefore restrict all of the underlying thermodynamical plasma states to LTE, neglecting the effects of radiation on the excitation and ionization of atoms and photo-dissociation of molecules. The cross-sections and level populations needed for the absorption and scattering coefficients then depend only on the gas density ρ and the temperature T. Microscopic plasma thermodynamics is treated with the Mihalas-Hummer-Däppen equation of state (EOS) for stellar envelopes (Hummer and Mihalas, 1988; Mihalas et al., 1988; Däppen et al., 1988; Mihalas et al., 1990) and used in tabulated form. The solar chemical composition for the 15 elements included in the EOS and for the opacities is taken from the abundances of Asplund (2005).

4.4.1 Continuum opacity

The most important continuous opacity sources are various transitions of hydrogen atoms, their ions and molecules. The H^- ionization opacity dominates the solar continuum around the optical surface in the visual band; the large temperature sensitivity of the weakly bound second electron in the hydrogen atom causes runaway radiation cooling and the strong temperature gradient found at the top of the granules in the Sun (Stein and Nordlund, 1998). Most solar continuum photons originate from this very thin layer. Among many other processes, photoionization of metals contributes significantly to the continuous opacity at shorter wavelengths. Table C.1 gives an overview of all sources considered in this work; our data is mostly identical to those used in the latest MARCS models (see Table 1 in Gustafsson et al., 2008), but includes additional bound-free data from the Opacity Project and the Iron Project (see Trampedach et al., in prep., for further details). We also include opacities of the second ionization stage for many metals, allowing 3D models to extend deeper into the convection zone than their 1D counterparts, which is a requirement for correctly simulating surface granulation.

The upper panel in Fig. 4.4 shows the wavelength and depth dependence of the continuum photon destruction probabilities ϵ^c_λ for the mean stratification of our 3D model, including all continuous absorption and scattering opacity sources considered here. Continuum scattering has a significant contribution mostly above the surface, photons thermalize beneath at almost all wavelengths. Note that the narrow features at the short-wavelength end are the scattering resonances of the Lyman series; Lyman lines are nevertheless treated as true absorbers if line scattering is not included in the simulations. The Rayleigh scattering tail of H I contributes mostly to the UV continuum opacity in the upper solar photosphere due to its comparatively small cross-section and strong wavelength dependence ($\sigma_\lambda \sim \lambda^{-4}$). The importance of elastic scattering on neutral hydrogen is outweighed by thermalizing processes closer to the surface and at short wavelengths. Electron scattering is wavelength-independent in the spectral range considered here, and becomes significant in the upper photosphere, where metals are the most important electron donors. It is mostly notable red-ward of the $1.644\,\mu$m edge of H^- bound-free, before H^- free-free absorption takes over. Rayleigh scattering on He I atoms only gives minor contributions to the UV continuum opacity in the upper photosphere. The scattering opacity of H_2 molecules is negligible. Rayleigh and electron scattering are treated as isotropic, neglecting their weak $(1 + \cos^2\theta)$ anisotropy, where θ is the scattering angle away from the incident direction (see, e.g., Mihalas, 1978).

Between 5000 Å and $1.644\,\mu$m, the strong H^- bound-free absorption opacity thermalizes the photons. Its dominance slightly decreases in the cool outermost layers owing to the lack of free electrons to form the ion.

4.4.2 Line opacity

Spectral line absorption and scattering are important processes which dictate the near-radiative equilibrium found in the solar photosphere. The heating/cooling effect of this line-blanketing forces the flatness of the observed temperature gradient, balancing the adiabatic dynamical gradient; see the discussion in Sect. 4.5.4. Spectral lines are particularly significant opacity sources at short wavelengths where many radiative bound-bound transitions of metals lie.

We obtain line opacities from extensive opacity sampling tables provided by B. Plez (2008, priv. comm.) as part of the MARCS collaboration. The data are based on VALD with some modifications; see Gustafsson et al. (2008) for further details. The original line data combine scattering and absorption contributions in a total opacity, which is sampled with ~ 100 000 wavelengths and tabulated for a range of temperatures and pressures. The tables assume Saha ionization equilibrium and Boltzmann level populations to obtain the absorber density fractions. Departures from LTE, e.g. through radiative ionization, are neglected.

Following Skartlien (2000), we estimate the importance of scattering in line transitions by computing a photon destruction probability ϵ_λ^1 for every line opacity sample, using the van Regemorter (1962) formula (see Appendix C.1). We assume all scattering atoms to be neutral, accounting for the large contribution of Fe I to the line-blanketing (Anderson, 1989), and all transitions to be permitted, in which case the assumptions of the van Regemorter (1962) formula yield reasonable estimates. Only electrons are taken into account for collisional de-excitation. The estimated photon destruction probability ϵ_λ^1 is then a function of wavelength, temperature and electron pressure, and independent of the actual transition. It may therefore also be applied in cases where the line opacity sample includes several transitions (see the discussion in Appendix C.1). Line transitions are treated as independent two-level processes without taking the coupling of the respective level populations into account, which is a reasonable assumption for resonance lines.

The center and lower panels in Fig. 4.4 show the wavelength and depth dependence of the estimated ϵ_λ^1 of spectral lines and the total photon destruction probabilities ϵ_λ, including all considered continuous and line processes. It is clear that collisional de-excitation dominates beneath the surface and at the longest wavelengths. Resonant line scattering becomes important towards optical and shorter wavelengths at increasing depth.

With the exception of very strong lines, line scattering is generally not coherent due to the Doppler shifts in the moving gas, which are not accounted for in our calculations. The two-level approximation probably gives a reasonably realistic picture of strong permitted lines, but departures from the LTE populations of the atomic levels are still neglected. The important Fe I opacity deviates from the LTE estimate in higher layers (see Fig. 7 in Short and Hauschildt, 2005), thereby affecting the overall magnitude of the line-blanketing in these regions. Moreover, the accuracy of the opacity sampling method itself deteriorates outwards, where fewer and fewer lines contribute to the opacity. The van Regemorter approximation assumes resonant line scattering and consequently produces poorer estimates for all non-resonant lines. In summary, we should expect to obtain an order-of-magnitude estimate for the effects of scattering on the atmospheric structure. A more detailed picture requires a full treatment of the departures from LTE level populations and velocity fields, which is still out of reach for time-dependent 3D simulations.

4.5 The effects of scattering on the photospheric temperature structure of a solar-type star

4.5.1 The 3D hydrodynamical surface convection model

To investigate the effects of scattering on the atmosphere of a solar-type star, we conduct time-dependent radiative hydrodynamical simulations of the quiet surface, neglecting the effects of magnetic fields. We solve the fully compressible Navier-Stokes equations, the mass conservation equation and the energy equation, along with the time-independent radiative transfer equation (Eq. (4.4)); see, e.g., Stein and Nordlund (1998) and Nordlund et al. (2009) for further details. Our $240 \times 240 \times 226$ model covers a horizontal area of 6 Mm × 6 Mm at a constant resolution of 25 km, and extends approximately 700 km above and 2.8 Mm below the surface. The vertical resolution reaches 7 km around the radiative cooling peak and decreases in the optically thick and thin parts of the simulation; radiative transfer is thus resolved well enough that only $\sim 3\,\%$ of the rays would be affected by overshoots (see Sect. 4.3.1). We test the accuracy of the vertical resolution using the adaptive refinement, inserting two extra layers before each computation of radiative transfer. Local differences between the two calculations reach $\sim 3 \cdot 10^{10}\,\mathrm{erg\ g^{-1}}$

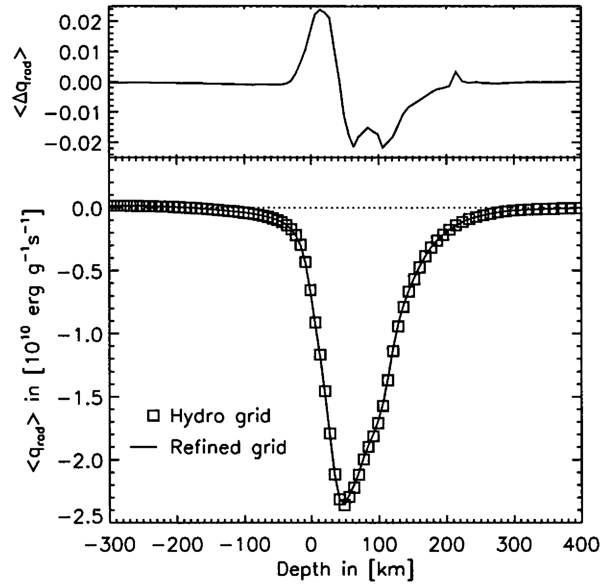

Figure 4.5: Horizontal average heating rate per unit mass around the stellar surface at an arbitrary time step of the simulation. Boxes show $\langle q_{\rm rad}\rangle$ when computed on the hydrodynamical grid; the vertical resolution reaches 7 km around the peak. The solid line shows the result after inserting two additional horizontal layers in each hydrodynamical cell. The upper panel gives the average deviation between the two cases in the same units.

s^{-1}, owing to the strong sensitivity of the heating rate per unit mass, $q_{\rm rad} \equiv Q_{\rm rad}/\rho$, to the local temperature gradients in the highly inhomogeneous granulation flow. On the average, however, the change in radiative flux divergence is negligible (see the upper panel of Fig. 4.5), and the radiation field is well resolved on the hydrodynamical grid. Note the difference between the magnitude of the cooling peaks in Fig. 4.5 and Fig. 4.6: the 1D calculation is based on the mean structure; in the 3D case, the average over each depth layer in the 3D box is taken and thus includes lateral inhomogeneities produced by the granulation flow.

Horizontal boundaries are periodic to mimic an infinitely extended atmosphere, vertical boundaries at the top and bottom of the simulation box are open to minimize the interference with the granulation flow. Mass conservation is ensured at the bottom by keeping the gas pressure constant; the underlying convection zone is mimicked by setting the entropy of the inflowing gas. The upper atmosphere is stabilized by setting internal energies to a slowly evolving average at the top.

We approximate the wavelength integral (Eq. (4.8)) with 12 opacity bins to account for the depth-dependence and wavelength-dependence of the absorption and scattering coefficients. The simulation box extends far into the optically thin atmosphere with $\langle\tau_{5000}\rangle \approx 10^{-6}$, where irradiation $I^{-}_{\rm top}$ from above is negligible. Rosseland optical depths at the bottom typically reach $\langle\tau_{\rm Ross}\rangle \approx 10^{7}$, where radiative transfer is entirely diffusive and the radiation field is completely thermalized. We therefore set the diffusion approximation $I^{+}_{\rm bot} = B_{\rm bot} + dB/d\tau$ for all ingoing intensities at the bottom.

The three simulations discussed in Sect. 4.5.3 have mean effective temperatures $T_{\rm eff}$ between 5804 K and 5811 K with average temporal fluctuations of about 13 K; they are thus slightly hotter than the Sun. For our purposes, there is no need to exactly reproduce the solar $T_{\rm eff}$. The simulations yield time-series of snapshots spanning $\sim$ 1 h of stellar time each, covering several granule lifetimes ($t \sim$ 10 min) and several periods of the dominant p-mode ($t \sim$ 5 min). Our

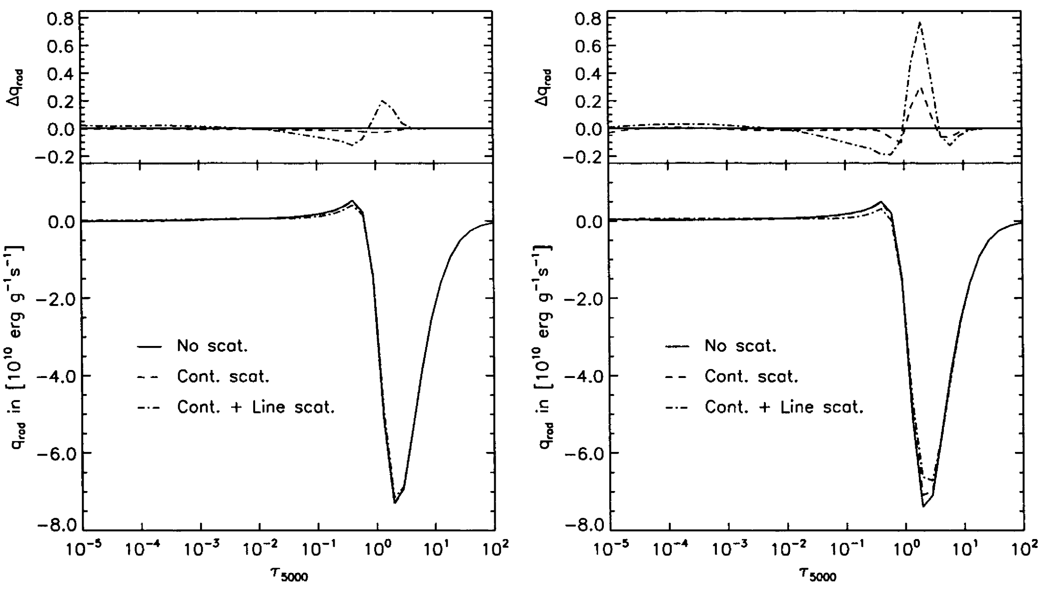

Figure 4.6: *Left*: Heating rates q_{rad} per unit mass as a function of monochromatic optical depth at 5000 Å, computed on the 1D mean structure with full opacity sampling for three cases: without scattering (solid line), with continuum scattering (dashed line), and with continuum and line scattering (dot-dashed line). The upper panel shows the deviations of the latter two cases from the computation without scattering (same axis units as in the lower panel). *Right*: Same computation, but using mean opacities and scattering albedos in 12 bins for the radiative transfer computations.

simulation box covers about 10 granules with typical sizes of the order of ~ 1 Mm, allowing us to obtain a statistically meaningful sample of the surface flow in terms of the ergodic hypothesis. The model without scattering was computed with a coarser radiation time step of 0.2 s, keeping the radiation field constant during the intermediate hydrodynamical calculations. The slow evolution of the flow field and the locality of the Planck source function allow such reduction of the computation time in very good approximation.

4.5.2 Scattering in the 1D mean stratification

We first test the importance of scattering in the 1D mean stratification of our 3D model (the $S = B$ case, see Sect. 4.5.3) by comparing the wavelength-integrated q_{rad}, using the full opacity-sampled spectrum. Radiative transfer was computed in 1D using a direct block matrix Feautrier-type solver with coherent scattering (for a detailed description see, e.g., Rutten, 2003) and 4th order Radau quadrature for the integral over the polar angle. The left-hand side of Fig. 4.6 shows q_{rad} without scattering and $S = B$, with continuum scattering only, and with both continuum and line scattering (lower panel), as well as the deviations from the first case (upper panel).

Continuum scattering seems to have very little impact on q_{rad} for the given mean structure; the cooling is slightly stronger near the surface. This behavior is expected from the mostly large photon destruction probabilities ϵ^{c}_{λ} shown in the upper panel of Fig. 4.4.

The differences are slightly larger when scattering is included in the line-blanketing: the small heating bump, where cool uprising gas is heated from beneath by hot granules (see the discussion in Stein and Nordlund, 1998), and the cooling peak beneath the surface both slightly weaken, since the fraction of scattered photons in the line-blanketing does not contribute to

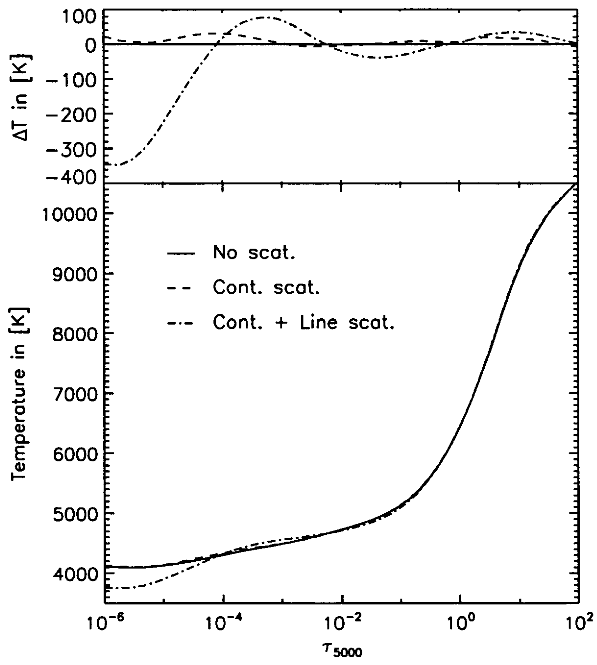

Figure 4.7: Horizontal and temporal average of the mean temperature structure as a function of optical depth at 5000 Å without scattering (solid line), with continuum scattering (dashed), and with continuum and line scattering (dot-dashed). The upper panel shows the deviation from the first case.

heat exchange (cf. the right-hand side of Eq. (4.7)). The upper atmosphere, however, now shows slight heating of the mean structure.

We repeat the same test with the binned opacities, computing 1D radiative transfer with and without scattering for 12 mean opacities, photon destruction probabilities and bin-integrated Planck functions. The right panels of Fig. 4.6 compare again the three different cases. The binning has been optimized for matching sampled and binned $q_{\rm rad}$ in the $S = B$ case (solid lines in the lower panels of Fig. 4.6). The continuum scattering calculation with opacity bins underestimates the cooling beneath the surface. The disparity increases further when line scattering is included; the relative deviations reach 7.5 % in the cooling peak (dot-dashed lines in Fig. 4.6). However, the overall impact of scattering radiative transfer on the temperature structure of the 3D atmosphere above $\tau_{5000} \gtrsim 10^{-3}$ is small (see Sect. 4.5.3 and Fig. 4.7), the same binning setup was therefore adopted for all three simulations. Higher up in the atmosphere, at $\tau_{5000} \lesssim 10^{-3}$, opacity binned radiative transfer shows slightly stronger heating of the gas.

4.5.3 Scattering in the mean 3D model

In order to assess the effects of continuum and line scattering, we perform three independent simulation runs: the first one treats radiation without scattering by adding all scattering opacity to the absorption opacity and assuming a Planck source function $S = B$. The second one includes continuum scattering in the source function and only adds line scattering opacity to the absorption opacity, and the third one includes scattering both in the continuum and in the line-blanketing. All three time series start from the same initial snapshot and span the exact same amount of simulation time. Snapshots are taken at regular intervals of $\Delta t_{\rm sim} = 10\,{\rm s}$. We consider time steps at $t_{\rm sim} > 8\,{\rm min}$ after the initial snapshot to allow the atmosphere to adjust to any changes in the radiative heating rates. Exploiting the tight correlation between gas temperature T and vertical optical depth τ (Stein and Nordlund, 1998), we interpolate the 3D temperature cube at each time step of the series onto surfaces with the same optical depth, using a reference τ-scale at 5000 Å. We then compute the average temperature of each surface in the 3D cube, which yields a 1D mean temperature profile for every snapshot. These profiles are finally averaged over time, and we obtain a very robust characteristic T-τ relation.

Figure 4.7 compares the resulting horizontal and temporal mean temperature profiles. The simulations without scattering and with continuum scattering have practically identical stratifications, as expected from the continuum photon destruction probabilities ϵ^{c}_{λ} (Fig. 4.4) and the 1D test presented in the previous section; continuum scattering is therefore insignificant for the atmospheric stratification in solar-type stars.

The effects of scattering on line-blanketing in and below the photosphere are also rather weak (dot-dashed line in Fig. 4.7). The gas temperatures above $\tau_{5000} \gtrsim 10^{-2}$ deviate up to 40 K from the stratification without scattering, resulting in a slightly steeper temperature gradient around the surface ($\tau_{5000} = 1$). Since our adopted binning setup overestimates the deviations for the 1D mean structure (right-hand side of Fig. 4.6), the impact of line scattering is probably even smaller at $\tau_{5000} \gtrsim 10^{-2}$. The temperature structure in the lower photosphere is thus hardly affected by scattering. The opposite is the case in the high photosphere and above ($\tau_{5000} \lesssim 10^{-4}$), where we observe temperatures that are about 350 K lower, resulting in a significantly steeper mean gradient.

4.5.4 Comparison of the 1D and 3D calculations and with other model atmospheres

The effects of line scattering on the temperature structure of the 3D model seem to be opposite of 1D hydrostatic models in radiative equilibrium, where heating of the highest layers rather than cooling is observed. Indeed, the 1D calculations on the mean 3D atmosphere exhibit slight heating in this region when scattering is included (Fig. 4.6). The temperature gradient would therefore become shallower if the 1D calculations were iterated under the assumption of radiative equilibrium (see, e.g., the discussion in Rutten, 2003).

The total radiative flux divergence includes several components: hot radiation from deeper layers at short wavelengths dominates the heating of the gas; the steep outward dB_{λ}/dT gradient causes a positive growing $(J - S)$ split. The effect declines in higher layers due to the rapidly decreasing opacity (cf. Eq. (4.7)). Strong LTE lines may heat or cool the higher atmosphere (since $J \approx B$ in deeper parts), depending on the spectral region and local temperature gradient, which determine the sign of the $(J - S)$ split. Including coherent scattering in line-blanketing effectively reduces both radiative heating and cooling in high layers through the outwards decreasing ϵ^{l} (see Fig. 4.1). As a consequence, strong resonance lines become unimportant for the temperature structure in high layers, and radiative heating at shorter wavelengths decreases.

In the 1D mean atmosphere, scattering-weakened line cooling shifts the total q_{rad} slightly towards positive values. The behavior of the 3D case can be understood by considering the dynamical nature of our 3D models. Following a derivation in Mihalas and Mihalas (1984), we insert the continuity equation

$$\frac{D\rho}{Dt} + \rho\nabla \cdot \mathbf{u} = 0, \tag{4.23}$$

where ρ is the gas density, D/Dt is the material derivative and $\mathbf{u}$ is the gas velocity, into the energy equation,

$$\frac{De}{Dt} + \frac{P}{\rho}\nabla \cdot \mathbf{u} = q_{\mathrm{rad}}, \tag{4.24}$$

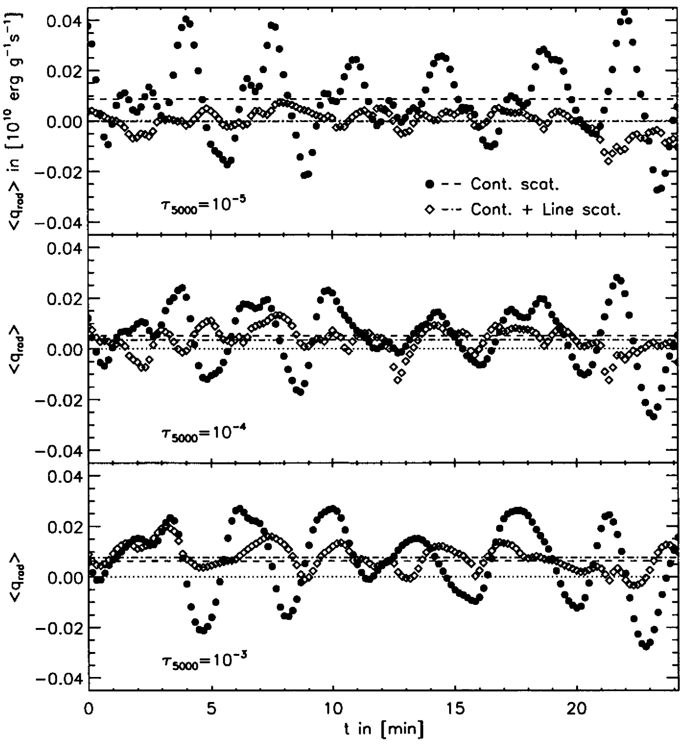

Figure 4.8: Horizontal averages of the radiative heating rates $q_{\rm rad}$ for the continuum scattering case (circles) and the continuum and line scattering case (diamonds) as a function of simulation time t, at optical depths $\tau_{5000} = 10^{-5}$ (upper panel), $\tau_{5000} = 10^{-4}$ (center panel) and $\tau_{5000} = 10^{-3}$ (lower panel). Dashed lines show the spatial and temporal averages for the continuum scattering case, where line scattering is treated as true absorption; dot-dashed lines show the spatial and temporal averages for the line scattering case. Dotted lines indicate zero heating.

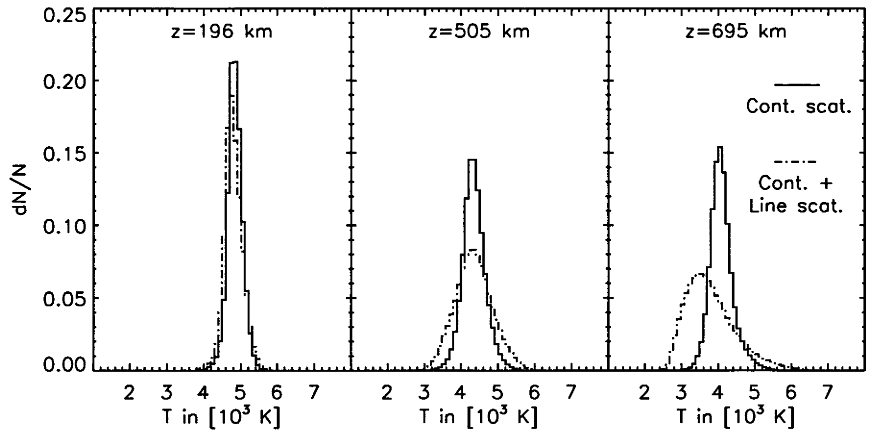

Figure 4.9: Temperature histograms at three different geometrical heights z above the optical surface, integrated over each simulation run. Solid lines show the radiative transfer computation with continuum scattering, dot-dashed lines the case where continuum and line scattering are included. Each temperature distribution is normalized.

where e is the internal energy per unit mass, P is the gas pressure, and $q_{\rm rad}$ is the radiative heating rate per unit mass; we omit the viscous dissipation term for simplicity. The resulting expression,

$$\frac{De}{Dt} - \frac{P}{\rho^2}\frac{D\rho}{Dt} = q_{\rm rad}, \tag{4.25}$$

is the first law of thermodynamics. An upflowing (downflowing) gas parcel cools (heats) through expansion (compression) represented by the $D\rho/Dt$ term in Eq. (4.25), and is exposed to radiative heating through the $q_{\rm rad}$ term. Equation (4.25) is equivalent to the expression

$$T\frac{Ds}{Dt} = q_{\rm rad}, \tag{4.26}$$

where T is the gas temperature and s is the entropy per unit mass, and it is immediately clear that gas motion is adiabatic when $q_{\rm rad} \to 0$. In the photosphere of the 3D simulation, temperatures are not affected by scattering. In the upper atmosphere, below $\tau_{5000} \approx 10^{-4}$, scattering strongly reduces the line-blanketing. Small or vanishing heating rates $q_{\rm rad}$ cause the temperature stratification to steepen towards an adiabatic gradient.

Figure 4.8 compares the time evolution of radiative heating rates at three optical depths in the atmosphere, averaged over surfaces of constant optical depth to approximately account for vertical gas motion. The plot shows a sequence of snapshots taken at regular simulation time intervals of 10 s; the zero point on the abscissa is arbitrary. At $\tau_{5000} = 10^{-3}$ and $\tau_{5000} = 10^{-4}$ (lower and center panels), the continuum scattering case (circles) and the continuum and line scattering case (diamonds) exhibit similar positive heating rates on the average (dashed and dot-dashed lines) and thus similar average temperatures (Fig. 4.7). Line scattering radiative transfer produces slightly stronger mean heating at $\tau_{5000} = 10^{-3}$, but fluctuates with lower amplitude. At $\tau_{5000} = 10^{-5}$, $q_{\rm rad}$ practically vanishes on the time average in the line scattering case, but there is still significant radiative heating with line scattering as true absorption. Note the dynamical variation of the sequences: contrary to 1D hydrostatic models, where the radiation field is time-independent by definition, the evolution of the 3D simulations produces fluctuating radiative heating.

Wedemeyer et al. (2004) presented 3D radiation-hydrodynamical simulations of the solar atmosphere that include a chromosphere, using radiative transfer without scattering and solving the equation only for the Rosseland mean opacity to suppress radiative cooling by strong LTE lines. They found an increasing asymmetry of the gas temperature distribution with increasing height above the surface, and a bifurcation in the chromosphere. Wedemeyer et al. (2004) further observed that treating strong spectral lines as true absorption with the opacity binning method reduces the amplitude of temperature fluctuations, which are caused by outward propagating acoustic waves, resulting in unrealistically low maximum temperatures in high layers. Skartlien (2000) investigated scattering radiative transfer in the chromosphere, comparing radiative heating with and without scattering, and came to the conclusion that including line scattering reduces this damping effect of LTE lines.

Our simulations do not include a chromosphere; the internal energy at the top boundary is set to a slowly evolving mean instead. In the line scattering case, where radiative transfer has only weak influence on the gas, the temperature gradient is sensitive to this boundary condition and thus not well-constrained. However, this does not compromise our conclusions, since the boundary is free to adapt to any upward or downward shift in the mean energies of the gas beneath.

Figure 4.9 shows temperature distributions of the simulations with continuum scattering and with continuum and line scattering at three different heights above the surface. Our simulations do not reach the same geometrical heights as those of Skartlien (2000) and Wedemeyer et al. (2004), and we use a more realistic radiative transfer treatment with 12 opacity bins. We find a similarly growing asymmetry in the temperature distribution of the line scattering simulation in the outer layers (cf. Fig. 7 in Wedemeyer et al., 2004). Treating strong lines as absorbers shifts the mean temperature upward and removes the high temperature tail of the distribution, in qualitative agreement with the findings of Skartlien (2000) and Wedemeyer et al. (2004).

Figure 4.10 shows horizontal and temporal averages of the relative temperature fluctuations, which we define as

$$\frac{\Delta T_{\mathrm{rms}}}{\langle T \rangle} = \frac{\sqrt{\langle (T - \langle T \rangle)^2 \rangle}}{\langle T \rangle} \tag{4.27}$$

in every geometrical depth layer (cf. Eq. 2 and Fig. 9 in Wedemeyer et al., 2004). The comparison between the cases with continuum scattering and with continuum and line scattering confirms the damping of temperature fluctuations through line absorption. Note the decreasing ΔT_{rms} at the top of the simulation, which is induced by the hydrodynamical boundary conditions.

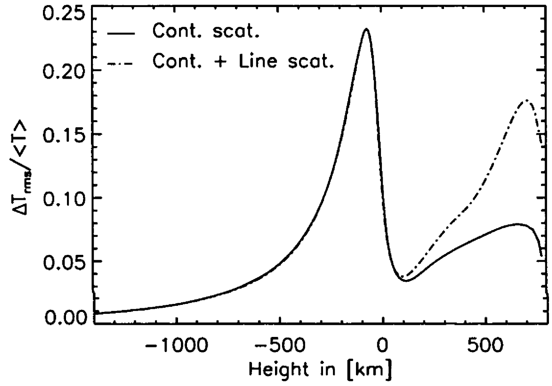

Figure 4.10: Horizontal and temporal averages of the relative temperature fluctuations $\Delta T_{\mathrm{rms}} / \langle T \rangle$ as a function of atmospheric height, computed with continuum scattering (solid line) and with continuum and line scattering (dot-dashed line).

We conclude that line scattering is an important ingredient for model atmospheres of solar-type stars that include a chromosphere; while gray radiative transfer reduces damping through strong LTE lines, it cannot produce a realistic temperature structure.

Anderson (1989) presented simplified, and Short and Hauschildt (2005) presented full 1D non-LTE line-blanketing calculations, respectively, for hydrostatic model atmospheres of solar-type stars. The departures of line-blanketing from LTE through iron-group elements heat up the atmosphere in the height range $10^{-6} \lesssim \tau_{5000} \lesssim 10^{-2}$. Our 3D model predicts a predominant temperature decrease as we discussed above. However, it is not clear how departures from LTE in the absorber populations through the ionization balance etc. would affect the atmospheric structure in our 3D simulations, making a direct comparison with the 1D models difficult.

Doppler shifts may have a significant influence on line absorption in higher layers, which expose line cores to hot radiation from deeper in. Vögler et al. (2004) estimated the effects to be insignificant in the photosphere, but their work was based on 1D tests. The large scattering albedo of strong resonance lines, however, should reduce the impact of Doppler shifts higher up.

4.6 Conclusions

We presented a 3D radiative transfer method with coherent scattering for time-dependent 3D (M)HD simulations of stellar atmospheres with the new `BIFROST` code (Gudiksen et al., in prep.). The simulations are parallelized through domain-decomposition to take advantage of large-scale computer clusters. The solver is based on short characteristics and the Gauss-Seidel scheme for an iterative computation of the radiation field and the radiative flux divergence in the whole simulation domain. We use monotonic interpolation to reduce the numerical diffusion effect of short characteristics and represent the source function integral with Bézier polynomials to suppress interpolation overshoots. A partial grid refinement scheme is included to improve the resolution of the radiative transfer computation where strong vertical opacity gradients occur. The wavelength integral is treated in the opacity binning approximation, using 12 bins that divide the opacity spectrum by formation height and wavelength.

The effects of coherent scattering on the temperature structure of a solar-type star are investigated with 3D time-dependent hydrodynamical simulations of magnetically quiet surface convection, including Rayleigh scattering and electron scattering in the continuum and estimated line scattering using the van Regemorter formula. While continuum scattering processes are not important for the mean temperature stratification, we find lower temperatures in the upper atmosphere when scattering is included in the line-blanketing. 3D radiative-hydrodynamical atmospheres thus show the opposite behavior of 1D hydrostatic atmospheres in radiative equilibrium, where scattering in strong lines effectively heats the outer layers.

3D LTE models of solar surface convection have been very successful at reproducing various observational tests, and our results indicate that the solar photosphere is indeed well represented when scattering is not included in radiative transfer. It therefore seems that a refined treatment of the line-blanketing through, e.g., opacity distribution functions or opacity sampling will be the next significant step to improve the realism of 3D radiative-hydrodynamical model atmospheres. Scattering radiative transfer is nevertheless an important ingredient of consistent 3D MHD models of the solar chromosphere, transition region and corona.

While it is not unexpected to see only small differences in the photospheres of solar-type stars when scattering is taken into account, this is likely to change for the much less dense atmospheres of giants, where the importance of Rayleigh scattering increases. The case of metal-poor giants is particularly interesting in that respect, owing to their significance for understanding galactic chemical evolution and the origin of the elements.

Acknowledgements. This research project has been supported by a Marie Curie Early Stage Research Training Fellowship of the European Community's Sixth Framework Programme under contract number MEST-CT-2005-020395: The USO-SP International School for Solar Physics.

Chapter 5

The effects of scattering on the temperature structure of metal-poor giants

W. Hayek, R. Collet, M. Asplund, B. V. Gudiksen, *in prep.*

5.1 Introduction

Metal-poor giant stars are important probes for understanding the chemical evolution of the Galaxy and the origin of the elements. Their envelopes preserve the chemical composition of the interstellar medium (ISM) out of which they formed; the oldest objects exhibit abundance patterns that contain the signatures of only a small number of nucleosynthesis events. Observations and chemical analyses of metal-poor stars are thus an important instrument for identifying the different nuclear processes that produce chemical elements and for finding the astrophysical sites that host the physical environment to support the reactions, such as supernovae or AGB stars. The various mechanisms, e.g., the slow and the rapid neutron capture processes (s-process and r-process), produce a distinct abundance pattern that has been observed in different metal-poor stars (e.g., Sneden et al., 1996; Johnson and Bolte, 2004; Hayek et al., 2009).

Analyses of stellar abundances often rely on 1D hydrostatic model atmospheres, such as the `MARCS` models (Gustafsson et al., 1975, 2008), which enforce radiative equilibrium in the energy equation above the stellar surface. 1D models cannot take convective heat transfer and other dynamical effects into account. Asplund et al. (1999) showed that 3D time-dependent radiation-hydrodynamical models of metal-poor giants exhibit different atmospheric temperature stratifications than 1D hydrostatic models: adiabatic expansion and compression of upflowing and downflowing gas parcels steepen the temperature gradient towards an adiabatic curve, as the weak coupling between the radiation field and the gas due to the low metallicity provides less radiative heating compared to stars with higher metallicity. The lower atmospheric temperatures have important consequences for line formation and thus for abundance measurements, which results in large 3D abundance corrections for many species (Collet et al., 2007).

An important limitation of 3D radiation-hydrodynamical model atmospheres is the treatment of radiative transfer in the LTE approximation without taking the effects of scattering into account. Scattering processes transfer very little energy between the radiation field and the gas and thus do not contribute to radiative heating. Rayleigh scattering is an important continuous opacity source in the blue and UV wavelength regions in metal-poor giants, which is often treated as an absorption process to avoid the complexity and numerical expense of scattering radiative transfer. While this approximation is valid for solar-type stars, where Rayleigh opacity is not significant compared to absorption opacity (Hayek et al., 2010), the situation is different in the much more dilute atmospheres of giant stars.

We explore the effects of scattering in metal-poor giant stars by comparing the temperature structure of 3D radiation-hydrodynamical simulations where scattering is treated as absorption with coherent scattering radiative transfer computations. We also test an approximation where Rayleigh scattering is removed from the opacities above the optical surface and a Planck source function is used, imitating the behavior of a coherent scattering calculation. Such a simplification can reduce the computational expense by about an order of magnitude, depending on the numerical radiative transfer method (see Skartlien, 2000; Hayek et al., 2010). Section 5.2 describes the 3D radiation-hydrodynamical models and the opacity treatment. The results of the simulations are presented in Sect. 5.3; Sect. 5.4 summarizes our investigations.

5.2 3D radiation-hydrodynamical model atmospheres

We solve the fully compressible hydrodynamical equations and the radiative transfer equation with a coherent scattering term using the `BIFROST` code (Gudiksen et al., in prep.), producing time-sequences of the surface granulation flow in a 3D cube that represents a small fraction of the stellar surface. The radiative transfer treatment includes a coherent scattering term in the source function; see Hayek et al. (2010) for a detailed description of the method.

T_{eff} [K]	$\log g$ [cgs]	[Fe/H]	[α/Fe]
5091 ± 21	2.2	−3.0	+0.4
5040 ± 12	2.2	−2.0	0.0

Table 5.1: Stellar parameters of the 3D radiation-hydrodynamical model atmospheres.

Two metal-poor giant stars with metallicities [Fe/H] $= -3.0$ and [Fe/H] $= -2.0$ (Table 5.1) are analyzed. The lower surface gravity of giants increases pressure and density scale heights, which results in larger granulation structures compared to the Sun to satisfy mass conservation (see the discussion in Nordlund and Dravins, 1990). Our models span 1140 Mm on both horizontal axes and include ~ 10 granules at a time. A height of 94 Mm is reached above the optical surface and a depth of 335 Mm below; the 3D cube is resolved with $240 \times 240 \times 230$ grid points. The simulations assume periodic horizontal boundaries. A pressure node and isentropic inflows from beneath are enforced at the bottom by damping out fluctuations in densities and internal energies with a preset decay time constant. We use open boundaries at the top and at the bottom, allowing gas to freely enter and leave the simulation box. Time scales for radiative heating of the dilute metal-poor gas in the higher atmosphere of the giants are significantly longer than in solar-type stars. The temperature stratification near the top of the simulation box is thus more sensitive to the internal energy boundary condition, which mainly determines the temperature of inflows from above. In the absence of physical constraints from observations, we use a boundary condition that enforces a monotonic temperature gradient at the boundary by requiring the internal energy of inflowing gas to be smaller than the minimum of the first layers in each individual column. Outflows are left unchanged.

The wavelength-dependence of radiative opacities is approximated using the opacity binning method (Nordlund, 1982), which reduces the problem of solving the radiative transfer equation for millions of spectral lines for obtaining the wavelength-integrated radiative heating rate to computing the radiation field for only a small number of mean opacities. Opacity binning sorts continuous and line opacities into 4 representative groups; membership at a given wavelength is determined by the atmospheric height of the monochromatic optical surface. In order to correctly reproduce the behavior of radiative transfer in the optically thick and thin regimes, Nordlund and Dravins (1990) refined the method by using an optical depth-weighted sum in each bin i that combines an intensity-weighted mean opacity χ_i^J, which provides a good approximation for spectral line absorption, with the Rosseland mean opacity χ_i^{Ross}, which produces the correct radiative flux in the diffusion region:

$$\chi_i = e^{-f\tau_i^{\text{Ross}}} \chi_i^J + \left(1 - e^{-f\tau_i^{\text{Ross}}}\right) \chi_i^{\text{Ross}}, \tag{5.1}$$

where τ_i^{Ross} is the Rosseland optical depth in bin i and f is a scaling factor, which is set to 30 to suppress χ_i^J beneath the surface. Skartlien (2000) defined a coherent scattering coefficient for each opacity bin and calculated mean opacities for all bins explicitly rather than extrapolating the first bin as in the method of Nordlund (1982). The intensity-weighted mean opacity χ_i^J is computed using 1D radiative transfer calculations based on the mean stratification of the 3D model. The 1D solver uses the Feautrier (1964) method, which includes a scattering term (see, e.g., the description in Rutten, 2003) if an opacity table for coherent scattering simulations is computed.

The radiative heating rate in the hydrodynamical energy equation is given by the expression

$$Q_{\text{rad}} = 4\pi \sum_{i=1}^{N_{\text{bins}}} \chi_i (J_i - S_i) = 4\pi \sum_{i=1}^{N_{\text{bins}}} \kappa_i (J_i - B_i), \tag{5.2}$$

where J_i is the bin-integrated mean intensity in bin i, S_i is the bin-integrated source function, κ_i is the mean absorption coefficient, and B_i is the bin-integrated Planck function. The second equality holds for the case of a coherent scattering source function,

$$S_i = (1 - \epsilon_i)J_i + \epsilon_i B_i, \tag{5.3}$$

where $\epsilon_i \equiv \kappa_i/\chi_i$ is the mean photon destruction probability in bin i (see Skartlien, 2000, for a detailed discussion). While it is possible to account for line scattering using the van Regemorter (1962) formula, the inherent approximations can only provide an estimate of the effect (see Hayek et al., 2010). We restrict the present simulations to continuum scattering and treat line scattering as absorption opacity, based on large opacity sampling tables with $\sim$ 100000 wavelength points, which are sorted into 4 opacity bins.

Only absorption opacity κ contributes to heat exchange while scattering opacity σ has no such effect in the case of coherent scattering (Eq. (5.2)). This behavior can be approximated at low optical depths by removing σ from χ_i^J (Eq. (5.1)), provided that J_i is only weakly affected by scattering. σ nevertheless needs to be included in the Rosseland mean opacity χ_i^{Ross} to obtain the correct radiative flux at high optical depths.

5.3 The effects of scattering on the temperature structure

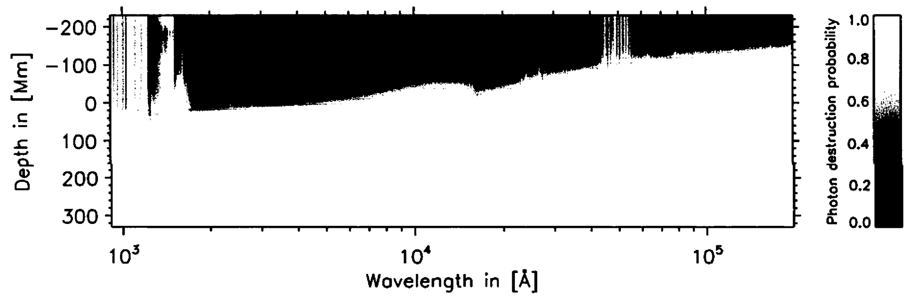

Figure 5.1: Wavelength-dependence and atmospheric depth-dependence of photon destruction probabilities ϵ_λ for the mean structure of the [Fe/H] = -3.0 model. The zero point of the depth axis marks the stellar surface.

Rayleigh scattering on neutral hydrogen atoms and electron scattering are the most important continuous scattering opacity sources in metal-poor giant stars. Figure 5.1 shows the wavelength-dependence and depth-dependence of the total photon destruction probabilities ϵ_λ of continuum and spectral line opacity for the mean structure of the [Fe/H] = -3.0 model. Below the stellar surface at depths $\gtrsim$ 50 Mm, absorption dominates the interaction of photons with the gas. Closer to the surface, Rayleigh scattering on H I becomes an important opacity source for continuum formation between 2000 Å $\lesssim \lambda \lesssim$ 5000 Å; at smaller wavelengths, bound-free absorption of metals thermalizes the radiation field. Above the surface, scattering opacity dominates in large wavelength ranges, owing to the small density of spectral lines (narrow vertical lines in Fig. 5.1) compared to solar-metallicity stars (see Fig. 4 in Hayek et al., 2010); electron scattering becomes important at large wavelengths. Rayleigh scattering on hydrogen molecules and helium does not contribute significant opacity.

We investigate the effects of scattering on the temperature structure by computing time-sequences of stellar surface granulation, treating continuum scattering as absorption, computing radiative transfer with scattering and approximating scattering by removing the opacity above the surface. The simulations for the three cases start from the same snapshot; we analyze model atmospheres with [Fe/H] $= -3.0$ and [Fe/H] $= -2.0$ (see Table 5.1).

Figure 5.2 shows a time sequence of average temperatures as a function of optical depth at 5000 Å for four snapshots of the [Fe/H] $= -3.0$ simulation, taken at 1 h, 2 h, 5 h and 8 h of simulation time where $t = 0$ is the start snapshot. Note that the optical depth scale is based on the same opacities for all cases. After 1 h, the atmosphere of the absorption model has heated at optical depths below $\tau_{5000} \lesssim 0.1$, the temperature deviation relative to the scattering case grows monotonically towards higher layers (upper left panel of Fig. 5.2). The differences around the continuum optical surface and below are negligible; the approximate scattering model exhibits no significant deviation from the coherent scattering model. At $t = 2\,\mathrm{h}$ and $t = 5\,\mathrm{h}$ after the beginning of the simulation, the absorption model heats continuously, but the optical depth at which the deviation starts remains at $\tau_{5000} \approx 0.1$ (upper right and lower left panel of Fig. 5.2). The average temperatures in the approximate scattering model still agree well with the predictions of the coherent scattering model. At $t = 8\,\mathrm{h}$, the temperature stratification of the absorption model stabilizes, reaching $\Delta \langle T \rangle \approx 900\,\mathrm{K}$ near the top of the simulation box at $\tau_{5000} \approx 10^{-5}$ (lower right panel of Fig. 5.2). Above $\tau_{5000} \gtrsim 0.1$, differences are negligibly small; there is no significant deviation between the approximate scattering model and the coherent scattering model.

The depth-dependence of the temperature deviation between the absorption model and the approximate scattering model follows the deviation between binned opacities with and without scattering: Fig. 5.3 shows horizontal average group-mean opacities in the four bins as a function of optical depth at 5000 Å for the start snapshot of the [Fe/H] $= -3.0$ model, calculated with scattering opacity (dotted lines) and without scattering opacity (solid lines). Differences appear beneath $\tau_{5000} \lesssim 0.1$, similar to the temperatures in Fig. 5.2. The contribution of scattering to the total opacity decreases with increasing bin number and becomes insignificant in bin 4, which contains the strongest opacities. The optical depth at which the opacities diverge in each bin is affected by the weighting between χ_i^J and χ_i^{Ross}(Eq. (5.1)), as scattering opacity σ is present above $\tau_i^{\mathrm{Ross}} \gtrsim 1/f \approx 0.03$ in all simulations and scattering is still significant close to the optical surface (see Fig. 5.1). However, the small temperature differences between the coherent scattering simulation, which includes scattering opacity at all optical depths and the approximate scattering simulation around $\tau_{5000} \sim 0.1$ indicate that the average temperatures should not be strongly affected.

We derive a mean temperature stratification from the model atmospheres by averaging time sequences over surfaces of constant vertical optical depth and over the time period of the fundamental pressure oscillation mode, to include a statistical sample of the convective flow. The results for the three radiative transfer treatments and metallicity [Fe/H] $= -3.0$ are shown in the left panel of Fig. 5.4. The deviation between the simulation with scattering radiative transfer and the absorption model reaches $\Delta \langle T \rangle \approx 1000\,\mathrm{K}$ at the top of the simulation box ($\tau_{5000} \approx 10^{-5}$) and decreases monotonically towards the stellar surface. At optical depths $\tau \gtrsim 0.1$, differences between the two models become small. Approximating scattering by removing its opacity above the optical surface reproduces the temperature structure of the simulation with scattering radiative transfer with very good accuracy, the deviation is smaller than 50 K.

The opacity tables of all three simulations are based on the same mean temperature stratification of the approximate scattering case for computing the intensity weights of the mean opacities χ_i^J above the surface. Deviations from this assumed stratification in the higher atmosphere affect the weighting of spectral line opacity, which has an important influence on radiative heating. The temperature differences of the absorption simulation are therefore an approximation; a quantitatively more accurate result is not critical for our conclusions.

Figure 5.5 shows the temperature-pressure distribution of a snapshot of the approximate scattering model with [Fe/H] $= -3.0$; darker shades indicate higher number density, solid lines trace the adiabatic curves in the temperature-pressure plane. The simulation produces isentropic upflows in the granulation zone beneath the surface (upper right corner in Fig. 5.5). In the atmosphere (lower left corner), the stratification is close to adiabatic, too, as radiative heating time scales in the metal-poor gas are too long to force the atmosphere into radiative equilibrium and the compression/expansion term in the hydrodynamical energy equation becomes important. It is clear that the choice of internal energy boundary condition at the top, which determines the temperature of gas inflows, leaves some uncertainty in the temperature gradient of the higher atmospheric layers. While the magnitude of the heating effect of treating scattering opacity as absorption may change, it is unlikely that a physically plausible boundary condition cancels or reverses the temperature deviation.

The histograms in the left column of Fig. 5.6 compare the temperature distribution of the [Fe/H] $= -3.0$ models at three optical depths, integrated over the same period of simulation time that was used for deriving the mean stratification in Fig. 5.4. Close to the optical surface at $\tau_{5000} = 0.1$, the distributions are very similar in all cases (lower left panel). At smaller optical depths, the coherent scattering simulation and the approximate scattering simulation still exhibit similar distributions with a maximum at low temperatures and a high-temperature tail (cf. Fig. 5.5). The absorption case exhibits a very different shape with a maximum at higher temperatures, as the gas is driven towards radiative equilibrium. A low-temperature tail forms in the optically thin region, which is fed by cool inflowing gas from the top of the simulation box.

At metallicity [Fe/H] $= -2.0$, treating scattering as absorption leads to larger temperatures below $\tau_{5000} = 0.1$ as well, reaching $\Delta \langle T \rangle \approx 300\,\mathrm{K}$ near $\tau_{5000} = 10^{-5}$ (right panel of Fig. 5.4). The depth-dependence of the scattering effect is similar to the [Fe/H] $= -3.0$ model; the temperature deviation increases monotonically towards higher atmospheric layers. Removing scattering opacity rather than computing scattering radiative transfer leads to a good approximation over a large atmospheric height range. However, temperatures deviate by $\Delta \langle T \rangle \approx 100\,\mathrm{K}$ at the top of the simulation box. The histograms of the [Fe/H] $= -2.0$ scattering and approximate scattering models at $\tau_{5000} = 10^{-3}$ exhibit a maximum at cool temperatures, which is less pronounced than for the [Fe/H] $= -3.0$ models and average temperatures are higher due to increased radiative heating. The absorption simulation has a more symmetric distribution without a low-temperature tail. At $\tau_{5000} = 10^{-2}$, the three distributions are more similar compared to the simulations with [Fe/H] $= -3.0$; at $\tau_{5000} = 0.1$, the differences become small.

5.4 Summary

The effects of continuum scattering on the temperature structure of metal-poor giant stars are investigated by comparing 3D radiation-hydrodynamical simulations where scattering is treated as absorption to simulations with coherent scattering radiative transfer. We compute time-sequences of two model atmospheres with metallicity [Fe/H] $= -3.0$ and [Fe/H] $= -2.0$ and derive mean temperature stratifications by averaging gas temperatures over surfaces of constant optical depth at 5000 Å and over a period of the fundamental pressure oscillation mode.

Rayleigh scattering on H I is an important continuous opacity source in atmospheres of metal-poor giant stars at blue and UV wavelengths. Treating scattering opacity as absorption leads to significantly higher temperatures at optical depths $\tau_{5000} \lesssim 0.1$, reaching $\langle \Delta T \rangle \approx 1000\,\mathrm{K}$ for the [Fe/H] $= -3.0$ model and $\langle \Delta T \rangle \approx 300\,\mathrm{K}$ for the [Fe/H] $= -2.0$ model, as the atmosphere is driven towards radiative equilibrium. The temperature distributions in the higher atmosphere deviate between the scattering and the absorption cases: the coherent scat-

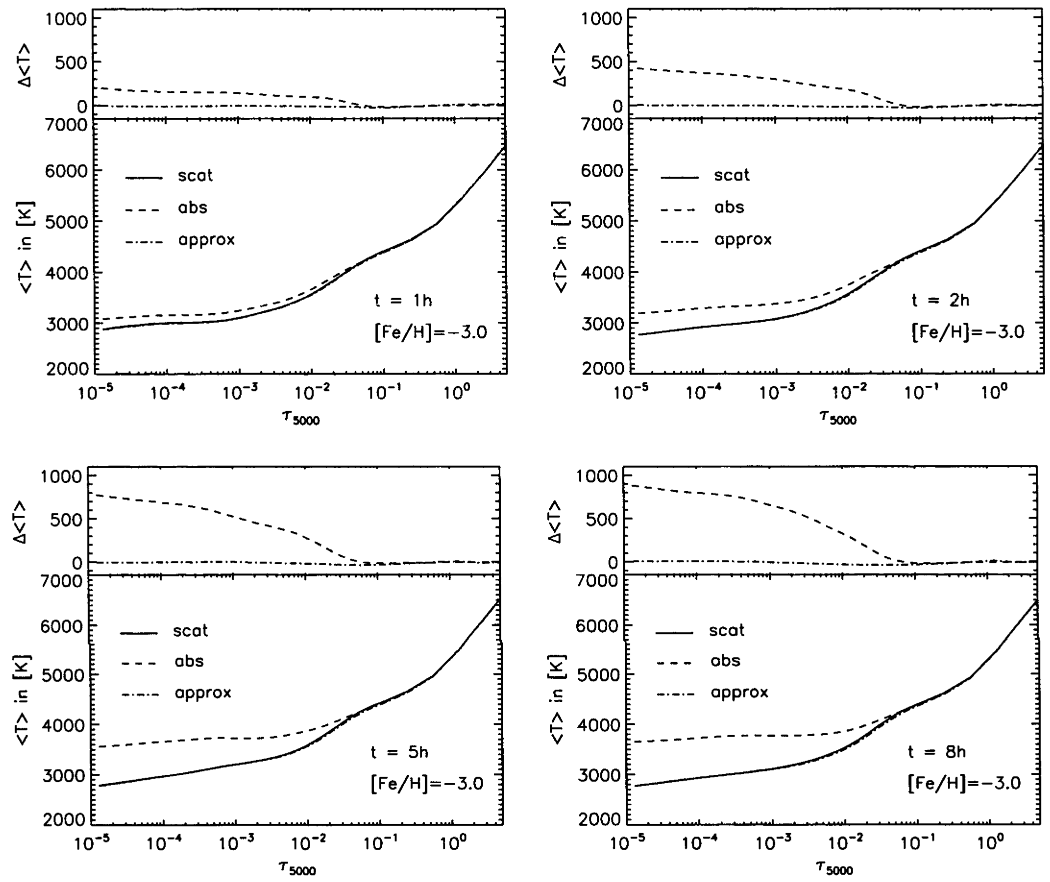

Figure 5.2: Time evolution of temperatures of the [Fe/H] $= -3.0$ model as a function of vertical optical depth at 5000 Å, averaged over surfaces of constant optical depth. Snapshots were taken at simulation time $t = 1\,\mathrm{h}$ (upper left panel), $t = 2\,\mathrm{h}$ (upper right panel), $t = 5\,\mathrm{h}$ (lower left panel) and $t = 8\,\mathrm{h}$ (lower right panel). Solid lines show the average temperature structure for the scattering simulation, dashed lines show the case were scattering is treated as absorption, dot-dashed lines show the approximate scattering simulation. The upper panels show the deviation of the absorption simulation and the approximate scattering simulation from the coherent scattering case.

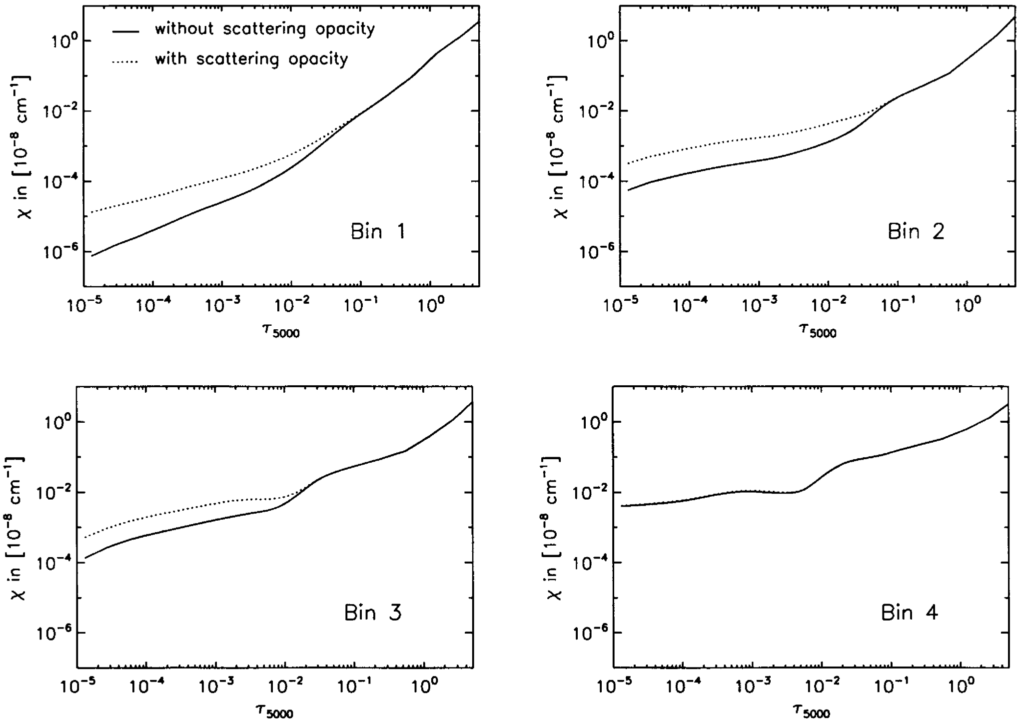

Figure 5.3: Group-mean opacities in the 4 bins (upper left to lower right) as a function of optical depth at 5000 Å, averaged over surfaces of constant vertical optical depth, computed for the start snapshot of the [Fe/H] = −3.0 model with scattering opacity (dotted lines) and without (solid lines).

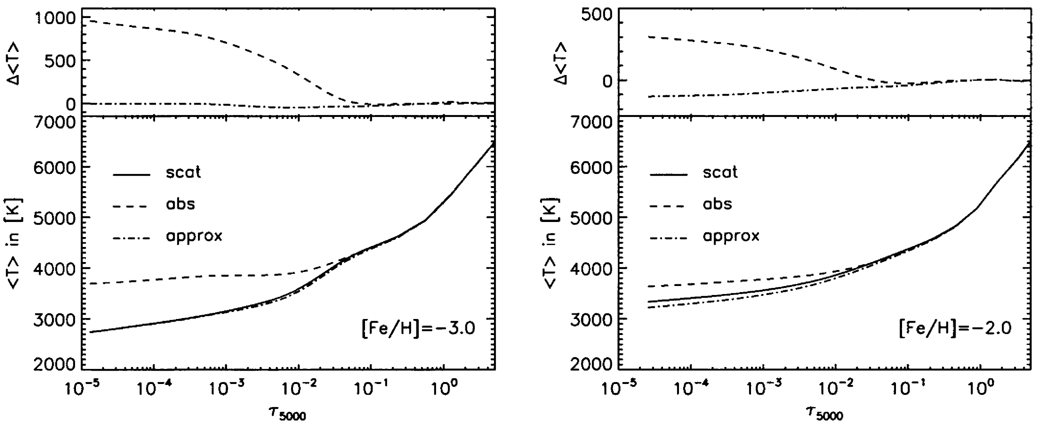

Figure 5.4: Temperature as a function of vertical optical depth at 5000 Å, averaged over surfaces of constant optical depth and over a time sequence, computed for the scattering simulation (straight lines), for the absorption simulation (dashed lines), and for the approximate scattering simulation (dot-dashed lines). The left panel shows the [Fe/H] = −3.0 model, the right panel shows the [Fe/H] = −2.0 model. The upper panels show the deviation of the average temperatures from the scattering simulation.

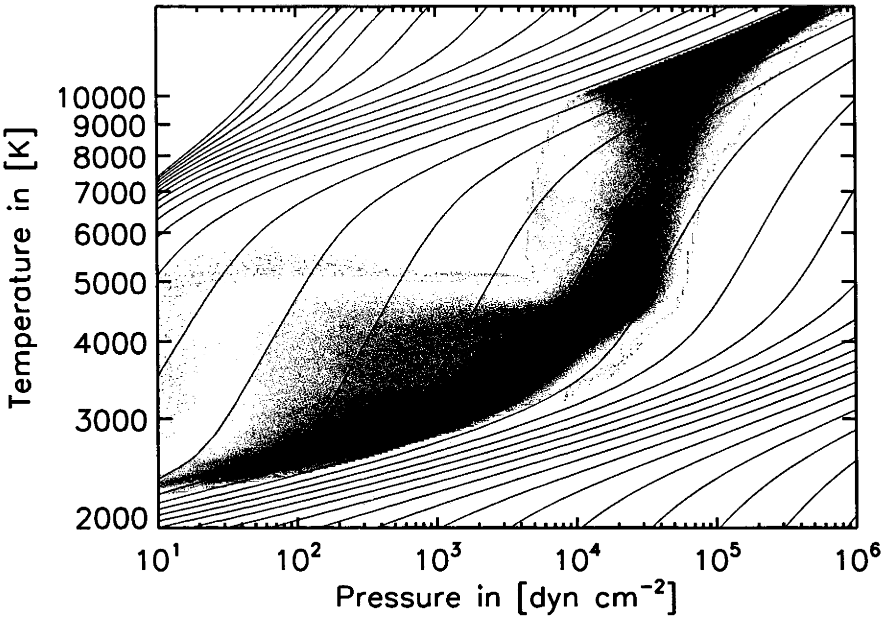

Figure 5.5: Temperature-pressure distribution of the approximate scattering model with [Fe/H] = -3.0 at $t = 33.5$ h of simulation time. Solid lines trace adiabatic curves of the equation of state.

tering simulation forms a temperature maximum at low temperatures due to its nearly adiabatic stratification, as well as a high-temperature tail. Treating scattering as absorption exhibits a low-temperature tail at [Fe/H] = -3.0 and a more symmetric distribution at [Fe/H] = -2.0.

The magnitude of the heating effect is approximate, since the dependence of the opacity weighting on the mean stratification has been neglected in the absorption case. The choice of internal energy boundary condition at the top of the simulation box can also affect $\langle \Delta T \rangle$; it is however unlikely that the temperature deviation is cancelled or reversed.

We test an approximation where scattering is removed from the opacities above the optical surface and a Planck source function is used, which significantly reduces the computational expense of the problem. The temperature stratification exhibits a very small deviation from the scattering radiative transfer simulation in case of the [Fe/H] = -3.0 model. At metallicity [Fe/H] = -2.0, the approximation is still in good agreement in the deeper photosphere and below the surface. However, temperature differences reach 100 K beneath $\tau_{5000} \lesssim 10^{-3}$. We expect that radiative transfer with approximate scattering yields again a better approximation towards [Fe/H] = 0.0, where scattering opacity is less important.

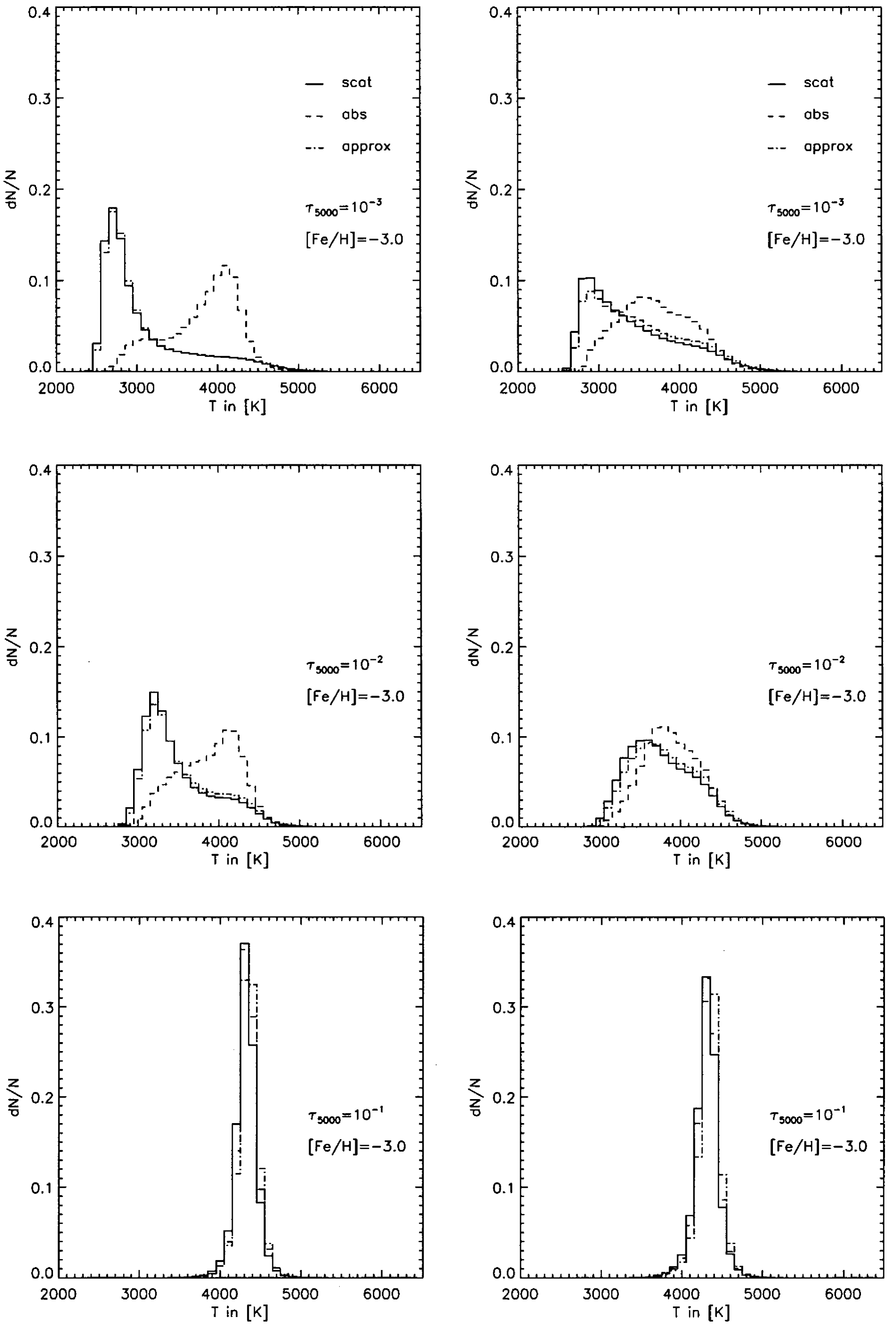

Figure 5.6: Normalized temperature histograms integrated over a period of the fundamental pressure oscillation mode, computed at optical depths $\tau_{5000} = 10^{-3}$ (upper panels), $\tau_{5000} = 10^{-2}$ (center panels) and $\tau_{5000} = 10^{-1}$ (lower panels) of the [Fe/H] = −3.0 model (left column) and the [Fe/H] = −2.0 model (right column), treating scattering as absorption (dashed lines), computing coherent scattering radiative transfer (solid lines) and approximate scattering (dot-dashed lines). The temperature bin size is 100 K.

Chapter 6

Spectral line formation

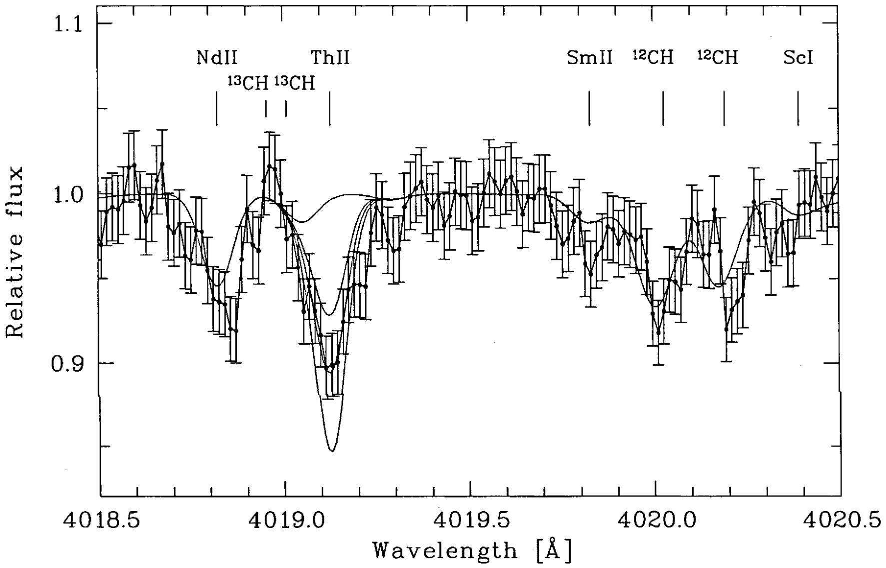

Figure 6.1: Observated spectrum near a Th II line at 4019 Å in the atmosphere of a metal-poor giant (black dots) and numerical line formation computations (gray lines), taken from Hayek et al. (2009).

The analysis of spectral lines is a fundamental discipline in astrophysical research. Spectral lines enable "remote sensing" of the physical state of matter in distant objects, such as stellar atmospheres, planetary atmospheres, the interstellar medium etc.; they form through absorption and emission of radiation by bound-bound transitions in atoms and molecules, providing opacity with strong frequency dependence. The shapes and depths of the absorption and emission profiles that appear in the spectrum depend on gas temperature, pressure, the chemical composition and velocity fields in the radiating gas. Spectral line profiles can therefore be used to determine stellar parameters (e.g., Barklem et al., 2000b) or the detailed chemical composition of the Sun (Asplund et al., 2009) and other stars. The analysis of spectral line bisectors has been used by, e.g., Dravins and Nordlund (1990), Asplund et al. (2000b), Allende Prieto et al. (2002), Ramírez et al. (2009) to investigate macroscopic velocity fields in stellar atmospheres.

The complexity of the radiative transfer problem requires a numerical treatment of spectral line formation. A much more detailed account of physical processes is required to obtain realistic line profiles compared to radiative transfer in radiation-hydrodynamical simulations, where the focus lies on energy and momentum transfer between the radiation field and the surrounding matter.

6.1 Spectral line opacity

The treatment of photon extinction from a beam by spectral line absorption and scattering in the radiative transfer equation assumes bulk interaction between a large number of particles and photons. The opacity is approximated using statistical occupation numbers for all accessible atomic states, and the different mechanisms that contribute to shaping the line profile are handled as independent processes.

6.1.1 Spectral line opacity in LTE

The amount of radiation dI_ν per unit path length ds that is removed from an incident beam with specific intensity I_ν through radiative excitation of an electron in the atomic restframe is given by

$$dI_\nu = -\frac{h\nu_0}{4\pi} n_\mathrm{l} B_\mathrm{lu} \phi(\nu - \nu_0) I_\nu ds \equiv -\chi_\nu^\mathrm{l} I_\nu ds, \tag{6.1}$$

where h is the Planck constant, n_l is the number density of interacting particles in the lower state of the transition, B_lu is the Einstein coefficient for radiative excitation and ϕ is a normalized profile function with center frequency ν_0; Eq. (6.1) thereby defines the line opacity χ_ν^l. Radiative de-excitation competes with collisional de-excitation after a photon has excited an atom or molecule. The LTE approximation requires that collisions dominate, thermalizing all absorbed photons; line opacity χ_ν^l and line absorption κ_ν^l are then identical quantities.

Emission through induced de-excitation of the atom by incident radiation adds photons to the beam:

$$dI_\nu = \frac{h\nu_0}{4\pi} n_\mathrm{u} B_\mathrm{ul} \chi(\nu - \nu_0) I_\nu ds; \tag{6.2}$$

n_u is the number density of the upper state, B_ul is the Einstein coefficient for stimulated emission and χ is the normalized induced emission profile function. Stimulated emission is counted towards the opacity rather than to the source function to simplify the equation. Using the Einstein relation $g_\mathrm{l} B_\mathrm{lu} = g_\mathrm{u} B_\mathrm{ul}$, where g_l and g_u are the statistical weights of the lower and upper states, one obtains the total line opacity

$$\chi_\nu^\mathrm{l} = \frac{h\nu_0}{4\pi} n_\mathrm{l} B_\mathrm{lu} \phi(\nu - \nu_0) \left[1 - \frac{n_\mathrm{u} g_\mathrm{l} \chi(\nu - \nu_0)}{n_\mathrm{l} g_\mathrm{u} \phi(\nu - \nu_0)}\right]. \tag{6.3}$$

The term in brackets constitutes a correction term for induced emission. In general, the extinction profile $\phi(\nu - \nu_0)$ and the induced emission profile $\chi(\nu - \nu_0)$ are different. If LTE holds, detailed balancing between absorption and emission at all frequencies requires

$$\phi(\nu - \nu_0) = \chi(\nu - \nu_0). \tag{6.4}$$

Collisional excitation dominates the population of atomic states in LTE; population densities n_l and n_u are related by a Boltzmann factor

$$\frac{n_\mathrm{u}}{n_\mathrm{l}} = \frac{g_\mathrm{u}}{g_\mathrm{l}} e^{-\frac{h\nu_0}{kT}}, \tag{6.5}$$

with the Boltzmann constant k and the temperature T. Inserting Eq. (6.4) and Eq. (6.5) into Eq. (6.3), one obtains the LTE line opacity,

$$\chi_\nu^\mathrm{l} = \frac{h\nu_0}{4\pi} n_\mathrm{l} B_\mathrm{lu} \phi(\nu - \nu_0) \left[1 - e^{-\frac{h\nu_0}{kT}}\right]. \tag{6.6}$$

In real stellar atmospheres, lines may be blended with lines from other transitions, and opacities include a background continuum. The different contributions then combine to the total opacity

$$\chi_\nu^{\text{tot}} = \chi^{\text{c}} + \sum_i \chi_{\nu,i}^{\text{l}}, \tag{6.7}$$

where the dropped frequency subscript in the continuum opacity χ^{c} indicates slow variation across a line profile.

6.1.2 LTE absorber populations

Spectral line opacity χ_ν^{l} is proportional to the number density of the interacting particles. Their population depends on several factors: the total abundance of the atom or molecule, the ionization fraction, and the population of the lower excitation level.

Different molecular species, such as H_2, CO, and CN, can form in cool layers of stellar atmospheres with significant abundances. Photo-dissociation processes are usually neglected to simplify the treatment of molecules. LTE then requires that the formation of compounds through a reaction $AB \rightleftharpoons A + B$ is in detailed statistical equilibrium. The number densities are governed by the law

$$\frac{P_{\text{A}} P_{\text{B}}}{P_{\text{AB}}} = K(T), \tag{6.8}$$

where $K(T)$ is a dissociation equilibrium function that depends on the temperature T, and P_{A}, P_{B} and P_{AB} are the partial pressures of the components and the molecule. In practice, equilibrium functions are approximated by a polynomial of the kind

$$\log K(\theta) = \sum_{n=0}^{n_{\max}} a_n (\log \theta)^n - D_0 \theta, \tag{6.9}$$

with the reciprocal temperature $\theta = 5040/T$ and the dissociation energy D_0 per particle; polynomial coefficients a_n are available in tabulated form in the literature (e.g., Sauval and Tatum, 1984). In order to determine atomic and molecular population densities, a system of non-linear equations that are coupled by equilibrium laws (Eq. (6.8)) needs to be solved numerically.

LTE ionization is treated in an analogous way, considering an equilibrium reaction $A \rightleftharpoons A^+ + e^-$. This yields the Saha ionization equilibrium,

$$\frac{n_{\text{e}} n_{\text{A}^+}}{n_{\text{A}}} = \frac{2 g_{\text{A}^+}}{g_{\text{A}}} \left(\frac{2\pi m_e kT}{h^2} \right)^{\frac{3}{2}} e^{-\frac{\chi^{\text{ion}}}{kT}}, \tag{6.10}$$

with the ionization potential χ^{ion}. Note that the free electron contributes statistical weight 2 in the dissociation function on the right-hand side, as every electron state can accommodate two spin orientations.

The LTE population number density of an atomic excitation level i with respect to the total number density n_{tot} is given by a Boltzmann factor,

$$\frac{n_i}{n_{\text{tot}}} = \frac{g_i}{U(T)} e^{-\frac{\chi_i^{\text{ex}}}{kT}} \qquad U(T) = \sum_i g_i e^{-\frac{\chi_i^{\text{ex}}}{kT}}, \tag{6.11}$$

where $U(T)$ denotes the partition function, which needs to include all accessible excitation levels. $U(T)$ diverges for an isolated atom as an infinite number of excitation levels is theoretically available. In real stellar atmospheres, highly excited electron states will be destroyed by collisions with other particles, and $U(T)$ can be truncated. Polynomial approximations for partitions functions are available in the literature in tabulated form (e.g., Irwin, 1981).

The Saha ionization equilibrium (Eq. (6.10)) and the Boltzmann excitation equilibrium (Eq. (6.11)) deliver ratios of level populations for a particle in ionization stage i and excitation level k, and the ionized particle in stage $j = i + 1$ and excitation level l. Summing over all possible excitation levels from which the particle can be ionized delivers the Saha-Boltzmann equilibrium formula

$$\frac{n_\mathrm{e} n_{j,l}}{n_i} = \frac{2 g_{j,l}}{U_i(T)} \left(\frac{2\pi m_e k T}{h^2} \right)^{\frac{3}{2}} e^{-\frac{\chi_i^\mathrm{ion} + \chi_{j,l}^\mathrm{ex}}{kT}} . \tag{6.12}$$

Combining molecular equilibrium calculations with Saha-Boltzmann equilibrium, one obtains a total absorber abundance for species m in ionization stage j and excitation level l through

$$n_{j,l,m} = n_\mathrm{tot,m} g_l \Phi\left(T, n_\mathrm{e}, \left\{n_{\mathrm{tot},m'}\right\}_{m' \neq m}\right) , \tag{6.13}$$

where the equilibrium function Φ depends on the chemical composition $\{n_{\mathrm{tot},m'}\}$ of the star through molecule formation. The total number densities $n_{\mathrm{tot},m'}$ of the different atomic species are derived from the chemical composition of the star and the gas densities. Elemental abundances in stellar atmospheres are usually given in spectroscopic notation using logarithmic abundance fractions

$$\log_{10} \epsilon_m = \log_{10} \left(\frac{n_m}{n_\mathrm{H}} \right) + 12.0, \tag{6.14}$$

normalized to the number of hydrogen atoms n_H and 10^{12}. In general, stellar gas is composed of a mixture of different elements. With given abundance fractions $A_m \equiv n_m / n_\mathrm{H}$, one obtains a mean molecular weight μ and the hydrogen number fraction f_H:

$$\mu = \frac{\sum_m m_m A_m}{\sum_m A_m} \tag{6.15}$$

$$f_\mathrm{H} = \frac{1}{\sum_m A_m} . \tag{6.16}$$

Using the gas density ρ provided by the model atmosphere, one obtains the global elemental abundance

$$n_{\mathrm{tot},m} = A_m f_\mathrm{H} \frac{\rho}{\mu} . \tag{6.17}$$

6.1.3 Oscillator strength

The photo-excitation rate B_lu depends on the processes which govern the transition of wave functions between the two electron states. Laboratory experiments provide accurate data for many important atomic and molecular transitions, but in some cases, theoretical calculations or calibrations with observed spectra need to be used.

For practical reasons, it is useful to describe transitions through a classical harmonic oscillator model, in which the electron oscillations are excited by the electromagnetic field of incident radiation. This simple model does not produce accurate interaction cross-sections for, e.g., forbidden lines where quantum-mechanical effects play an important role. However, it can be corrected through the oscillator strength f_lu, which is introduced with the expression

$$\int_0^\infty \chi_\nu^1 d\nu = \frac{h\nu_0}{4\pi} B_\mathrm{lu} n_\mathrm{l} \equiv \frac{\pi e^2}{m_\mathrm{e} c} f_\mathrm{lu} n_\mathrm{l}, \tag{6.18}$$

the factor $\pi e^2/(m_e c)$ is the cross-section for a classical harmonic oscillator, with the elementary charge e, the electron mass m_e and the speed of light c. Oscillator strengths are available in the literature for large amounts of lines (e.g., from the VALD database (Piskunov et al., 1995; Kupka et al., 1999; Ryabchikova et al., 1997) or from the NIST database (Ralchenko et al., 2009)).

6.1.4 Line profiles

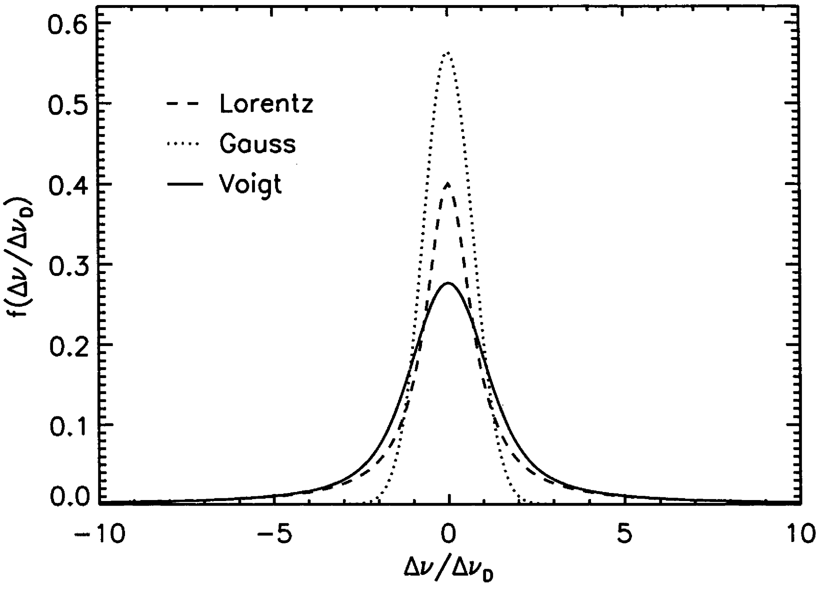

Figure 6.2: Examples of a Lorentzian profile (dashed line) for radiative damping and collisional broadening in the impact approximation, a Gaussian profile (dotted line) for thermal broadening through Doppler shifts, and a Voigt profile (solid line) as functions of frequency offset $\Delta\nu$ from the line center in units of the Doppler width $\Delta\nu_D$. The Voigt profile is the convolution of the Lorentzian and the Gaussian profiles.

The profile of a spectral line is determined by many different physical processes. Lines exhibit a natural profile of finite width, which is broadened through Doppler-shifts by random thermal motion of the radiating particles, and through collisions with other particles in the atmosphere. Although the underlying mechanisms of atomic physics are in principle understood, it is often difficult to obtain an accurate description due to the complex electromagnetic interactions and quantum mechanical effects. For the important case of collisional broadening through neutral hydrogen, the Unsöld (1955) formula was often used in the past. Detailed quantum-mechanical calculations by Anstee and O'Mara (1995) and other authors have become available, improving the atomic data significantly. Classical approximations still need to be used for some species or in other situations, such as inelastic collisions of particles in non-LTE calculations (see the discussion in Asplund, 2005). In addition to broadening, spectral line profiles are shifted by macroscopic gas motion in the moving atmosphere, which needs to be taken into account for realistic line formation studies.

Radiative damping

Radiative damping results from the finite lifetime of an excited state, which may decay through radiative transitions to one or more lower levels in the atom. The quantum-mechanical nature of electron states requires a broadening of energy levels through Heisenberg's uncertainty principle, and thus a broadening of the spectral line profile. Natural broadening produces a Lorentzian profile shape (dashed line in Fig. 6.2),

$$\phi(\nu - \nu_0) = \frac{\gamma^{\mathrm{rad}}/4\pi^2}{(\nu - \nu_0)^2 + (\gamma^{\mathrm{rad}}/4\pi)^2}. \tag{6.19}$$

If laboratory measurements are not available, the profile width γ^{rad} can be estimated using the Einstein coefficient for spontaneous radiative de-excitation (see, e.g., Gray, 2005). Assuming that only one transition exists through which the excited state can decay and using the Einstein relations as well as the definition of the oscillator strength (Eq. (6.18)), one obtains an estimated natural profile width of

$$\gamma^{\mathrm{rad}} \approx A_{\mathrm{ul}} = \frac{8\pi^2 e^2}{m_e c} \frac{1}{\lambda^2} \frac{g_{\mathrm{l}} f_{\mathrm{lu}}}{g_{\mathrm{u}}}, \tag{6.20}$$

where λ is the transition wavelength.

Collisional broadening

Collisions of radiating particles with electrons, ions and neutral atoms in the atmosphere cause additional profile broadening: the fluctuating electromagnetic field that the perturber imposes on the atom modulates its energy levels with an amplitude and frequency that depends on the type of particle, the relative speed and the number density of the perturbers. The statistical distribution of particle velocities turns the individual line shifts effectively into profile broadening.

Neutral hydrogen atoms dominate collisional broadening for transitions of metal lines in late-type stars due to their large number density; van der Waals interaction provides the underlying physical mechanism. The strength of the interaction scales with particle distance as d^{-6} due to the screening of the proton by the electron in H I, resulting in a small perturbation cross-section. The duration of such collisions is therefore very short, making the impact approximation valid.

In the impact approximation, each encounter of the radiating atom with a perturber produces an immediate phase shift in the emitted radiation field. The outgoing electromagnetic wave then consists of several distinct wave trains. Fourier transformation into frequency space and integration over a statistical distribution of perturbations yields a Lorentzian broadening profile (dashed line in Fig. 6.2). Its width is $\gamma = 2/\Delta t_0$, where Δt_0 is the inverse collision rate (see, e.g., Gray, 2005, for a detailed discussion).

Cross-sections for collisional broadening through H I have been calculated for different transition types of neutral atoms and selected transitions of ions by Anstee and O'Mara (1995), Barklem and O'Mara (1997), Barklem et al. (1998), Barklem et al. (2000a), Barklem and O'Mara (2001), and Barklem and Aspelund-Johansson (2005). The dependence of collisional cross-sections σ on the relative velocity v of the two interacting particles is approximated by a power law

$$\sigma(v) = \sigma(v_0) \left(\frac{v}{v_0} \right)^{-\alpha}, \tag{6.21}$$

where $\sigma(v_0)$ and α are tabulated, and v_0 is a reference velocity. A collision rate $C_{\mathrm{H\,I}}$ is obtained through the expression

$$C_{\mathrm{H\,I}}(v) = n_{\mathrm{H\,I}} v \sigma(v), \tag{6.22}$$

where $n_{\mathrm{H\,I}}$ is the number density of neutral hydrogen atoms. Assuming that relative particle speeds follow a Maxwellian velocity distribution for a reduced mass μ, the number of hydrogen atoms $dn_{\mathrm{H\,I}}$ per velocity bin dv is given by

$$dn_{\mathrm{H\,I}} = \sqrt{\frac{2}{\pi}} \left(\frac{\mu}{kT}\right)^{\frac{3}{2}} v^2 e^{-\frac{\mu v^2}{2kT}} dv. \tag{6.23}$$

The profile width $\gamma = 2/\Delta t_0 = 2C_{\mathrm{H\,I}}$ is obtained by integration over the distribution:

$$\gamma^{\mathrm{H\,I}} = 2\left(\frac{4}{\pi}\right)^{\frac{\alpha}{2}} \Gamma\left(\frac{4-\alpha}{2}\right) \bar{v}\sigma(v_0) \left(\frac{\bar{v}}{v_0}\right)^{-\alpha} n_{\mathrm{H\,I}}, \tag{6.24}$$

with the gamma function Γ and the average velocity $\bar{v} = \sqrt{8kT/\pi\mu}$.

In the absence of quantum mechanical calculations, an approximation by Unsöld (1955) may be used:

$$\log \gamma^{\mathrm{H\,I}} = 20 + 0.4 \log C_6 + \log P - 0.7 \log T, \tag{6.25}$$

for quantities given in cgs units (see Gray, 2005); P is the gas pressure. The interaction constant C_6 is approximated by

$$C_6 = 0.3 \cdot 10^{-30} \left[\left(\chi_{\mathrm{u}}^{\mathrm{ion}}\right)^{-2} - \left(\chi_{\mathrm{l}}^{\mathrm{ion}}\right)^{-2}\right], \tag{6.26}$$

with the ionization potentials $\chi_{\mathrm{u}}^{\mathrm{ion}}$ and $\chi_{\mathrm{l}}^{\mathrm{ion}}$ of the upper and lower level of the transition, both given in eV (see Gray, 2005).

Thermal broadening

Thermal motion of the absorbing particles widens the line profile through Doppler shifts. Such thermal broadening is important in line cores, and dominates the profiles of weak lines.

A non-relativistic particle that moves with velocity $\mathbf{v}$ absorbs a photon of frequency ν in direction $\hat{\mathbf{n}}$ in the laboratory frame with a frequency

$$\nu' = \left(1 - \frac{\hat{\mathbf{n}} \cdot \mathbf{v}}{c}\right)\nu \tag{6.27}$$

in its local rest frame due to the Doppler effect. Note that light aberration is negligible at non-relativistic velocities (see, e.g., Mihalas and Mihalas, 1984). Thermal velocities $\mathbf{v}$ in LTE follow a Maxwellian distribution (Eq. (6.23)). For the case of an infinitely sharp line extinction profile where $\phi(\nu - \nu_0) = \delta(\nu - \nu_0)$, a Galilean transformation from the rest frame of the atom into the rest frame of a macroscopic gas parcel and integration over the velocity distribution produces a Gaussian line profile (dotted line in Fig. 6.2):

$$\phi(\nu - \nu_0) = \frac{1}{\sqrt{\pi}\Delta\nu_{\mathrm{D}}} e^{-\left(\frac{\nu-\nu_0}{\Delta\nu_{\mathrm{D}}}\right)^2}, \tag{6.28}$$

where the Doppler width $\Delta\nu_{\mathrm{D}}$ is defined using the rms velocity v^{rms} of the distribution function for particle mass m,

$$\Delta\nu_{\mathrm{D}} = \frac{\nu_0}{c} v^{\mathrm{rms}} = \frac{\nu_0}{c}\sqrt{\frac{2kT}{m}}. \tag{6.29}$$

The Voigt profile

Real line profiles in the atomic rest frame have a finite width due to radiation damping and collisional broadening. Assuming complete independence of these mechanisms, one obtains the combined profile by convolution of the individual Lorentzians, which yields a new Lorentzian with

$$\gamma = \gamma^{\mathrm{rad}} + \gamma^{\mathrm{H\,I}}. \tag{6.30}$$

Galilean transformation into the rest frame of a gas parcel and assuming a Maxwellian velocity distribution produces the line profile through the convolution

$$\phi(\nu - \nu_0) = \frac{\gamma/4\pi^2}{(\nu' - \nu_0)^2 + (\gamma/4\pi)^2} * \frac{1}{\sqrt{\pi}\Delta\nu_{\mathrm{D}}} e^{-\left(\frac{\nu-\nu'}{\Delta\nu_{\mathrm{D}}}\right)^2}, \tag{6.31}$$

which is called the Voigt profile (solid line in Fig. 6.2). Equation (6.31) is usually abbreviated with the Voigt function H:

$$\phi(\nu - \nu_0) = \frac{H(a, v)}{\Delta\nu_{\mathrm{D}}}, \tag{6.32}$$

where $a = \gamma/(4\pi\Delta\nu_{\mathrm{D}})$ is the damping parameter and $v = (\nu - \nu_0)/\Delta\nu_{\mathrm{D}}$ is the frequency parameter. The Voigt function H is given by the expression

$$H(a, v) = \frac{a}{\pi} \int_{-\infty}^{\infty} \frac{e^{-y^2}}{(v - y)^2 + a^2} dy \qquad y = \frac{v}{v^{\mathrm{rms}}}. \tag{6.33}$$

Various numerical recipes to evaluate Eq. (6.33) exist in the literature. The vectorizable approximation by Hui et al. (1978) is well-suited for 3D applications where a very large number ($\gtrsim 10^6$) of Voigt functions needs to be evaluated in the model atmosphere.

The Voigt profile approximately reduces to a Gaussian profile for weak lines, where continuum extinction hides the damping wings (see the discussion in Rutten, 2003).

Macroscopic velocity fields in the atmosphere

Convective motion in the atmosphere of late-type stars causes significant Doppler shifts of the entire line profile; gas velocities reach $\sim 5\,\mathrm{km\,s^{-1}}$ in updrafts and $\sim 7\,\mathrm{km\,s^{-1}}$ in downdrafts at the solar surface (Stein and Nordlund, 1998). Macroscopic motion is thus comparable to the average thermal velocity of hydrogen ($\sim 11\,\mathrm{km\,s^{-1}}$ at $T = 5777\,\mathrm{K}$), which is the fastest-moving atom in the atmosphere. The profile functions in the observer's frame are obtained using the Doppler formula:

$$\phi(\nu - \nu_0) = \phi\left(\nu - \nu_0' - \nu_0' \frac{\hat{\mathbf{n}} \cdot \mathbf{u}}{c}\right), \tag{6.34}$$

where $\hat{\mathbf{n}}$ is the direction of the incident photon and $\mathbf{u}$ is the local gas velocity.

Microturbulence and macroturbulence

Microturbulent broadening has been traditionally used in 1D line formation to generate missing broadening of spectral lines through non-thermal motion. Assuming that length scales of particle motion are smaller than photon mean free paths, a microturbulent broadening parameter ξ is added to the local thermal velocities and calibrated with observed spectral lines. Macroturbulent broadening accounts for velocity fields on length scales that are larger than photon mean free paths; the line profiles are convolved with a Gaussian profile to approximate the effect.

Microturbulence and macroturbulence are both artificial parameters that need to be calibrated through observations. They strongly affect the accuracy of line profile computations, as they mask imperfections in the underlying models and atomic data through the calibration. Using high-resolution 3D radiation-hydrodynamical models of the solar atmosphere, Asplund et al. (2000b) found that observed line profiles were accurately reproduced by 3D spectral line formation without artificial broadening.

6.2 The line source function with a background continuum

Similar to absorption and scattering of photons away from the beam, emission from the gas through different atomic or molecular transitions and continuous sources is treated as a bulk contribution from a large number of particles to the radiation field. Spectral lines are assumed to form in strict LTE in this discussion; the energy of line photons is drawn from the thermal pool, while the source function of the background continuum includes a scattering contribution.

6.2.1 The LTE line source function

The amount of monochromatic radiation dI_ν per path length ds that is added to a beam by a spectral line in the atomic rest frame is given by

$$dI_\nu = \frac{h\nu_0}{4\pi} n_\mathrm{u} A_\mathrm{ul} \varphi(\nu - \nu_0) ds \equiv j^\mathrm{l}_\nu ds, \qquad (6.35)$$

where n_u is the population density of the upper level, A_ul is the Einstein coefficient for spontaneous de-excitation and $\varphi(\nu - \nu_0)$ is the emission profile. Induced emission is treated with a correction factor for the line opacity (see Sect. 6.1.1). For matter in thermodynamic equilibrium, the Kirchhoff-Planck relation requires that photons are absorbed and emitted at equal rates:

$$j_\nu = \kappa_\nu I_\nu \qquad \longrightarrow \qquad j_\nu = \kappa_\nu B_\nu. \qquad (6.36)$$

The second equality follows, since radiation in thermodynamic equilibrium follows a Planck distribution B_ν. It is important to note that Eq. (6.36) is not strictly fulfilled in LTE, as radiation from non-local sources perturbs the equilibrium and photons escape from the gas (see, e.g., Mihalas and Mihalas, 1984). Detailed balancing in equilibrium implies the equivalence of the absorption and emission profiles,

$$\phi(\nu - \nu_0) = \varphi(\nu - \nu_0) = \chi(\nu - \nu_0). \qquad (6.37)$$

Treating line opacity as absorption ($\chi^\mathrm{l}_\nu = \kappa^\mathrm{l}_\nu$), the LTE line source function is given by the Planck function:

$$S^\mathrm{l}_\nu = \frac{j^\mathrm{l}_\nu}{\chi^\mathrm{l}_\nu} = B_\nu. \qquad (6.38)$$

6.2.2 Scattering and redistribution

In addition to thermal radiation (Eq. (6.38)), atoms emit photons through scattering processes. The radiative transfer equation then includes source terms of the kind

$$j^\sigma_\nu = \frac{\sigma}{4\pi} \int_0^\infty \int_{S^2} R(\nu, \nu', \hat{\mathrm{n}}, \hat{\mathrm{n}}') I_{\nu'}(\hat{\mathrm{n}}') d\Omega' d\nu'. \qquad (6.39)$$

Scattering emission j^σ_ν is proportional to scattering opacity σ, which depends on the population density and the detailed transition (see the discussion of line opacity in Sect. 6.1). Doppler-shifts and the angle-dependence of scattering cross-sections redistribute the incident radiation $I_{\nu'}(\hat{\mathrm{n}}')$

in angle and frequency. The scattering term (Eq. (6.39)) integrates the radiation field at all angles and frequencies, weighting the individual contributions with a redistribution function R.

Rayleigh scattering and electron scattering, which are important opacity sources in stellar atmospheres, depend only weakly on the scattering angle, angular redistribution is therefore often neglected. Scattering is approximately coherent in the rest frame of an isolated particle, but thermal motion and collisional broadening break this coherence. The result is a very complex coupling of the radiation field across a wide range of frequencies and angles. The redistribution function R depends on the local physical conditions and varies with the different scattering mechanisms; Mihalas (1978) and Peraiah (2001) give examples for several important cases.

While a detailed treatment of redistribution is difficult, it is often sufficient to approximate R: Rayleigh scattering and electron scattering can be assumed isotropic and also coherent if the radiation field varies slowly with frequency, which yields $R = \delta(\nu - \nu')$. The emission term (Eq. (6.39)) then simplifies to

$$j_\nu^\sigma = \frac{\sigma}{4\pi}\int_0^\infty \int_{S^2} \delta(\nu - \nu') I_{\nu'}(\hat{\mathrm{n}}') d\Omega' d\nu' = \sigma J_\nu. \tag{6.40}$$

However, this approximation is not strictly valid in the presence of spectral lines, where J_ν changes rapidly across the profile.

Complete redistribution, where emitted photons are assumed to have lost their correlation with the incident radiation, is usually a good approximation for weak spectral lines. The redistribution function reduces to $R = \varphi(\nu - \nu_0)\phi(\nu' - \nu_0)$, which results in an emission term

$$j_\nu^\sigma = \frac{\sigma}{4\pi}\int_0^\infty \int_{S^2} \varphi(\nu - \nu_0)\phi(\nu' - \nu_0) I_{\nu'}(\hat{\mathrm{n}}') d\Omega' d\nu' = \sigma\varphi(\nu - \nu_0)\bar{J}_{\nu_0}, \tag{6.41}$$

where $\bar{J}_{\nu_0}$ is the profile-averaged mean intensity. Complete redistribution breaks down in the case of strong lines, which require a more detailed treatment (see, e.g., Uitenbroek and Bruls, 1992). For LTE lines, $j_\nu^\sigma = 0$, as only thermal emission processes are considered.

6.2.3 LTE lines with a scattering background continuum

The monochromatic time-independent radiative transfer equation for a spectral line with coherent scattering in the background continuum is given by

$$\hat{\mathrm{n}} \cdot \nabla I_\nu = -(\chi_\nu^{\mathrm{l}} + \chi^{\mathrm{c}}) I_\nu + \chi_\nu^{\mathrm{l}} B + \sigma^{\mathrm{c}} J_\nu + \kappa^{\mathrm{c}} B, \tag{6.42}$$

where the frequency dependences of the Planck function and the continuous absorption and scattering coefficients have been dropped as they are almost constant across the profile of a weak line. Dividing Eq. (6.42) by the total opacity $\chi_\nu = \chi_\nu^{\mathrm{l}} + \chi^{\mathrm{c}}$ and introducing the optical depth $d\tau_\nu = \chi_\nu ds$, one obtains

$$\frac{dI_\nu}{d\tau_\nu} = -I_\nu + \frac{\chi_\nu^{\mathrm{l}}}{\chi_\nu} B + \frac{\chi^{\mathrm{c}}}{\chi_\nu}\left[\frac{\sigma^{\mathrm{c}}}{\chi^{\mathrm{c}}} J_\nu + \frac{\kappa^{\mathrm{c}}}{\chi^{\mathrm{c}}} B\right] \tag{6.43}$$

$$= -I_\nu + \frac{\chi_\nu^{\mathrm{l}}}{\chi_\nu} B + \frac{\chi^{\mathrm{c}}}{\chi_\nu}\left[(1 - \epsilon^{\mathrm{c}}) J_\nu + \epsilon^{\mathrm{c}} B\right], \tag{6.44}$$

where the continuum photon destruction probability $\epsilon^{\mathrm{c}} = \kappa^{\mathrm{c}}/\sigma^{\mathrm{c}}$ has been introduced in the second equality, weighting between thermal emission of continuum photons and scattering of radiation. The factors $\chi_\nu^{\mathrm{l}}/\chi_\nu$ and $\chi^{\mathrm{c}}/\chi_\nu$ assume the role of weighting functions as well; they represent the probability that a photon was created by thermal emission from the line or by thermal or scattering emission from the background continuum. In the presence of macroscopic velocity fields, the source function in Eq. (6.44) becomes anisotropic due to Doppler shifts of the spectral line profile. The probability of thermal emission from the line then depends on frequency, direction and flow velocity of the radiating gas.

6.3 Numerical methods for spectral line formation

Spectral line synthesis with a scattering background continuum in 3D involves detailed coupling of the radiation field at different angles, frequencies and spatial locations in the model atmosphere. Analytical solutions of the radiative transfer problem exist only in few very simplified cases (see Sect. 3.5). In general, a numerical solution of the equations is required. A large variety of methods for solving the radiative transfer equation is available (see Wehrse and Kalkofen, 2006). Characteristics-based schemes are a popular choice in the field of stellar atmospheres, due to their efficiency and straightforward implementation.

The spectral line formation computations with the `SCATE` code use a short characteristics scheme with Gauss-Seidel-type ALI acceleration (see Sect. 3.3) for determining the source function with coherent scattering, to benefit from the fast convergence of the method. Surface intensities are then computed using a Feautrier-type solver on long characteristics, which extend through the entire 3D atmosphere cube; angle-resolved radiative transfer with short characteristics schemes suffers from larger numerical diffusion.

6.3.1 The Gauss-Seidel method for anisotropic source functions

The Gauss-Seidel ALI method of Trujillo Bueno and Fabiani Bendicho (1995, see Sect. 3.3.4 and Sect. 4.3.2) is well-suited for computing the mean radiation field with coherent scattering, as it is numerically stable when scattering is important at large optical depths and converges fast. The solver needs to handle a radiative transfer problem with a complex anisotropic source function due to the appearance of continuum scattering:

$$S_\nu = \frac{\chi^{\mathrm{l}}_\nu}{\chi_\nu} B + \frac{\chi^{\mathrm{c}}}{\chi_\nu} \left[(1-\epsilon^{\mathrm{c}})J_\nu + \epsilon^{\mathrm{c}} B\right] \equiv (1-\eta_\nu)\, S^{\mathrm{l}} + \eta_\nu S^{\mathrm{c}}_\nu, \tag{6.45}$$

where η_ν weights between emission from the line and from the continuum. Doppler-shifts through macroscopic velocity fields introduce a direction dependence in S_ν through η_ν, despite the isotropy of S^{l} and S^{c}_ν. The ALI scheme for an isotropic coherent scattering source function (Eq. (3.47)) requires some adaption for a correct treatment.

The Λ_ν operator that delivers the mean monochromatic radiation field J_ν for a given source function S_ν combines integration of the radiative transfer equation and integration over solid angle:

$$J_\nu = \Lambda_\nu S_{\mu\nu} = \frac{1}{4\pi} \int_{S^2} d\Omega \Lambda_{\mu\nu} S_{\mu\nu}. \tag{6.46}$$

The subscript μ indicates the direction dependence of the source function (Eq. (6.45)). The new operator $\Lambda_{\mu\nu}$ delivers specific intensities $I_{\mu\nu}$ in direction $\hat{\mathrm{n}}_\mu$. Inserting Eq. (6.46) into the continuum source function (Eq. (6.45)) yields

$$S^{\mathrm{c}}_\nu = (1-\epsilon^{\mathrm{c}}) \frac{1}{4\pi} \int_{S^2} d\Omega \Lambda_{\mu\nu} (\eta_{\mu\nu} S^{\mathrm{c}}_\nu + (1-\eta_{\mu\nu}) S^{\mathrm{l}}) + \epsilon^c B \tag{6.47}$$

$$= (1-\epsilon^{\mathrm{c}}) \frac{1}{4\pi} \int_{S^2} d\Omega \Lambda_{\mu\nu} \eta_{\mu\nu} S^{\mathrm{c}}_\nu + (1-\epsilon^{\mathrm{c}}) J^{\mathrm{l}}_\nu + \epsilon^c B, \tag{6.48}$$

where J^{l}_ν abbreviates the angle-integrated contribution of line photons that are scattered by a continuum process. Solving Eq. (6.48) for the continuum source function and discretizing the result, one obtains a system of linear equations for S^{c}_ν,

$$\left[\mathbb{1} - (1-\epsilon^{\mathrm{c}}) \frac{1}{4\pi} \sum_\mu w_\mu \Lambda_{\mu\nu} \eta_{\mu\nu}\right] S^{\mathrm{c}}_\nu = (1-\epsilon^{\mathrm{c}}) J^{\mathrm{l}}_\nu + \epsilon^c B, \tag{6.49}$$

in analogy to the derivation in Sect. 3.3.4. Introducing the approximate operator $\Lambda^*_{\mu\nu}$ and the matrices

$$A = \left[\mathbb{1} - (1-\epsilon^{\rm c})\frac{1}{4\pi}\sum_\mu w_\mu \Lambda_{\mu\nu}\eta_{\mu\nu}\right] \tag{6.50}$$

$$A^* = \left[\mathbb{1} - (1-\epsilon^{\rm c})\frac{1}{4\pi}\sum_\mu w_\mu \Lambda^*_{\mu\nu}\eta_{\mu\nu}\right], \tag{6.51}$$

one obtains an iterative scheme which produces continuum source function corrections $\Delta S^{\rm c}_\nu$ for the approximate solution $S^{{\rm c},n}_\nu$ through

$$A^*\Delta S^{\rm c}_\nu = (1-\epsilon^{\rm c})J^{\rm l}_\nu + \epsilon^c B - AS^{{\rm c},n}_\nu \tag{6.52}$$

$$= (1-\epsilon^{\rm c})\frac{1}{4\pi}\sum_\mu w_\mu \Lambda_{\mu\nu}(\eta_{\mu\nu}S^{\rm c}_\nu + (1-\eta_{\mu\nu})S^{\rm l}) + \epsilon^c B - S^{{\rm c},n}_\nu \tag{6.53}$$

$$= S^{\rm c,FS}_\nu - S^{{\rm c},n}_\nu, \tag{6.54}$$

where $S^{\rm c,FS}_\nu$ is the continuum source function for the radiation field of the last formal solution. The iteration method is thus identical to the case of an isotropic source function, apart from the emission weighting through $\eta_{\mu\nu}$ in the approximate operator A^*: in the absence of line opacity, $\eta_{\mu\nu} = 1$ for all angles and Eq. (6.54) reduces to the isotropic case of Sect. 3.3.4. If line opacity dominates, $\eta_{\mu\nu} \to 0$ suppresses continuum emission, and the local source function only depends weakly on the radiation field as most absorbed photons are thermalized.

6.3.2 The Feautrier method

The Feautrier (1964) method provides a fast and numerically stable solver for the radiative transfer equation in 1D or along characteristics in 3D, which is based on finite difference discretization. The method obtains stability and second-order accuracy by solving a second-order version of the radiative transfer equation for pairs of opposite ray directions, instead of a direct discretization of the equation. Feautrier (1964) introduces a mean-intensity-like variable P_ν and a flux-like variable Q_ν for a given ray direction $\hat{\rm n}$ through the expressions

$$P_\nu = \frac{1}{2}(I_\nu(\hat{\rm n}) + I_\nu(-\hat{\rm n})) \tag{6.55}$$

$$Q_\nu = \frac{1}{2}(I_\nu(\hat{\rm n}) - I_\nu(-\hat{\rm n})). \tag{6.56}$$

Using a separate radiative transfer equation for each ray direction, one obtains

$$\frac{dI_\nu(\hat{\rm n})}{d\tau_\nu} = -I_\nu(\hat{\rm n}) + S_\nu \tag{6.57}$$

$$-\frac{dI_\nu(-\hat{\rm n})}{d\tau_\nu} = -I_\nu(-\hat{\rm n}) + S_\nu. \tag{6.58}$$

It is important to note that the Feautrier method requires isotropic opacities and source functions. In the presence of macroscopic velocity fields that break isotropy through Doppler shifts, opacities along ingoing and outgoing rays differ. For a known source function, the Feautrier method still produces correct surface intensities if optical depths are computed consistently for outgoing rays, as outgoing intensities $I_\nu(\hat{\rm n})$ are independent of the incorrectly treated ingoing intensities $I_\nu(-\hat{\rm n})$. In the case of completely symmetric line profiles in the local rest frame of the gas, the Feautrier method can alternatively be adapted to produce consistent results (see Mihalas, 1978).

Combining Eq. (6.57) and Eq. (6.58) using definitions Eq. (6.55) and Eq. (6.56) results in the coupled system of equations

$$\frac{dP_\nu}{d\tau_\nu} = -Q_\nu \tag{6.59}$$

$$\frac{dQ_\nu}{d\tau_\nu} = -P_\nu + S_\nu. \tag{6.60}$$

Inserting each equation into the derivative of the other one yields two second-order transport equations for P_ν and Q_ν,

$$\frac{d^2P_\nu}{d\tau_\nu^2} = P_\nu - S_\nu \tag{6.61}$$

$$\frac{d^2Q_\nu}{d\tau_\nu^2} = Q_\nu + \frac{dS_\nu}{d\tau_\nu}. \tag{6.62}$$

The first equation is used for spectral line formation problems, while the second equation is sometimes employed for computing radiative heating rates in radiation-hydrodynamical simulations. Discretizing Eq. (6.61) using centered finite differences, one obtains the expression (e.g., Rutten, 2003)

$$A_iP_{i-1} - B_iP_i + C_iP_{i+1} = -S_i; \tag{6.63}$$

The three coefficients A_i, B_i and C_i are defined by

$$A_i = \frac{2}{\Delta\tau_{i-1}(\Delta\tau_{i-1} + \Delta\tau_i)} \tag{6.64}$$

$$B_i = 1 + \frac{2}{\Delta\tau_{i-1}\Delta\tau_i} \tag{6.65}$$

$$C_i = \frac{2}{\Delta\tau_i(\Delta\tau_{i-1} + \Delta\tau_i)}; \tag{6.66}$$

similar expressions are found for the upper and lower ends of the ray through Taylor expansion. For a known source function S_ν, the radiative transfer problem on a characteristic is reduced to solving a system of linear equations, which is represented by a tridiagonal matrix. The Thomas algorithm or other numerical methods are then used to obtain P_i on each point along the ray. The outgoing intensities at the surface are given by

$$I_\nu^+(\tau_\nu = 0) = 2P_1, \tag{6.67}$$

since $I_\nu^-(\tau_\nu = 0) = 0$ was used as a boundary condition.

6.4 Rotational broadening

Stellar rotation leads to blueshifts in light emission from the approaching half of the disk and to redshifts on the receding half with respect to a line of sight. As the disk itself is usually not resolved, the observed line profiles appear broadened. Stellar rotation is often approximated by assuming a rigid rotator; the amount of broadening then depends on the equatorial velocity v and the inclination i of the rotational axis with respect to the line of sight through a factor $v \sin i$ (e.g. Gray, 2005). In general, i is unknown and only $v \sin i$ may be determined from the observed spectrum.

Dravins and Nordlund (1990) used the following recipe for rotational broadening: assuming an angular velocity $\mathbf{\Omega}$ of the rotating star, the line-of-sight velocity v_{LOS} in direction $\hat{\mathbf{n}}$ at position $\mathbf{r}$ on the disk is given by

$$v_{\mathrm{LOS}} = (\mathbf{\Omega} \times \mathbf{r})\cdot\hat{\mathbf{n}} = (\hat{\mathbf{n}} \times \mathbf{\Omega})\cdot\mathbf{r} = |\mathbf{\Omega}| R \sin i (\sin\theta \cos\phi) = v \sin i (\sin\theta\cos\phi) \tag{6.68}$$

where R is the equatorial radius. θ and ϕ are projection angles, the disk center is located at $\theta = 0$. 3D radiation-hydrodynamical models represent stellar atmospheres in a statistical sense; the stellar disk is approximated by identifying positions on the surface with the projection angles (θ, ϕ) off the vertical axis and a horizontal axis in the model. The line-of-sight velocity (Eq. (6.68)) produces a Doppler-shift of the line profile as a function of θ and ϕ; limb darkening is automatically taken into account in the flux integration.

Tests by Ludwig (2007) show that an accurate description of rotational broadening through the recipe of Dravins and Nordlund (1990) requires solving the radiative transfer problem for a large number of ray angles ($N_\theta \gtrsim 4$) to produce reliable results. However, this is not a major restriction on modern parallel computer systems, which allow fast concurrent computation of radiative transfer on many ray angles.

Chapter 7

3D LTE spectral line formation with scattering in red giant stars

W. Hayek, M. Asplund, R. Collet, Å. Nordlund, *A&A submitted*

Abstract

Aims. We investigate the effects of coherent isotropic continuum scattering on the formation of spectral lines in local thermodynamic equilibrium (LTE) using 3D radiation-hydrodynamical model atmospheres of red giant stars.
Methods. Detailed radiative transfer with coherent and isotropic continuum scattering is computed for realistic 3D radiation-hydrodynamical models of late-type stellar atmospheres using the SCATE code. The calculations take the full 3D surface structure and Doppler-shifts from convective motions into account. Opacities are computed in LTE, while a coherent and isotropic scattering term is added to the continuum source function. We test the importance of scattering by comparing continuum flux levels and spectral line profiles of different species with calculations that treat scattering as absorption. The role of velocity fields and inhomogeneities of the 3D atmosphere models in determining profile shapes and the curve of growth is further explored by repeating the analysis for a 3D model with zero gas velocities and for a classical 1D hydrostatic model.
Results. Rayleigh scattering is the dominant source of scattering opacity in the continuum of red giant stars. Photons may escape from deeper, hotter layers through scattering, resulting in significantly higher continuum flux levels beneath a wavelength of $\lambda \lesssim 5000$ Å. The magnitude of the effect is determined by the importance of scattering opacity with respect to absorption opacity; we observe the largest changes in continuum flux at the shortest wavelengths and lowest metallicities, and intergranular lanes are more strongly affected than granules. Continuum scattering acts to increase the profile depth of LTE lines: continua gain more brightness than line cores due to their larger thermalization depth in hotter layers. We thus observe the strongest changes in line depth for high-excitation species and ionized species, which contribute significantly to photon thermalization through their absorption opacity near the continuum optical surface. Scattering desaturates the line profiles, leading to larger abundance corrections for stronger lines, which reach -0.5 dex at 3000 Å for Fe II lines with excitation potential $\chi = 2$ eV at [Fe/H] $= -3.0$. The corrections are less severe for longer wavelengths and higher metallicity. Velocity fields increase the effect of scattering by separating emission from granules and intergranular lanes in wavelength.

7.1 Introduction

Spectral line formation is an important discipline in the field of stellar astronomy. It is used as a diagnostic tool for numerical models of stellar atmospheres by comparing their predictions with observations, as well as for measuring quantities of astrophysical interest, such as stellar parameters, chemical abundances, surface velocity fields and many more. Spectral lines sample the physical conditions in stellar atmospheres in a wide height range and can thereby reveal useful information about the atmospheric structure.

The physics of line formation involves many different processes that require a detailed treatment of the interaction between radiation and matter. Beside the transition itself, these processes include, e.g., Doppler-shifts through thermal and non-thermal particle motion, collisional interaction, photoionization etc. The physical state of matter depends in general not only on local conditions, such as the gas temperature and pressure, but also on conditions in other parts of the atmosphere that are connected through the radiation field. Ignoring such non-local coupling enables the approximation of local thermodynamic equilibrium (LTE), which allows a tremendous simplification of line formation computations and is therefore frequently used. However, LTE is in general a bad approximation, and it can be only applied to specific cases in which its validity has been proven or when only estimated quantities are needed. A more accurate non-LTE treatment involves detailed atomic models, which require a significant amount of additional physical data (see, e.g., the discussion in Asplund, 2005). Owing to their much lower complexity and computational demands, analyses based on 3D LTE line formation are nevertheless useful tools for cases that are known to show weak or vanishing departures from LTE, such as the often-used forbidden [O I] line at 6300 Å.

Late-type stellar atmospheres are bounded by the underlying convection zone, which is responsible for horizontal inhomogeneities in gas temperature and pressure, and flow fields that affect the line profile shape through Doppler-shifts (e.g., Nordlund et al., 2009). Accurate line formation computations need to take this 3D structure of the atmosphere into account to obtain correct line profiles. The complexity of 3D calculations is rewarded by the elimination of additional parameters such as microturbulence and macroturbulence (e.g. Asplund et al., 2000b).

Metal-poor halo stars are particularly interesting targets for stellar abundance analyses: they are among the oldest objects in the Galaxy and largely preserve the chemical composition of the ISM in their envelopes, allowing detailed studies of nucleosynthesis processes and Galactic chemical evolution (e.g., Beers and Christlieb, 2005). Most abundance studies of metal-poor stars rely either on 1D LTE or on 1D non-LTE syntheses. The effects of 3D line formation have not been widely explored yet: Asplund et al. (1999), Collet et al. (2007) and Behara et al. (2010) showed that the temperature stratification and inhomogeneous structure of 3D model atmospheres have an important effect on line formation in metal-poor giant stars and dwarf stars. Molecular species, low-excitation lines and atomic minority species are thus particularly affected by 3D effects through their high temperature-sensitivity; molecules are important instruments for determining CNO abundances of such stars. Full 3D non-LTE studies of lithium abundances in metal-poor stars have been presented by Asplund et al. (2003), Cayrel et al. (2007) and Sbordone et al. (2010), following earlier work of Kiselman (1997) and Uitenbroek (1998), who used simplified methods to approximate the effect of photospheric inhomogeneities.

An important issue for the accuracy of abundance analyses of metal-poor giants is the role of Rayleigh scattering opacity for continuum formation in the blue and UV wavelength regions, where transitions of many important elements are found. Such scattering processes can increase the thermalization depth of photons, which may escape from deeper, hotter layers in the star, resulting in higher continuum flux. Chemical abundance studies by Cayrel et al. (2004), Bihain et al. (2004) and Lai et al. (2008) using 1D LTE line formation have found that treating continuum scattering as absorption instead of computing radiative transfer with scattering leads to significantly larger abundances and trends with transition wavelength.

We investigate the effects of coherent scattering in the background continuum by computing 3D LTE line profiles for a selection of typical transitions, including neutral and singly ionized iron, as well as various molecular species. Section 7.2 discusses important aspects of the underlying radiative transfer model for spectral line formation, which builds on 3D time-dependent radiation-hydrodynamical model atmospheres of red giant stars discussed in Sect. 7.3. We analyze continuum formation with scattering in Sect. 7.5, and investigate its effects on LTE line formation in Sect. 7.6. Besides exploring the scattering in the 3D case, we also compare our results with calculations based on a classical 1D LTE model atmosphere. Section 7.7 gives a summary of our results.

7.2 Line formation with continuum scattering

We solve the 3D time-independent radiative transfer problem for stellar spectral lines and a background continuum with coherent isotropic scattering. Excitation level populations, ionization and molecule formation needed to derive gas opacities are computed assuming local thermodynamic equilibrium (LTE); the line profiles include collisional broadening by neutral hydrogen and Doppler-shifts through macroscopic velocity fields (see Sect. 7.4 and Appendix D for a description of the numerical methods).

The time-independent radiative transfer equation evaluates the monochromatic specific intensity I_ν in direction $\hat{\mathbf{n}}$ at frequency ν in the observer's frame:

$$\frac{dI_\nu(\tau_\nu)}{d\tau_\nu} = -I_\nu(\tau_\nu) + S_\nu(\tau_\nu), \tag{7.1}$$

where S_ν is the monochromatic source function. The optical depth $d\tau_\nu$ of a photon path length ds on a light ray is defined as

$$d\tau_\nu \equiv \left(\chi^{\mathrm{l}}_\nu + \chi^{\mathrm{c}}\right) ds, \tag{7.2}$$

with the line opacity χ^{l}_ν and the continuum opacity χ^{c}. The source function S_ν at optical depth τ_ν includes contributions from spectral lines and continuum processes:

$$S_\nu = \frac{\chi^{\mathrm{l}}_\nu}{\chi^{\mathrm{l}}_\nu + \chi^{\mathrm{c}}} B + \frac{\chi^{\mathrm{c}}}{\chi^{\mathrm{l}}_\nu + \chi^{\mathrm{c}}} \left(\left[1 - \epsilon^{\mathrm{c}}\right] J_\nu + \epsilon^{\mathrm{c}} B\right); \tag{7.3}$$

B is the Planck function, ϵ^{c} is the continuum photon destruction probability and J_ν is the monochromatic mean intensity. Note that frequency subscripts have been dropped in Eq. (7.1) through Eq. (7.3) for all quantities that depend only weakly on frequency across a line profile and are therefore assumed constant in our computation.

The line opacity χ^{l}_ν may include contributions from several transitions of different species. At each point in the atmosphere, the individual line profiles are evaluated in the local rest frame of the gas around the center frequency ν'_0 of the transition. In the observer's frame, the profiles appear Doppler-shifted through the non-relativistic velocity field $\mathbf{u}$ predicted by the 3D hydrodynamical model atmosphere. The line center frequency ν_0 is then given by

$$\nu_0 = \left(1 + \frac{\hat{\mathbf{n}} \cdot \mathbf{u}}{c}\right) \nu'_0 \tag{7.4}$$

in the observer's frame for a light ray in direction $\hat{\mathbf{n}}$ (see, e.g., Mihalas and Mihalas, 1984); c is the speed of light. Relative to the frequency ν of photons that stream in the same direction as the flowing gas, the absorption profile appears blue-shifted; the same holds for line emission from the observer's point of view. In the solar atmosphere, upflowing gas in the bright granules dominates the emitted radiative flux (Stein and Nordlund, 1998), and the resulting Doppler-shifts along the line of sight distort profile bisectors dominantly towards higher frequencies (see the discussion in Sect. 7.6 and, e.g., Asplund et al., 2000b).

The opacity quotients $\chi_\nu^{\mathrm{l}} / \left(\chi_\nu^{\mathrm{l}} + \chi^{\mathrm{c}}\right)$ and $\chi^{\mathrm{c}} / \left(\chi_\nu^{\mathrm{l}} + \chi^{\mathrm{c}}\right)$ in Eq. (7.1) yield the probabilities that a photon was created by a line transition or by a continuous process. The direction-dependence of line opacity in the observer's frame through Doppler-shifts (Eq. (7.4)) induces a direction-dependence of these emission probabilities, and the combined source function S_ν becomes anisotropic.

The continuum photon destruction probability ϵ^{c} is defined by the ratio

$$\epsilon^{\mathrm{c}} \equiv \frac{\kappa^{\mathrm{c}}}{\kappa^{\mathrm{c}} + \sigma^{\mathrm{c}}}, \tag{7.5}$$

with the continuous absorption coefficient κ^{c} and the continuous scattering coefficient σ^{c}. In analogy to the above described opacity quotients, ϵ^{c} can be interpreted as the probability that a photon was fed into the beam from the thermal pool rather than from a scattering event. In late-type stellar atmospheres, Rayleigh scattering on H I atoms and electron scattering mainly contribute to continuous scattering opacity, while continuous absorption includes many bound-free and free-free transitions of hydrogen, helium and metals (see, e.g., the discussion in Hayek et al., 2010).

Continuous scattering may be treated as a coherent mechanism to very good approximation when the radiation field J_ν varies only slowly with frequency. In the presence of spectral lines, J_ν exhibits much stronger frequency-dependence, and scattering leads to a complex coupling of the radiation field in frequency and angle through Doppler-shifts (see, e.g., discussions in Mihalas, 1978; Peraiah, 2001). Auer and Mihalas (1968a,b) analyzed the effects of non-coherent electron scattering on line formation in early-type stars. They assumed redistribution through thermal motion of the electrons, which occurs across a very wide frequency band compared to thermal redistribution in the line: the ratio between the thermal profile widths of electrons with mass m_{e} and line-forming atoms with mass m_{atom} is given by $\sqrt{m_{\mathrm{atom}}/m_{\mathrm{e}}} \approx 42.7\sqrt{A}$, where A is the atomic mass number. In late-type stars, Rayleigh scattering dominates scattering opacity at the continuum optical surface in the blue and UV wavelength regions, and the ratio of Doppler widths scales only with $\sqrt{A} \lesssim 15$. Although electron scattering is an important continuous opacity source in early-type stars, Auer and Mihalas (1968b) find a relatively small effect of non-coherence on the wings of He II profiles. We therefore expect the assumption of coherent scattering to be a reasonable approximation for the rather weakly scattering background continua of red giant stars.

Rayleigh scattering and electron scattering cross-sections depend on the scattering angle θ through the angular redistribution function $(1 + \cos^2\theta)$, which may be neglected to good approximation (see, e.g., Mihalas, 1978).

7.3 3D radiation-hydrodynamical model atmospheres

Various studies have shown that the formation of spectral lines in the atmospheres of late-type stars can be severely affected by the presence of inhomogeneities in the temperature structure and velocity fields (e.g., Nordlund, 1980; Dravins and Nordlund, 1990; Asplund et al., 2000b; Steffen and Holweger, 2002; Allende Prieto et al., 2002; Caffau et al., 2008; Ramírez et al., 2009). Synthetic line computations based on the current generation of 3D radiation-hydrodynamical models are capable of providing realistic predictions of the observations; see

T_{eff} [K]	$\log g$ [cgs]	[Fe/H]	[α/Fe]
5100 ± 14	2.2	−3.0	+0.4
5051 ± 13	2.2	−2.0	0.0
4730 ± 11	2.2	−1.0	0.0
5063 ± 21	2.2	0.0	0.0

Table 7.1: Stellar parameters of the 3D radiation-hydrodynamical model atmospheres.

Pereira et al. (2009b,a) for the important case of the Sun. Classical 1D hydrostatic model atmospheres, which are still widely used, simply cannot achieve this degree of realism.

An important aspect in this context is the coupling of radiative transfer and hydrodynamics in 3D models, which leads to significantly cooler gas temperatures above the surface of metal-poor stars than predicted by 1D hydrostatic models (Asplund et al., 1999). Low metallicity strongly reduces radiative heating in these objects, and the photospheric temperature stratification steepens towards an adiabatic gradient, while the assumption of radiative equilibrium that is inherent to 1D models keeps the gradient shallow. The lower temperatures of 3D models have a strong impact on the formation of molecules and thus on the predicted molecular line strengths (Asplund and García Pérez, 2001; Collet et al., 2007); molecules are frequently used for determining the abundances of carbon, nitrogen and oxygen (e.g., Spite et al., 2006).

We base our analysis on 3D radiation-hydrodynamical model atmospheres of red giant stars with similar effective temperatures, a surface gravity of $\log g = 2.2$ (in cgs units) and metallicities[1] between $[\mathrm{Fe/H}] = -3.0$ and $[\mathrm{Fe/H}] = 0.0$ (see Table 7.1); the chemical abundance mixture adopts the solar composition of Asplund et al. (2009), scaled by metallicity and with a +0.4 dex enhancement of α-elements for the most metal-poor model.

The simulations were created with the `StaggerCode` (Nordlund and Galsgaard, 1995), which solves the coupled equations of compressible hydrodynamics and time-independent radiative transfer, computing radiative heating rates in LTE. Line-blanketing is approximated using the opacity binning method (Nordlund, 1982; Skartlien, 2000) with 4 opacity bins. Calculations by Collet et al. (2010, in preparation) demonstrate that the effects of coherent scattering on the temperature structure of metal-poor giant stars may be reproduced in reasonable approximation by removing the scattering contribution from the opacities in the optically thin parts of the atmosphere and using a Planck source function, which we applied to the models used for the analysis.

The effective temperature of 3D radiation-hydrodynamical model atmospheres is an observable rather than a parameter: it is determined by the entropy of the inflowing gas at the bottom of the simulation, but exhibits some temporal variation due to the convective motions. T_{eff} therefore varies between the different model atmospheres, which is not critical for our differential investigation of continuum scattering effects. After the initial scaling of the model atmosphere to reach the desired stellar parameters, each simulation was run until the atmospheric stratification reached a quasi-steady state with little temporal variation.

Figure 7.1 shows the temperature distribution of an arbitrary snapshot of the $[\mathrm{Fe/H}] = -3.0$ model as a function of optical depth at 5000 Å. The atmospheres cover several pressure scale heights above and below the continuum optical surface of the stars to include the relevant line-forming regions and to avoid boundary effects on the granulation flow. The simulation domains have a resolution of 240 × 240 × 230 grid points and assume periodic horizontal boundaries. Synthetic curves of growth were computed using time-series of simulation snapshots that span over a period of the fundamental pressure oscillation mode. A representative

---

[1] Metallicity is defined here in spectroscopic notation as the logarithmic iron abundance relative to the Sun, $[\mathrm{Fe/H}] \equiv \log_{10}(N_{\mathrm{Fe}}/N_{\mathrm{H}})_{*} - \log_{10}(N_{\mathrm{Fe}}/N_{\mathrm{H}})_{\odot}$.

sample of line profiles is thereby obtained that includes statistical variation in the predicted line strengths through convective motions.

We include a MARCS model atmosphere with $T_{\rm eff} = 5100\,{\rm K}$, $\log g = 2.2$, $[{\rm Fe/H}] = -3.0$ and $[\alpha/{\rm Fe}] = +0.4$ in our analysis to compare the effects of scattering between 3D hydrodynamical and 1D hydrostatic atmospheres. The 1D model is converted into a 3D cube with zero gas velocity, horizontally homogeneous layers and with the same T-τ_{5000} relation; line formation is computed using the exact same method as in the 3D case.

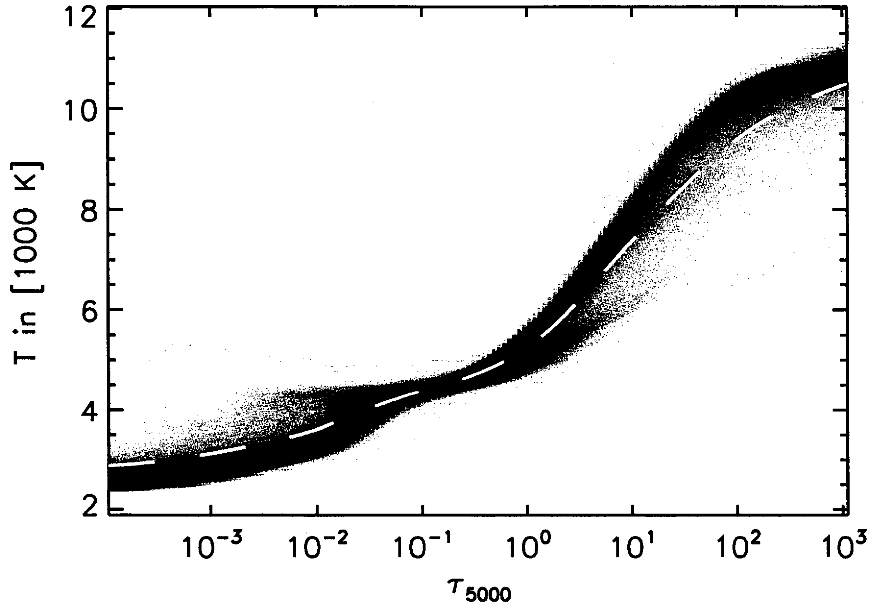

Figure 7.1: Temperature distribution as a function of vertical continuum optical depth τ at 5000 Å, computed for an arbitrary snapshot of a 3D radiation-hydrodynamical model atmosphere with $T_{\rm eff} = (5100 \pm 14)\,{\rm K}$, $\log g = 2.2$ (cgs) and $[{\rm Fe/H}] = -3.0$. The dashed line indicates the average temperature at each optical depth.

7.4 3D line formation computations

Synthetic continuum flux and line flux profiles are calculated using the SCATE code. The program first computes the monochromatic continuum source function with coherent isotropic scattering using a short characteristics-based radiative transfer solver with Gauss-Seidel-type approximate Λ-iteration (Trujillo Bueno and Fabiani Bendicho, 1995). A detailed description of the implementation can be found in Appendix D and in Hayek et al. (2010). Continuum opacities and photon destruction probabilities are looked up in precomputed tables, line opacities are calculated during runtime. All quantities assume the LTE approximation.

The numerical method takes Doppler-shifts of line profiles into account, which influence absorption and line-to-continuum photon emission probabilities as a function of ray direction, gas velocity and frequency according to Eq. (7.4). Including this inherent coupling is essential for correctly predicting the impact of scattering on the local radiation field and consequently on the profile shapes (see Sect. 7.6). A minimum resolution in solid angle and frequency is furthermore needed to reproduce the effects of Doppler-shifts. For the case of continuum scattering with LTE lines in late-type stellar atmospheres, where gas flow reaches only moderate velocities, Carlson (1963) quadrature with 24 ray directions provides sufficient accuracy; computing radiative transfer with 48 angles changes the spatially averaged flux level by $\lesssim 0.3\,\%$. Carlson quadrature also has the advantage of rotational invariance, which avoids directional bias for determining the local mean radiation field J_ν. Line profiles for synthetic curves of growth are computed with typically 40 frequency points. We use linear interpolation of (linear) quantities between the grid of the model atmosphere and the characteristics grid, as well as for the source function integral in the optically thin regime. Second-order interpolation is applied to the source function integral in optically thick regions to correctly recover the diffusion approximation.

Once the continuum source function has converged, it is passed to a second radiative transfer solver, which computes outgoing specific intensities on characteristics that span across the entire 3D atmosphere cube. This method has the advantage of reduced numerical diffusion with respect to the short characteristics method when angle-resolved surface intensities are needed. Local cubic interpolation translates the relevant quantities onto the tilted characteristics grid. The radiative transfer equation is then solved along vertical columns using the Feautrier (1964) method to obtain surface intensities.

The grid resolution of the model atmosphere is an important issue for 3D line formation calculations (see the discussion in Asplund et al., 2000a). The axis spacing in the vertical dominates the accuracy of the solution, due to the strong temperature gradients near the stellar surface. Our calculations are based on a mesh with 120 × 120 × 230 grid points, and we refine the vertical grid by automatic insertion of additional layers where needed to obtain robust intensity and flux profiles. Computation of the scattering source function excludes the deepest layers of the 3D model atmosphere, which are optically thick and dominated by local thermal radiation. The Feautrier-type solver starts at a continuum optical depth $\log_{10}\tau^{\mathrm{c}} \approx 2$ on each individual ray to integrate the entire contribution function of continuum and line emission.

Stellar spectroscopy measures the radiative flux integrated over the stellar disk in most cases of interest. The monochromatic flux $F_{\nu,z}$ that leaves the surface on the visible hemisphere into the observer's direction is given by

$$F_{\nu,z} = \int_{\mu=0}^{1} \int_{\phi=0}^{2\pi} \langle I_\nu \rangle \, (\mu,\phi)\mu d\mu d\phi, \tag{7.6}$$

where $\mu \equiv \cos\theta$ is the projection factor, θ is the polar angle, ϕ is the azimuth angle and $\langle I_\nu \rangle$ is the horizontal average surface intensity of the simulation cube. The 3D hydrodynamical model atmospheres are interpreted as local statistical representations of stellar surface convection. Each angle pair (μ, ϕ) for which radiative transfer is computed in the 3D cube corresponds to a different position on the disk. The flux integral (Eq. (7.6)) is thus equivalent to an integral over the stellar surface as seen by the observer; $F_{\nu,z}$ thereby automatically includes the limb darkening effect. Including stellar rotation in 3D spectral line formation computations requires additional consideration (Ludwig, 2007), we therefore assume zero rotation ($v \sin i = 0$) for simplicity.

We approximate the flux integral (Eq. (7.6)) using Gauss-Legendre quadrature for the polar angle and the trapezoid rule for the azimuth angle; 4 × 4 ray angles reproduce the surface flux with good accuracy. Doubling the number of polar angles or azimuth angles changes the spatial average flux level by $\lesssim 0.4\,\%$.

7.5 The effects of scattering on the continuum flux

We first seek to determine the wavelength range in which continuum scattering contributes sufficient opacity to influence continuum flux levels. Radiative transfer is computed with scattering

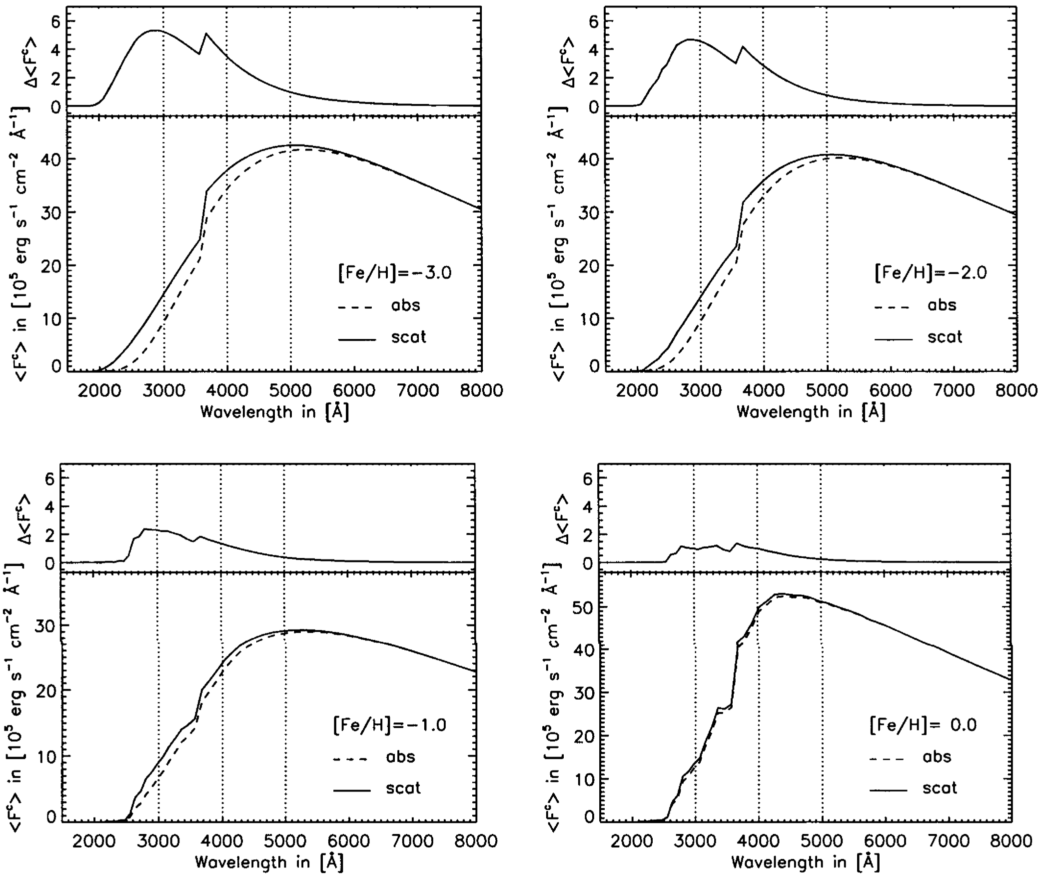

Figure 7.2: Spatial and temporal averages of the continuum flux distribution $\langle F^{\mathrm{c}} \rangle$ as a function of wavelength, computed for time sequences of the model atmospheres with metallicity $-3.0 \leq [\mathrm{Fe/H}] \leq 0.0$ (upper left to lower right), treating scattering as absorption (dashed lines) and as coherent scattering (solid lines). The upper panel of each plot shows the deviation $\Delta \langle F^{\mathrm{c}} \rangle$ of the coherent scattering cases from the continuum flux distribution where scattering is treated as absorption; vertical dotted lines indicate $\lambda = 3000$ Å, 4000 Å and 5000 Å where Fe line profiles were computed. Note the Balmer jump at 3647 Å.

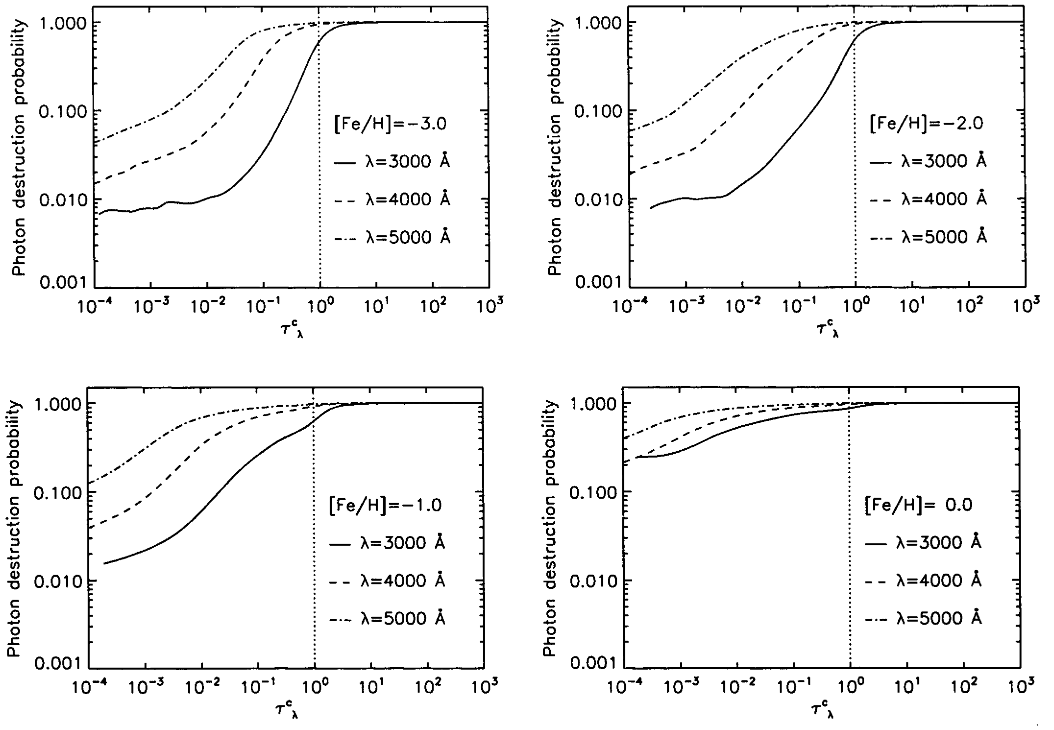

Figure 7.3: Continuum photon destruction probabilities for arbitrary snapshots of the model atmosphere with [Fe/H] = -3.0 (upper left panel), [Fe/H] = -2.0 (upper right panel), [Fe/H] = -1.0 (lower left panel), and [Fe/H] = 0.0 (lower right panel), averaged over surfaces of constant monochromatic continuum optical depth τ^c_λ for wavelengths $\lambda = 3000\,\text{Å}$ (solid lines), $\lambda = 4000\,\text{Å}$ (dashed lines) and $\lambda = 5000\,\text{Å}$ (dot-dashed lines). The monochromatic optical surfaces at $\tau^c_\lambda = 1$ are marked by vertical dotted lines.

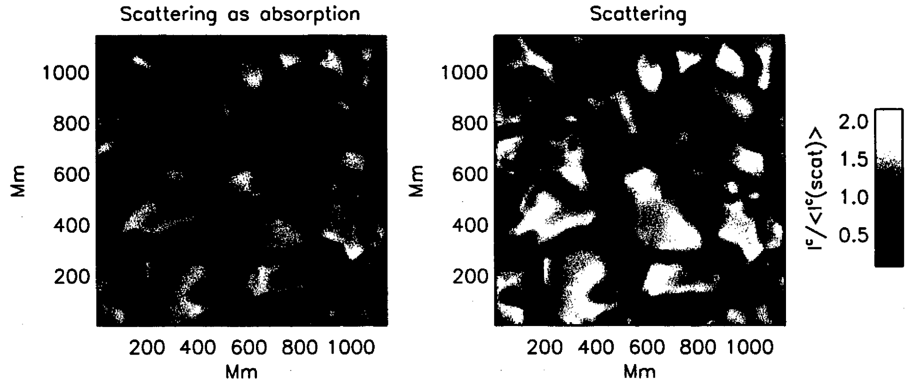

Figure 7.4: Continuum surface intensities in the disk center at 3000 Å computed for an arbitrary snapshot of the [Fe/H] = -3.0 model, treating scattering as absorption (left panel) and as coherent scattering (right panel). Intensities are normalized to the average continuum intensity with coherent scattering.

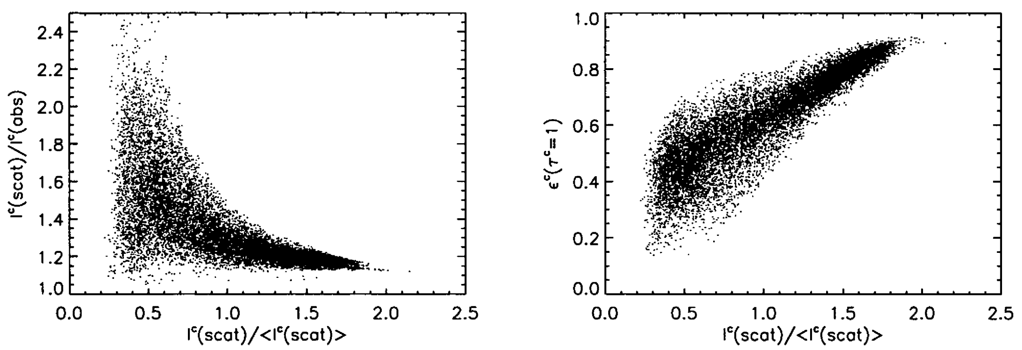

Figure 7.5: *Left:* Correlation between the continuum intensity ratio $I^{\mathrm{c}}(\mathrm{scat})/I^{\mathrm{c}}(\mathrm{abs})$ and the normalized continuum intensities with scattering $I^{\mathrm{c}}(\mathrm{scat})/\left\langle I^{\mathrm{c}}(\mathrm{scat})\right\rangle$ at 3000 Å, computed for an arbitrary snapshot of the $[\mathrm{Fe/H}] = -3.0$ model. *Right:* Correlation between the continuum photon destruction probabilities ϵ^{c} at the local monochromatic continuum optical surface $\tau^{\mathrm{c}} = 1$ and the normalized continuum intensities with scattering $I^{\mathrm{c}}(\mathrm{scat})/\left\langle I^{\mathrm{c}}(\mathrm{scat})\right\rangle$ at 3000 Å for the same model.

opacity treated as absorption and as coherent scattering for a set of wavelength points with logarithmic distribution in the range $1500\,\text{Å} \leq \lambda \leq 8000\,\text{Å}$, taking only continuum opacity into account; Fig. 7.2 shows the resulting flux distributions for the different model atmospheres (see Table 7.1 for stellar parameters). It is clear that continuum scattering is only significant in the UV in all cases, where Rayleigh scattering on H I atoms is mostly responsible for the increased flux levels compared with the case of treating scattering as absorption; the λ^{-4}-dependence of the Rayleigh cross-section and thermalizing bound-free transitions of primarily various metals at shorter wavelengths limit the spectral range. Scattering is therefore completely negligible in the infrared.

Continuum scattering evidently increases the thermalization depth in the UV, as a significant fraction $(1 - \epsilon^{\mathrm{c}})$ of outward streaming photons from deeper, hotter layers is scattered instead of absorbed. Figure 7.3 shows the vertical variation of photon destruction probabilities $\left\langle\epsilon^{\mathrm{c}}\right\rangle$ in arbitrary snapshots of the model atmospheres, averaged over surfaces of constant vertical continuum optical depth τ^{c} at the three wavelength points indicated by vertical dotted lines in Fig. 7.2. For the $[\mathrm{Fe/H}] = -3.0$ model (upper left panel of Fig. 7.3), all photons that interact with the gas above optical depth $\tau^{\mathrm{c}}_{\lambda} \gtrsim 10$ are absorbed and thermalize. At 3000 Å, the atmosphere becomes slightly translucent before the optical surface $(\tau^{\mathrm{c}}_{\lambda} = 1)$ is reached, allowing photons to escape from larger depths than in the case where scattering is treated as absorption, while photons at 4000 Å and 5000 Å are still trapped. Higher up in the atmosphere, scattering becomes increasingly important at all wavelengths. Photon destruction probabilities grow with metallicity, but exhibit only weak variation at the optical surface for the models with $[\mathrm{Fe/H}] < 0.0$. The lower effective temperature of the $[\mathrm{Fe/H}] = -1.0$ model reduces ϵ^{c} above the surface relative to the other model atmospheres due to the temperature-dependence of absorption opacity (see the discussion below). At $[\mathrm{Fe/H}] = 0.0$, absorption dominates almost everywhere in the photosphere and beneath.

Note the effect of the H I $(n = 2)$ bound-free absorption edge at 3647 Å (the so-called Balmer jump), which causes a depression in the continuum flux on the blue side. Absorption through photoionization increases the photon destruction probability and moves the thermalization depth outward into cooler layers, causing a spike in the flux deviation $\Delta\left\langle F^{\mathrm{c}}\right\rangle$ (upper panels of the plots in Fig. 7.2).

The granulation flow in 3D radiation-hydrodynamical simulations produces strong horizontal variations of the outward radiative intensities between the hot, bright granules and the cool, dark intergranular lanes. The left panel in Fig. 7.4 shows continuum intensities in the stellar disk center at 3000 Å, computed with scattering as absorption for an arbitrary snapshot of the $[\mathrm{Fe/H}] = -3.0$ model. The shapes of granules and intergranular lanes are similar to solar granulation, but extend to much larger spatial scales (see Collet et al., 2007). Note that radiative emission in the dark intergranular lanes is comparatively small but nonzero, which is important for the formation of line profiles (see the discussion in Sect. 7.6). The right panel in Fig. 7.4 shows disk center continuum intensities computed with scattering; both panels in Fig. 7.4 are normalized to the same average intensity. While the overall morphology of the granulation pattern is almost identical, the surface intensities appear slightly brighter due to the larger thermalization depth of the coherent scattering case.

The left panel of Fig. 7.5 quantifies the spatially resolved intensity ratio of the scattering and absorption calculations, showing the correlation with continuum surface intensities; the darker intergranular lanes gain more brightness in proportion to their intensity than the brighter granules. The reason for this variation is the temperature dependence of the continuum photon destruction probabilities ϵ^{c}, visible in their correlation with continuum intensity at local optical surfaces ($\tau^{\mathrm{c}} = 1$) in each column of the model atmosphere (right panel of Fig. 7.5): Rayleigh scattering cross-sections are independent of temperature if the gas is cool enough that hydrogen is dominantly neutral, Rayleigh opacity is therefore very similar at continuum optical surfaces in granules and lanes. Contrary to that, thermalizing opacity varies strongly with temperature. Absorption is thus dominant in hot granules, while scattering opacity is important in lanes. The result is a larger thermalization depth with respect to the optical surfaces in the lanes compared to granules and a relatively stronger intensity gain through scattering. The overall contrast in the continuum surface intensities reduces through scattering: while the horizontal average continuum intensity $\langle I^{\mathrm{c}} \rangle$ at 3000 Å of the snapshot shown in Fig. 7.4 increases by $\approx 27\,\%$ with respect to treating scattering as absorption, the relative rms variation at this wavelength decreases from $I^{\mathrm{c}}_{\mathrm{rms}} / \langle I^{\mathrm{c}} \rangle = 0.51$ to $I^{\mathrm{c}}_{\mathrm{rms}} / \langle I^{\mathrm{c}} \rangle = 0.43$ when coherent scattering is included in the radiative transfer computation.

7.6 Spectral line formation with a scattering continuum

We now add spectral lines from different atomic and molecular species to the continuum opacities. It is sufficient to restrict the wavelength range to $3000\,\text{Å} \leq \lambda \leq 5000\,\text{Å}$, in which radiative flux is accessible for measurements with current instruments and in which continuum scattering is important, as it was demonstrated in Sect. 7.5. The profile broadening in all Fe line formation computations assumes the Unsöld (1955) approximation for collisions with neutral hydrogen for simplicity, although the SCATE code includes tabulated collisional cross-sections based on quantum-mechanical calculations for many species and transitions (see Appendix D). No collisional broadening was applied to molecular line profiles.

7.6.1 Fe I lines at 3000 Å and metallicity [Fe/H]=-3.0

The effects of a background scattering continuum are demonstrated by analyzing the formation of fictitious Fe I lines at 3000 Å in the atmosphere of the $[\mathrm{Fe/H}] = -3.0$ model. The left panel of Fig. 7.6 shows spatial averages of disk-center intensity profiles of a low-excitation ($\chi = 0\,\mathrm{eV}$) transition, where scattering opacity is treated as absorption (dashed line) and as coherent scattering (solid line). Line core brightness increases along with the continuum in the spatial average profile. The right panel of Fig. 7.6 shows the same profiles normalized to their individual aver-

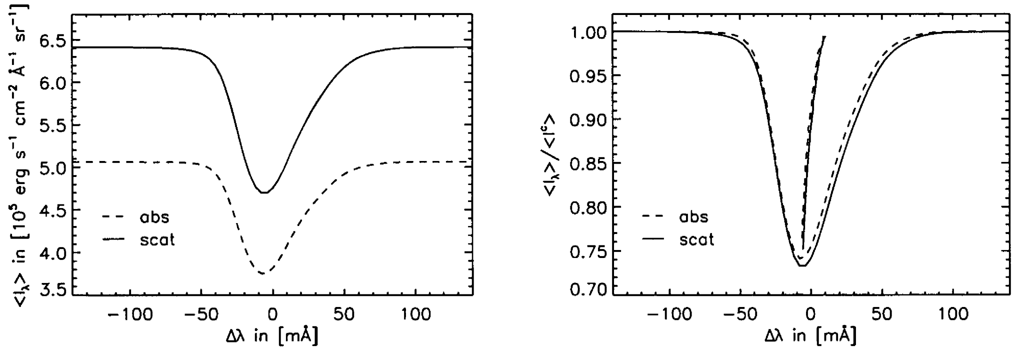

Figure 7.6: Spatial averages of disk-center intensity profiles (left panel) and normalized disk-center intensity profiles with bisectors (right panel) of a fictitious low-excitation ($\chi = 0$ eV) Fe I line plotted as functions of wavelength shift $\Delta\lambda$ in mÅ with $\lambda_0 = 3000$ Å, computed for an arbitrary snapshot of the [Fe/H] $= -3.0$ model with coherent continuum scattering (solid lines) and treating scattering as absorption (dashed lines).

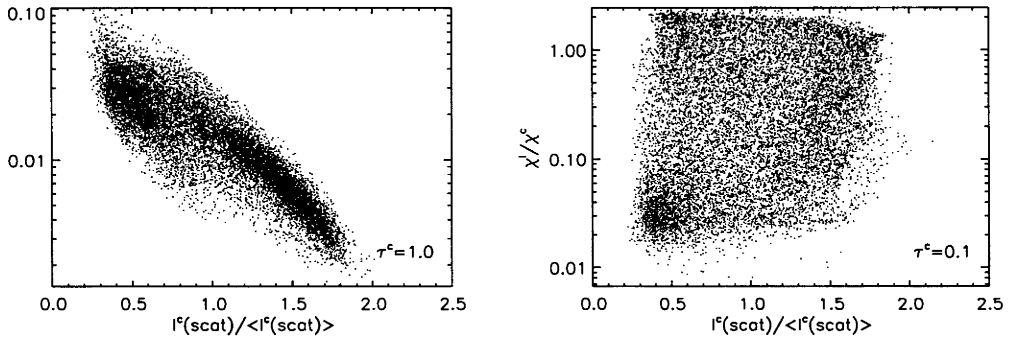

Figure 7.7: Correlation between wavelength-integrated line-to-continuum opacity ratios $\chi^{\mathrm{l}}/\chi^{\mathrm{c}}$ and normalized continuum intensities $I^{\mathrm{c}}(\mathrm{scat})/\left\langle I^{\mathrm{c}}(\mathrm{scat})\right\rangle$ at the continuum optical surface $\tau^{\mathrm{c}} = 1$ (left panel), and at continuum optical depth $\tau^{\mathrm{c}} = 0.1$ (right panel) for the Fe I line of Fig. 7.6.

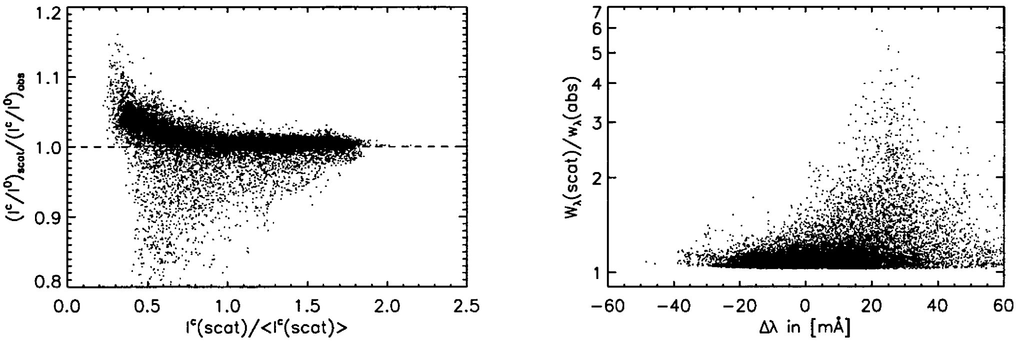

Figure 7.8: Correlation between the growth of continuum-to-line core intensity ratios $(I^{\mathrm{c}}/I^{0})_{\mathrm{scat}}/(I^{\mathrm{c}}/I^{0})_{\mathrm{abs}}$ through scattering and normalized continuum intensities $I^{\mathrm{c}}(\mathrm{scat})/\left\langle I^{\mathrm{c}}(\mathrm{scat})\right\rangle$ (left panel), as well as between the growth of equivalent widths $W_\lambda(\mathrm{scat})/W_\lambda(\mathrm{abs})$ through scattering and the line shift $\Delta\lambda_0$ (right panel) for the Fe I line of Fig. 7.6.

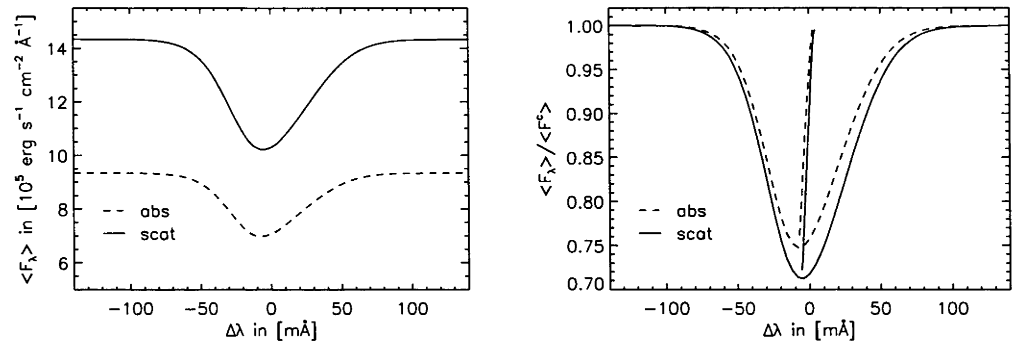

Figure 7.9: Spatial averages of flux profiles (left panel) and normalized flux profiles with bisectors (right panel) of the Fe I line of Fig. 7.6.

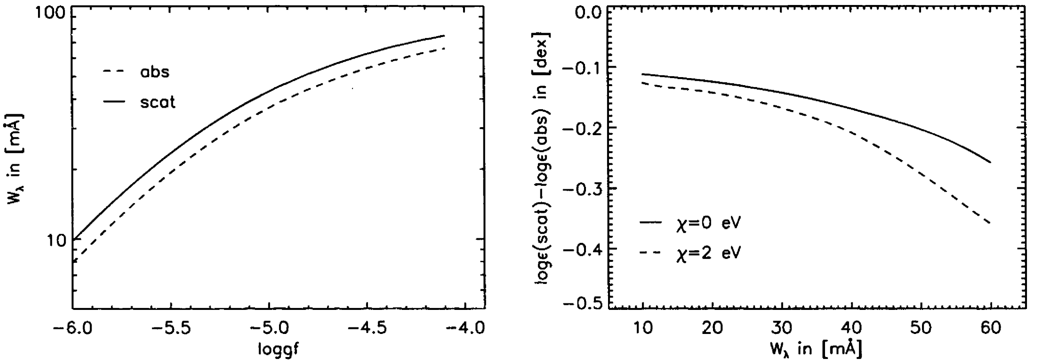

Figure 7.10: *Left:* Curves of growth for the Fe I line of Fig. 7.9 as a function of oscillator strength $\log gf$, computed with scattering as absorption (dashed line) and as coherent scattering (solid line). *Right:* Corresponding abundance corrections as a function of equivalent width W_λ for the curves of growth shown in the left panel where $\chi = 0\,\mathrm{eV}$ (solid line), and for a Fe I line with $\chi = 2\,\mathrm{eV}$ (dashed line).

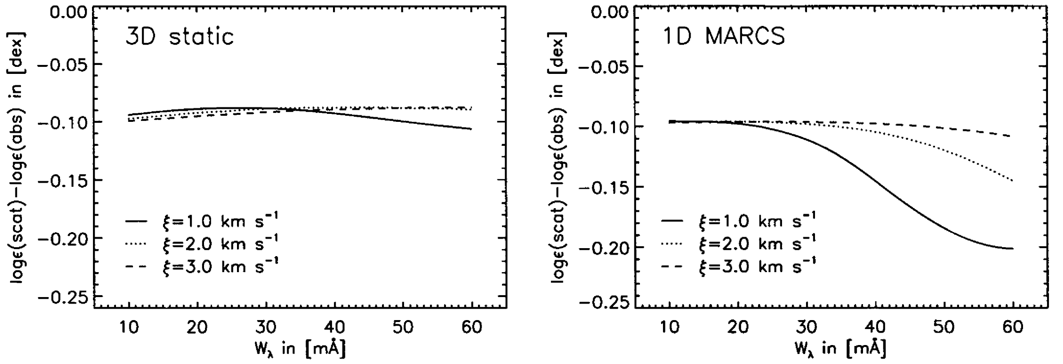

Figure 7.11: Abundance corrections for the same Fe I line as shown in Fig. 7.9, but computed for the [Fe/H] $= -3.0$ model with velocity fields set to zero (left panel) and with a 1D hydrostatic MARCS model (right panel), assuming microturbulent broadening with $\xi = 1.0\,\mathrm{km\,s^{-1}}$ (solid lines), $\xi = 2.0\,\mathrm{km\,s^{-1}}$ (dotted lines), and $\xi = 3.0\,\mathrm{km\,s^{-1}}$ (dashed lines).

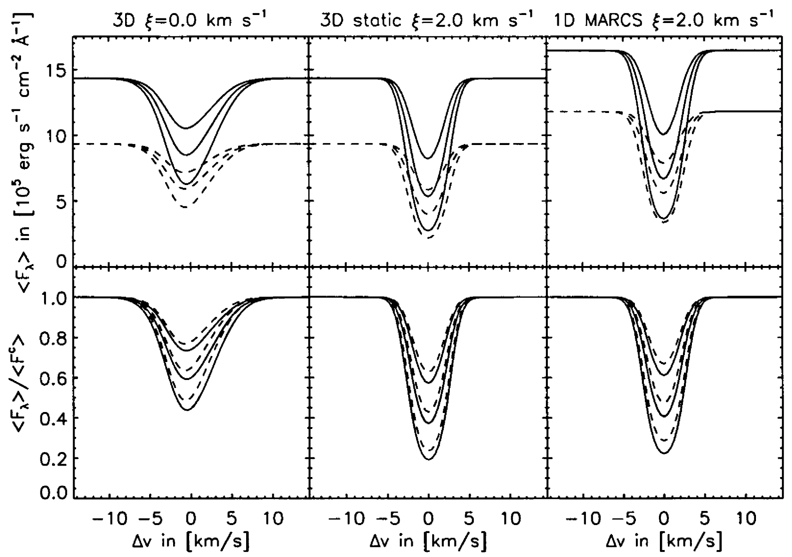

Figure 7.12: Spatial averages of Fe I flux profiles at 3000 Å as functions of Doppler shift Δv from the line center, computed treating scattering as absorption (dashed lines) and as coherent scattering (solid lines) using the 3D [Fe/H] $= -3.0$ model (left column), the 3D [Fe/H] $= -3.0$ model with velocity fields set to zero (3D static model, center column) and the 1D hydrostatic MARCS model (right column). The bottom row shows normalized profiles. The 3D static model and the 1D model assume microturbulent broadening with $\xi = 2.0\,\mathrm{km\,s^{-1}}$; line strengths of the 1D calculations were increased by +0.7 dex to obtain similar equivalent widths (see text).

age continuum intensity, as well as the line bisectors in the profile centers. Line depth increases when scattering is included, and the profile bisector shifts to slightly longer wavelengths. Note the characteristic C-shape of the bisector, a consequence of spatial dominance of the upflowing gas in the bright granules, which causes blueshifts in the emitted light (e.g., Dravins, 1982).

The depression of line core intensity in the normalized profile through continuum scattering stems from thermalization through line absorption. If line opacity is significant in continuum-forming layers, the thermalization depth of the radiation field moves outward into cooler parts of the atmosphere, since the joint photon destruction probability ϵ_ν of continuum and line opacity is larger than the continuum photon destruction probability ϵ^{c}:

$$\epsilon_\nu = \frac{\chi^{\mathrm{l}}_\nu}{\chi^{\mathrm{l}}_\nu + \chi^{\mathrm{c}}} + \frac{\chi^{\mathrm{c}}}{\chi^{\mathrm{l}}_\nu + \chi^{\mathrm{c}}}\epsilon^{\mathrm{c}} = \frac{\chi^{\mathrm{l}}_\nu + \kappa^{\mathrm{c}}}{\chi^{\mathrm{l}}_\nu + \chi^{\mathrm{c}}} \geq \epsilon^{\mathrm{c}}; \qquad (7.7)$$

line opacity χ^{l}_ν is treated as absorption in our computations. The radiation temperature in the deeper parts of the line contribution function decreases towards the lower local gas temperature, and the line core gains less brightness through scattering than the continuum. Normalization turns this disproportional growth into a deeper line profile. If line opacity is not significant in continuum-forming layers, line core brightness increases along with the continuum through the contribution from scattered photons, and the intensity gain is mostly divided out when the line profile is normalized.

Both magnitude and height-dependence of the line opacity thus determine the importance of continuum scattering for line formation: the ability of lines to thermalize the radiation field grows with χ^{l}_ν; the opacity contribution of low-excitation lines of neutral atoms such as the Fe I line in Fig. 7.6 is biased towards higher atmospheric layers (compare the distribution of line-to-continuum opacity ratios $\chi^{\mathrm{l}}/\chi^{\mathrm{c}}$ at the continuum optical surface $\tau^{\mathrm{c}} = 1.0$ and at $\tau^{\mathrm{c}} = 0.1$ in

Fig. 7.7), such species therefore have a weaker effect on the thermalization depth in continuum-forming layers. High-excitation lines exert larger influence, as the exponential temperature-dependence of the Boltzmann excitation equilibrium moves their opacity contribution closer to $\tau^{c} = 1.0$.

The growth of continuum-to-line core intensity ratios through scattering correlates with normalized continuum intensity across the stellar surface (left panel in Fig. 7.8): in the hot granules, lines gain less strength since line opacity is relatively small and continuum absorption relatively large in continuum-forming layers (left panel of Fig. 7.7 and right panel of Fig. 7.5), and both continua and cores increase in brightness (left panels of Fig. 7.5 and Fig. 7.8). In the cool intergranular lanes, continua gain more intensity than the cores since line opacity plays a more important role in thermalizing the radiation field.

The spatial dependence of line growth is translated into wavelength space as Doppler-shifts change sign between the upflowing gas in granules and downflowing gas in intergranular lanes. The right panel of Fig. 7.8 shows the correlation between the growth of equivalent widths W_λ through scattering and wavelength shifts $\Delta\lambda_0$ of the individual line profiles in each column. We define $\Delta\lambda_0$ through the deviation of the intensity profile bisector at half-depth from the center wavelength λ_0,

$$\Delta\lambda_0 = \frac{1}{2}\left(\lambda_{\mathrm{hd}}^{\mathrm{blue}} - \lambda_{\mathrm{hd}}^{\mathrm{red}}\right), \tag{7.8}$$

since the 3D velocity field may produce blended profiles with multiple minima in some columns. The stronger gains in line strength in the intergranular lanes are shifted towards larger wavelengths, causing the red wing of the normalized profile to appear relatively darker.

The flux profiles in Fig. 7.9 demonstrate that the effects of scattering also become stronger towards the limb: continuum optical surfaces move outward into cooler layers with smaller continuum photon destruction probability (see Fig. 7.3), which increases the brightness gain in the continuum and therefore produces stronger lines (right panel of Fig. 7.9) through the absorption mechanism that was discussed above.

We quantify the impact of scattering on flux profiles by computing synthetic curves of growth, treating scattering as absorption (dashed line in the left panel of Fig. 7.10) and as coherent scattering (solid line). The deeper profiles of the scattering case lead to larger equivalent widths W_λ. The distance between the two curves at each W_λ defines a logarithmic abundance correction[2]

$$\Delta \log \epsilon \equiv \log \epsilon(\mathrm{scat}) - \log \epsilon(\mathrm{abs}); \tag{7.9}$$

the solid line in the right panel of Fig. 7.10 shows the result. As larger thermalization of the radiation field near line core wavelengths produces increasingly deeper flux profiles, saturation in the curve of growth is delayed and stronger lines exhibit larger abundance corrections. $\Delta \log \epsilon$ also grows with excitation level χ of the transition (dashed line in the right panel of Fig. 7.10): larger line opacity in continuum-forming layers leads to abundance corrections of up to -0.4 dex at $W_\lambda = 60\,\mathrm{m\AA}$.

It is instructive to compare this result with lines that form in a 3D atmosphere with zero gas velocities and in a 1D hydrostatic MARCS model atmosphere. Missing broadening through convective motion is replaced by microturbulent broadening with $\xi = 1.0\,\mathrm{km\,s^{-1}}$, $\xi = 2.0\,\mathrm{km\,s^{-1}}$ and $\xi = 3.0\,\mathrm{km\,s^{-1}}$. Oscillator strengths for the calculations with the 1D model were increased by 0.7 dex for this $\chi = 0$ eV Fe I line to obtain approximately the same range of equivalent widths as in the 3D cases. The adjustment compensates for weaker line strength, which stems from the much shallower temperature gradient above the surface of the 1D model compared to

---

[2] In spectroscopic notation, $\log \epsilon(\mathrm{A}) \equiv \log_{10}(N_\mathrm{A}/N_\mathrm{H}) + 12.0$, where N_A and N_H are the number densities of species A and hydrogen

the 3D atmosphere; low-excitation transitions at low metallicity are particularly affected (see Collet et al., 2007). In the absence of Doppler-shifts, profiles are exactly symmetric (center column and right column of Fig. 7.12). Resulting abundance corrections are shown in Fig. 7.11. In the 3D static case, emission from granules and intergranular lanes is no longer separated in wavelength. At low microturbulence $\xi = 1.0\,\mathrm{km\,s^{-1}}$, the line profiles saturate earlier compared to the 3D case with velocity field. Desaturation through scattering effects is reduced as granules dominate the radiative flux, resulting in a weaker dependence of $\Delta \log \epsilon$ on line strength (solid line in the left panel of Fig. 7.11). Increasing microturbulent broadening delays saturation of line profiles in the scattering and absorption cases, extending the linear part of the curve of growth, and $\Delta \log \epsilon$ is almost constant (dotted line and dashed line in the left panel of Fig. 7.11). The weakest lines at $W_\lambda = 10\,\mathrm{m\AA}$ are independent from microturbulent broadening and yield approximately the same abundance corrections for all values of ξ.

The 1D MARCS model exhibits similar effects of scattering at the lowest equivalent widths. Abundance corrections are larger for stronger lines compared to the 3D case, reaching -0.2 dex at $W_\lambda = 60\,\mathrm{m\AA}$ for $\xi = 1.0\,\mathrm{km\,s^{-1}}$ due to the different atmospheric structure and the $+0.7$ dex adjustment of line opacity (right panel of Fig. 7.11). Increasing microturbulence desaturates both the absorption and scattering line profiles and weakens the dependence of $\Delta \log \epsilon$ on line strength.

7.6.2 Curves of growth for Fe I and Fe II lines

We compute abundance corrections for fictitious Fe I and Fe II lines with excitation potentials $\chi = 0\,\mathrm{eV}$ and $\chi = 2\,\mathrm{eV}$ at 3000 Å, 4000 Å and 5000 Å and for all models to investigate the dependence on ionization stage, excitation potential, wavelength and metallicity. Figure 7.13 shows the results for the $[\mathrm{Fe/H}] = -3.0$ model. As expected from the discussion in Sect. 7.6.1, we find the largest $\Delta \log \epsilon$ for the strongest high-excitation Fe II lines at 3000 Å, where thermalizing opacity becomes most important in continuum-forming layers near line core frequencies and desaturation has the strongest effect. Abundance corrections reach $\Delta \log \epsilon \approx -0.5$ dex at $W_\lambda = 60\,\mathrm{m\AA}$ (dot-dashed line in the upper left panel of Fig. 7.13). The corrections become less severe for neutral species and lower excitation levels. At 4000 Å (upper right panel), scattering effects are still significant; strong Fe II lines reach $\Delta \log \epsilon \approx -0.1$ dex at $W_\lambda = 60\,\mathrm{m\AA}$. At 5000 Å (lower left panel), scattering is negligible with $\Delta \log \epsilon \approx -0.02$ dex at $W_\lambda = 60\,\mathrm{m\AA}$, which is smaller than typical abundance measurement errors.

The results for the $[\mathrm{Fe/H}] = -2.0$ model and the $[\mathrm{Fe/H}] = -1.0$ model exhibit similar behavior as scattering opacity is equally important for continuum formation (Fig. 7.2 and Fig. 7.3). Abundance corrections are again largest for both metallicities at 3000 Å and for the strongest high-excitation Fe II lines, reaching $\Delta \log \epsilon \approx -0.4$ dex at $W_\lambda = 60\,\mathrm{m\AA}$. The smaller effective temperature of the $[\mathrm{Fe/H}] = -1.0$ leads to relatively larger scattering effects compared to the other models (see Sect. 7.5).

The situation changes at solar metallicity ($[\mathrm{Fe/H}] = 0.0$): scattering is weak around the optical surface at all wavelengths (lower right panel of Fig. 7.3), leading to generally smaller abundance corrections. At 3000 Å, $\Delta \log \epsilon$ reaches only -0.1 dex for the strongest high-excitation Fe II lines and only -0.03 dex at small equivalent widths. At 4000 Å and 5000 Å, scattering can be neglected.

7.6.3 Curves of growth for molecular lines

Spectral lines from molecules are important tools for abundance measurements of carbon, nitrogen and oxygen in metal-poor stars. Computing synthetic line profiles and curves of growth requires solving a set of equilibrium equations to obtain population numbers of the different atoms and molecules (see Appendix D). In late-type stellar atmospheres, simple molecules such as carbon monoxide (CO), the hydrides CH, NH and OH and cyanide (CN) form in sufficiently cool layers. CH, OH and NH molecules have observable transitions in the blue and UV wavelength regions. We follow Collet et al. (2007) and compute synthetic curves of growth for typical molecular lines at 3150 Å (OH), 3360 Å (NH) and 4360 Å (CH).

The resulting abundance corrections for the [Fe/H] $= -3.0$ model are shown in the lower right panel of Fig. 7.13. We find the largest scattering effect for the OH line due to its short wavelength, reaching -0.13 dex for the strongest lines (dashed line in the lower right panel of Fig. 7.13). NH lines at 3360 Å exhibit a slightly smaller abundance correction (dotted line) with $\Delta \log \epsilon = -0.10$ dex; CH lines at 4360 Å experience only weak influence from continuum scattering (solid line). The magnitude of $\Delta \log \epsilon$ for molecular lines is very similar to Fe I lines, as molecules form mostly in higher, cooler layers of the atmosphere.

The abundance corrections of molecular lines at [Fe/H] $= -2.0$ are equally large as for the most metal-poor model, but they become less severe at [Fe/H] $= -1.0$ where the OH correction reduces to -0.09 dex at $W_\lambda = 60$ Å. $\Delta \log \epsilon$ is almost negligible at [Fe/H] $= 0.0$, except for the strongest OH features which reach a correction of -0.04 dex.

Note that we vary oscillator strengths instead of elemental abundances to calculate the curve of growth. The resulting correction $\Delta \log \epsilon$ is therefore an approximation, as shifts in the molecular equilibria are not taken into account. Decreasing $\log \epsilon(\mathrm{O})$ by 0.13 dex in the [Fe/H] $= -3.0$ model and increasing $\log gf$ by the same amount leads to a deviation of the resulting equivalent widths of $\lesssim 2\,\%$, the systematic errors in the abundance corrections of Fig. 7.13 through Fig. 7.16 are therefore small.

7.7 Conclusions

We investigate the effects of a scattering background continuum on spectral line formation based on 3D radiation-hydrodynamical model atmospheres of giant stars with different metallicity. Continuum scattering is treated in the coherent and isotropic approximation; opacities assume LTE. We compute radiative transfer using the SCATE line formation code to determine synthetic continuum flux levels and line flux profiles of fictitious Fe I and Fe II lines between $3000\,\text{Å} \leq \lambda \leq 5000\,\text{Å}$, as well as selected CH, NH and OH molecular transitions.

Rayleigh scattering contributes significant opacity in the blue and UV wavelength bands, allowing photons to escape from larger atmospheric depths compared to the case of treating scattering as absorption. As a consequence, the continuum surface flux increases between 2000 Å and 5000 Å, while scattering is negligible in the infrared and at the shortest wavelengths, where photoionization processes thermalize the radiation field. The strongest relative brightness gain is observed in intergranular lanes, where scattering opacity is more important and photon destruction probabilities near the optical surface are smaller compared with the hot granules.

Continuum scattering affects the strength of LTE lines, depending on ionization stage, excitation potential, wavelength and metallicity. If a line contributes significant absorption opacity in continuum-forming layers, the thermalization depth near line core frequencies moves outward into cooler layers and the core gains less brightness through scattering than the continuum. Normalization of the flux profiles translates this disproportional intensity gain into a deepening of the line. We find the largest effects at the lowest metallicity, the shortest wavelengths, for singly ionized lines and for higher excitation levels, where continuum scattering is strongest and line opacity is significant in continuum-forming layers. The temperature contrast across the stellar surface results in differential line growth, as intergranular lanes experience a stronger scattering effect than granules. Doppler-shifts reverse sign between granules and intergranular lanes, translating spatial variation into wavelength space. The red wing of the lines thus ap-

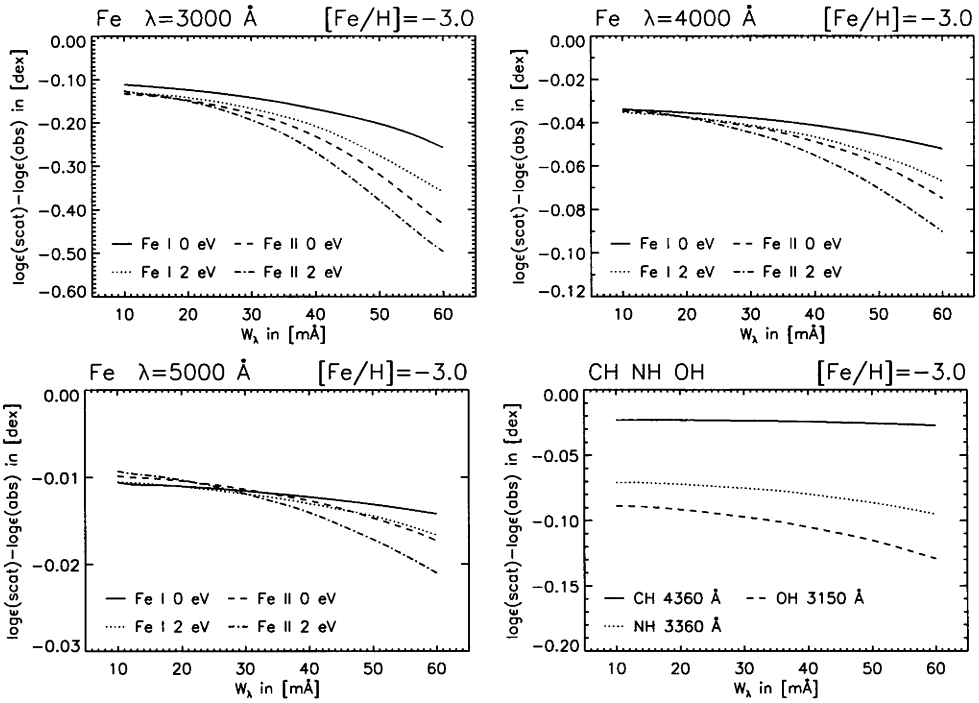

Figure 7.13: *Upper left panel to lower left panel:* Abundance corrections for fictitious Fe I lines and Fe II lines with excitation potential $\chi = 0\,\mathrm{eV}$ and $\chi = 2\,\mathrm{eV}$ at 3000 Å, 4000 Å and 5000 Å, computed for the [Fe/H] = −3.0 model. *Lower right panel:* Abundance corrections for typical CH, NH and OH lines for the same model.

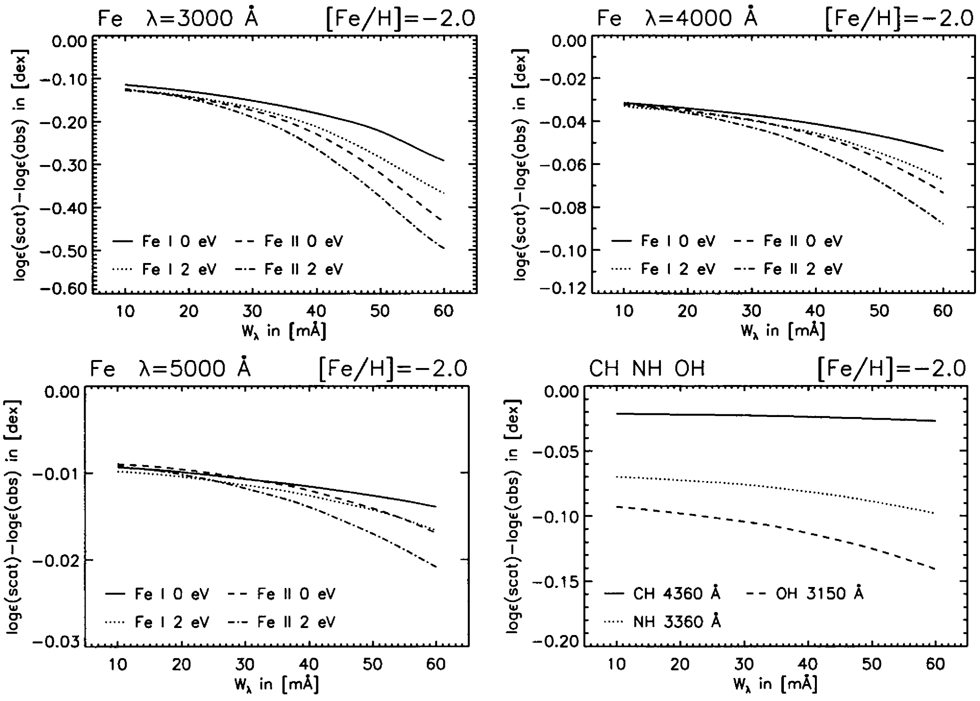

Figure 7.14: Same as Fig. 7.13, but computed with the [Fe/H] = −2.0 model.

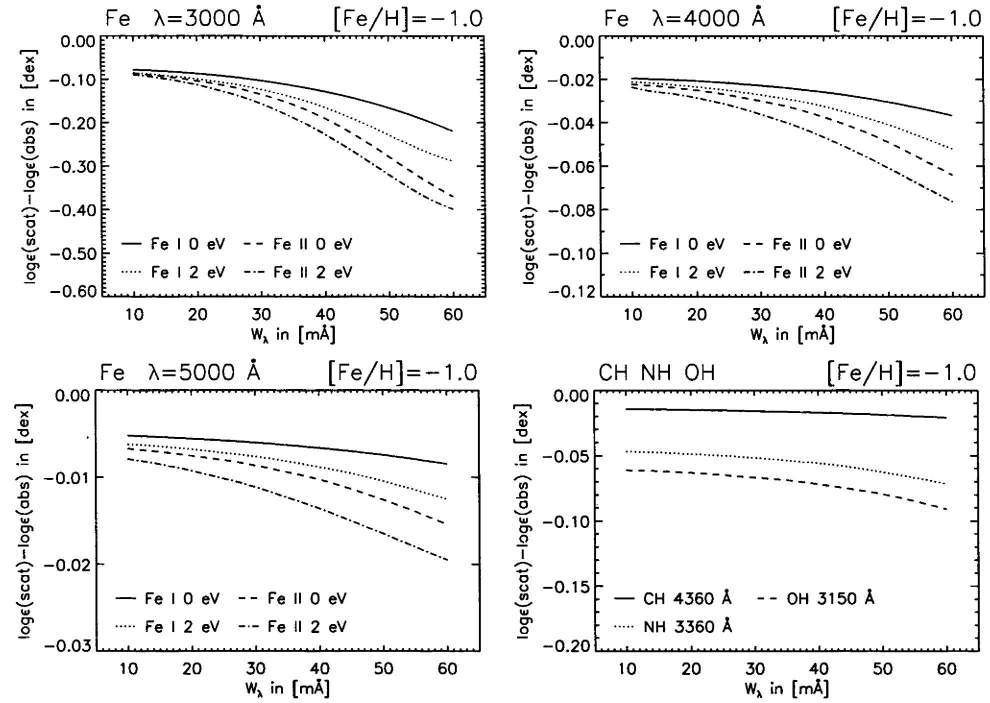

Figure 7.15: Same as Fig. 7.13, but computed with the [Fe/H] = −1.0 model.

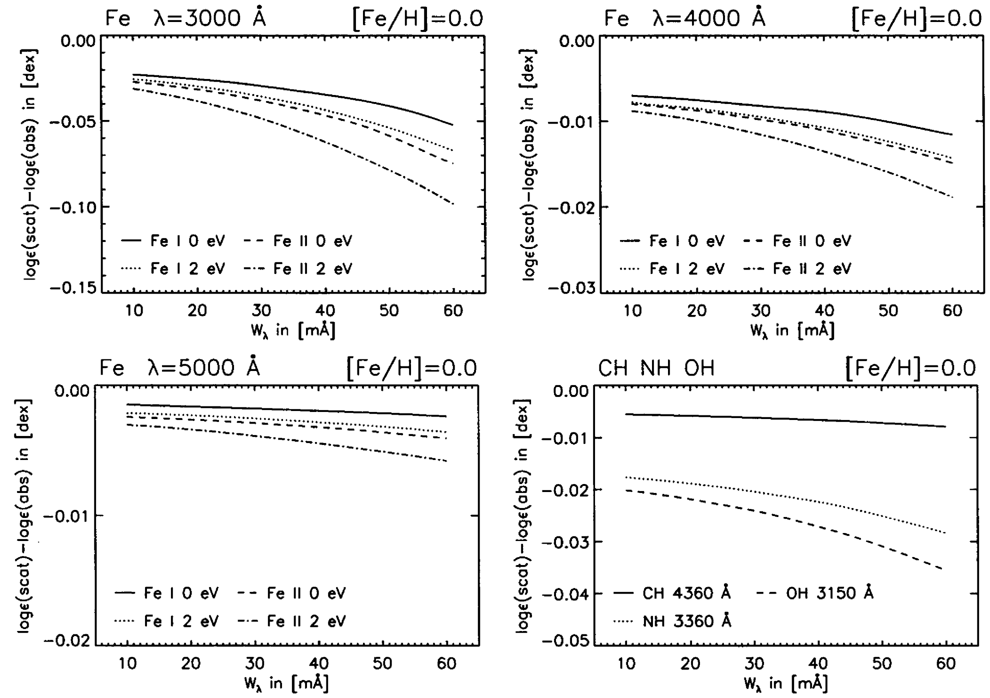

Figure 7.16: Same as Fig. 7.13, but computed with the [Fe/H] = 0.0 model. Note the different scaling of the vertical axes.

pears relatively darker than the blue wing, and the line center shifts slightly towards longer wavelengths.

We quantify the importance of continuum scattering by comparing synthetic curves of growth using scattering radiative transfer and treating scattering as absorption. Increasing line strength through scattering desaturates line profiles, leading to a growing deviation between the curves of growth for stronger lines. Transformed into an abundance correction for given equivalent width, we find up to ≈ -0.5 dex deviation for Fe II with $\chi = 2$ eV at 3000 Å and [Fe/H] $= -3.0$. At 4000 Å, the effects of scattering on line abundances are much smaller and only significant for the strongest lines; at 5000, Å, scattering can be neglected. Transitions of the CH, NH and OH molecules behave in an analogous way to neutral low-excitation atomic lines; the strongest abundance corrections appear at the shortest wavelengths. Scattering effects weaken towards higher metallicity as continuous absorption opacity becomes increasingly important; abundance corrections at solar metallicity ([Fe/H] $= 0.0$) only reach -0.1 dex for the strongest lines at 3000 Å, while they are practically negligible for weaker lines and at longer wavelengths.

The importance of velocity fields for line formation in the given wavelength range is tested by comparing the results with a 3D atmosphere with zero velocities and artificial microturbulent line broadening. In the absence of Doppler-shifts through the granulation flow, the line profiles become symmetric and saturate earlier for small microturbulence. The desaturating effect of scattering is weaker as granules dominate the emission, where photon destruction probabilities are larger, resulting in smaller abundance corrections. We repeat the analysis for a 1D hydrostatic MARCS model with [Fe/H] $= -3.0$ and find a similar result; abundance corrections for low-exctiation Fe I lines at 3000 Å reach ≈ -0.2 dex, depending on the microturbulence parameter.

Chemical abundance analyses of metal-poor giant stars that include spectral lines in the UV and blue regions should take background continuum scattering into account. Convective velocity fields change the profile shapes, which shift towards slightly longer wavelengths and produce larger abundance corrections for stronger lines compared to a 1D hydrostatic model; it is therefore important to conduct abundance analyses based on 3D radiation-hydrodynamical model atmospheres.

Our investigation assumes coherent isotropic scattering, neglecting redistribution of radiation through Doppler-shifts, which should only have a small effect on the synthetic line profiles. The LTE approximation is a more severe limitation: non-LTE effects, such as photoionization, are known to be important in metal-poor stars and need to be considered for a quantitative analysis of stellar line profiles (for a discussion, see Asplund, 2005).

Acknowledgements. The authors would like to thank R. Trampedach and T. M. D. Pereira for their contributions to the SCATE line formation code, opacity tables and atomic data sets. M. Carlsson and P. Barklem are thanked for their advice and fruitful discussions.

Chapter 8

Summary and outlook

Radiation-hydrodynamics

The field of 3D radiation-hydrodynamical simulations of late-type stellar atmospheres has experienced continuous growth in the last decade, as the availability of large-scale parallel computers enabled simulations of unprecedented complexity and physical realism. The success of realistic 3D models of the solar surface in reproducing different observations will support this development and the acceptance of model predictions.

The simulations in this PhD thesis use an enhanced 3D radiative transfer model with coherent photon scattering to explore its importance for the atmospheres of late-type stars. It was demonstrated in Chapter 4 that continuum scattering is weak in solar-type stars and therefore insignificant for their temperature structure; scattering opacity may be treated as absorption to very good approximation. However, simulations of higher atmospheric layers in the Sun require a scattering source function for a more realistic description of line-blanketing. Treating line scattering opacity as absorption strongly reduces radiative heating timescales, leading to a shallower temperature gradient and smaller thermal fluctuations above the photosphere, while the temperature structure steepens towards an adiabatic gradient when scattering is included; the mean temperature difference reaches $\langle \Delta T \rangle \approx 350\,\mathrm{K}$ in the highest layers. Line-blanketing with scattering is thus an important ingredient for realistic models of the solar chromosphere and corona (see also the discussion in Skartlien, 2000).

Rayleigh scattering on neutral hydrogen is an significant continuous opacity source for metal-poor giant stars, owing to their more dilute atmospheres and smaller absorption opacity compared to the Sun. By comparing 3D radiation-hydrodynamical simulations that treat continuum scattering as absorption with coherent scattering radiative transfer simulations, it was shown in Chapter 5 that the mean temperatures above the surface increase by approximately $\langle \Delta T \rangle \approx 1000\,\mathrm{K}$ in the absorption case at the lowest metallicity ($[\mathrm{Fe/H}] = -3.0$) and thus exhibit a shallower gradient. The effect is smaller at $[\mathrm{Fe/H}] = -2.0$, where the deviation reaches $\langle \Delta T \rangle \approx 300\,\mathrm{K}$. Test calculations indicate that coherent continuum scattering can be approximated with reasonable accuracy by ignoring scattering opacity above the optical surface and using a Planck source function. This simplification significantly reduces the computational expense of the radiative transfer calculations, as the source function only depends on local gas temperatures and an iterative computation of the radiation field is unnecessary.

Despite this improvement of the radiative transfer model, the accuracy is still limited by the assumption of LTE for computing opacities and emissivities. Departures from LTE populations could be important for radiative heating: analyses of non-LTE effects in 1D hydrostatic models by Anderson (1989) and by Short and Hauschildt (2005) indicate that mechanisms such as over-ionization of iron group elements with respect to Saha equilibria play an important role and result in significantly higher temperatures above the surface. It is not immediately clear how these departures from LTE will affect the stratification in the 3D case, where the radiative equilibrium condition is replaced with the hydrodynamical energy equation and dynamical effects need to be considered. First efforts to include non-equilibrium physics in the treatment of hydrogen ionization in the solar atmosphere have been presented by Leenaarts and Wedemeyer-Böhm (2006) and Leenaarts et al. (2007). Implementing consistent atomic models in 3D radiation-hydrodynamical simulations will provide a great challenge in terms of problem complexity and computational requirements, even if only the most important elements and transitions are considered.

The strong frequency dependence of opacities is still an important issue for time-dependent 3D model atmospheres: the opacity binning method that was briefly outlined in Sect. 4.2.2 reduces the computational load dramatically, sorting millions of spectral lines into a small number of opacity bins, but the approximation limits the accuracy of the temperature structure and cannot include the effects of velocity fields (see, e.g., the discussion in Vögler et al., 2004). A more detailed treatment using, e.g., opacity distribution functions (ODFs) or the opacity sampling technique, which is the current standard for 1D hydrostatic models (e.g. Gustafsson et al., 2008), could in principle by applied. However, opacity sampling requires a spectral resolution of $\sim$ 100000 wavelength points, resulting in very large computational load when applied to 3D time-dependent radiation-hydrodynamics. Recent developments in high-performance computing, such as parallel execution on Graphics Processing Units (GPUs) and the rapidly increasing performance of large-scale cluster computers may soon provide the necessary resources to enable more realistic spectrum integration.

The analysis of very cool objects, such as brown dwarfs and extrasolar planets, offers new exciting possibilities for research based on 3D radiation-hydrodynamical simulations. Their complex chemistry includes the formation of abundant molecules and dust, requiring some sophistication of the hydrodynamics treatment (e.g., Freytag et al., 2010), and non-equilibrium physics in the equation of state. Global models are needed for studying atmospheric circulation in irradiated extrasolar planets, to understand heat transport and the surface temperature distribution. Radiative transfer in such simulations has traditionally been treated using simple approximations such as Newtonian cooling, and only recently have first attempts been made to include a more realistic description of radiation effects (Showman et al., 2009). Detailed 3D radiation-hydrodynamical simulations have the capacity to provide new insight into atmospheric physics of irradiated exoplanets, in particular the strongly irradiated "Hot Jupiters", and they could be used as well to analyze effects of radiation on the Earth's climate.

An interesting development for the numerical solution of the radiative transfer equation in 3D are finite element methods (Kanschat, 1996; Richling et al., 2001), which can handle unstructured meshes naturally. They are highly suitable for situations where adaptive mesh refinement is desirable, such as simulations of giant stars with very low surface gravity, which exhibit large disparity in the resolution of hydrodynamical and radiative transfer length scales (see Sect. 4.3.3).

Spectral line formation

In the field of 3D spectral line formation, many advances have been made in the last years: complex numerical codes such as `MULTI3D` have become available, accompanied by an increasing amount of accurate data to support establishing detailed atomic models. Owing to the complexity of the problem, only a comparatively small number of studies has been presented in the literature, such as line formation analyses in the Sun and lithium abundance measurements in metal-poor stars. The importance of 3D effects and 3D non-LTE effects still needs to be explored for a large variety of cases.

The formation of LTE spectral lines with background continuum scattering in 3D radiation-hydrodynamical simulations of red giant stars was described in Chapter 7. It was demonstrated that continuum scattering deepens the line profile through a difference in thermalization depth between the core and the continuum if line opacity and continuous scattering opacity are important in continuum-forming layers. Gains in line strength desaturate the profile and lead to significant abundance corrections, derived from synthetic curves of growth. The effect is most pronounced at low metallicity, at the shortest wavelengths and for the strongest lines. High-excitation transitions and lines from ionized atoms produce larger corrections, as they form closer to the continuum optical surface and thus have a stronger effect on the radiation field. The gas velocities predicted by 3D radiation-hydrodynamical models further increase the scattering effect by separating emission from granules and intergranular lanes in frequency. Abundance corrections reach $\Delta \log \epsilon = -0.5$ dex for $\chi = 2$ eV Fe II lines at 3000 Å and $[\mathrm{Fe/H}] = -3.0$, while they become insignificant above $\lambda \gtrsim 5000$ Å and for solar metallicity.

The analysis should be extended to the 3D non-LTE case, to include scattering in the line and departures of level populations from LTE predictions through interaction with other transitions of the same element and photoionization. The effects can be large (e.g., Asplund et al., 2003), and detailed investigations with 3D non-LTE line formation may help solving outstanding problems, e.g., related to the chemical evolution of the Galaxy. The importance of magnetic fields for stellar abundance analyses also requires further exploration. Modern radiation-magneto-hydrodynamics codes such as `BIFROST` enable detailed simulations of magnetic phenomena at the solar surface surface, such as flux tubes, sun spots or coronal heating. Magnetic fields can change the temperature structure of the atmosphere, as well as the line profile through the Zeeman effect, and thereby affect chemical abundance measurements (Fabbian et al., 2010).

Abundance analyses of late-type stars based on 3D radiation-hydrodynamical model atmospheres are not yet commonplace: line formation in 3D is computationally more demanding, and widespread application requires a grid of 3D model atmospheres that covers a large range of stellar parameters. Such grids are currently being constructed at the Max Planck Institute for Astrophysics and other institutes (see Ludwig et al., 2009). The development time needed to create a 3D model atmosphere is significantly longer than 1D models, as each change of stellar parameters requires relaxation of the stratification to a quasi-steady state before the model can be used for analyses. Ongoing efforts will nevertheless soon provide large atmosphere data sets, offering a wide range of applications: besides improving the realism of stellar abundance analyses, they can be used to produce template spectra for automated determination of stellar parameters, for synthetic photometry, to investigate stellar oscillations in the field of asteroseismology etc.. Such astrophysical research in 3D will require fast and user-friendly tools to exploit the data: a spectral line formation code such as `SCATE` or `ASSεT` (Koesterke, 2009) could be combined with a web-based user interface to allow online spectral diagnostics and abundance measurements, making 3D models easily accessible for non-experts in radiation-hydrodynamics.

It is clear that 3D radiation-hydrodynamical simulations will play a key role in answering important questions in the field of stellar and planetary atmospheres. The development of sophisticated computational methods and analysis techniques, as well as the validation of the models through observations, will offer exciting research possibilities for astrophysicists and scientists from related fields in the near future.

Bibliography

C. Allende Prieto, M. Asplund, R. J. García López, and D. L. Lambert. Signatures of Convection in the Spectrum of Procyon: Fundamental Parameters and Iron Abundance. *ApJ*, 567: 544–565, March 2002.

A. C. Allison and A. Dalgarno. Photodissociation of Vibrationally Excited H_2, HD, and D_2 by Absorption into the Continua of the Lyman and Werner Systems. *AD*, 1:91, 1969.

L. S. Anderson. Line blanketing without local thermodynamic equilibrium. II - A solar-type model in radiative equilibrium. *ApJ*, 339:558–578, April 1989.

S. D. Anstee and B. J. O'Mara. Width cross-sections for collisional broadening of s-p and p-s transitions by atomic hydrogen. *MNRAS*, 276:859–866, October 1995.

M. Asplund. New Light on Stellar Abundance Analyses: Departures from LTE and Homogeneity. *ARA&A*, 43:481–530, September 2005.

M. Asplund and A. E. García Pérez. On OH line formation and oxygen abundances in metal-poor stars. *A&A*, 372:601–615, June 2001.

M. Asplund, Å. Nordlund, R. Trampedach, and R. F. Stein. 3D hydrodynamical model atmospheres of metal-poor stars. Evidence for a low primordial Li abundance. *A&A*, 346:17–20, June 1999.

M. Asplund, H.-G. Ludwig, Å. Nordlund, and R. F. Stein. The effects of numerical resolution on hydrodynamical surface convection simulations and spectral line formation. *A&A*, 359: 669–681, July 2000a.

M. Asplund, Å. Nordlund, R. Trampedach, C. Allende Prieto, and R. F. Stein. Line formation in solar granulation. I. Fe line shapes, shifts and asymmetries. *A&A*, 359:729–742, July 2000b.

M. Asplund, M. Carlsson, and A. V. Botnen. Multi-level 3D non-LTE computations of lithium lines in the metal-poor halo stars HD 140283 and HD 84937. *A&A*, 399:31–34, March 2003.

M. Asplund, N. Grevesse, and A. J. Sauval. The Solar Chemical Composition. In T. G. Barnes and F. N. Bash, editors, *Cosmic Abundances as Records of Stellar Evolution and Nucleosynthesis*, volume 336 of *ASP Conf. Ser.*, page 25, September 2005.

M. Asplund, N. Grevesse, A. J. Sauval, and P. Scott. The Chemical Composition of the Sun. *ARA&A*, 47:481–522, September 2009.

L. Auer. Formal Solution: EXPLICIT Answers. In I. Hubeny, D. Mihalas, and K. Werner, editors, *Stellar Atmosphere Modeling*, volume 288 of *ASP Conf. Ser.*, page 3, January 2003.

L. H. Auer and D. Mihalas. Line Formation with Non-Coherent Scattering by Electrons. I. Parameterized Models. *ApJ*, 153:245, July 1968a.

L. H. Auer and D. Mihalas. Line Formation with Non-Coherent Scattering by Electrons. II. Calculations with Model Atmospheres. *ApJ*, 153:923, September 1968b.

T. R. Ayres and L. Testerman. Fourier Transform Spectrometer observations of solar carbon monoxide. I - The fundamental and first overtone bands in the quiet sun. *ApJ*, 245:1124–1140, May 1981.

P. S. Barklem and J. Aspelund-Johansson. The broadening of Fe II lines by neutral hydrogen collisions. *A&A*, 435:373–377, May 2005.

P. S. Barklem and B. J. O'Mara. The broadening of p-d and d-p transitions by collisions with neutral hydrogen atoms. *MNRAS*, 290:102–106, September 1997.

P. S. Barklem and B. J. O'Mara. Comments on alternative calculations of the broadening of spectral lines of neutral sodium by H-atom collisions. *Journal of Physics B Atomic Molecular Physics*, 34:4785–4799, December 2001.

P. S. Barklem, B. J. O'Mara, and J. E. Ross. The broadening of d-f and f-d transitions by collisions with neutral hydrogen atoms. *MNRAS*, 296:1057–1060, June 1998.

P. S. Barklem, N. Piskunov, and B. J. O'Mara. A list of data for the broadening of metallic lines by neutral hydrogen collisions. *A&AS*, 142:467–473, March 2000a.

P. S. Barklem, N. Piskunov, and B. J. O'Mara. Self-broadening in Balmer line wing formation in stellar atmospheres. *A&A*, 363:1091–1105, November 2000b.

M. A. Bautista. Atomic data from the IRON Project. XX. Photoionization cross-sections and oscillator strengths for Fe I. *A&AS*, 122:167–176, April 1997.

M. A. Bautista. Atomic data from the Iron Project. XXXIX. Photoionization cross-sections and oscillator strengths for N I II. *A&AS*, 137:529–535, June 1999.

T. C. Beers and N. Christlieb. The Discovery and Analysis of Very Metal-Poor Stars in the Galaxy. *ARA&A*, 43:531–580, September 2005.

N. T. Behara, P. Bonifacio, H.-G. Ludwig, L. Sbordone, J. I. González Hernández, and E. Caffau. Three carbon-enhanced metal-poor dwarf stars from the SDSS. Chemical abundances from CO^{5}BOLD 3D hydrodynamical model atmospheres. *A&A*, 513:72, April 2010.

K. L. Bell. The free-free absorption coefficient of the negative ion of molecular hydrogen. *J. Phys. B*, 13:1859–1865, May 1980.

K. L. Bell and K. A. Berrington. Free-free absorption coefficient of the negative hydrogen ion. *J. Phys. B*, 20:801–806, February 1987.

K. L. Bell, A. Hibbert, and K. A. Berrington. The free-free absorption coefficient of the negative carbon ion. *J. Phys. B*, 21:2319–2325, June 1988.

M. Bergemann and T. Gehren. NLTE abundances of Mn in a sample of metal-poor stars. *A&A*, 492:823–831, December 2008.

G. Bihain, G. Israelian, R. Rebolo, P. Bonifacio, and P. Molaro. Cu and Zn in the early Galaxy. *A&A*, 423:777–786, September 2004.

K.-H. Böhm. Die Temperaturschichtung der Sonnenatmosphäre im nichtgrauen Strahlungsgleichgewicht. Mit 8 Textabbildungen. *ZAp*, 34:182, 1954.

A. Borysow, U. G. Jørgensen, and Y. Fu. High temperature (1000-7000 K) collision induced absorption of H_2 pairs computed from the first principles, with application to cool and dense stellar atmospheres. *JQSRT*, 68(235), 2001.

A. Brandenburg. *Computational aspects of astrophysical MHD and turbulence*, volume Advances in Nonlinear Dynamics, page 269. Taylor and Francis Group, 2003.

J. T. Broad and W. P. Reinhardt. One- and two-electron photoejection from H^-: A multichannel J-matrix calculation. *Phys. Rev. A*, 14:2159–2173, December 1976.

J. H. M. J. Bruls, P. Vollmöller, and M. Schüssler. Computing radiative heating on unstructured spatial grids. *A&A*, 348:233–248, August 1999.

E. Caffau, H.-G. Ludwig, M. Steffen, T. R. Ayres, P. Bonifacio, R. Cayrel, B. Freytag, and B. Plez. The photospheric solar oxygen project. I. Abundance analysis of atomic lines and influence of atmospheric models. *A&A*, 488:1031–1046, September 2008.

C. J. Cannon. Frequency-Quadrature Perturbations in Radiative-Transfer Theory. *ApJ*, 185: 621–630, October 1973.

B. G. Carlson. *Statistical Physics*, volume 1 of *Methods in Computational Physics*, chapter 1. Academic Press, New York and London, 1963.

M. Carlsson and R. F. Stein. Formation of Solar Calcium H and K Bright Grains. *ApJ*, 481:500, May 1997.

M. Carlsson, R. J. Rutten, J. H. M. J. Bruls, and N. G. Shchukina. The non-LTE formation of Li I lines in cool stars. *A&A*, 288:860–882, August 1994.

R. Cayrel, E. Depagne, M. Spite, V. Hill, F. Spite, P. François, B. Plez, T. Beers, F. Primas, J. Andersen, B. Barbuy, P. Bonifacio, P. Molaro, and B. Nordström. First stars V - Abundance patterns from C to Zn and supernova yields in the early Galaxy. *A&A*, 416:1117–1138, March 2004.

R. Cayrel, M. Steffen, H. Chand, P. Bonifacio, M. Spite, F. Spite, P. Petitjean, H.-G. Ludwig, and E. Caffau. Line shift, line asymmetry, and the ^{6}Li/^{7}Li isotopic ratio determination. *A&A*, 473:37–40, October 2007.

S. Chandrasekhar. The radiative equilibrium of the outer layers of a star, with special reference to the blanketing effect of the reversing layer. *MNRAS*, 96:21, November 1935.

R. Collet, M. Asplund, and R. Trampedach. Three-dimensional hydrodynamical simulations of surface convection in red giant stars. Impact on spectral line formation and abundance analysis. *A&A*, 469:687–706, July 2007.

W. Däppen, D. Mihalas, D. G. Hummer, and B. W. Mihalas. The equation of state for stellar envelopes. III - Thermodynamic quantities. *ApJ*, 332:261–270, September 1988.

R. O. Doyle. The Astrophysical Significance of the Continuous Spectrum of the Hydrogen Quasi-Molecule. *ApJ*, 153:987, September 1968.

D. Dravins. Photospheric spectrum line asymmetries and wavelength shifts. *ARA&A*, 20:61–89, 1982.

D. Dravins and Å. Nordlund. Stellar Granulation - Part Five - Synthetic Spectral Lines in Disk Integrated Starlight. *A&A*, 228:203, February 1990.

M. Eidelsberg, J.-Y. Roncin, A. Le Floch, F. Launay, C. Letzelter, and J. Rostas. Reinvestigation of the vacuum ultraviolet spectrum of CO and isotopicspecies: the $B^1\Sigma^+$ downarrow $X^1\Sigma^+$ transition. *Journal of Molecular Spectroscopy*, 121:309–336, 1987.

D. Fabbian, E. Khomenko, F. Moreno-Insertis, and Å. Nordlund. Solar abundance corrections derived through 3D magnetoconvection simulations. *ArXiv e-prints*, June 2010.

P. Feautrier. Sur la résolution numérique de l'equation de transfert. *Comptes Rendus Académie des Sciences (série non spécifiée)*, 258:3189, 1964.

B. Freytag, M. Steffen, and B. Dorch. Spots on the surface of Betelgeuse – Results from new 3D stellar convection models. *Astronomische Nachrichten*, 323:213–219, July 2002.

B. Freytag, F. Allard, H.-G. Ludwig, D. Homeier, and M. Steffen. The role of convection, overshoot, and gravity waves for the transport of dust in M dwarf and brown dwarf atmospheres. *A&A*, 513:A19, April 2010.

F. N. Fritsch and J. Butland. A method for constructing local monotone piecewise cubic interpolants. *SIAM J. Sci. Stat. Comput.*, 5(2):300, June 1984.

M. Gavrila. Elastic Scattering of Photons by a Hydrogen Atom. *Physical Review*, 163:147–155, November 1967.

J. P. Goedbloed and S. Poedts. *Principles of Magnetohydrodynamics.* Cambridge University Press, 2004.

D. F. Gray. *The Observation and Analysis of Stellar Photospheres.* Cambridge University Press, September 2005.

B. V. Gudiksen and Å. Nordlund. An Ab Initio Approach to the Solar Coronal Heating Problem. *ApJ*, 618:1020–1030, January 2005.

B. Gustafsson, R. A. Bell, K. Eriksson, and Å. Nordlund. A grid of model atmospheres for metal-deficient giant stars. I. *A&A*, 42:407–432, September 1975.

B. Gustafsson, B. Edvardsson, K. Eriksson, U. G. Jørgensen, Å. Nordlund, and B. Plez. A grid of MARCS model atmospheres for late-type stars. I. Methods and general properties. *A&A*, 486:951–970, August 2008.

M. Gustafsson and L. Frommhold. Infrared Absorption Spectra of Collisionally Interacting He and H Atoms. *ApJ*, 546:1168–1170, January 2001.

M. Gustafsson and L. Frommhold. The H_2-H infrared absorption bands at temperatures from 1000 K to 2500 K. *A&A*, 400:1161–1162, March 2003.

V. H. Hansteen. Initial simulations spanning the upper convection zone to the corona. In A.V. Stepanov, E.E. Benevolenskaya, and E.G. Kosovichev, editors, *IAU Symp. 223: Multi Wavelength Investigations of Solar Activity*, pages 385–386, 2004.

V. H. Hansteen, M. Carlsson, and B. Gudiksen. 3D Numerical Models of the Chromosphere, Transition Region, and Corona. In P. Heinzel, I. Dorotovič, & R. J. Rutten, editor, *The Physics of Chromospheric Plasmas*, volume 368 of *ASP Conf. Ser.*, page 107, May 2007.

P. H. Hauschildt and E. Baron. A 3D radiative transfer framework. I. Non-local operator splitting and continuum scattering problems. *A&A*, 451:273–284, May 2006.

P. H. Hauschildt, F. Allard, and E. Baron. The NextGen Model Atmosphere Grid for $3000<=T_{\rm eff}<=10{,}000$ K. *ApJ*, 512:377–385, February 1999.

W. Hayek, U. Wiesendahl, N. Christlieb, K. Eriksson, A. J. Korn, P. S. Barklem, V. Hill, T. C. Beers, K. Farouqi, B. Pfeiffer, and K.-L. Kratz. The Hamburg/ESO R-process enhanced star survey (HERES). IV. Detailed abundance analysis and age dating of the strongly r-process enhanced stars CS 29491-069 and HE 1219-0312. *A&A*, 504:511–524, September 2009.

W. Hayek, M. Asplund, M. Carlsson, R. Trampedach, R. Collet, B. V. Gudiksen, V. H. Hansteen, and J. Leenaarts. Radiative transfer with scattering for domain-decomposed 3D MHD simulations of cool stellar atmospheres. Numerical methods and application to the quiet, non-magnetic, surface of a solar-type star. *A&A*, 517:49, July 2010.

T. Heinemann, W. Dobler, Å. Nordlund, and A. Brandenburg. Radiative transfer in decomposed domains. *A&A*, 448:731–737, March 2006.

H. Holweger. Ein empirisches Modell der Sonnenatmosphäre mit lokalem thermodynamischem Gleichgewicht. *ZAp*, 65:365, 1967.

H. Holweger and E. A. Müller. The photospheric barium spectrum - Solar abundance and collision broadening of Ba II lines by hydrogen. *Sol. Phys.*, 39:19–30, November 1974.

Y. Huang, S. A. Barts, and J. B. Halpern. Heat of formation of the cyanogen radical. *The Journal of Physical Chemistry*, 96(1):425–428, 1992.

A. K. Hui, B. H. Armstrong, and A. A. Wray. Rapid computation of the Voigt and complex error functions. *JQSRT*, 19(5):509 - 516, 1978.

D. G. Hummer and D. Mihalas. The equation of state for stellar envelopes. I - an occupation probability formalism for the truncation of internal partition functions. *ApJ*, 331:794–814, August 1988.

J. Hyman. A method of lines approach to the numerical solution of conservation laws. In R. Vichnevetsky and R. Stepleman, editors, *Advances in Computer Methods for Partial Differential Equations - III*, number 313-321 in Proceedings of the Third IMACS International Symposium on Computer Methods for Partial Differential Equations. IMACS, 1979.

A. W. Irwin. Polynomial partition function approximations of 344 atomic and molecular species. *ApJS*, 45:621–633, April 1981.

L. Jacoutot, A. G. Kosovichev, A. A. Wray, and N. N. Mansour. Numerical Simulation of Excitation of Solar Oscillation Modes for Different Turbulent Models. *ApJ*, 682:1386–1391, August 2008.

T. L. John. The continuous absorption coefficient of atomic and molecular negative ions. *MNRAS*, 172:305–311, August 1975.

T. L. John. The reliability of absorption coefficients for free-free transitions of the negative helium ion. *J. Phys. B*, 28:23–32, January 1995.

J. A. Johnson and M. Bolte. The s-Process in Metal-Poor Stars: Abundances for 22 Neutron-Capture Elements in CS 31062-050. *ApJ*, 605:462–471, April 2004.

U. G. Jørgensen, D. Hammer, A. Borysow, and J. Falkesgaard. The atmospheres of cool, helium-rich white dwarfs. *A&A*, 361:283–292, September 2000.

G. Kanschat. *Parallel and Adaptive Galerkin Methods for Radiative Transfer Problems*. PhD thesis, University of Heidelberg, 1996.

W. J. Karzas and R. Latter. Electron Radiative Transitions in a Coulomb Field. *ApJS*, 6:167, May 1961.

R. Kippenhahn and A. Weigert. *Stellar Structure and Evolution*. Springer, 1990.

D. Kiselman. Formation of Li I Lines in Photospheric Granulation. *ApJ*, 489:107, November 1997.

D. Kiselman and Å. Nordlund. 3D non-LTE line formation in the solar photosphere and the solar oxygen abundance. *A&A*, 302:578, October 1995.

L. Koesterke. Quantitative Spectroscopy in 3D. In I. Hubeny, J. M. Stone, K. MacGregor, & K. Werner, editor, *American Institute of Physics Conference Series*, volume 1171 of *American Institute of Physics Conference Series*, pages 73–84, September 2009.

P. Kunasz and L. H. Auer. Short characteristic integration of radiative transfer problems: formal solution in two-dimensional slabs. *JQSRT*, 39:67–79, 1988.

F. Kupka, N. Piskunov, T. A. Ryabchikova, H. C. Stempels, and W. W. Weiss. VALD-2: Progress of the Vienna Atomic Line Data Base. *A&AS*, 138:119–133, July 1999.

R. L. Kurucz. Model atmospheres for G, F, A, B, and O stars. *ApJS*, 40:1–340, May 1979.

R. L. Kurucz. A new opacity-sampling model atmosphere program for arbitrary abundances. In A. Wehlau, D. F. Gray, & J. Rice, editor, *Stellar Surface Structure*, volume 176 of *IAU Symposium*, page 523, 1996.

R. L. Kurucz, E. F. van Dishoeck, and S. P. Tarafdar. OH and CH continuous opacity in solar and stellar atmospheres. *ApJ*, 322:992–998, November 1987.

D. K. Lai, M. Bolte, J. A. Johnson, S. Lucatello, A. Heger, and S. E. Woosley. Detailed Abundances for 28 Metal-poor Stars: Stellar Relics in the Milky Way. *ApJ*, 681:1524–1556, July 2008.

P. W. Langhoff, J. Sims, and C. T. Corcoran. Stieltjes-integral approximations to photoabsorption and dispersion profiles in atomic helium. *Phys. Rev. A*, 10:829–841, September 1974.

J. Leenaarts and S. Wedemeyer-Böhm. Time-dependent hydrogen ionisation in 3D simulations of the solar chromosphere. Methods and first results. *A&A*, 460:301–307, December 2006.

J. Leenaarts, M. Carlsson, V. Hansteen, and R. J. Rutten. Non-equilibrium hydrogen ionization in 2D simulations of the solar atmosphere. *A&A*, 473:625–632, October 2007.

H.-G. Ludwig. *Nichtgrauer Strahlungstransport in numerischen Simulationen stellarer Konvektion.* PhD thesis, Universität Kiel, 1992.

H.-G. Ludwig. 3D spectral synthesis and rotational line broadening. *A&A*, 471:925–927, September 2007.

H.-G. Ludwig, E. Caffau, M. Steffen, B. Freytag, P. Bonifacio, and A. Kučinskas. The CIFIST 3D model atmosphere grid. *Mem. Soc. Astron. Italiana*, 80:711, 2009.

J. B. Marquette, C. Rebrion, and B. R. Rowe. Reactions of N^+ (^3P) ions with normal, para, and deuterated hydrogens at low temperatures. *J. Chem. Phys.*, 89:2041–2047, August 1988.

L. Mashonkina, G. Zhao, T. Gehren, W. Aoki, M. Bergemann, K. Noguchi, J. R. Shi, M. Takada-Hidai, and H. W. Zhang. Non-LTE line formation for heavy elements in four very metal-poor stars. *A&A*, 478:529–541, February 2008.

D. Mihalas. *Stellar atmospheres, 2nd edition.* W. H. Freeman and Co., San Francisco, 1978.

D. Mihalas and B. W. Mihalas. *Foundations of radiation hydrodynamics.* Oxford University Press, New York, 1984.

D. Mihalas, L. H. Auer, and B. R. Mihalas. Two-dimensional radiative transfer. I - Planar geometry. *ApJ*, 220:1001–1023, March 1978.

D. Mihalas, W. Däppen, and D. G. Hummer. The equation of state for stellar envelopes. II - Algorithm and selected results. *ApJ*, 331:815–825, August 1988.

D. Mihalas, D. G. Hummer, B. W. Mihalas, and W. Däppen. The equation of state for stellar envelopes. IV - Thermodynamic quantities and selected ionization fractions for six elemental mixes. *ApJ*, 350:300–308, February 1990.

E. A. Milne. Radiative equilibrium in the outer layers of a star. *MNRAS*, 81:361–375, March 1921.

H. J. Muthsam, B. Löw-Baselli, C. Obertscheider, M. Langer, P. Lenz, and F. Kupka. High-resolution models of solar granulation: the two-dimensional case. *MNRAS*, 380:1335–1340, October 2007.

H. J. Muthsam, F. Kupka, B. Löw-Baselli, C. Obertscheider, M. Langer, and P. Lenz. ANTARES - A Numerical Tool for Astrophysical RESearch with applications to solar granulation. *New Astronomy*, 15:460–475, July 2010.

S. N. Nahar. Electron-Ion Recombination Rate Coefficients for Si I, Si II, S II, S III, C II, and C-like Ions C i, N II, O III, F IV, Ne V, Na VI, Mg VII, Al VIII, Si IX, and S XI. *ApJS*, 101: 423, December 1995.

S. N. Nahar. Photoionization cross-sections and oscillator strengths for Fe III. *Phys. Rev. A*, 53: 1545–1552, March 1996.

S. N. Nahar. Photoionization cross-sections and oscillator strengths for oxygen ions: O I-O VII. *Phys. Rev. A*, 58:3766–3782, November 1998.

S. N. Nahar. Electron-Ion Recombination Rate Coefficients and Photoionization Cross-Sections for Astrophysically Abundant Elements. III. Si-Sequence Ions: Si I, S III, Ar V, Ca VII, and Fe XIII. *ApJS*, 126:537–550, February 2000.

S. N. Nahar. Relativistic photoionization cross-sections for C II. *Phys. Rev. A*, 65(5):052702, May 2002.

S. N. Nahar and A. K. Pradhan. Photoionization and electron-ion recombination - The carbon sequence. *Phys. Rev. A*, 44:2935–2948, September 1991.

S. N. Nahar and A. K. Pradhan. Atomic data for opacity calculations. XVIII. Photoionization and oscillator strengths of Si-like ions Si^0, S^{2+}, Ar^{4+}, Ca^{6+}. *Journal of Physics B Atomic Molecular Physics*, 26:1109–1127, March 1993.

S. N. Nahar and A. K. Pradhan. Atomic data for opacity calculations: XX. Photoionization cross-sections and oscillator strengths for Fe II. *Journal of Physics B Atomic Molecular Physics*, 27:429–446, February 1994a.

S. N. Nahar and A. K. Pradhan. Unified treatment of electron-ion recombination in the close-coupling approximation. *Phys. Rev. A*, 49:1816–1835, March 1994b.

S. N. Nahar and A. K. Pradhan. Electron-Ion Recombination Rate Coefficients, Photoionization Cross-Sections, and Ionization Fractions for Astrophysically Abundant Elements. I. Carbon and Nitrogen. *ApJS*, 111:339, July 1997.

Å. Nordlund. Numerical simulation of granular convection - Effects on photospheric spectral line profiles. In D. F. Gray and J. L. Linsky, editors, *IAU Colloq. 51: Stellar Turbulence*, volume 114 of *Lecture Notes in Physics, Berlin Springer Verlag*, pages 213–224, 1980.

Å. Nordlund. Numerical simulations of the solar granulation. I - Basic equations and methods. *A&A*, 107:1–10, March 1982.

Å. Nordlund and D. Dravins. Stellar granulation. III - Hydrodynamic model atmospheres. *A&A*, 228:155–217, February 1990.

Å. Nordlund and K. Galsgaard. A 3D MHD code for parallel computers. Technical report, Astronomical Observatory, Copenhagen University, 1995.

Å. Nordlund and R. F. Stein. Dynamics of an Radiative Transfer in Inhomogeneous Media. In *NATO ASIC Proc. 341: Stellar Atmospheres - Beyond Classical Models*, page 263, 1991.

Å. Nordlund, R. F. Stein, and M. Asplund. Solar Surface Convection. *Living Reviews in Solar Physics*, 6:2, April 2009.

G. L. Olson and P. B. Kunasz. Short characteristic solution of the non-LTE transfer problem by operator perturbation. I. The one-dimensional planar slab. *JQSRT*, 38:325–336, 1987.

G. L. Olson, L. H. Auer, and J. R. Buchler. A rapidly convergent iterative solution of the non-LTE radiation transfer problem. *JQSRT*, 35:431–442, 1986.

J. Oxenius. *Kinetic theory of particles and photons. Theoretical foundations of Non-LTE plasma spectroscopy.* Springer, 1986.

E. N. Parker. Magnetic Neutral Sheets in Evolving Fields - Part Two - Formation of the Solar Corona. *ApJ*, 264:642, January 1983.

C. H. Payne. *Stellar Atmospheres; a Contribution to the Observational Study of High Temperature in the Reversing Layers of Stars.* PhD thesis, Radcliffe College, 1925.

G. Peach. Continuous absorption coefficients for non-hydrogenic atoms. *MmRAS*, 73:1, 1970.

A. Peraiah. *An Introduction to Radiative Transfer.* Cambridge University Press, December 2001.

T. M. D. Pereira, M. Asplund, and D. Kiselman. Oxygen lines in solar granulation. II. Centre-to-limb variation, NLTE line formation, blends, and the solar oxygen abundance. *A&A*, 508: 1403–1416, December 2009a.

T. M. D. Pereira, D. Kiselman, and M. Asplund. Oxygen lines in solar granulation. I. Testing 3D models against new observations with high spatial and spectral resolution. *A&A*, 507: 417–432, November 2009b.

E. Peytremann. Line-blanketing and Model Stellar Atmospheres. I. Statistical Method and Calculation of a Grid of Models. *A&A*, 33:203, July 1974.

N. E. Piskunov, F. Kupka, T. A. Ryabchikova, W. W. Weiss, and C. S. Jeffery. VALD: The Vienna Atomic Line Data Base. *A&AS*, 112:525, September 1995.

William H. Press, Saul A. Teukolsky, William T. Vetterling, and Brian P. Flannery. *Numerical recipes in Fortran 90 (2nd ed.): the art of parallel scientific computing.* Cambridge University Press, New York, NY, USA, 1996.

Yu. Ralchenko, A. E. Kramida, J. Reader, and NIST ASD Team. NIST atomic spectra database (version 3.1.5). *http://physics.nist.gov/asd3*, 2009.

I. Ramírez, C. Allende Prieto, L. Koesterke, D. L. Lambert, and M. Asplund. Granulation in K-type dwarf stars. II. Hydrodynamic simulations and 3D spectrum synthesis. *A&A*, 501: 1087–1101, July 2009.

C. A. Ramsbottom, K. L. Bell, and K. A. Berrington. The free-free absorption coefficient of the negative nitrogen ion. *Journal of Physics B Atomic Molecular Physics*, 25:1443–1449, April 1992.

S. Richling, E. Meinköhn, N. Kryzhevoi, and G. Kanschat. Radiative transfer with finite elements. I. Basic method and tests. *A&A*, 380:776–788, December 2001.

B. Ruscic, A. F. Wagner, L. B. Harding, R. L. Asher, D. Feller, D. A. Dixon, K. A. Peterson, Y. Song, X. Qian, C.-Y. Ng, J. Liu, W. Chen, and D. W. Schwenke. On the enthalpy of formation of hydroxyl radical and gas-phase bond dissociation energies of water and hydroxyl. *The Journal of Physical Chemistry A*, 106(11):2727–2747, 2002.

R. J. Rutten. *Radiative Transfer in Stellar Atmospheres.* Utrecht University lecture notes, 8 edition, 2003.

T. A. Ryabchikova, N. E. Piskunov, F. Kupka, and W. W. Weiss. The Vienna Atomic Line Database : Present State and Future Development. *Baltic Astronomy*, 6:244–247, March 1997.

A. J. Sauval and J. B. Tatum. A set of partition functions and equilibrium constants for 300 diatomic molecules of astrophysical interest. *ApJS*, 56:193–209, October 1984.

L. Sbordone, P. Bonifacio, E. Caffau, H. -. Ludwig, N. T. Behara, J. I. Gonzalez Hernandez, M. Steffen, R. Cayrel, B. Freytag, C. Van't Veer, P. Molaro, B. Plez, T. Sivarani, M. Spite, F. Spite, T. C. Beers, N. Christlieb, P. Francois, and V. Hill. The metal-poor end of the Spite plateau. 1: Stellar parameters, metallicities and lithium abundances. *ArXiv e-prints*, March 2010.

G. B. Scharmer. Solutions to radiative transfer problems using approximate lambda operators. *ApJ*, 249:720–730, October 1981.

A. Schuster. Radiation Through a Foggy Atmosphere. *ApJ*, 21:1, January 1905.

M. J. Seaton, Y. Yan, D. Mihalas, and A. K. Pradhan. Opacities for Stellar Envelopes. *MNRAS*, 266:805, February 1994.

C. I. Short and P. H. Hauschildt. A Non-LTE Line-Blanketed Model of a Solar-Type Star. *ApJ*, 618:926–938, January 2005.

A. P. Showman, J. J. Fortney, Y. Lian, M. S. Marley, R. S. Freedman, H. A. Knutson, and D. Charbonneau. Atmospheric Circulation of Hot Jupiters: Coupled Radiative-Dynamical General Circulation Model Simulations of HD 189733b and HD 209458b. *ApJ*, 699:564–584, July 2009.

R. Skartlien. A Multigroup Method for Radiation with Scattering in Three-Dimensional Hydrodynamic Simulations. *ApJ*, 536:465–480, June 2000.

C. Sneden, A. McWilliam, G. W. Preston, J. J. Cowan, D. L. Burris, and B. J. Armosky. The Ultra–Metal-poor, Neutron-Capture–rich Giant Star CS 22892-052. *ApJ*, 467:819, August 1996.

M. Spite, R. Cayrel, V. Hill, F. Spite, P. François, B. Plez, P. Bonifacio, P. Molaro, E. Depagne, J. Andersen, B. Barbuy, T. C. Beers, B. Nordström, and F. Primas. First stars IX - Mixing in extremely metal-poor giants. Variation of the ^{12}C/^{13}C, [Na/Mg] and [Al/Mg] ratios. *A&A*, 455:291–301, August 2006.

P. C. Stancil. Continuous absorption by He_2^+ and H_2^+ in cool white dwarfs. *ApJ*, 430:360–370, July 1994.

M. Steffen and H. Holweger. Line formation in convective stellar atmospheres. I. Granulation corrections for solar photospheric abundances. *A&A*, 387:258–270, May 2002.

R. F. Stein and Å. Nordlund. Simulations of Solar Granulation. I. General Properties. *ApJ*, 499: 914, May 1998.

R. Trampedach, W. Däppen, and V. A. Baturin. A Synoptic Comparison of the Mihalas-Hummer-Däppen and OPAL Equations of State. *ApJ*, 646:560–578, July 2006.

J. Trujillo Bueno and P. Fabiani Bendicho. A Novel Iterative Scheme for the Very Fast and Accurate Solution of Non-LTE Radiative Transfer Problems. *ApJ*, 455:646, December 1995.

H. Uitenbroek. The Effect of Photospheric Granulation on the Determination of the Lithium Abundance in Solar-Type Stars. *ApJ*, 498:427, May 1998.

H. Uitenbroek and J. H. M. J. Bruls. The formation of helioseismology lines. III - Partial redistribution effects in weak solar resonance lines. *A&A*, 265:268–277, November 1992.

A. Unsöld. Konvektion in der Sonnenatmosphäre (nebst einer Bemerkung zur Deutung der Novae). *ZAp*, 1:138, 1930.

A. Unsöld. *Physik der Sternatmosphären, mit besonderer Berücksichtigung der Sonne.* Springer, 1955.

R. S. Urdahl, Y. Bao, and W. M. Jackson. An experimental determination of the heat of formation of C_2 and the C—H bond dissociation energy in C_2H. *Chemical Physics Letters*, 178: 425–428, March 1991.

H. van Regemorter. Rate of Collisional Excitation in Stellar Atmospheres. *ApJ*, 136:906, November 1962.

J. E. Vernazza, E. H. Avrett, and R. Loeser. Structure of the Solar Chromosphere. Basic Computations and Summary of the Results. *ApJ*, 184:605–632, September 1973.

G. A. Victor and A. Dalgarno. Dipole Properties of Molecular Hydrogen. *J. Chem. Phys.*, 50: 2535–2539, March 1969.

A. Vögler, J. H. M. J. Bruls, and M. Schüssler. Approximations for non-grey radiative transfer in numerical simulations of the solar photosphere. *A&A*, 421:741–754, July 2004.

A. Vögler, S. Shelyag, M. Schüssler, F. Cattaneo, T. Emonet, and T. Linde. Simulations of magneto-convection in the solar photosphere. Equations, methods, and results of the MURaM code. *A&A*, 429:335–351, January 2005.

S. Wedemeyer, B. Freytag, M. Steffen, H.-G. Ludwig, and H. Holweger. Numerical simulation of the three-dimensional structure and dynamics of the non-magnetic solar chromosphere. *A&A*, 414:1121–1137, February 2004.

R. Wehrse and W. Kalkofen. Advances in radiative transfer. *A&A Rev.*, 13:3–29, April 2006.

J. H. Williamson. Low-Storage Runge-Kutta Schemes. *Journal of Computational Physics*, 35:48, March 1980.

A. W. Wishart. The bound-free photo-detachment cross-section of H^-. *MNRAS*, 187:59–610, May 1979.

Acknowledgments

A PhD program officially consists of conducting research, giving talks and writing a thesis, but it involves more than that. Traveling, living abroad, meeting and working with different people from different countries, cultures and with different languages is included as much as good times and strenuous times. I was lucky enough to share this episode of life with people who made it a remarkable one, and to whom I would like to express my gratitude.

First of all, I want to thank my supervisor Martin Asplund for his continuous support during the years, and for having the time and patience, despite his many obligations, for long discussions on scientific and non-scientific matters, in person, by email or phone. His everlasting optimism and scientific intuition gave the project a solid foundation on which it could thrive and develop during the years, and he persistently provided motivation, which is an indispensable element for completing a PhD program.

I am also very indebted to Mats Carlsson for inviting me to Oslo and providing his profound and patient advice on the numerous problems of computational science. Without his guidance, I would have certainly got lost in the dense jungle of scientific programming. It was a pleasure to work with the solar physics group at the Institute of Theoretical Astrophysics in Oslo.

At my australian home institute, I would like to thank Mike Bessell for his support with all kinds of smaller and larger issues that appear during a PhD program, Jorge Meléndez for sharing his truly astronomical knowledge with me and all the students and staff at the Research School of Astronomy and Astrophysics for the enjoyable times both at and outside work during my initial stay and regular visits. I am particularly grateful to Tiago and Cathy Pereira, as well as to Wolfgang Kerzendorf for their hospitality on which I relied more than once, and which I hopefully will be able to return. I would also like to thank Remo Collet, Emily McNeil, Andrea Chiavassa, Nicolaas Groeneboom, Emma Kirby and many other friends and colleagues in Australia, Norway and Germany for making the last few years a great time.

My deepest gratitude goes to my family and to Mary Williams for their support and encouragement in all thinkable ways and for accompanying me through the years.

Traveling leaves a lot of time for reading. I found some memorable words in a book by Ryszard Kapuściński, which were presumably not related to astronomy. In some ways, his thoughts nonetheless apply to the stars, and in many ways to us all:

> We are standing in darkness, surrounded by light.

Wolfgang Hayek
August 2010

Appendix A

Plasma physics

A.1 The first law of thermodynamics

Microscopic processes in 3D radiation-hydrodynamical simulations are often treated in the approximation of local thermodynamic equilibrium (LTE); all thermodynamic quantities, such as pressure and temperature, are determined by a pair of independent variables through the equation of state (EOS). The gas density ρ and the internal energy e are directly predicted by the hydrodynamical solver and thus chosen as the fundamental pair of state variables. In the context of realistic simulations of stellar surface granulation, it is not sufficient to use the EOS of an ideal gas, since ionization and molecule formation occur which store a significant amount of latent heat in the gas. It is therefore necessary to use a more general treatment based on the first law of thermodynamics, which will be transformed into hydrodynamical variables in the following.

The first law of thermodynamics for a system in chemical equilibrium is given by the equation

$$dE = TdS - PdV, \tag{A.1}$$

where the internal energy E is a function of entropy S and volume V; T is the temperature and P is the pressure. Mass conservation requires that a gas parcel with mass dm has

$$dm = d(\rho V) = \rho dV + V d\rho \equiv 0. \tag{A.2}$$

This is equivalent to the expression

$$dV = -\frac{V}{\rho} d\rho. \tag{A.3}$$

Inserting Eq. (A.3) in Eq. (A.1) yields

$$dE = TdS + \frac{PV}{\rho} d\rho. \tag{A.4}$$

In fluid dynamics, energy and entropy are redefined as specific internal energy $\epsilon = E/\rho V$ and specific entropy $s = S/\rho V$, which leads to the transformations

$$dE = \rho V d\epsilon + \epsilon d(\rho V) = \rho V d\epsilon \tag{A.5}$$

$$dS = \rho V ds + s d(\rho V) = \rho V ds, \tag{A.6}$$

where Eq. (A.2) has been used. The first law of thermodynamics may now be expressed through hydrodynamical variables:

$$d\epsilon = T ds + \frac{P}{\rho^2} d\rho. \tag{A.7}$$

A.2 Plasma relaxation timescales

The macroscopic fluid description of stellar plasma using the hydrodynamical equations requires that the gas relaxes to a local equilibrium on very short time scales through frequent particle collisions. If gradients in the flow are sufficiently small and typical length scales are larger than particle mean free paths, it is then sufficient to describe gas dynamics using moment equations rather than detailed particle distribution functions. Assuming Coulomb interaction in a plasma of electrons and protons, Goedbloed and Poedts (2004) estimate a relaxation time for electron-electron collisions and electron-proton collisions of

$$\tau_{\mathrm{e}} = \frac{3\sqrt{2}}{8\sqrt{\pi}} \frac{\sqrt{m_{\mathrm{e}}}(kT_{\mathrm{e}})^{3/2}}{\log \Lambda e^4 n_{\mathrm{p}}} \tag{A.8}$$

in the cgs unit system, where m_e is the electron mass, k is the Boltzmann constant, T_e is the temperature of the electron gas, e is the elementary charge, and n_p is the proton density. $\log \Lambda$ is a screening term of the Coulomb potential for particles that are separated by a distance larger than the Debye length (see below), for which Goedbloed and Poedts (2004) use the expression (in cgs units)

$$\log \Lambda = \log \left(\frac{3}{\sqrt{4\pi}} \frac{(kT_{\mathrm{e}})^{3/2}}{e^3 \sqrt{n_{\mathrm{e}}}} \right). \tag{A.9}$$

Below the surface, where hydrogen is dominantly ionized, solar plasma reaches temperatures of $T \sim 20000\,\mathrm{K}$, gas densities of $\rho \sim 10^{-5}\,\mathrm{g\,cm^{-3}}$ and electron densities of $n_{\mathrm{e}} \sim 10^{18}\,\mathrm{cm^{-3}}$. The electron relaxation time (Eq. (A.8)) for such a proton-electron gas is

$$\tau_{\mathrm{e}} \approx 5 \cdot 10^{-14}\,\mathrm{s}. \tag{A.10}$$

The relaxation timescale for proton-proton collisions is given by the same expression (Eq. (A.8)), replacing m_{e} with m_{p}:

$$\tau_{\mathrm{p}} = \sqrt{\frac{m_{\mathrm{p}}}{m_{\mathrm{e}}}} \tau_{\mathrm{e}} \approx 2 \cdot 10^{-12}\,\mathrm{s}. \tag{A.11}$$

The two separate electron and proton fluids still need to equilibrate their individual temperatures through electron-proton collisions. This is the slowest process, since energy exchange between particles of very different masses is inefficient. Goedbloed and Poedts (2004) estimate an equilibration timescale of

$$\tau_{\mathrm{eq}} = \frac{m_{\mathrm{p}}}{2m_{\mathrm{e}}} \tau_{\mathrm{e}}. \tag{A.12}$$

For solar plasma, one obtains

$$\tau_{\mathrm{eq}} \approx 5 \cdot 10^{-11}\,\mathrm{s}. \tag{A.13}$$

The shortest time scales of hydrodynamic flow in simulations of solar surface granulation are set by the propagation times of sound waves, which are numerically resolved with time steps of typically $\Delta t_{\mathrm{hyd}} \approx 0.1\,\mathrm{s}$. Relaxation to an equilibrium state at the bottom of the simulation box thus happens quasi-instantaneously for each simulation time step, and the essential condition

$$\Delta t_{\mathrm{hyd}} \gg \tau_{\mathrm{eq}} \tag{A.14}$$

is easily satisfied. Higher up in the atmosphere, equilibration times increase due to smaller particle densities. Mihalas and Mihalas (1984) estimate $\tau_{\mathrm{eq}} \approx 10^{-6}\,\mathrm{s}$ at $T = 10^4\,\mathrm{K}$ and $n_{\mathrm{e}} = n_{\mathrm{p}} = 10^{14}\,\mathrm{cm^{-3}}$ using similar arguments.

The assumption of instant equilibration can break down above the surface for certain internal degrees of freedom such as hydrogen ionization, requiring a more detailed treatment of the plasma states (see, e.g., Leenaarts and Wedemeyer-Böhm, 2006).

Having established two fluids in thermodynamic equilibrium, a macroscopic description of the plasma as a single fluid further requires a restriction to large length scales. Charge separation of the plasma through thermal fluctuations happens on Debye lengths

$$l_{\mathrm{D}} = \sqrt{\frac{1}{4\pi}\frac{kT}{e^2 n_{\mathrm{e}}}} \tag{A.15}$$

in the cgs unit system. For solar subsurface conditions, charges are separated on average by a Debye length of

$$l_{\mathrm{D}} \approx 10^{-7}\,\mathrm{cm}, \tag{A.16}$$

and the plasma appears as a single fluid. If magnetic fields are included, further restrictions on macroscopic length scales and time scales apply through cyclotron frequencies and radii (see the discussion in Goedbloed and Poedts, 2004).

Appendix B

Numerical methods

B.1 Bézier interpolation of source functions and opacities

The discrete formal solution (Eq. (4.14)) of the radiative transfer equation (Eq. (4.4)) requires interpolating the source function $S(\tau)$ along the short characteristic. While linear interpolation never overshoots, its accuracy is not sufficient in optically thick media, since the discrete expression is not equivalent to the diffusion approximation. Second-order interpolation significantly improves the accuracy, but suffers from strong overshoots where $\Delta S/\Delta\tau$ gradients change rapidly between the upwind and downwind halves of the characteristic. In extreme cases, this can even destabilize the solver and produce spikes in the local flux divergences.

Bézier-type interpolation techniques allow for a direct detection and suppression of such overshoots by virtue of a control point in the polynomial which shapes its curve (see Auer, 2003). A second-order Bézier polynomial may be written in the parameterized form

$$S(t) = S_\mathrm{u}(1-t)^2 + S_0 t^2 + 2S_\mathrm{c}t(1-t), \tag{B.1}$$

where S_u and S_0 are the source functions at the upwind end and the center point of the characteristic, between which interpolation is needed, $t = (\tau - \tau_\mathrm{u})/(\tau_0 - \tau_\mathrm{u})$ is the curve parameter, and S_c is the control point. A Bezièr curve is always bounded by the convex hull of the three points S_u, S_c and S_0. Using the abbreviations

$$\Delta\tau_\mathrm{u} = \tau_0 - \tau_\mathrm{u}; \qquad \Delta\tau_\mathrm{d} = \tau_\mathrm{d} - \tau_0 \tag{B.2}$$

for the optical depths along the characteristic and choosing the control point

$$\begin{aligned} S_\mathrm{c} &= S_0 - \frac{\Delta\tau_\mathrm{u}}{2} S_0' \\ &= S_0 - \frac{\Delta\tau_\mathrm{u}}{2}\left(\frac{\Delta\tau_\mathrm{d}}{\Delta\tau_\mathrm{u}+\Delta\tau_\mathrm{d}}\frac{S_0 - S_\mathrm{u}}{\Delta\tau_\mathrm{u}} + \frac{\Delta\tau_\mathrm{u}}{\Delta\tau_\mathrm{u}+\Delta\tau_\mathrm{d}}\frac{S_\mathrm{d} - S_0}{\Delta\tau_\mathrm{d}}\right) \end{aligned}$$

yields second-order interpolation of S, which now also depends on the source function S_d at the downwind end. Introducing the three functions

$$\begin{aligned} U_0(t) &= 1 - e^{-t} \\ U_1(t) &= t - U_0(t) \\ U_2(t) &= t^2 - 2U_1(t), \end{aligned}$$

and evaluating the integral of the Bézier polynomial results in the familiar second-order integration constants for Eq. (4.14),

$$\begin{aligned}
\Psi_{\rm u} &= U_0(\Delta\tau_{\rm u}) + \frac{U_2(\Delta\tau_{\rm u}) - (\Delta\tau_{\rm d} + 2\Delta\tau_{\rm u})U_1(\Delta\tau_{\rm u})}{\Delta\tau_{\rm u}(\Delta\tau_{\rm u} + \Delta\tau_{\rm d})} \\
\Psi_0 &= \frac{(\Delta\tau_{\rm u} + \Delta\tau_{\rm d})U_1(\Delta\tau_{\rm u}) - U_2(\Delta\tau_{\rm u})}{\Delta\tau_{\rm u}\Delta\tau_{\rm d}} \\
\Psi_{\rm d} &= \frac{U_2(\Delta\tau_{\rm u}) - \Delta\tau_{\rm u}U_1(\Delta\tau_{\rm u})}{\Delta\tau_{\rm d}(\Delta\tau_{\rm u} + \Delta\tau_{\rm d})}
\end{aligned}$$

(cf. Eq. 8 and 9 in Kunasz and Auer, 1988). If the source functions $S_{\rm u}$, S_0 and $S_{\rm d}$ have an extremum at S_0, choosing $S_{\rm c} = S_0$ enforces $S_0' = 0$, yielding the constants

$$\begin{aligned}
\Psi_{\rm u} &= U_0(\Delta\tau_{\rm u}) + \frac{U_2(\Delta\tau_{\rm u}) - 2\Delta\tau_{\rm u}U_1(\Delta\tau_{\rm u})}{\Delta\tau_{\rm u}^2} \\
\Psi_0 &= \frac{2\Delta\tau_{\rm u}U_1(\Delta\tau_{\rm u}) - U_2(\Delta\tau_{\rm u})}{\Delta\tau_{\rm u}^2} \\
\Psi_{\rm d} &= 0.
\end{aligned}$$

Overshoots are avoided by limiting $S_{\rm c}$ to the range of the data points: $\min(S_{\rm u}, S_0) \leq S_{\rm c} \leq \max(S_{\rm u}, S_0)$. If $S_{\rm c}$ lies outside these limits, choosing $S_{\rm c} = S_{\rm u}$ results in the constants

$$\begin{aligned}
\Psi_{\rm u} &= U_0(\Delta\tau_{\rm u}) - \frac{U_2(\Delta\tau_{\rm u})}{\Delta\tau_{\rm u}^2} \\
\Psi_0 &= \frac{U_2(\Delta\tau_{\rm u})}{\Delta\tau_{\rm u}^2} \\
\Psi_{\rm d} &= 0.
\end{aligned}$$

Note that, contrary to the first two cases, suppressing such overshoots leads to discontinuous left-hand and right-hand derivatives at S_0.

Optical depths are computed in an analogue fashion to avoid negative results. A second-order Bézier polynomial $\chi(s)$ interpolates opacities over the path length Δs along the ray; integration over s yields the optical depth interval

$$\Delta\tau = \int_0^{\Delta s} \chi(\sigma) d\sigma = \frac{\Delta s}{3}\left(\chi_{\rm u} + \chi_0 + \chi_{\rm c}\right), \tag{B.3}$$

where the control point $\chi_{\rm c}$ is selected according to the same criteria as discussed above for $S_{\rm c}$.

B.2 Local cubic monotonic interpolation

The radiative transfer solver uses local cubic interpolation for interpolating data from the hydrodynamical grid onto the characteristics grid. This choice of method improves the accuracy compared to linear interpolation, while ensuring local control of the interpolating polynomial to reduce artifacts. In addition to being a one-pass algorithm, the method also exhibits good computational performance through its instruction-per-data ratio, which is well-suited for modern multi-core CPUs, where high computation speeds are contrasted with slow memory access.

2D interpolation is approximated by consecutive 1D interpolation using a cubic polynomial

$$f(t) = at^3 + bt^2 + ct + d, \tag{B.4}$$

with the curve parameter $t \in [0,1]$. The coefficients a, b, c and d depend on the adjacent data points f_1 and f_2 and their derivatives f_1' and f_2'. Inserting the data and reordering the terms, the polynomial may be rewritten in the form

$$f(t) = \alpha(t) f_1 + \beta(t) f_2 + \gamma(t) f_1' + \delta(t) f_2', \tag{B.5}$$

where the interpolation weights α, β, γ and δ now depend on the parameter t:

$$\begin{aligned}
\alpha(t) &= 2t^3 - 3t^2 + 1 \\
\beta(t) &= 3t^2 - 2t^3 \\
\gamma(t) &= \left(t^3 - 2t^2 + t\right) \Delta x \\
\delta(t) &= \left(t^3 - t^2\right) \Delta x
\end{aligned}$$

with the grid spacing Δx between the two data points. The shape of the curve is defined by the derivatives f_1' and f_2'. A natural choice is the mean of the left-handed and right-handed difference quotients f_L' and f_R' at both end points. An unweighted arithmetic mean leads to wiggles and overshoots where strong gradients appear. We therefore adopt a recipe by Fritsch and Butland (1984), which uses a weighted harmonic mean

$$f' = \begin{cases} \dfrac{f_\mathrm{L}' f_\mathrm{R}'}{(1-\alpha) f_\mathrm{L}' + \alpha f_\mathrm{R}'} & f_\mathrm{L}' f_\mathrm{R}' > 0 \\ 0 & f_\mathrm{L}' f_\mathrm{R}' \leq 0 \end{cases} \tag{B.6}$$

with the weighting factor

$$\alpha = \frac{1}{3}\left(1 + \frac{\Delta x_\mathrm{R}}{\Delta x_\mathrm{L} + \Delta x_\mathrm{R}}\right), \tag{B.7}$$

which depends on the grid spacing Δx_L and Δx_R on the left and right sides of the data point. The weighted harmonic mean biases f' towards the smaller of the two difference quotients f_L' and f_R' where strong gradients occur, effectively suppressing overshoots.

Quadratic interpolation uses only one of the two derivatives f_1' and f_2', depending on the interpolation parameter t. The interpolation coefficients are

$$\begin{array}{llll}
t \leq \frac{1}{2}: & & t > \frac{1}{2}: & \\
\\
\alpha(t) = 1 - t^2 & & \alpha(t) = (1-t)^2 & \\
\beta(t) = t^2 & & \beta(t) = t(2-t) & \\
\gamma(t) = t(1-t)\Delta x & & \gamma(t) = 0 & \\
\delta(t) = 0 & & \delta(t) = t(t-1)\Delta x &
\end{array} \tag{B.8}$$

B.3 Angle quadrature

Moment integrals of specific intensities yield the mean intensity J and radiative flux $\mathbf{F}$, which are frequently needed for solving radiative transfer problems. Integration over solid angle is approximated by an appropriate quadrature. The best choice of method and order of accuracy depends on the problem: Gauss-type quadrature generally yields good accuracy, providing a mathematically optimal choice of quadrature nodes and weights. However, it is only applicable to integrals in one dimension, and low quadrature orders may introduce directional bias through the angle distribution. Gauss-Legendre quadrature is commonly used for radiative transfer calculations to approximate the integral over polar angle $\mu = \cos\theta$, supplemented by

n	μ_1	μ_2	μ_3	μ_4
2	±0.57735027			
3	0.0	±0.77459667		
4	±0.33998104	±0.86113631		
5	0.0	±0.53846931	±0.90617985	
6	±0.23861919	±0.66120939	±0.93246951	
7	0.0	±0.40584515	±0.74153119	±0.94910791
8	±0.18343464	±0.52553241	±0.79666648	±0.96028986

n	w_1	w_2	w_3	w_4
2	1.0			
3	0.88888889	0.55555556		
4	0.65214515	0.34785485		
5	0.56888889	0.47862867	0.23692689	
6	0.46791393	0.36076157	0.17132449	
7	0.41795918	0.38183005	0.27970539	0.12948497
8	0.36268378	0.31370665	0.22238103	0.10122854

Table B.1: Gauss-Legendre quadrature nodes μ and weights w for quadrature orders n, computed using an algorithm from the Numerical Recipes (Press et al., 1996).

the trapezoid rule for the integral over azimuth angle ϕ in 3D. Table B.1 lists quadrature nodes and weights for the first eight quadrature orders.

Carlson (1963) proposed a ray discretization that is invariant under rotation by 90° to avoid directional bias when a transport equation is solved numerically. The requirement of invariance leads to a set of angles with equal projection factors for the three spatial axes. The lowest order ($n = 2$) is equivalent to Gauss-Legendre quadrature with a 4-point trapezoid rule. Figure B.1 shows the distribution of quadrature nodes on an octant (see Table B.2 for the numerical values). The weighting of the nodes is also constrained by the invariance. As nodes lie on concentric circles around the center of the quadrant (e.g., the quadrature nodes lie on two circles for $n = 8$), symmetry requires that all nodes on the same circle receive the same weight; the nodes closer to the axes are weighted higher.

n	μ_1	μ_2	μ_3	μ_4
2	0.57735027			
4	0.33333333	0.88191710		
6	0.25819889	0.68313005	0.93094934	
8	0.21821790	0.57735027	0.78679579	0.95118972

n	w_1	w_2	w_3	
2	1.00000000			
4	0.33333333			
6	0.15000000	0.18333333		
8	0.07075470	0.09138352	0.12698139	

Table B.2: Projection factors μ (upper panel) and weights w (lower panel) for Carlson A quadrature of order $n = 2, 4, 6, 8$.

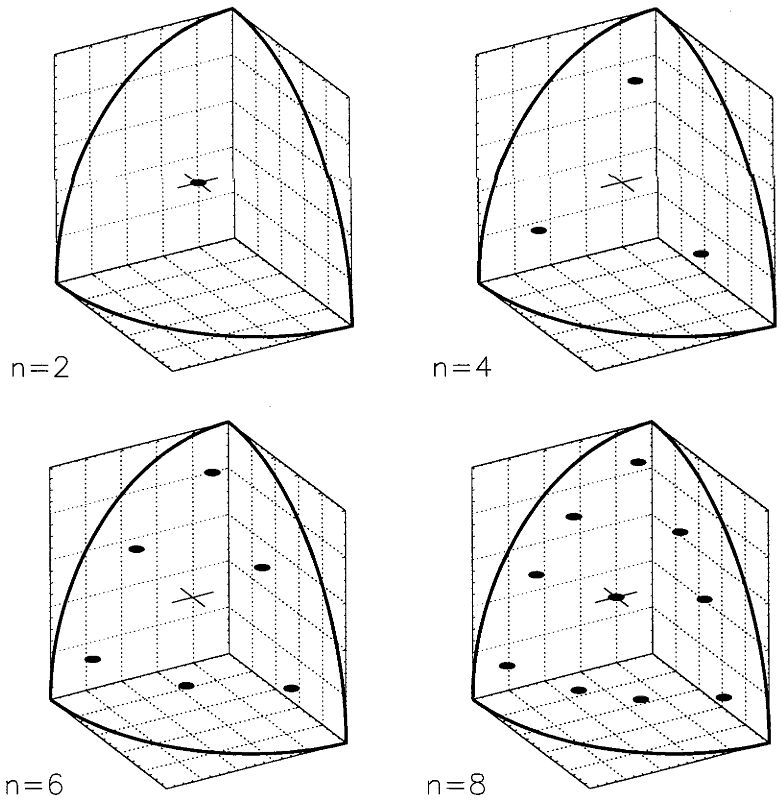

Figure B.1: Distribution of Carlson A quadrature angles on an octant with increasing quadrature order $n = 2, 4, 6, 8$ (upper left to lower right, see Table B.2). Note the alignment of quadrature angles on concentric circles around the center of the octant (crosses).

Appendix C

Opacities

C.1 Line scattering with the van Regemorter formula

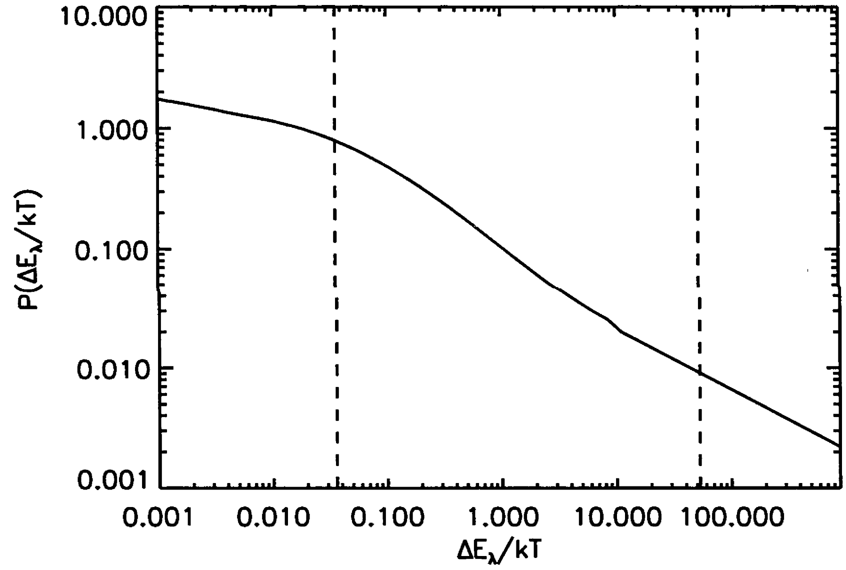

Figure C.1: Dependence of the tabulated Gaunt factor integral $P(\Delta E_\lambda, T)$ for collisions of electrons with neutral atoms in the van Regemorter (1962) formula on the transition energy ΔE_λ and the gas temperature T. The dashed lines mark the boundaries for typical values of $\Delta E_\lambda / kT$ found in solar surface convection simulations (Sect. 4.5.1).

The photon destruction probabilities in line transitions may be estimated using the semi-empirical van Regemorter (1962) formula to obtain electron collision rates, following the discussion in Skartlien (2000). Neglecting other contributions from, e.g., collisions with neutral hydrogen atoms, the de-excitation rate for electron collisions according to this formula is given by

$$C_{21} \sim \lambda^3 N_\mathrm{e} T^{-1/2} A_{21} P(\Delta E_\lambda, T), \tag{C.1}$$

where λ is the transition wavelength, N_e is the electron density, T is the gas temperature, and A_{21} is the Einstein coefficient for the corresponding spontaneous radiative transition. The function $P(\Delta E_\lambda, T)$ abbreviates the velocity integral over the empirically calibrated Gaunt factor of the scattered electron, and depends on the transition energy ΔE_λ and the gas temperature T. We adopt the tabulated data for neutral atoms of van Regemorter (1962), see Fig. C.1.

The photon destruction probability for a two-level atom is given by

$$\epsilon_\lambda = \frac{\kappa_\lambda}{\kappa_\lambda + \sigma_\lambda} = \frac{C_{21}}{C_{21} + A_{21} + B_{21} B_\lambda}, \tag{C.2}$$

where B_{21} is the rate for induced de-excitation, and B_λ is the Planck function. Neglecting the induced de-excitation term, Eq. (C.2) simplifies to

$$\epsilon_\lambda \approx \frac{1}{1 + A_{21}/C_{21}}. \tag{C.3}$$

ϵ_λ is independent of the actual transition after inserting the van Regemorter formula Eq. (C.1), and thus only a function of λ, N_e and T.

Line opacities in stellar spectra often combine contributions from many transitions at a given wavelength. The total monochromatic photon destruction probability of an opacity sample at wavelength λ is given by the sum over all transitions,

$$\epsilon^1_\lambda = \frac{\sum_i \kappa^1_{\lambda,i}}{\sum_i \chi^1_{\lambda,i}}. \tag{C.4}$$

Inserting Eq. (C.3), thus assuming the above mentioned approximations, yields

$$\epsilon^1_\lambda \approx \frac{\sum_i \epsilon_\lambda \chi^1_{\lambda,i}}{\sum_i \chi^1_{\lambda,i}} = \epsilon_\lambda, \tag{C.5}$$

where the equality holds since ϵ_λ is independent of the actual transition i. The absorption and scattering contributions κ^1_λ and σ^1_λ to each opacity sample χ^1_λ are then isolated using ϵ^1_λ and added to the coefficients of the continuum processes (see Table C.1).

C.2 Continuum opacity sources

Table C.1: Continuum opacity sources

Absorber and process	Reference
H^- b-f	Broad and Reinhardt (1976); Wishart (1979)
H^- f-f	Bell and Berrington (1987)
H I b-f, f-f	Karzas and Latter (1961)
H I+H I	Doyle (1968)
H I+He I	Gustafsson and Frommhold (2001)
H_2+H I	Gustafsson and Frommhold (2003)
H_2+He I	Jørgensen et al. (2000)
H_2+H_2	Borysow et al. (2001)
H_2^- f-f	Bell (1980)
H_2 photo-dissociation	Allison and Dalgarno (1969)
H_2^+ b-f, f-f	Stancil (1994)
He^- f-f	John (1995)

continued on next page

Absorber and process	Reference
He I b-f	TOPbase[1]
He I f-f	Peach (1970)
He II b-f	TOPbase[1]
C^- f-f	Bell et al. (1988)
C I b-f	Nahar and Pradhan (1991)
C I f-f	Peach (1970)
C II b-f	Nahar (1995, 2002)
C II f-f	Peach (1970)
C III b-f	Nahar and Pradhan (1997)
N^- f-f	Ramsbottom et al. (1992)
N I b-f	Nahar and Pradhan (1997)
N II b-f	Nahar and Pradhan (1991)
N III b-f	Nahar and Pradhan (1997)
O^- f-f	John (1975)
O I, O II b-f	Nahar (1998)
O III b-f	Nahar and Pradhan (1994b)
Ne I, Ne II, Ne III b-f	TOPbase[1]
Na I, Na II, Na III b-f	TOPbase[1]
Mg I, Mg II, Mg III b-f	TOPbase[1]
Al I, Al II, Al III b-f	TOPbase[1]
Si I b-f	Nahar and Pradhan (1993)
Si II b-f	Nahar (1995)
Si III b-f	TOPbase[1]
S I b-f	TOPbase[1]
S II b-f	Nahar (1995)
S III b-f	Nahar (2000)
Ar I, Ar II, Ar III b-f	TOPbase[1]
Ca I, Ca II, Ca III b-f	TOPbase[1]
Fe I b-f	Bautista (1997)
Fe II b-f	Nahar and Pradhan (1994a)
Fe III b-f	Nahar (1996)
Ni II b-f	Bautista (1999)
CO^- f-f	John (1975)
H_2O^- f-f	John (1975)
OH b-f	Kurucz et al. (1987)
CH b-f	Kurucz et al. (1987)
H I scattering	Gavrila (1967)
H_2 scattering	Victor and Dalgarno (1969)
e^- scattering	Thomson
He I scattering	Langhoff et al. (1974)

[1] Contains Opacity Project data (Seaton et al., 1994)

Appendix D

The SCATE code

The SCATE spectral line formation code for stellar atmospheres computes 3D radiative transfer for blended spectral lines and a background continuum with coherent isotropic scattering. Local thermodynamic equilibrium (LTE) is assumed to compute level populations for lines and continuous opacity sources, using Saha-Boltzmann equilibrium calculations. A lookup-table is used for monochromatic continuum opacities, continuum photon destruction probabilities, Saha ionization equilibria, molecular equilibria (for hydrogen, carbon, nitrogen and oxygen) and partition functions to speed up the 3D line formation computations, in particular when a time-series of profiles is required.

The code was originally developed by Å. Nordlund and later extended by M. Asplund, R. Trampedach, R. Collet and T. Pereira. The author of this thesis rewrote most of the code in Fortran 90 language and implemented some optimizations to enhance code performance, including OpenMP parallelization over ray angles for long characteristics computations. A short characteristics solver was added as well, which provides a source function with continuum scattering.

D.1 Numerical solution of the radiative transfer equation

Computation of a line profile is divided into two steps: a short-characteristics-based radiative transfer solver with Gauss-Seidel-type convergence acceleration (Trujillo Bueno and Fabiani Bendicho, 1995) computes the monochromatic radiation field at each frequency point ν across the profile to obtain the continuum source function with coherent scattering. The Gauss-Seidel method uses an upper/lower triangular approximate Λ^* operator, which computes source function corrections during the formal solution and yields fast convergence; see Hayek et al. (2010) for a detailed description of the implementation. The solver takes the anisotropy of the combined continuum and line source function in the observer's frame into account, which is due to the angle-frequency coupling of line opacity through Doppler-shifts. Linear or higher-order local interpolation is available for translating opacities, source functions and upwind intensities onto the characteristics grid. The discretized source function integral is computed using linear interpolation or second-order interpolation, which is required at high optical depths to correctly reproduce the diffusion approximation.

A second solver delivers angle-resolved surface intensities and surface fluxes for obtaining the line profiles. SCATE offers the differential Feautrier (1964) scheme as well as an integral scheme which is based on the formal solution of the transfer equation. The integral scheme computes the source function integral using the same interpolation methods as the scattering solver. The radiative transfer equation is solved on long characteristics that begin in the top layer of the hydrodynamical mesh and span across the simulation domain, until they reach the optically thick diffusion region. Before each calculation of surface intensities, the 3D model atmosphere is tilted into the ray direction using local cubic interpolation.

Both solution steps are parallelized over angle using OpenMP directives for shared-memory architectures, allowing for fine resolution of the angle-frequency coupling in the scattering computation and for integrating surface intensities over a large number of rays when radiative fluxes are needed. A modern 8-core cluster node delivers a line profile with scattering (see Sect. 7.4) in $\approx 15\,\mathrm{min}$ per atmosphere snapshot, while the radiative transfer problem without scattering is solved within $< 1\,\mathrm{min}$.

`SCATE` uses partial grid refinement on the vertical axis to improve the resolution of continuum optical surfaces. Additional layers are automatically inserted into the 3D model where vertical optical depth steps are large using cubic spline interpolation. The mesh is truncated when the optically thick diffusion region is reached and the radiation field is entirely thermal.

D.2 Line opacities in the LTE approximation

The line opacity at frequency ν' in the local rest frame of a gas parcel in the stellar atmosphere is computed using the expression

$$\chi_{\nu'} = \frac{\pi e^2}{m_\mathrm{e} c} f_\mathrm{lu} n_\mathrm{l} \left[1 - e^{-\frac{h\nu'}{kT}}\right] \psi\left(\nu' - \nu_0'\right), \tag{D.1}$$

with the electron charge e, the electron mass m_e, the speed of light c, the Planck constant h, the Boltzmann constant k and the temperature T. Literature values of the oscillator strength f_lu are usually combined with the statistical weight g_l of the lower level of the transition, which enters the opacity through Boltzmann excitation factors for the level population density n_l. The code computes Saha-Boltzmann equilibria with tabulated partition functions that were calculated using the NIST database (Ralchenko et al., 2009). Molecule formation is taken into account for 12 important species by computing LTE equilibrium populations (see Table D.1). The term in brackets in Eq. (D.1) corrects the line opacity for stimulated emission, assuming atomic level populations in LTE.

The line profile ψ is given by a Voigt function around the laboratory wavelength ν_0' of the transition. Doppler-shifts through macroscopic velocity fields $\mathbf{u}$ in the observer's frame are included in the non-relativistic approximation, which yields the line profile

$$\psi\left(\nu - \nu_0\right) = \psi\left(\nu - \nu_0' - \nu_0' \frac{\hat{\mathbf{n}} \cdot \mathbf{u}}{c}\right) \tag{D.2}$$

in the observer's frame, for a ray in direction $\hat{\mathbf{n}}$ and gas velocity $\mathbf{u}$. The vectorizable recipe of Hui et al. (1978) is used to evaluate the Voigt profile numerically.

Line profiles include Doppler broadening to account for shifts through random thermal gas motion. Microturbulent broadening may be included in the computations, but it is generally unnecessary for line formation with 3D hydrodynamical atmospheres (see the discussion in Asplund et al., 2000b).

Natural line broadening through radiative de-excitation is set by the profile width parameter Γ^rad using laboratory data if available, or it may be estimated using the expression

$$\Gamma^\mathrm{rad} \approx \frac{8\pi^2 e^2}{m_\mathrm{e} c} \frac{1}{\lambda^2} \frac{g_\mathrm{l}}{g_\mathrm{u}} f_\mathrm{lu}, \tag{D.3}$$

which assumes a two level atom; λ is the transition wavelength and g_u is the statistical weight of the upper level.

Pressure broadening through collions of neutral atoms and ions with neutral hydrogen atoms is taken into account in the impact approximation. Profile widths are based on quantum mechanical calculations by Anstee and O'Mara (1995); Barklem and O'Mara (1997); Barklem et al. (1998, 2000a); Barklem and O'Mara (2001); Barklem and Aspelund-Johansson (2005). Collisional cross-sections are estimated using the power law

$$\sigma(v) = \sigma(v_0)\left(\frac{v}{v_0}\right)^{-\alpha}, \tag{D.4}$$

where v is the relative velocity of the particle and the perturbing H I atom, $\sigma(v_0)$ and α are tabulated, and v_0 is a reference velocity. The width parameter of the Lorentzian broadening profile is obtained by integrating over a Maxwell-Boltzmann distribution for v, which yields

$$\gamma^{\mathrm{H\,I}} = 2\left(\frac{4}{\pi}\right)^{\frac{\alpha}{2}} \Gamma\left(\frac{4-\alpha}{2}\right) \bar{v}\sigma(v_0)\left(\frac{\bar{v}}{v_0}\right)^{-\alpha} n_{\mathrm{H\,I}}, \tag{D.5}$$

with the gamma function Γ, the number density $n_{\mathrm{H\,I}}$ of neutral hydrogen, and the average velocity $\bar{v} = \sqrt{8kT/\pi\mu}$, where μ is the reduced mass of the particle and the perturbing H I atom. In the absence of quantum mechanical data, the classical Unsöld (1955) approximation is used in the formulation found in Gray (2005):

$$\log\gamma^{\mathrm{H\,I}} = 20.0 + 0.4\log C_6 + \log P - 0.7\log T, \tag{D.6}$$

for quantities given in cgs units; P is the gas pressure. The interaction constant C_6 is approximated through the expression

$$C_6 = 0.3\cdot 10^{-30}\left[\left(\chi_{\mathrm{u}}^{\mathrm{ion}}\right)^{-2} - \left(\chi_{\mathrm{l}}^{\mathrm{ion}}\right)^{-2}\right], \tag{D.7}$$

with the ionization potentials $\chi_{\mathrm{u}}^{\mathrm{ion}}$ and $\chi_{\mathrm{l}}^{\mathrm{ion}}$ from the upper and lower level of the transition, both given in eV. For the more complicated case of hydrogen lines, broadening recipes of N. Piskunov and P. S. Barklem (priv. comm.) are available. The contribution from He I atoms to pressure broadening is estimated through

$$\gamma^{\mathrm{H\,I+He\,I}} \approx \gamma^{\mathrm{H\,I}}\left(1.0 + c_{\mathrm{He\,I}}\frac{n_{\mathrm{He\,I}}}{n_{\mathrm{H\,I}}}\right), \tag{D.8}$$

using an approximate scaling factor $c_{\mathrm{He\,I}} \approx 0.41$.

Molecule	Dissociation energy
H_2	Sauval and Tatum (1984)
H_2^+	Sauval and Tatum (1984)
H_2O	Ruscic et al. (2002)
CH	Sauval and Tatum (1984)
C_2	Urdahl et al. (1991)
CN	Huang et al. (1992)
CO	Eidelsberg et al. (1987)
OH	Ruscic et al. (2002)
O_2	Sauval and Tatum (1984)
NH	Marquette et al. (1988)
N_2	Sauval and Tatum (1984)
NO	Sauval and Tatum (1984)

Table D.1: Molecular data included in the equilibrium calculations; partition functions were computed using the NIST database (Ralchenko et al., 2009).